# DYNAMICS OF THE NOVA SCOTIA CURRENT AND LINKAGES WITH ATLANTIC SALMON MIGRATION PATTERNS OVER THE SCOTIAN SHELF

by

Mathieu Dever

Submitted in partial fulfillment of the requirements
for the degree of Doctor of Philosophy

at

Dalhousie University
Halifax, Nova Scotia
March 2017

*À mes parents, pour leur soutien inconditionnel tout au long de ce marathon académique,*

*And to my wife, for encouraging me every time I wanted to stop running.*

# TABLE OF CONTENTS

# LIST OF TABLES

# LIST OF FIGURES

# ABSTRACT

Over the 2008-2015 period, the Ocean Tracking Network provided unprecedented spatiotemporal coverage of the hydrography and currents along the Halifax Line (HL) on the Scotian Shelf, using several different monitoring techniques (e.g., moorings and underwater gliders). The observations are analyzed here to provide an extensive description of the physical oceanographic conditions over the Scotian Shelf, as well as the spatiotemporal variability observed over this period. The analysis of observations identifies the distribution of key water masses present along the HL. The water mass analysis demonstrates that the large warming event observed in 2012 was primarily due to the advection of already anomalously warm water from the Shelf Slope. The ocean circulation along the HL during this period is examined, with a focus on the seasonal cycle and the inter-annual variability of the Nova Scotia Current (NSC). A conceptual model is developed to investigate the main mechanisms driving the NSC. The relative roles of buoyancy-driven and wind-driven flows to the NSC are estimated at the HL to study the seasonal variability of the forcing and the relative importance of these two mechanisms in driving the NSC. Generally, the NSC is dominated by the buoyancy-driven component of the current, throughout the year and at all four transects between Cabot Strait and Cape Sable. The relative contributions of buoyancy and alongshore surface winds to the NSC's dynamics are remarkably similar across transects having the same coastal orientation, but significantly vary where the coastline orientation changes. The newly-acquired oceanographic knowledge along the HL is also combined with acoustic detections of Atlantic salmon postsmolts coming from the Penobscot River to study the temporal and spatial distribution of the migrating fish in the context of oceanographic conditions. It is shown that postsmolts tend to be in greater abundance in the colder and fresher coastal water mass, while the abundance is not related to the direction or magnitude of local currents.

# List of Abbreviations and Symbols Used

| Abbreviation | Description |
|---|---|
| ADCP | Acoustic Doppler Current Profiler |
| AZMP | Atlantic Zone Monitoring Program |
| AZOMP | Atlantic Zone Offshore Monitoring Program |
| CBSs | Cabot Strait Subsurface |
| CBS-CIL | Cabot Strait Cold Intermediate Layer |
| CIL | Cold Intermediate Layer |
| CTD | Conductivity-Temperature-Depth |
| EOF | Empirical Orthogonal Function |
| GoM | Gulf of Maine |
| GPS | Global Positioning System |
| GSL | Gulf of St. Lawrence |
| GSW | Gibbs-SeaWater |
| HEOF | Hilbert Empirical Orthogonal Function |
| HL | Halifax Line |
| HWI | Hydrographic Wind Index |
| InLC | Inshore Labrador Current |
| LSW | Labrador Slope Water |
| MSS | Multi-Station Sequences |
| NSC | Nova Scotia Current |
| OTN | Ocean Tracking Network |
| OTN-HL | Ocean Tracking Network Halifax Line |

| Abbreviation | Description |
|---|---|
| PSD | Power Spectral Density |
| SAB | St. Anns Bank |
| SI | Sinuosity Index |
| SVD | Singular Value Decomposition |
| T-S | Temperature-Salinity |
| TWI | Traditional Wind Index |
| WSW | Warm Slope Water |

| Symbol | Description | Units |
|---|---|---|
| Chapter 2 | | |
| $\theta_p$ | Angle of rotation of coordinate system (clockwise) | degrees |
| $u_0$ | Eastward velocity | m/s |
| $v_0$ | Northward velocity | m/s |
| $\bar{\cdot}$ | Average operator | |
| $u$ | Alongshore velocity | m/s |
| $v$ | Cross-shore velocity | m/s |
| $D$ | Distance between two sets of coordinates | m |
| $R_T$ | Earth radius | m |
| $\phi_i$ | longitude | degrees |
| $\lambda_i$ | latitude | degrees |
| $g$ | Gravitational acceleration | m/s$^2$ |
| $f$ | Coriolis parameter | 1/s |
| $\sigma_\theta$ | Potential density | kg/m$^3$ |
| $\epsilon(\Delta^2)$ | Truncation error at a second order of accuracy | |
| $R_b$ | Rossby radius of deformation | m |
| $g'$ | Reduced gravitational acceleration | m/s$^2$ |

| Symbol | Description | Units |
|---|---|---|
| $H$ | Thickness of the upper-layer | m |
| $\rho_a$ | Density of ambient shelf water | kg/m$^3$ |
| $\rho_c$ | Density of coastal plume water | kg/m$^3$ |
| $f_{44}$ | Coriolis parameter at 44°N | 1/s |
| $R^2$ | Coefficient of determination | |
| $c_{xy}(\tau)$ | Cross-covariance function between $x$ and $y$ | |
| $\tau$ | Lag between the two time series | |
| $N$ | Length of time series | |
| $.^\star$ | Complex conjugate operator | |
| $\rho_{xy}(\tau)$ | Normalized cross-covariance | |
| $H(\cdot)$ | Hilbert transform operator | |
| $\mathbf{u}$ | Complex alongshore velocity field | m/s |
| $n$ | HEOF mode $n$ | |
| $\lambda_n$ | SVD eigenvalue of mode $n$ | |
| $B_n$ | HEOF of mode $n$ | |
| $A_n$ | HEOF score of mode $n$ | |
| $\sigma_n^2$ | Variance explained by HEOF mode $n$ | m$^2$/s$^2$ |
| $\theta_n$ | Spatial phase function of mode $n$ | degrees |
| $\Re\{\}$ | Real part of a complex number | |
| $\Im\{\}$ | Imaginary part of a complex number | |
| $S_n$ | Spatial amplitude function of mode $n$ | m/s |
| $\phi_n$ | Temporal phase function of mode $n$ | degrees |
| $R_n$ | Temporal amplitude function of mode $n$ | m/s |
| $a$ | Wave amplitude | |
| $k$ | Wavenumber in $x$-direction | 1/m |

| Symbol | Description | Units |
|---|---|---|
| $\omega$ | Wave frequency | 1/s |
| Chapter 3 | | |
| $\delta^{18}O$ | Ratio of stable isotopes oxygen-18 and oxygen-16 | |
| $T$ | Temperature | °C |
| $S$ | Salinity | PSU |
| $P$ | Percentage | |
| $R^2$ | Coefficient of determination | |
| $t$ | Time | s |
| $p$ | p-value | |
| $r$ | Correlation coefficient | |
| Chapter 4 | | |
| $c_{UU}$ | Cross-covariance function between alongshore currents | |
| $c_{VV}$ | Cross-covariance function between cross-shore currents | |
| $R^2$ | Coefficient of determination | |
| $\sigma$ | Standard deviation | |
| $N$ | Length of time series | |
| $\theta_n$ | Spatial phase function | degrees |
| $S_n$ | Spatial amplitude function | m/s |
| $\phi_n$ | Temporal phase function | degrees |
| $R_n$ | Temporal amplitude function | m/s |
| $\bar{\cdot}$ | Average operator | |
| $U_{wind}$ | Wind-driven alongshore flow | m/s |
| $U_{geo}$ | Buoyancy-driven alongshore flow | m/s |
| $\partial\cdot$ | Partial derivative | |
| $(u, v)$ | Alongshore and cross-shore velocities | m/s |

| Symbol | Description | Units |
|---|---|---|
| $f$ | Coriolis parameter | 1/s |
| $\rho_0$ | Reference water density | kg/m$^3$ |
| $P$ | Pressure | kg/m/s$^2$ |
| $A_V$ | Vertical eddy viscosity parameter | m$^2$/s |
| $g$ | Gravitational acceleration | m/s$^2$ |
| $(u_{geo}, v_{geo})$ | Alongshore and cross-shore geostrophic velocities | m/s |
| $\rho_a$ | Density of ambient shelf water | kg/m$^3$ |
| $\rho_c$ | Density of coastal plume water | kg/m$^3$ |
| $h_f$ | $z$-coordinate of the interface in a two-layer system | m |
| $(u_{wind}, v_{wind})$ | Alongshore and cross-shore wind-driven velocities | m/s |
| $(U_{wind}, V_{wind})$ | Depth-averaged wind-driven velocities | m/s |
| $\tau_{sx}$ | Alongshore surface wind stress | kg/m/s$^2$ |
| $\tau_{bx}$ | Alongshore bottom stress | kg/m/s$^2$ |
| $\tau_{sy}$ | Cross-shore surface wind stress | kg/m/s$^2$ |
| $\tau_{by}$ | Cross-shore bottom stress | kg/m/s$^2$ |
| $h$ | Water depth | m |
| $g'$ | Reduced gravitational acceleration | m/s$^{-2}$ |
| $H$ | Frontal depth | m |
| $L$ | Frontal width | m |
| $Q_{geo}$ | Alongshore transport within coastal plume | m$^3$/s |
| $R_b$ | Rossby radius of deformation | m |
| $U_{dis}$ | Buoyancy-driven alongshore flow determined from river discharge $Q_r$ | m/s |
| $Q_r$ | River discharge | m$^3$/s |
| $\rho_r$ | Average river water density | kg/m$^3$ |

| Symbol | Description | Units |
|---|---|---|
| $g'_r$ | Reduced gravitational acceleration based on river water density | m/s$^{-2}$ |
| $\rho_{air}$ | Average air density | kg/m$^3$ |
| $C_{10}$ | Surface drag coefficient | |
| $U_{10}$ | Alongshore wind speed at 10 m | m/s |
| $C_{Da}$ | Depth-averaged bottom drag coefficient | |
| $C_D$ | Bottom drag coefficient | |
| $\Delta L_s$ | Surface change in frontal width | m |
| $z_{Ek}$ | Ekman depth | m |
| $\Delta t$ | Adjustment time | s |
| $\Delta L_b$ | Change in frontal width at bottom | m |
| $\Delta H$ | Change in frontal depth | m |
| $\alpha$ | Bottom slope | |
| $U^c_{geo}$ | Corrected buoyancy-driven alongshore flow | m/s |
| $U^c_{wind}$ | Corrected wind-driven alongshore flow | m/s |
| $H^c$ | Corrected frontal depth | m |
| $L^c$ | Corrected frontal width | m |
| $HWI^c$ | Corrected Hydrographic Wind Index | |
| $Q_{wind}$ | Wind-driven alongshore transport | m$^3$/s |
| $U_{ADCP}$ | Alongshore velocity derived from ADCPs | m/s |
| $Q$ | Alongshore transport | m$^3$/s |
| Chapter 5 | | |
| $U_{geo}$ | Depth-averaged buoyancy-driven alongshore flow | m/s |
| $U_{wind}$ | Depth-averaged wind-driven alongshore flow | m/s |
| $\mathrm{sgn}()$ | Signum function | |
| $\tau_{sx}$ | Alongshore surface wind stress | kg/m/s$^2$ |

| Symbol | Description | Units |
|---|---|---|
| $\rho$ | Average water density | kg/m$^3$ |
| $C_{Da}$ | Depth-averaged bottom drag coefficient | |
| $Q$ | Alongshore transport | m$^3$/s |
| $g'$ | Reduced gravitational acceleration | m/s$^2$ |
| $H$ | Frontal depth | m |
| $\rho_a$ | Density of ambient shelf water | kg/m$^3$ |
| $\rho_c$ | Density of coastal plume water | kg/m$^3$ |
| $L$ | Frontal width | m |
| $r$ | Pearson correlation coefficient | |
| Chapter 6 | | |
| $D_m$ | Modeled detection percentage | |
| $a$ | Amplitude of Gaussian distribution | |
| $t$ | Detection date | s |
| $\mu$ | Mean of Gaussian distribution | s |
| $\sigma$ | Standard deviation of Gaussian distribution | s |
| $i$ | Detection sequence | |
| $T_i$ | Temperature per detection sequence $i$ | °C |
| $S_i$ | Salinity per detection sequence $i$ | PSU |
| $U_i$ | Current velocity per detection sequence $i$ | m/s |
| $\bar{\cdot}$ | Average operator | |
| $\beta_0$ | Multiple linear regression coefficient | |
| $\beta_1$ | Multiple linear regression coefficient | 1/°C |
| $\beta_2$ | Multiple linear regression coefficient | 1/PSU |
| $\beta_3$ | Multiple linear regression coefficient | s/m |
| $t$ | t-test | |
| $p$ | p-value | |

| Symbol | Description | Units |
|---|---|---|
| $SI$ | Sinuosity Index | |
| $R^2$ | Coefficient of determination | |
| $df$ | Degrees of freedom | |
| $N$ | Number of observations | |
| Appendix A | | |
| $T_1$ | Time of the glider's last GPS fix before diving | s |
| $T_2$ | Time of the glider's surfacing | s |
| $T_3$ | Time of the glider's first GPS fix after surfacing | s |
| $T_4$ | Time of the glider's second GPS fix after surfacing | s |
| $(x_i, y_i)$ | Glider coordinates at a time $i$ | |
| $(U_g, V_g)$ | Glider-derived, depth-averaged current velocity | m/s |
| $(U_{ADCP}, V_{ADCP})$ | ADCP-derived, depth-averaged current velocity | m/s |
| $R^2$ | Coefficient of determination | |
| Appendix B | | |
| $h_f$ | $z$-coordinate of the interface in a two-layer system | m |
| $\zeta$ | Free surface height | m |
| $\rho_c$ | Density of the upper layer | kg/m$^3$ |
| $\rho_a$ | Density of the lower layer | kg/m$^3$ |
| $f$ | Coriolis parameter | 1/s |
| $\partial\cdot$ | partial derivative | |
| $g$ | Gravitational acceleration | m/s$^2$ |
| $P_{atm}$ | Atmospheric pressure at the sea surface | kg/m/s$^2$ |
| $P_c$ | Pressure in the upper layer | kg/m/s$^2$ |
| $P_a$ | Pressure in the lower layer | kg/m/s$^2$ |
| ($u_{geo,c}$, $v_{geo,c}$) | Velocity in the upper layer | m/s |
| ($u_{geo,a}$, $v_{geo,a}$) | Velocity in the lower layer | m/s |

| Symbol | Description | Units |
|---|---|---|
| Appendix C | | |
| $U_{geo}$ | Buoyancy-driven alongshore flow | m/s |
| $g'$ | Reduced gravitational acceleration | m/s$^2$ |
| $H$ | Frontal depth | m |
| $L$ | Frontal width | m |
| $\rho_a$ | Density of ambient shelf water | kg/m$^3$ |
| $\rho_c$ | Density of coastal plume water | kg/m$^3$ |
| $U_{wind}$ | Wind-driven alongshore flow | m/s |
| $\rho_{air}$ | Average air density | kg/m$^3$ |
| $\rho$ | Average water density | kg/m$^3$ |
| $C_{10}$ | Surface drag coefficient | |
| $U_{10}$ | Alongshore wind speed at 10 m | m/s |
| $C_{Da}$ | Depth-averaged bottom drag coefficient | |
| $C_D$ | Bottom drag coefficient | |
| $Q$ | Alongshore transport | m$^3$/s |
| $\sigma_x$ | Uncertainty associated with the variable $x$ | |

# ACKNOWLEDGEMENTS

I would like to thank my co-supervisors for their help in making this thesis a reality. Dave Hebert, for the countless Fridays we spent discussing my work, but also for making sure I was getting the most out of my PhD experience. He sent me to sea, he sent me to conferences, he even sent me abroad, trusting that, every time, I would come back as a more accomplished oceanographer. Jinyu Sheng, for his constructive reviews and advices, as well as his encouragements to always go forward. His support was welcomed and very much needed at times.

I would also like to thank the members of my advisory committee, Katja Fennel and Dan Kelley, for their contributions and helpful comments to improve this thesis. My thanks extend to previous committee members: Peter Smith, for making me come to Dalhousie and discover the beautiful life Nova Scotia has to offer, and Blair Greenan for the tremendous amount of time he invested in my work, even after stepping down as an advisory committee member.

I want to thank the great colleagues I have met along the way: Øystein Skagseth and Ken Drinkwater for their fantastic welcome in Bergen and continuing guidance, John Kocik and his research group for an inspiring collaboration, and Shiliang Shan for our synergetic interactions. Thanks also go to Daniel Morrison and Jackie Hurst for their support on both a professional and a personal level.

Of course, none of this could have happened without the continuous support of good friends and fellow grad students. Special thanks go to my Haligonian family, as well as to Jessica Carrière-Garwood for our long debates and lively discussions, to Will Burt for introducing me to the Seadogs and becoming the best teammate I have ever had, and to Justine McMillan for her incredible friendship that did so much more than just keeping me off the ledge.

Finally, I want to thank my wife Alexandra Herrán-Magee, now Dever, for her love and support throughout the (many) ups and (many) downs I have experienced over the last few years. She believed in me when I didn't, and deserves so much more than a few lines in the acknowledgments section. I count myself unbelievably lucky to have had you by my side for this endeavor, and to be able to count on you for whatever is next.

# CHAPTER 1

# INTRODUCTION

The Scotian Shelf is located in the northwest Atlantic Ocean and is part of a large geographic system known as the Eastern Canadian Shelf. Bounded by the Laurentian Channel to the east, the Northeast Channel to the west and the continental shelf break to the south, the Scotian Shelf is centrally located and connects dynamically important areas such as the Grand Banks, the Gulf of Maine (GoM) and the Gulf of St. Lawrence (GSL) (Figure 1.1). The Scotian Shelf is more than 700 km long and has a width ranging between 120 km and 240 km. With an average depth of about 90 m, the Scotian Shelf is characterized by a complex topography consisting of numerous shallow banks and basins as deep as 300 m.

Major currents in the region, such as the GSL outflow through Cabot Strait and the Labrador Current, interact with the irregular topography and result in complex circulation patterns that make the Scotian Shelf a region of interest. While significant modeling efforts have been made on simulating the oceanographic conditions over the Shelf, only a few observational datasets are available to both validate these models and to investigate the ocean dynamics in this region. Until recently, monitoring programs were either too short (e.g., the Canadian Atlantic Storm Program only covered 3 months during the winter of 1985-1986; *Anderson and Smith*, 1989), or had a temporal resolution that is too low (e.g., the Atlantic Zone Monitoring Program only samples twice a year beginning in 1999; *Therriault et al.*, 1998) to properly resolve both the seasonal and inter-annual variabilities. A new monitoring program developed as part of the Ocean Tracking Network (OTN)

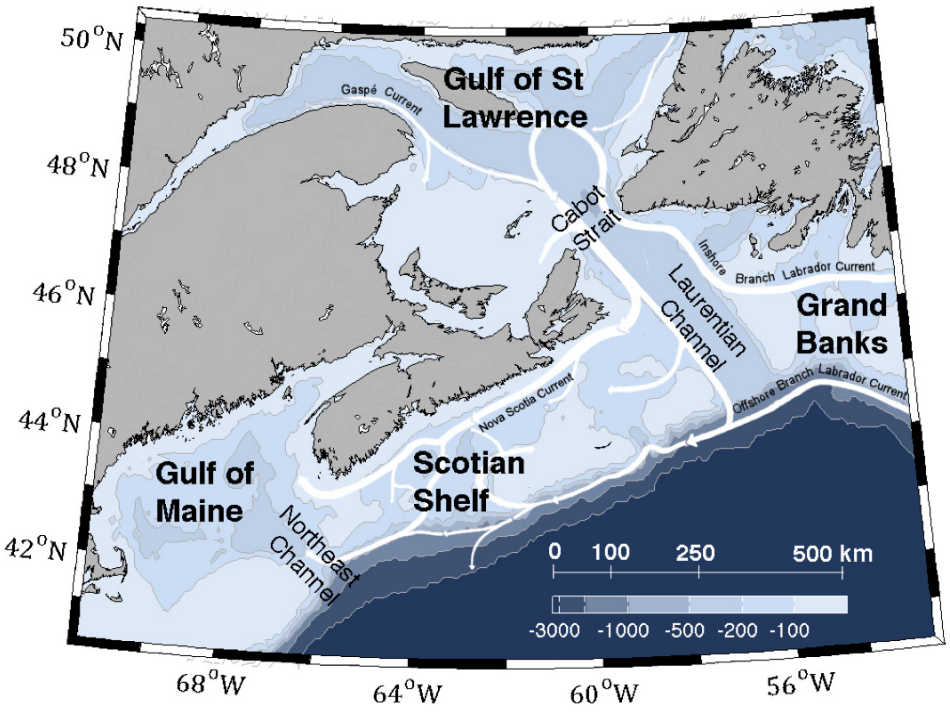


Figure 1.1: Bathymetric map of the eastern Canadian continental shelf where key regions (bold font) and major topographic features are labeled. Some of the principal circulation patterns are sketched (arrows) and the most significant currents are indicated.

provided relatively high temporal and spatial coverage of oceanographic conditions in this region. The Scotian Shelf is also recognized to be ecologically important, as many commercial species inhabit or migrate through the Scotian Shelf (*King M. and A.*, 2016). Concurrent datasets of acoustic detections of Atlantic salmon postsmolts (*Salmo salar*) along the Halifax Line (HL) were also collected to study the linkages between migratory behavior and oceanographic conditions.

The following sections present a summary of the circulation over the Scotian Shelf, the physics involved in buoyancy-driven coastal currents and the relationship between oceanographic conditions and fish migration patterns. Finally, the objectives and outline of the thesis are detailed.

## 1.1 Mean Circulation and Variability over the Scotian Shelf

The mean circulation on the Scotian Shelf is characterized by a persistent southwestward coastally-trapped current known as the Nova Scotia Current (NSC), and a southwestward alongslope current located at the Shelf break (Figure 1.1)(*Smith and Schwing*, 1991; *Loder et al.*, 1997). The former is linked to the outflow from the GSL that exits the Gulf through the western side of Cabot Strait and veers southwestward over the eastern Scotian Shelf. The latter originates from the offshore branch of the Labrador Current, combined with a branch of the outflow from the GSL that flows along the southern bank of the Laurentian Channel (Figure 1.1). The mesoscale structure of the flow on the Scotian Shelf is affected by the irregular topography composed of banks and basins, which generate anticyclonic and cyclonic circulation features, respectively (*Han and Loder*, 2003).

Previous studies demonstrated that the major physical processes affecting the circulation on the Scotian Shelf involved both baroclinic (*Smith and Schwing*, 1991) and barotropic (*Thompson and Sheng*, 1997) processes over a broad range of timescales. *Smith and Schwing* (1991) found that the winter circulation measured along the HL agreed roughly with the geostrophic currents estimated from density. This result suggests that the buoyancy fluxes associated with the advection of the freshwater discharge from the St. Lawrence Estuary through the western GSL and Cabot Strait could be a major forcing mechanism for the NSC (*Drinkwater et al.*, 1979).

Temporal variability in the circulation over the Scotian Shelf is significantly affected by the time-varying local surface wind stress, particularly in the inertial (17–22 hours) and synoptic (2–10 days) frequency bands, with a greater response in water columns shallower than 100 m (*Schwing*, 1989, 1992a). The temporal variability at lower frequencies ($<$0.5 cycle per day) in the subsurface pressure field and in the bottom temperature was found to correlate with traveling shelf waves generated by remote winds (*Schwing*, 1992a,b) and

other large-scale meteorological forcing. The latter was found to affect the strength and hydrographic signature of the Labrador Current (*Petrie*, 2007). Over seasonal timescales, the net surface heat flux has also been identified as a contributing factor in modulating the upper ocean stratification, with some impacts on circulation features (*Umoh and Thompson*, 1994).

Previous ocean monitoring programs conducted over the Scotian Shelf generally focused on sampling along the HL, which is a cross-shelf transect running from the coastal water off Halifax to the Shelf Break (Figure 2.1). During the winter of 1985-1986, for example, continuous current velocity and hydrographic measurements were made on the Scotian Shelf as part of the Canadian Atlantic Storm Program. Unfortunately, observations during this period were only collected at a few depths and covered a short period (of about 3 months; *Anderson and Smith*, 1989). As a result, the oceanographic observations made by this program were too short to be used in characterizing the seasonal, or inter-annual, variability of the ocean circulation and hydrography over the Scotian Shelf. The ongoing Atlantic Zone Monitoring Program (AZMP) partially addresses this issue by measuring hydrographic variables twice a year on average along the HL since 1999 (*Therriault et al.*, 1998). However, the low temporal resolution of this program prevents a proper study of the seasonal cycle, and also introduces issues when looking at the inter-annual variability, since semi-annual observations can suffer from significant aliasing (*Mann and Needler*, 1967; *Mann*, 1969; *Petrie*, 2004).

Over the 2008-2014 period, a long-term ocean monitoring program was developed as part of the OTN to monitor oceanographic conditions along the HL. The goal was to sample at high spatial and temporal resolutions using a variety of platforms, including moored current profilers, bottom-mounted CTDs, and underwater gliders. This OTN monitoring program provided a dataset that, for the first time, allows the study of the seasonal and inter-annual variability in both the circulation and hydrography along the HL.

## 1.2 Dynamics of Buoyancy-driven Coastal Currents

A buoyancy-driven coastal current generally occurs where a large volume of freshwater is discharged into the ocean (e.g., river estuaries, fjord mouths, etc.). The low-salinity estuarine plume grows until it is affected by the Coriolis force (i.e., Rossby radius of deformation) and veers to the right (left) in the northern (southern) hemisphere to propagate "downshelf" (in terms of propagation direction of Kelvin waves). This type of buoyancy-driven currents can be found off coasts all around the globe and can be classified into two categories: (1) single-source currents, where a large source of buoyant water dominates the system (e.g., Delaware Coastal Current, Gaspé Current, and Nova Scotia Current; see *Munchow and Garvine*, 1993; *Sheng*, 2001; *Dever et al.*, 2016), and (2) multi-source currents, where several sources of buoyant water are distributed throughout the systems (e.g., Alaska Coastal Current and Norwegian Coastal Current; *Mork*, 1981; *Johnson et al.*, 1988; *Sætre*, 2007).

Buoyancy-driven coastal currents are coherent over long distances in the alongshore direction (*Drinkwater et al.*, 1979; *Brink*, 2015). Because spatial and temporal variability in such currents can significantly affect the distribution of freshwater, nutrients, larvae and pollutants over a continental shelf, many previous studies were made to improve our understanding of the dynamics driving buoyancy-driven coastal currents and their variability (*Csanady*, 1982; *Chapman and Lentz*, 1994; *Yankovsky and Chapman*, 1997; *Lentz and Helfrich*, 2002). Studies conducted for many different shelf circulation systems (e.g., GoM, Scotian Shelf, Norwegian Shelf, etc.) identified buoyancy and surface winds as the main driving mechanisms of buoyancy-driven coastal currents (*Mork*, 1981; *Munchow and Garvine*, 1993; *Fong and Geyer*, 2001; *Yankovsky et al.*, 2001).

Buoyancy forces for the coastal current associated with freshwater runoff arise from the density gradient between the lower-salinity estuarine water and the higher-salinity ambient shelf water over the continental shelf. The lower-density coastal water is separated

from the higher-density ambient shelf water by a sharp density front, where an alongshore geostrophic current is generated. The slope of the density front can be related to the current strength, and is also affected by surface winds through cross-shore Ekman transport. Upwelling (downwelling) favorable winds will generate an offshore (onshore) Ekman transport in the surface layer, which is compensated by an onshore (offshore) transport in the lower layer. This results in the flattening (steepening) of the density front through isopycnal tilting.

Past studies also showed that alongshore buoyancy-driven coastal currents, such as the NSC, have a barotropic response to surface wind forcing (*Sandstrom*, 1980; *Schwing*, 1989, 1992a). In an observational study conducted over the Scotian Shelf, *Sandstrom* (1980) demonstrated that, at low frequencies, the barotropic alongshore momentum balance is between the alongshore components of the surface wind stress and bottom friction. Low frequencies mentioned here are characterized by periods longer than the "adjustment time" defined by *Csanady* (1974), at which the author scales the maximum expected wind-driven alongshore current to be approximately 3% of the alongshore wind speed. These results were obtained under the assumption that the water depth is relatively shallow, where the bottom friction is not negligible. Based on both observations (*Schwing*, 1992a) and numerical simulations (*Schwing*, 1992b), *Schwing* demonstrated that this approximation seems to hold reasonably well over the Scotian Shelf for water depths as deep as 100 m.

The study of the relative roles played by buoyancy and winds in driving coastal currents has therefore become an important research topic, especially in a changing climate where freshwater discharges and wind patterns are expected to evolve (*Core Writing Team and Reisinger*, 2007). *Whitney and Garvine* (2005, hereafter referred to as WG05) developed an approach based on a "Wind Index", referred to as the Traditional Wind Index (TWI) in this study. This index attempts to separate and quantify the relative contributions of wind and buoyancy forcings to the Delaware Coastal Current. In this study, we propose a different approach relying on hydrographic sections that resolve the slope of the density

front. This approach decouples the Wind Index calculation from knowledge of upstream conditions (e.g., the river discharge, see WG05), but consider the effects of wind-driven isopycnal tilting due to the Ekman transport generated by alongshore winds. We apply this "Hydrographic Wind Index" (HWI) to the NSC using field data collected by underwater gliders along the HL to discuss the advantages and potential applications of the HWI.

## 1.3 Linkages between Oceanographic Conditions and Salmon Migratory Behavior.

Atlantic salmon (*Salmo salar*) in the GoM has been listed as an endangered species, with stocks currently at record lows (*Fay et al.*, 2006; *ICES*, 2015). Atlantic salmon are spawned in coastal rivers and juveniles move seaward in the spring as smolts. Upon ocean entry, the fish, which are termed as postsmolts, migrate northward and spend the next year or more growing to adulthood at sea. Marine survival has been identified as a major factor in the population's decline since 1990 (*Chaput et al.*, 2005). Though investigating marine survival of the GoM Atlantic salmon remains an important issue, there is great difficulty in collecting field data over a migration route that ranges from the GoM to the coast of Greenland (*Paloheimo and Elson*, 1974; *Chaput et al.*, 2005). As a result, the role of environmental factors on spatial distribution and survival are poorly characterized.

While monitoring migration of marine animals remains a challenge, the recent development of fish tracking techniques using acoustic transmitters and fixed listening receivers deployed in arrays has led to unprecedented opportunities to characterize Atlantic salmon behavior and survival. These advances have begun to shed light on the relationships between fish behavior and oceanographic variables in previously unattainable ways (*Hussey et al.*, 2015). Over the last decade, nearly 2,700 Atlantic salmon smolts were released into the Penobscot River (Maine, USA) as part of ongoing acoustic telemetry studies (*Holbrook et al.*, 2011; *Stich et al.*, 2014, 2015). The exodus of these fish into the GoM provided an opportunity to understand the early phase of the species' migration. The

installation of an organized network of receivers on the Scotian Shelf made tracking these fish possible. As part of the OTN, a series of acoustic receivers covering 180 km from shore and across the Scotian Shelf were deployed along the HL. These receivers detected, among other species, Atlantic salmon postsmolts from the Penobscot River (*Cooke et al.*, 2011), providing spatial and temporal data for migrating postsmolts at sea. The OTN research program also included an observational component that collected measurements of both the hydrography and circulation along the HL, providing a unique opportunity to monitor the local oceanographic conditions experienced by Atlantic salmon postsmolts.

Oceanographic variables, particularly ocean temperatures, are known to potentially affect salmon postsmolts growth directly (*Todd et al.*, 2008; *Friedland et al.*, 2012), and indirectly, through a change in prey and predator distribution and interaction (*Friedland et al.*, 2012; *MacKenzie et al.*, 2012; *Mills et al.*, 2013; *Renkawitz et al.*, 2015). The GoM and the Scotian Shelf have rapidly warmed over the last decade (*Hebert et al.*, 2013), putting local fish stocks at risk (*Pershing et al.*, 2015). When postsmolts pass the HL in early spring, the hydrography along the HL is characterized by a coastally-trapped, wedge-shaped water mass composed of water colder and fresher than the ambient offshore water. The cold and fresh coastal water originates from the St. Lawrence River and flows onto the inner Scotian Shelf from the western GSL (*Loder et al.*, 2003; *Hebert et al.*, 2013). This water mass is separated from the warmer and more saline water covering most of the Scotian Shelf by a sharp density front. The location of this density front varies on the synoptic timescale, but generally outcrops about 45 km from shore, and intersects the bottom along the 100 m isobath, located roughly 30 km offshore (*Loder et al.*, 2003).

This offshore density gradient leads to a strong southwestward buoyancy-driven alongshore current forming the NSC (*Drinkwater et al.*, 1979; *Smith and Schwing*, 1991). The speed of the NSC is strongest near the surface, reaching up to 30 cm/s, and is weaker at deeper depths. It spreads between 30 and 60 km offshore on average, with the maximum velocity located approximately 45 km from shore. Temperature and salinity in the top

20 m generally co-vary across the Scotian Shelf, depending on the dominant water mass (colder and fresher vs. warmer and more saline). In spring, ocean temperature and salinity have different spatiotemporal variability in the surface layer, due to the seasonal increase in the net surface heat flux that warms the upper layer and generates a sharper thermocline (*Umoh and Thompson*, 1994; *Loder et al.*, 2003).

The above-mentioned environmental variables vary both spatially and temporally through the region, therefore, good understanding of where migrating fish are observed will help to characterize the conditions these fish may select or avoid. In this study, we sought to combine acoustic detections of Atlantic salmon postsmolts with oceanographic conditions to characterize the seascape through which these fish migrated.

## 1.4 Objectives and Thesis Outline

The main goal of this thesis is to characterize aspects of the hydrography and circulation over the Scotian Shelf to further improve our understanding of the main dynamics driving the NSC. This main objective of this thesis is separated into several sub-objectives, corresponding to each chapter of the thesis:

Chapter 2 provides a description of different data sources used throughout the thesis (e.g., mooring location, sampling rate, spatial resolution, etc.) and discusses important processing steps required for the analysis. This chapter also includes the theory and method behind some of the statistical tools used in the analysis.

Chapter 3 characterizes the oceanographic conditions along the HL. It presents a description of the seasonal and inter-annual variability in hydrography and circulation, and provides insights into the dynamical processes driving this variability. The objective of this chapter is to examine the low-frequency oceanographic conditions across the Scotian Shelf based on field observations.

Chapter 4 uses the results from Chapter 3 to focus on the main circulation feature over the Scotian Shelf: the NSC. It presents the characteristics of this buoyancy-driven

coastal current and sheds light on the main mechanisms driving the NSC's variability over seasonal and inter-annual timescales. A simple analytical model that separates and quantifies the buoyancy-driven flow and the wind-driven flow is developed to assess their relative roles in driving the NSC at the HL.

Chapter 5 makes use of numerical simulations produced by a three-dimensional ocean circulation model to apply the Wind Index developed in the previous chapter. The objective of this chapter is to use the newly-developed Wind Index in various locations along the NSC to investigate the spatial variability associated with the major driving mechanisms of the coastal current.

Chapter 6 couples the oceanographic knowledge acquired in Chapter 3 with the migratory behavior of Atlantic salmon postsmolts at the HL in an inter-disciplinary case-study. The objective of this chapter is to identify the physical oceanographic variables linked to the presence of salmon postsmolts at the HL.

Chapter 7 summarizes the main results of the study, and provides directions for future work.

# CHAPTER 2

# DATA SOURCES, PROCESSING STEPS, AND STATISTICAL TOOLS

The work presented in this thesis is primarily based on in situ measurements collected through different monitoring programs and ocean observing networks operating over the Scotian Shelf and adjacent regions (Figure 2.1). In addition, results produced by an ocean circulation model are also used for part of this study to complement the observational datasets. The objective of this chapter is to introduce these data sources and to provide context for the rest of the study. Details on the different datasets, such as station names, mooring locations, sampling resolutions and processing steps are summarized. The theory and method behind some of the statistical techniques used in this study are also described.

This chapter is therefore organized as follows: Section 2.1 provides information on the main field data sources for both currents and hydrographic measurements used in this thesis. Section 2.2 presents the data processing steps systematically applied to the different datasets (e.g., smoothing, gridding, filtering, etc.). This section also discusses important processing techniques, such as the algorithm used to derive cross-track geostrophic current speed from glider-based observations. Finally, information on the theory and the approach taken for some of the key statistical techniques used in the study are presented in Section 2.3.

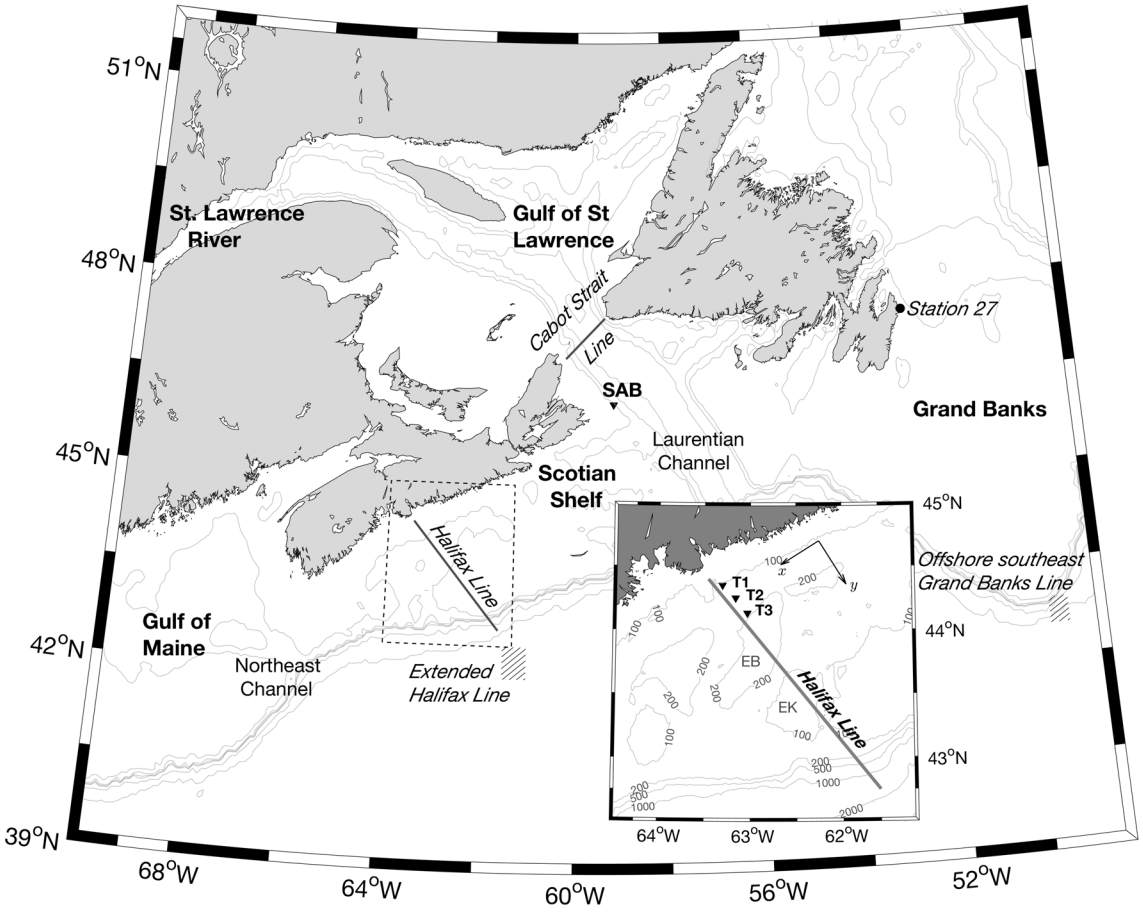


Figure 2.1: Map showing key regions (bold font), AZMP sampling areas (italic font and hatched regions) and major topographic features over the eastern Canadian Continental Shelf. The location of the mooring located on St. Anns Bank (SAB) is also indicated. Bathymetric contours are shown for the 150, 250, 400, 500, 1000, and 2000 m isobaths. Inset shows the central Scotian Shelf with the Halifax Line. The location of the ADCP stations (triangles) and the orientation chosen for the alongshore ($x$) and cross-shore ($y$) components at the Halifax Line are included. Emerald Basin (EB) and Emerald Bank (EK) are identified.

## 2.1 Data Sources

### 2.1.1 Currents Observations

#### 2.1.1a Halifax Line

The Halifax Line is a cross-shelf transect running from the coastal water off Halifax to the Shelf Break and transects both Emerald Basin (EB; 250 m deep) and Emerald Bank (EK; 75 m deep) before reaching the Shelf Slope (see Figure 2.1). Current measurements were collected using three bottom-mounted Acoustic Doppler Current Profilers (ADCPs) at stations T1 (110 m water depth), T2 (170 m) and T3 (175 m) along the HL (see inset in Figure 2.1). Currents were recorded from April 2008 to April 2015 with several data gaps caused by instrument failures or moorings turn-overs (i.e., the time between mooring recovery and deployment; Figure 2.2). The sampling protocol was identical at all three T-stations, which was that, every 30 minutes, the ADCP sent 100 pings with a 3-second delay between each ping. The 100 readings were averaged together to produce a 5 min average of the current speed in the conventional Cartesian coordinate system (east right, north up). Currents were measured at a 4 m vertical resolution (or bin), from 10 m off the bottom to minimum 10 m below the surface. A signal frequency of 300 KHz was used at T1, due to the shallower depth, while T2 and T3 used a frequency of 150 KHz.

Two types of current data were deduced from glider movements and measurements; Firstly, gliders used in this study were equipped with a dead-reckoning positioning system that is solely based on the flight characteristics of the glider (i.e., pitch, heading, and depth change). The dead-reckoning algorithm estimates the lift, drag, and buoyancy forces experienced by the glider and extrapolates the longitude and latitude in time between surfacings. The algorithm therefore provides an estimate of the glider's location to the on-board computer, ignoring external forces applied to the glider (e.g., ocean currents; *Merckelbach et al.*, 2008). When the location of the glider is obtained by the Global Positioning System (GPS) at each surfacing, a comparison between the GPS positioning and the extrapolated positioning based on dead-reckoning provides a measure of the time-

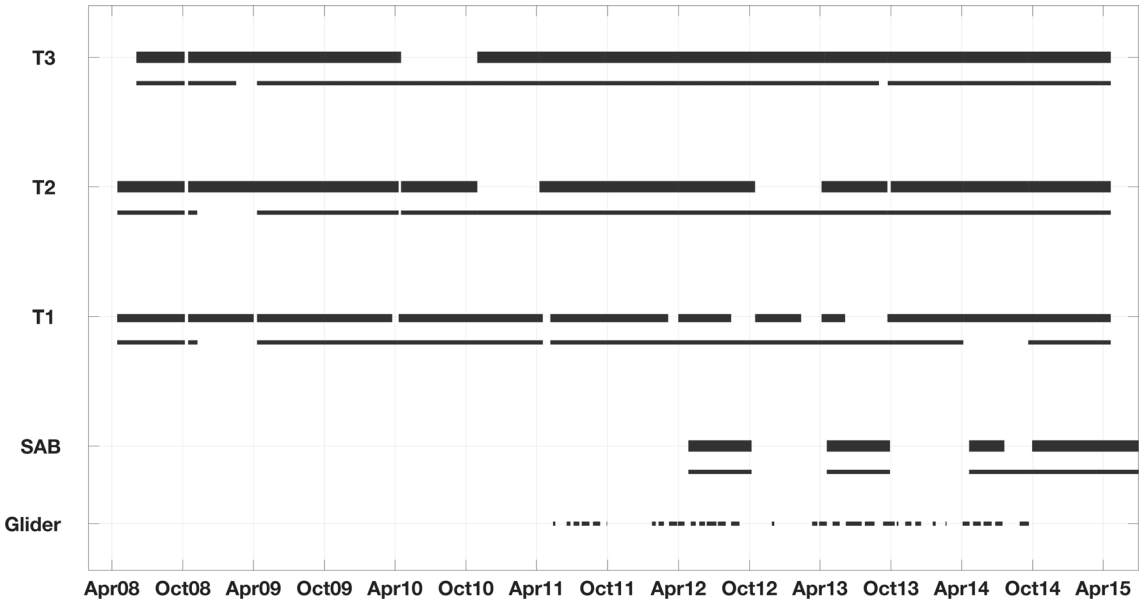


Figure 2.2: Data coverage of OTN's ocean monitoring program. The thick lines show the ADCP coverage, while the thin lines represent the coverage of the co-deployed near-bottom CTD. Readers may refer to Figure 2.1 for the geographical locations of the stations.

and depth-averaged current the glider experienced throughout its last dive (see Appendix A for a detailed description of depth-averaged currents estimation and validation). The uncertainty associated with this depth-averaged current estimation largely depends on the accuracy of the flight model used to simulate the glider's path under water. These uncertainties are difficult to quantify, since the hydrodynamics forces on the gliders (e.g., lift, drag, etc.) are not well-known (*Williams et al.*, 2008; *Moat et al.*, 2016).

Secondly, the temperature and conductivity measurements from the glider were used to compute the density field using the Gibbs-SeaWater (GSW) oceanographic toolbox in MATLAB (*McDougall and Barker*, 2011). The density gradient along the glider's track was then used to estimate the geostrophic flow across the glider's track based on thermal wind dynamics (*Gill*, 1982). A detailed description of the algorithm used to derive glider-based geostrophic currents is provided in Section 2.2.

#### 2.1.1b St. Anns Bank

A bottom-mounted, upward-looking ADCP was deployed at St. Anns Bank (SAB; Figure 2.1). Deployment periods covered from May to October 2012, from April to October 2013, and from April 2014 to October 2015 (Figure 2.2). Unfortunately, no data were recorded between July 2, 2014 and September 30, 2015 due to an instrument failure. The ADCP's sampling configuration was identical to those at the three T-stations at the HL, with an exception for the first deployment. During the first deployment, the ADCP data at SAB were time means of instantaneous velocity measurements made by 20 pings at a time interval of every 30 s, and the current speed recorded every 10 min. The current measurements collected at SAB are used to study the alongshore coherency of the NSC, by comparing the alongshore currents measured at SAB and along the HL.

### 2.1.2 Hydrographic Observations

#### 2.1.2a Eastern Canadian Shelf: the Atlantic Zone Monitoring Program

The AZMP started in 1999 with the mandate of providing regular sampling of oceanographic conditions across the eastern Canadian shelf (*Therriault et al.*, 1998). This program includes multiple transects and permanent stations distributed over the eastern Canadian shelf. While transects are occupied twice a year on average (spring and fall), permanent stations are sampled at least once a month. The in situ AZMP measurements used in this thesis include observations made at Station 27 near St. John's (Newfoundland, Canada), as well as three AZMP transects: the Cabot Strait Line (6 stations), the Southeast Grand Banks Line (21 stations), and the HL (7 stations). The Atlantic Zone Offshore Monitoring Program (AZOMP), which is AZMP's offshore counterpart, samples the "Extended Halifax Line" and provides information on oceanographic conditions over the continental slope at the HL (Figure 2.1). At each station of AZMP and AZOMP, vertical profiles of pressure, temperature and conductivity were measured. The corresponding salinity and density were then computed using the GSW oceanographic toolbox in MATLAB.

#### 2.1.2b Halifax Line

As part of the OTN, hydrographic data were collected from bottom-mounted Conductivity-Temperature-Depth (CTD) sensors that were co-deployed with the ADCPs at the three T-stations. Near-bottom pressure, temperature, and conductivity were recorded every 5 min from April 2008 to April 2015 (Figure 2.2). These long time series provide an unprecedented temporal coverage of near-bottom hydrography at the HL. However, these OTN CTD observations lack vertical and horizontal coverage, since they only provide information on the oceanographic conditions near the bottom at the three T-stations.

To compensate this low spatial coverage, Teledyne Webb Research Slocum gliders were used as part of OTN's ocean monitoring program. From June 2011 to September 2014, 62 transects over the central Scotian Shelf were completed along the HL using gliders (Figure 2.1). Gliders are autonomous underwater vehicles that are able to sample the water column down to 200 m by changing their buoyancy using a ballast pump. Some of the induced vertical momentum of the glider is transferred horizontally by the wings installed on both sides, resulting in a triangle wave sampling pattern. The horizontal and vertical resolutions of the gliders datasets are, therefore, not uniform and depend on the angle of attack of the glider (about 22 to 26 degrees from the horizontal), the average speed of the glider ($\sim$ 0.3 m/s), the depth of the water column, and the speed of the glider relative to the surrounding water. The glider data collected during this period had an average vertical resolution of about 0.3 m and a finest horizontal resolution of approximately 850 m. Depending on its spatial coverage, it took from 3 to 11 days for the glider to complete a mission, during which pressure, temperature, conductivity, and other variables were recorded. Both salinity and potential density were computed using the Gibbs Seawater toolbox in MATLAB.

#### 2.1.2c St. Anns Bank

Similarly to the T-stations, a CTD was co-deployed with the ADCP at SAB (Figures 2.1). Near-bottom conductivity, temperature, and pressure were recorded every 5 min from May

to October 2012, every 30 min from April to October in 2013 and 2014, and every 5 min from October 2014 to October 2015 (Figure 2.2). Ship-based hydrographic transects were also collected at SAB as part of AZMP but were not used in this study. Hydrographic transects collected across Cabot Strait were preferred, due to a more frequent sampling at Cabot Strait than at SAB.

### 2.1.3 Numerical Model Results

Most of the field observations described above were made along the HL, across Cabot Strait, and at SAB. Far from the HL, however, the in situ oceanographic observations mentioned above lack the necessary temporal and spatial resolutions for the research work of this thesis. As a result, we used numerical results produced by two outer submodels (L1 and L2) of a multi-nested ocean circulation modeling system (*Shan et al.*, 2016). The following paragraphs summarize the configuration of these two outermost submodels detailed in *Shan et al.* (2016).

While both the submodels are based on the Princeton Ocean Model (*Mellor*, 2004), they differ in their configurations. The outer submodel L1 is a 2D barotropic model with a rectangular domain covering latitudes ranging from $38^o$N to $60^o$N, and longitudes covering from $43^o$W to $71^o$W, with a horizontal resolution of $1/12^o$. This submodel domain covers the Labrador Sea, Grand Banks, GSL, Scotian Shelf, and GoM (Figure 2.3). The inner submodel domain covers a smaller area than submodel L1 that includes the GSL, Scotian Shelf and GoM, with a horizontal resolution of $1/16^o$. L2 is a 3D baroclinic model and possess 40 $\sigma$-layers in the vertical. The horizontal subgrid-scale mixing parameterization in both the submodels is based on the scheme of *Smagorinsky* (1963). A vertical subgrid-scale mixing parameterization is only required in L2, and is based on the *Mellor and Yamada* (1982) level-2.5 turbulent closure scheme.

Numerical simulations were conducted for the years 2011 and 2012. The modeling system was forced by realistic atmospheric forcing, the net heat flux at the sea surface, and freshwater input. The atmospheric forcing was taken from the North American Regional

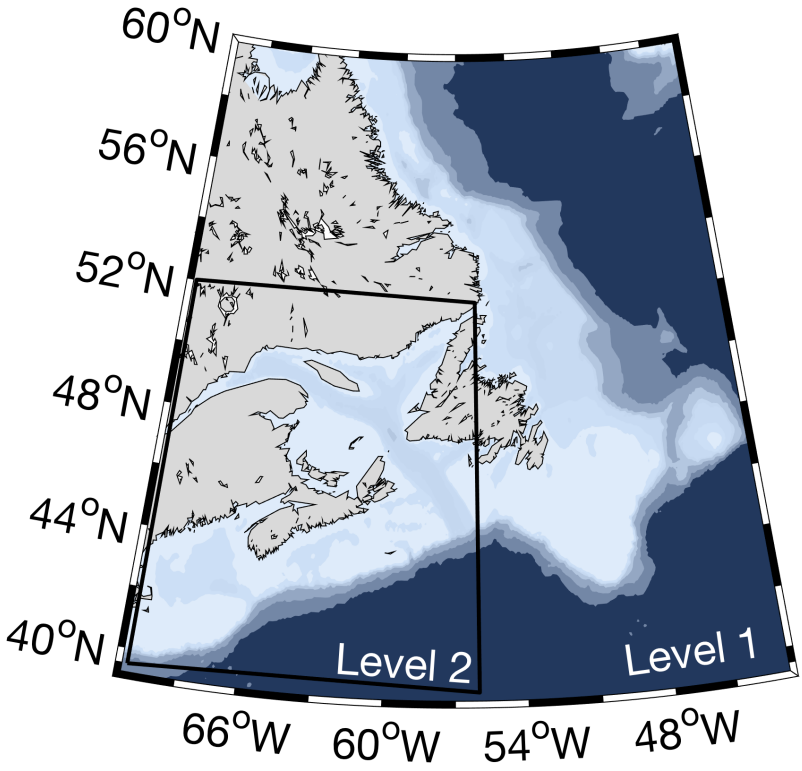


Figure 2.3: Domain and major topography of the two outer submodels (Level 1 and Level 2) of the multi-nested ocean circulation modeling system described in *Shan et al.* (2016). Level 1 is a barotropic model with a horizontal resolution of $1/12^o$ and is used for the boundary conditions in the Level 2 submodel. Level 2 is a 3D baroclinic model with a horizontal resolution of $1/16^o$ and 40 $\sigma$-layers in the vertical.

Reanalysis with a resolution of $\sim$ 32 km (*Mesinger et al.*, 2006). The reanalysis includes sea level pressures and wind speeds. The latter was converted into wind stress using a bulk formula (*Large and Pond*, 1981; *Powell et al.*, 2003). The sea surface heat fluxes used to drive the submodel L2 were extracted from the same reanalysis product. Finally, the freshwater discharge from major rivers were included in L2 and implemented using a simple numerical scheme based on the salt and volume conservation (*Ohashi and Sheng*, 2013; *Shan et al.*, 2016).

The conditions at the open boundaries of the inner submodel L2 (i.e., surface elevation and depth-averaged currents) are derived from the outer submodel L1(see *Shan et al.*, 2016 for details). Within L2's domain, a monthly-mean temperature and salinity climatology

with a horizontal resolution of $1/6^o$ is used to initialize the submodel (*Geshelin et al.*, 1999). While physical conditions in the upper 40 m of the water column are free to evolve according to the influence of external forcing, the temperature and salinity below 40 m are spectrally nudged towards the seasonal-mean climatologies (*Thompson and Sheng*, 1997).

The monthly-averaged sea surface temperature, salinity, and density in January, May, August, and November 2012 produced by submodel L2 are shown in Figure 2.4. The seasonal cycle of the sea surface temperature follows roughly the seasonal cycle of the net surface heat flux (Figures 2.4a, 2.4b, 2.4c, and 2.4d). Surface water is therefore coldest in winter and warmest in the summer. The observed spatial variability is also simulated by the model, where the cold water coming from the GSL and exiting through western Cabot Strait is visible (see Figure 2.4d). The low-salinity signature of the outflow from the GSL is visible in the modeled sea surface salinity (Figures 2.4e, 2.4f, 2.4g, and 2.4h). In the model, the coastal water is freshest in November but a tongue of relatively fresh water can be observed along the coast of Nova Scotia all year long. This low temperature and salinity translate to relatively lighter coastal water, compared to ambient shelf water. The low-density water associated with the NSC is well represented in the model, and is visible throughout the year (Figures 2.4i, 2.4j, 2.4k, and 2.4l).

Figure 2.5 shows the monthly mean and depth-averaged currents over regions with water depths shallower than 3000 m calculated from L2 submodel results. The circulation features described in Chapter 1 are present in the dynamical model results. Both the inflow of water into the GSL through the eastern Cabot Strait and the outflow from the GSL through the western Cabot Strait are represented by submodel L2. The NSC flowing southwestward along the coast of Nova Scotia is also captured by the model, with a relative intensification of the flow over the central Scotian Shelf. The southwestward shelf break current located along between the 200 and 1000 m isobaths is the strongest over the eastern Scotian Shelf and intensifies in the winter in the model.

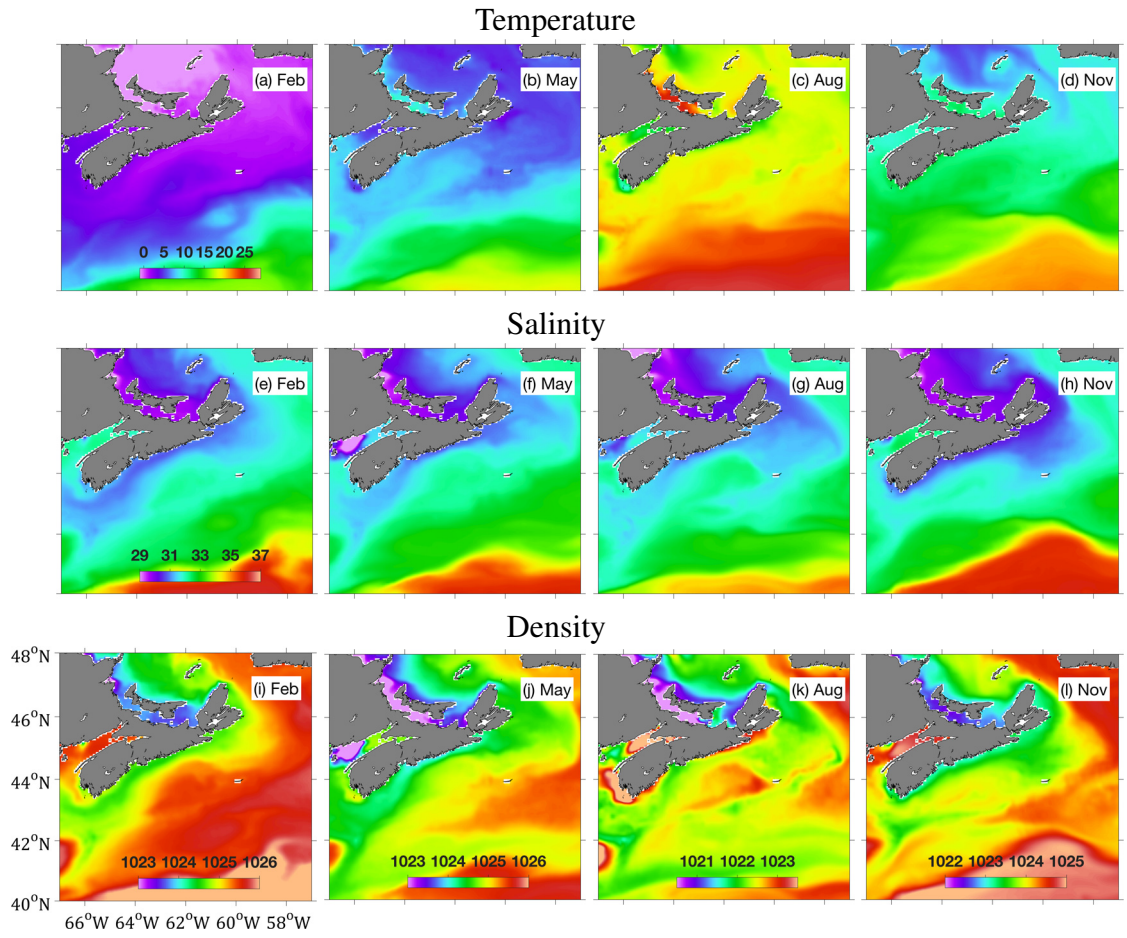


Figure 2.4: Monthly-averaged sea surface temperature (in $^{o}$C), salinity, and density (in kg/m$^3$) in February, May, August, and November 2012 simulated by submodel L2. Note different color scales are used in the sea surface density fields. Monthly-mean sea surface temperature and salinity are adapted from "Eulerian and Lagrangian Studies of Circulation on the Scotian Shelf and Adjacent Deep Waters of the North Atlantic with Biological Implications" by *Shan*, 2016. Adapted with permission.

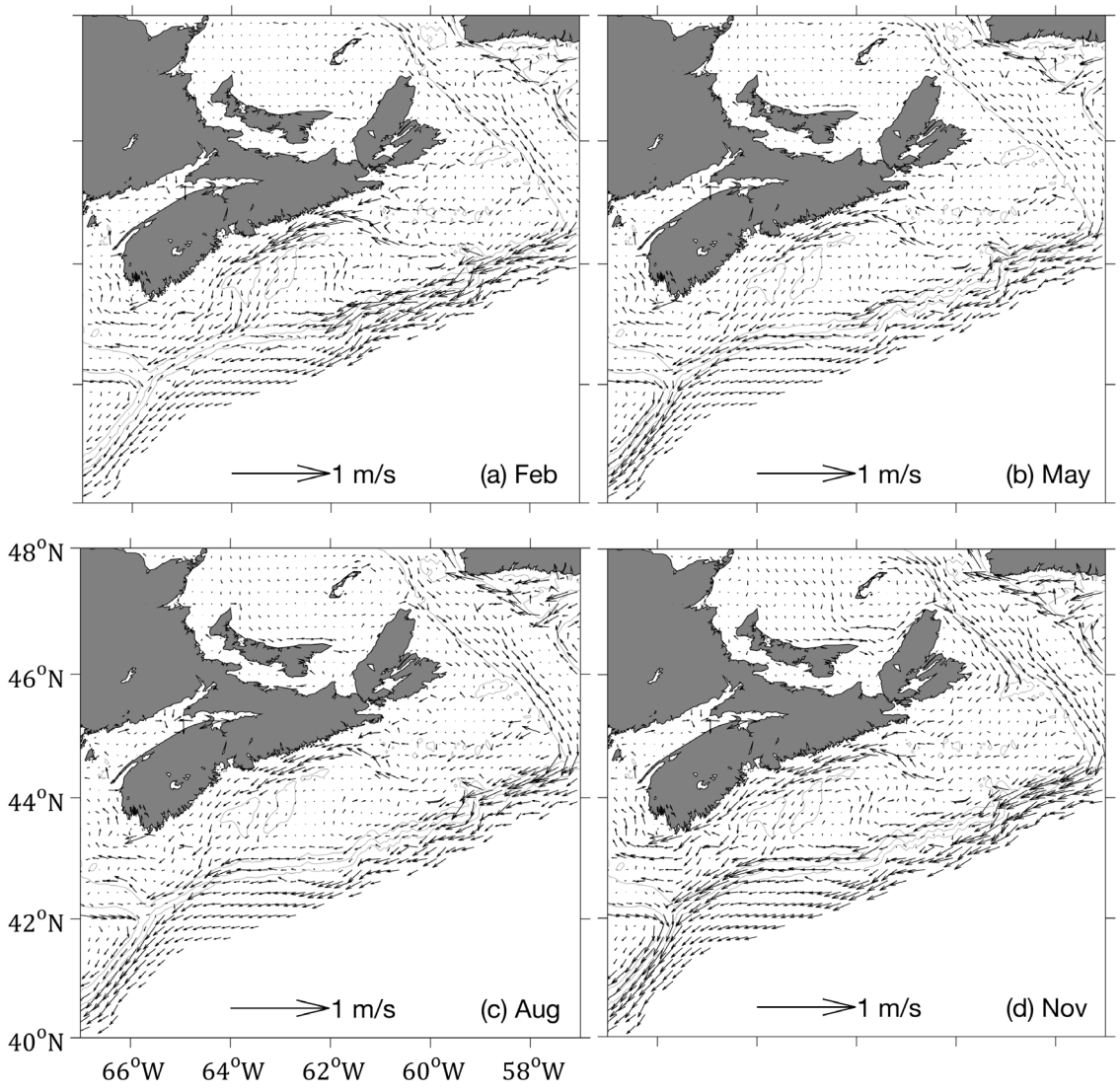


Figure 2.5: Monthly mean and depth-averaged currents over regions with water depths shallower than 3000 m in (a) February, (b) May, (c) August, and (d) November 2012 calculated from three-dimensional results produced by submodel L2. Arrows are shown at every third model grid point.

## 2.2 Data Processing

### 2.2.1 Velocity Vector Rotation

All current measurements recorded by bottom-mounted ADCPs were rotated from the eastward and northward directions into the alongshore and cross-shore directions using the new coordinate system defined in Figure 2.1. Because Nova Scotia's shoreline is highly

irregular and has a different orientation at different portions of the coastline, the alongshore component is defined in this study as the direction in which the variance in the observed velocity fluctuations is maximized. This is justified by the fact that the density front is trapped along a specific isobath, thereby increasing the role of topographic steering. Due to the relatively shallow water depth and the proximity of the coast, the isobaths are aligned with the general orientation of Nova Scotia's shoreline. The following expression is used to determine the angle of rotation at the three T-stations (*Emery and Thomson*, 2001):

$$\theta_p = \frac{1}{2}\tan^{-1}\left[\frac{2\overline{u_0' v_0'}}{\overline{u_0'^2} - \overline{v_0'^2}}\right] \tag{2.1}$$

where ($u_0$, $v_0$) are the zonal and meridional velocity components, respectively. The prime denotes the deviation from the mean and the overline is used as a symbol for the time average. At the three T-stations, Equation 2.1 yields an average clockwise rotation of $148^o$ from the Cartesian coordinate system (east right, north-up; see Figure 2.1). This rotated coordinate system is used to define the alongshore and cross-shore directions at the HL and relies on the assumption that the angle with most variance is aligned with the alongshore direction. For comparison, the direction of the HL corresponds to a rotation of $138^o$ and previous studies (*Schwing*, 1989, 1992a) used a rotation angle of $158^o$. The same calculation was applied to velocity records collected at SAB and yielded a clockwise rotation angle of $50^o$. Henceforth, the notations $u$ and $v$ will be used to denote the alongshore and cross-shore velocity components, respectively (Figure 2.1).

### 2.2.2 Butterworth Filter

To remove the tidal signal from the time series, a $5^{th}$ order, low-pass, "squared" Butterworth filter is applied to all temperature, salinity, pressure, and velocity records. Here, the term "squared" means that the filter was run both in the forward and backward directions through the time series to remove any phase lag introduced by the Butterworth filter. A Butterworth filter has been preferred to other low-pass filters (e.g., Chebyshev, Lanczos, etc.) because

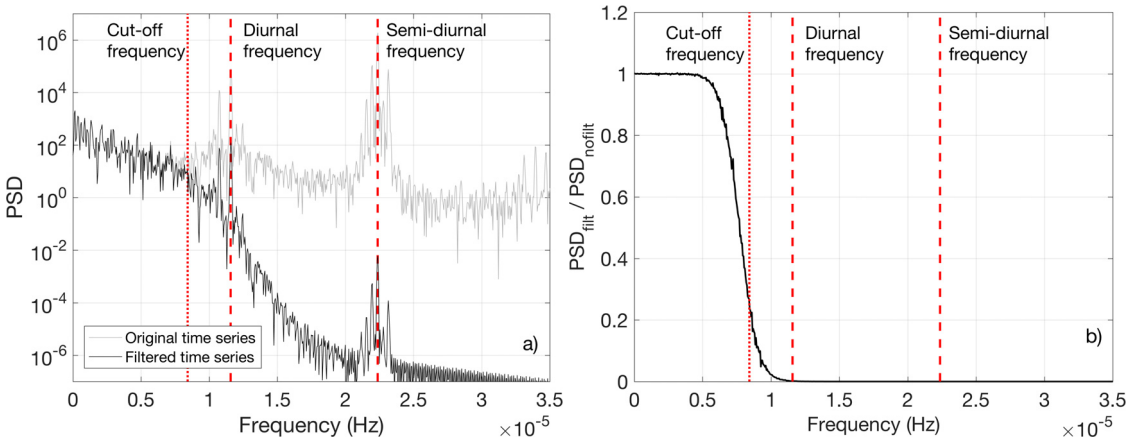


Figure 2.6: Illustration of the effects of a $5^{th}$ order "squared" Butterworth low-pass filter with a cut-off period of 33 hours ($8.4 \times 10^{-6}$ Hz) on a bottom pressure time series recorded between April and October 2009. (a) Power Spectral Density (PSD, in $kg^2/m^2/s^4/Hz$) of both the original (gray) and the filtered (black) time series. (b) PSD ratio of the filtered time series ($PSD_{filt}$) and the original time series ($PSD_{nofilt}$). In both panels, the cut-off frequency (dotted red line) and the diurnal and semi-diurnal frequencies (dashed red line) are indicated.

of the limited ripple effect in the passband (also known as the Gibbs phenomenon), at the cost of having a wider transition band (*Emery and Thomson*, 2001). The cut-off period (frequency) is set at 33 hours ($8.4 \times 10^{-6}$ Hz), at which the power spectral density (PSD) of the filtered time series is about three times smaller than the PSD of the initial time series (Figure 2.6). When applying the squared Butterworth filter, the PSD at both the diurnal ($\sim 1.2 \times 10^{-5}$ Hz) and semidiurnal frequencies ($\sim 2.3 \times 10^{-5}$ Hz) is greatly reduced in amplitude.

### 2.2.3 Glider-based Measurements: Gridding Technique and Geostrophic Velocities

As part of the OTN, underwater gliders were used to collect information on the ocean hydrography and circulation along the HL. Because of the glider's sampling pattern and its sensitivity to ocean currents, glider observations were not uniformly spaced in both horizontal and vertical directions. For each transect, observations collected by gliders were gridded based on the following two-step approach. Firstly, the great-circle distance from

shore of each data point was computed. The great-circle distance was calculated using the Haversine Formula from a reference point set on Devil's Island, located in the mouth of Halifax Harbour (-63.4572 $^o$W, 44.5824 $^o$N):

$$D = 2\,R_T\,\arcsin\left(\sqrt{\sin^2\left(\frac{\phi_1-\phi_0}{2}\right)+\cos\,\phi_0\,\cos\,\phi_1\,\sin^2\left(\frac{\lambda_1-\lambda_0}{2}\right)}\right) \tag{2.2}$$

where D is the great-circle distance, ($\phi_0$, $\lambda_0$) are the longitude and latitude of the reference point (i.e., Devil's Island), respectively. ($\phi_1$, $\lambda_1$) are the coordinates of the considered data point and $R_T$ is the Earth radius. Because glider tracks are roughly aligned with the cross-shelf direction, the distance from Devil's Island is used to collapse all glider transects onto one cross-shelf line.

Secondly, a block average function with a horizontal resolution of 1 km and a vertical resolution of 0.5 m was then applied to each transect. Due to the high sampling frequency of the glider, no interpolation or smoothing was required, as averaging blocks contained between 10 and 150 observations, with an average of about 24 observations per block. For each glider transect along the HL, temperature, salinity, and potential density were gridded using this technique.

Using the gridded potential density transects, the vertical velocity shear of horizontal currents was calculated for the cross-track velocity component using the along-track density field and the thermal wind equation (*Gill*, 1982), which, under the "Boussinesq approximation", is written as:

$$\frac{\partial u}{\partial z} = -\frac{g}{(\overline{\sigma_\theta}+1000)f}\frac{\partial \sigma_\theta}{\partial y} \tag{2.3}$$

where $u$ is the current speed normal to the glider track, $g$ is the gravitational acceleration, $\overline{\sigma_\theta}$ is the average water potential density, $f$ is the Coriolis parameter and $\partial\sigma_\theta/\partial y$ is the along-track potential density gradient.

The horizontal along-track density gradient $\partial\sigma_\theta/\partial y$ was computed using the Taylor

series expansion at a second order of accuracy. Centered differencing was preferred, unless the presence of a lateral boundary (i.e., bottom topography) made the calculation impossible. Forward (backward) differencing was thus used in the presence of an inshore (offshore) boundary:

$$\left.\frac{\partial \sigma_\theta}{\partial y}\right|_i \approx \frac{\sigma_{\theta_{i+1}} - \sigma_{\theta_{i-1}}}{2\Delta y} + \varepsilon(\Delta^2); \quad \text{centered differencing} \tag{2.4a}$$

$$\left.\frac{\partial \sigma_\theta}{\partial y}\right|_i \approx \frac{-\sigma_{\theta_{i+2}} + 4\sigma_{\theta_{i+1}} - 3\sigma_{\theta_i}}{2\Delta y} + \varepsilon(\Delta^2); \quad \text{forward differencing} \tag{2.4b}$$

$$\left.\frac{\partial \sigma_\theta}{\partial y}\right|_i \approx \frac{\sigma_{\theta_{i-2}} - 4\sigma_{\theta_{i-1}} + 3\sigma_{\theta_i}}{2\Delta y} + \varepsilon(\Delta^2); \quad \text{backward differencing} \tag{2.4c}$$

where $\varepsilon(\Delta^2)$ is the truncation error at a second order of accuracy, and $i$ is the grid point where the density gradient is computed. The magnitude of $\Delta y$ is taken as the length scale at which the geostrophic balance (between the horizontal pressure gradient and the Coriolis force) becomes important. This length scale was estimated by taking the maximum observed internal Rossby radius of deformation for the NSC:

$$\Delta y = R_b = \sqrt{\frac{g'H}{f_{44}^2}} \approx 15 \text{ km} \tag{2.5}$$

where $R_b$ is the internal Rossby radius of deformation, $g'$ is the reduced gravity based on the density difference between the fresher, less dense coastal water ($\rho_c$) and the more saline, denser ambient shelf water ($\rho_a$) defined by $g' = g(\rho_a - \rho_c)/\rho_a$, $H$ is the thickness of the upper layer and $f_{44}$ is the Coriolis parameter at 44 $^o$N.

The velocity shear was therefore calculated by combining Equation 2.4 with Equation 2.3. It was then vertically integrated assuming a zero-velocity at the bottom. A depth-mean current was finally added to the above-calculated geostrophic velocity so that the total depth-averaged geostrophic velocity matched the across-path depth-averaged current deduced from the glider drift (see Section 2.1.1a; *Todd et al.*, 2009).

## 2.3 Statistical Techniques

### 2.3.1 Reconstruction of the Alongshore Transport at the Halifax Line

For each of the ADCP deployment periods at the T-stations, the alongshore transport between T1 and T3 was computed using the current speed measurements collected at all three T-stations. A 7-year time series of the alongshore transport covering the period from April 2008 to April 2015 was constructed. Estimates of the alongshore transport for the NSC were not made during the period when any of the ADCPs located at the T-stations had failed, which occurred 32.4% of the time (i.e., 826 days). In order to fill these data gaps, the longest continuous time series of alongshore transport using all three ADCPs (referred to as the "complete transport") was used to compute a series of empirical linear regressions between the complete transport and the transport calculated using only one or two T-stations (referred to as the "incomplete transport") for the same period. Regressions were therefore computed using the daily-averaged transport time series from April 2011 to April 2012, for the following 6 different scenarios (Figure 2.7):

1. Failure of Station T3 only (8.6% of the time series, or 219.3 days)
2. Failure of Station T2 only (11.4% of the time series, or 290.7 days)
3. Failure of Station T1 only (9.2% of the time series, or 234.6 days)
4. Failure of Stations T2 and T3 (1.0% of the time series, or 25.5 days)
5. Failure of Stations T1 and T3 (0.0% of the time series, or 0 days)
6. Failure of Stations T1 and T2 (2.0% of the time series, or 51 days)

About 0.2% of the total time series was missing all three stations simultaneously, making a transport reconstruction impossible at those times. The coefficients of determination ($R^2$) of the regressions vary between 0.31 and 0.88 and are consistently high in scenarios where observations from T2 were included in the incomplete transport (scenarios 1, 3 and

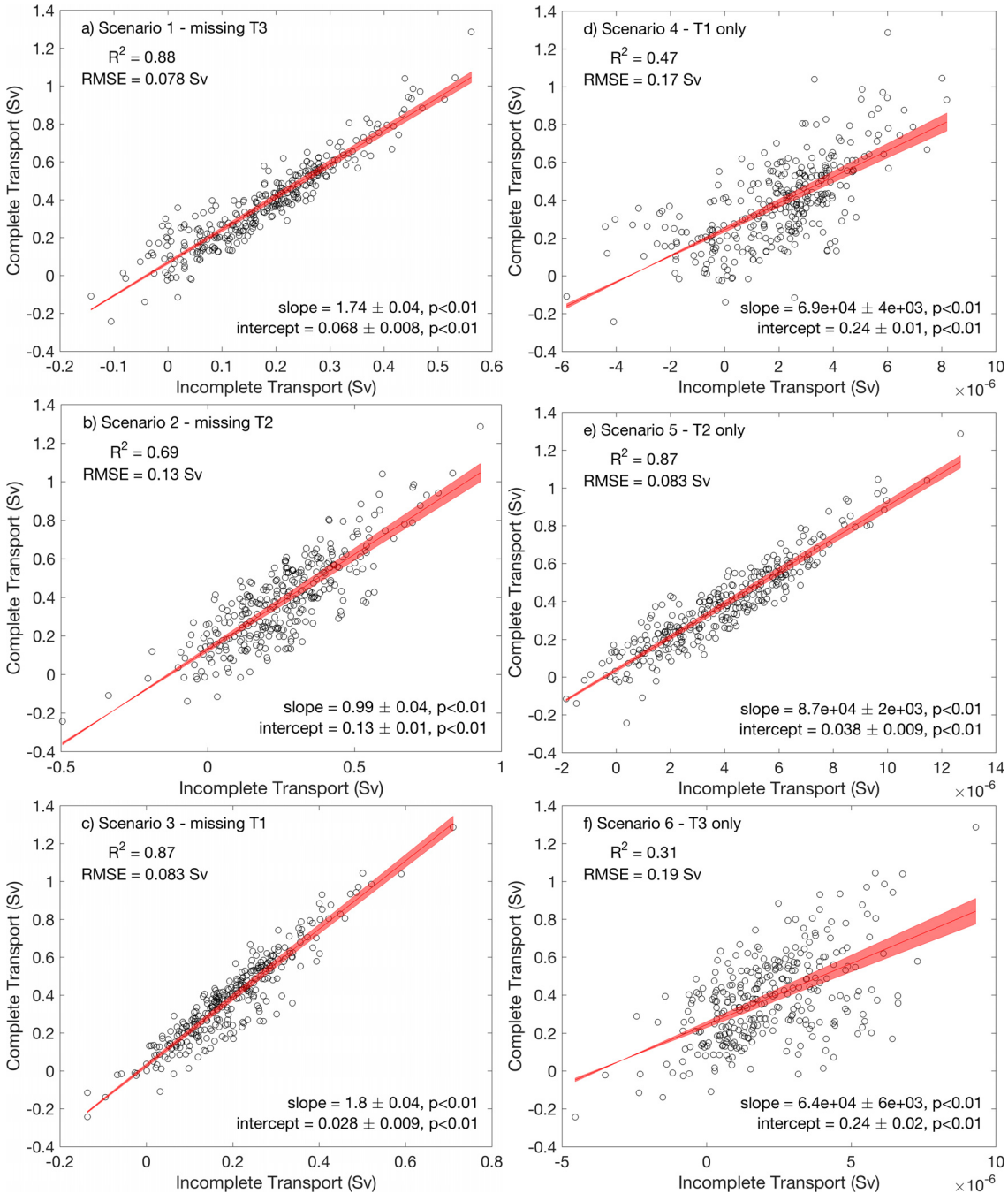


Figure 2.7: Linear regressions used to reconstruct the alongshore transport (in Sv, 1 Sv = $10^6$ $m^3/s$) associated with the NSC based on ADCP observations at the T-stations (positive means southwestward). For each of the 6 possible scenarios, the slope and intercept of the regressions (red line) are indicated, along with their corresponding error and p-value. The coefficient of determination ($R^2$) and Root-Mean-Squared-Error (RMSE) are included in each panel.

5). In comparison, the coefficients of determination are lower in scenarios where only T1 or T3 was considered (scenarios 4 and 6). Using the linear regressions, we were able to reconstruct a quasi-continuous time series of the alongshore transport between T1 and T3 over the 2008-2015 period. The scattering shown around the regression line in Figure 2.7 introduces some degree of uncertainty in the reconstructed transport, especially for scenarios 2, 4, and 6. These uncertainties are represented by the Root-Mean-Squared-Error (RMSE) asociated with each linear regression. However, we consider this uncertainty to have a limited impact on our analysis, due to the relatively high variance explained by three of the linear regressions (scenarios 1, 3, and 5; see Figure 2.7), and the relatively short period covered by the scenarios 2, 4, and 6 (14.4% of the total time series, or 367.2 days).

### 2.3.2 Cross-Covariance Function and Bootstrapping

The cross-covariance function $c_{xy}$ between time series $x$ and $y$ were calculated according to the following equation:

$$c_{xy}(\tau) = \sum_{n=0}^{N-\tau-1} \left( x_{n+\tau} - \frac{1}{N} \sum_{i=0}^{N-1} x_i \right) \left( y_n^\star - \frac{1}{N} \sum_{i=0}^{N-1} y_i^\star \right) \tag{2.6}$$

where $\tau$ is the time lag, $N$ is the length of the time series $x$ and $y$, and the star denotes the complex conjugate. The normalized cross-covariance was then calculated by scaling the cross-covariance so that the auto-covariances at zero lag ($\tau = 0$) equal 1.

$$\rho_{xy}(\tau) = \frac{c_{xy}(\tau)}{\sqrt{c_{xx}(0) c_{yy}(0)}} \tag{2.7}$$

To provide an estimate of the confidence intervals, a bootstrapping method was used, which does not make the assumption of normality in the probability distribution of the cross-covariance. For each time lag $\tau$, the time series were re-sampled with repetition a thousand times. The cross-covariance was computed every time, providing a probability distribution at each time lag. The 99% confidence intervals were estimated from this

distribution by taking the first and 99th percentiles.

### 2.3.3 Hilbert Empirical Orthogonal Function

To study the temporal and spatial variability of the NSC and to investigate the possible forcing mechanisms, a Hilbert Empirical Orthogonal Function (HEOF) decomposition was applied to the velocity records at the T-stations. Empirical Orthogonal Functions (EOFs) are widely used in oceanography as a data reduction technique, separating the observed signal in modes of variability that may be linked to possible dynamical mechanisms. While a conventional EOF analysis finds stationary patterns (i.e., that do not evolve with time), the HEOF analysis is capable of extracting propagating signals from the dataset by applying the analysis to a complex process formed of the original field and its Hilbert transform (*Barnett*, 1983; *Horel*, 1984; *Von Storch and Zwiers*, 2001; *Hannachi et al.*, 2007; *Urrego-Blanco and Sheng*, 2012).

We consider the anomalies in the alongshore velocity field $u'(\vec{x}, t)$, where $\vec{x}$ is the spatial position (i.e., depth and station location), and $t$ is time. A new complex field **u'** for the HEOF analysis can therefore be constructed based on:

$$\mathbf{u'} = u' + iH(u') \tag{2.8}$$

The imaginary part of **u'**, $H(u')$, is the Hilbert transform of the original time series. It can be interpreted as a simple phase shift of $\pi/2$ in time, and is sometimes also referred to as the quadrature function (*Thomas*, 1969; *Barnett*, 1983). The complex time series **u'** carries both the in-phase and quadrature information on the temporal fluctuations in $u'$, allowing the zero-lag covariance matrix to be used to investigate propagating features in $u'$. Each element of the covariance matrix is calculated using:

$$c(i, j) = \text{cov}\{\mathbf{u'}(i, :), \mathbf{u'}(j, :)\} \tag{2.9}$$

where the covariance is calculated using Equation 2.6 at a zero-lag. To compensate for the

data gaps, any columns where **u'**$(i,:)$ or **u'**$(j,:)$ have a missing value were removed from the time series prior to computing $c(i,j)$.

The Singular Value Decomposition (SVD) method was applied to the covariance matrix of the complex field (*Emery and Thomson*, 2001). From this decomposition, the real eigenvalues $\lambda_n$ and the complex space-dependent eigenvectors $B_n(\vec{x})$ can be extracted from the main diagonal of the singular matrix and from the right singular vectors, respectively, for $n$ modes. The time series **u'** can now be expressed as a sum over $n$ modes of the product of a complex time-dependent score $A_n(t)$ and a complex space-dependent EOF $B_n(\vec{x})$:

$$\mathbf{u'}(\vec{x},t) = \sum_n A_n(t) B_n^{\star}(\vec{x}) \tag{2.10}$$

where the time-dependent scores are given by

$$A_n(t) = \sum_x \mathbf{u'}(\vec{x},t) B_n(\vec{x}) \tag{2.11}$$

The variance explained by the $n^{th}$ mode can be estimated using the real eigenvalues $\lambda_n$:

$$\sigma_n^2 = \frac{\lambda_n}{\sum_n(\lambda_n)} \tag{2.12}$$

Four functions can be calculated using the time-dependent score $A_n(t)$ and the complex space-dependent EOF $B_n(\vec{x})$: (1) the spatial phase function ($\theta_n$), (2) the spatial amplitude function ($S_n$), (3) the temporal phase function ($\phi_n$), and (4) the temporal amplitude function ($R_n$). The time series **u'** can therefore be expressed as:

$$\mathbf{u'}(\vec{x},t) = \sum_n R_n(t) e^{i\phi_n(t)} S_n(\vec{x}) e^{i\theta_n(\vec{x})} \tag{2.13}$$

While HEOFs have proven to be a useful tool for the study of propagating features in both meteorology and oceanography (*Barnett*, 1983; *Horel*, 1984; *Von Storch and Zwiers*,

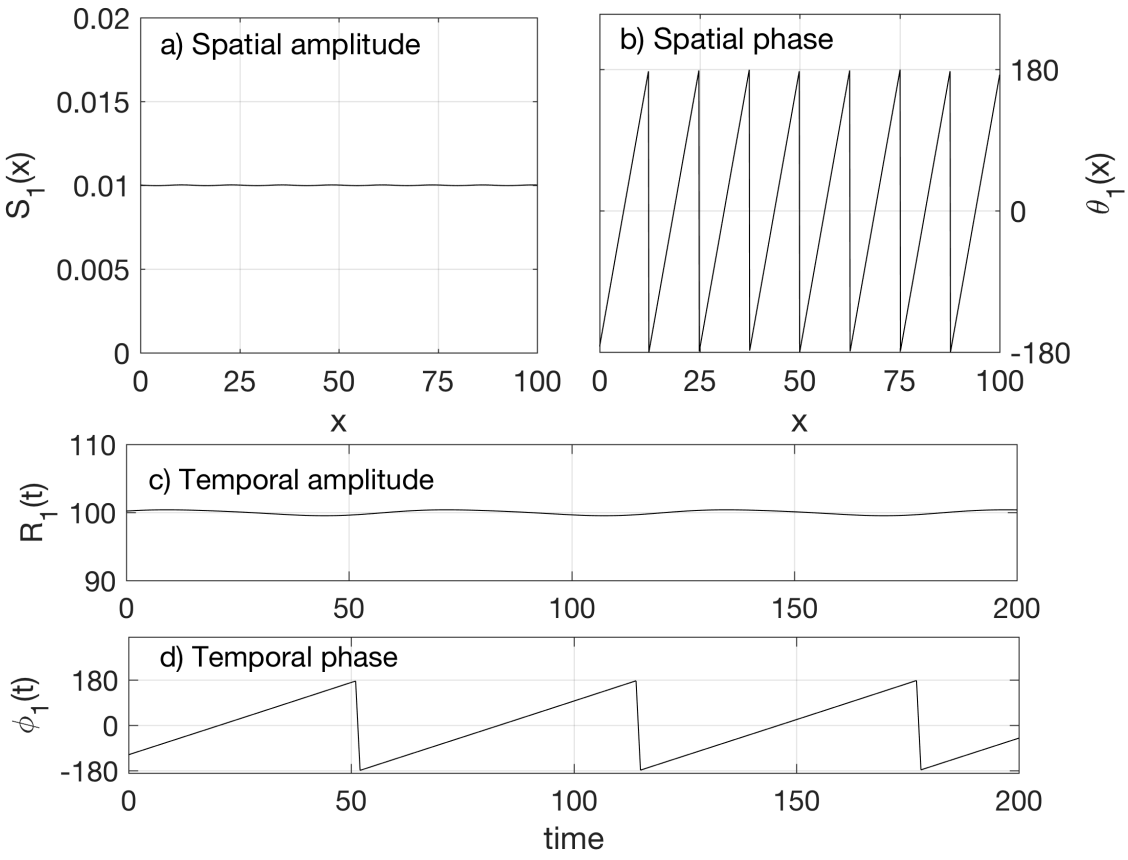


Figure 2.8: Plots of the four measures for the first mode of variability of a one-dimensional wave extracted using the HEOF analysis. a) Spatial amplitude, b) Spatial phase, c) Temporal amplitude, and d) Temporal phase.

2001; *Hannachi et al.*, 2007; *Urrego-Blanco and Sheng*, 2012), the interpretation of the modes of variability through those four measures is not straightforward and can rapidly become too complex for a clear mechanistic interpretation. We therefore introduce each of the four functions in the context of a simple one-dimensional wave propagating in the positive x-direction, with constant amplitude $a = 1$, wavenumber $k = 0.50$, and frequency $\omega = 0.10$ to illustrate how wave characteristics can be extracted using HEOFs (Figure 2.8; *Barnett*, 1983). In this example, only the first mode of variability is considered since it explains almost the entirety of the one-dimensional wave.

1. The spatial amplitude function, $S_n(\vec{x})$, is a measure of the spatial homogeneity in the magnitude of **u'**$(\vec{x}, t)$. It is defined by:

$$S_n(\vec{x}) = [B_n(\vec{x}) B_n^{\star}(\vec{x})]^{1/2} \tag{2.14}$$

   The value of the spatial magnitude in Figure 2.8 is constant as the amplitude of the one-dimensional wave is a constant and independent of $\vec{x}$. The spatial amplitude function can be interpreted in the same way as in a normal EOF analysis.

2. The spatial phase function, $\theta_n(\vec{x})$, is a measure of the phase lag between different spatial locations. This phase lag is only to be interpreted as a relative time lag, as it represents the lag of a location compared to an arbitrary reference. It is defined by:

$$\theta_n(\vec{x}) = \arctan\left[\frac{\Im\{B_n(\vec{x})\}}{\Re\{B_n(\vec{x})\}}\right] \tag{2.15}$$

   In the case of the one-dimensional wave, we can see that $\theta_1(\vec{x})$ goes through a complete cycle (i.e., $360^o$) over 12.2 spatial units, corresponding to a wavenumber of $k = 0.51$, which agrees with the set value of $k = 0.50$ (Figure 2.8). The spatial derivative $d\theta_n/d\vec{x}$ therefore provides an estimate of the wavenumber (*Barnett*, 1983).

3. The temporal amplitude function, $R_n(t)$, describes the magnitude of **u'**$(\vec{x}, t)$ over time and is proven useful when describing cyclostationary processes (*Barnett*, 1983). It is defined by:

$$R_n(t) = [A_n(t) A_n^{\star}(t)]^{1/2} \tag{2.16}$$

   As for the spatial amplitude function, this measure should be constant in the case of our one-dimensional wave, as the amplitude of the wave is independent of time (Figure 2.8).

4. The temporal phase function, $\phi_n(t)$ describes the variation of phase in **u'**$(\vec{x}, t)$ in

time. Again, the phase is relative to an arbitrary time, and should not be interpreted as an absolute time lag. It is defined by:

$$\phi_n(t) = \arctan\left[\frac{\Im\{A_n(t)\}}{\Re\{A_n(t)\}}\right] \tag{2.17}$$

The temporal phase lag showed in Figure 2.8 experiences a full cycle over 62.8 time units, which precisely corresponds to the set frequency of the one-dimensional wave of $\omega = 0.10$. The temporal derivative $d\phi_n/dt$ therefore provides an estimate of the frequency (*Barnett*, 1983).

Combining information extracted from all of these functions provides valuable knowledge on the signal studied. A conventional EOF analysis would only provide information on the spatial and temporal amplitude functions, which provide limited information on the decomposed signal. This simple example highlights that the other two metrics yielded by the HEOF analysis (i.e., temporal and spatial phase functions) are key to gain knowledge about the signal propagation throughout the time series. The temporal functions are also a useful tool to identify and describe cyclostationary processes in the dataset, if present.

## 2.4 Summary

In this chapter, the principal data sources used in this study were introduced. Data sources included hydrographic observations from moorings (bottom-mounted CTDs), repeated CTD casts at fixed locations, and underwater gliders. Current measurements were collected from bottom-mounted moored upward-looking ADCPs, and derived from underwater gliders' flight characteristics. The three-dimensional numerical model outputs used to complement observations to attain specific objectives in this study were also described.

An overview of the data processing steps was presented, including the algorithm used to extract horizontal velocities from the glider measurements. Statistical techniques were used to reconstruct missing data, and extract information from the field data.

# CHAPTER 3

# HYDROGRAPHY AND CIRCULATION ALONG THE HALIFAX LINE

In this chapter, the oceanographic datasets described in Chapter 2 (e.g., from ADCPs, gliders, CTDs, etc.) are used to characterize the oceanographic conditions along the HL using temperature, salinity and current velocity. The temporal resolution and coverage of the time series allow a detailed description of the temporal variability in hydrography and oceanic currents on both seasonal and inter-annual timescales. The high spatial resolution of glider measurements is complementary to the other data sources by providing a much finer spatial coverage than the moored instruments.

The main objectives of this chapter are therefore to develop a reasonably comprehensive knowledge of oceanographic conditions along the HL, as well as to characterize the seasonal and inter-annual variability of circulation and hydrography over the region. The anomalously warm conditions observed in 2012 over the Scotian Shelf and the Grand Banks (herein referenced to as the "2012 anomaly"; *Hebert et al.*, 2013; *Chen et al.*, 2015) were captured by the observed time series, which provides an opportunity for the study of the physical mechanisms affecting the conditions over the Scotian Shelf. The analysis presented in this chapter provides the background knowledge and oceanographic context necessary for the subsequent chapters.

Section 3.1 describes the hydrographic variability. Section 3.2 focuses on the local

circulation and alongshore transport. In these two sections, the inter-annual variability and the 2012 anomaly are discussed. A short summary is provided in Section 3.3.

## 3.1 Hydrographic Variability Along the Halifax Line

The low-frequency variability (i.e., seasonal and inter-annual) in the hydrography along the HL is determined by combining different data sources. The data sources include bottom-mounted CTDs, underwater glider transects and large scale monitoring programs (i.e., AZMP and AZOMP). Based on a water mass analysis, the general dynamics of the system are investigated, and possible mechanisms responsible for the 2012 warm anomaly are discussed.

### 3.1.1 Mixing Triangle: End-Members, Projections and Maxwell's Triangle

Hydrographic observations collected as part of AZMP and AZOMP over the 2011-2014 period (see Chapter 2) are used to characterize the important water masses along the HL previously identified in the literature (*McLellan*, 1954; *Gatien*, 1976; *Petrie and Drinkwater*, 1993). The end-members used in our water mass analysis are defined using four regions sampled by AZMP and AZOMP (temperature and salinity distributions are shown in Figure 3.1).

1. Observations collected across Cabot Strait were used to characterize low-salinity waters originating from the St. Lawrence River and transiting mainly through the western part of the GSL (Figure 2.1). The hydrographic observations were used to define two different water masses: Cabot Strait subsurface water (CBSs) found between 30 and 50 m, and the Cold Intermediate Layer (CIL) locally formed in the GSL and located between 50 and 120 m (CBS-CIL; *Gilbert and Pettigrew*, 1997; *Galbraith et al.*, 2013). The top 30 m of the water column at Cabot Strait was not included in the analysis to reduce the effects of seasonal variability in the net surface

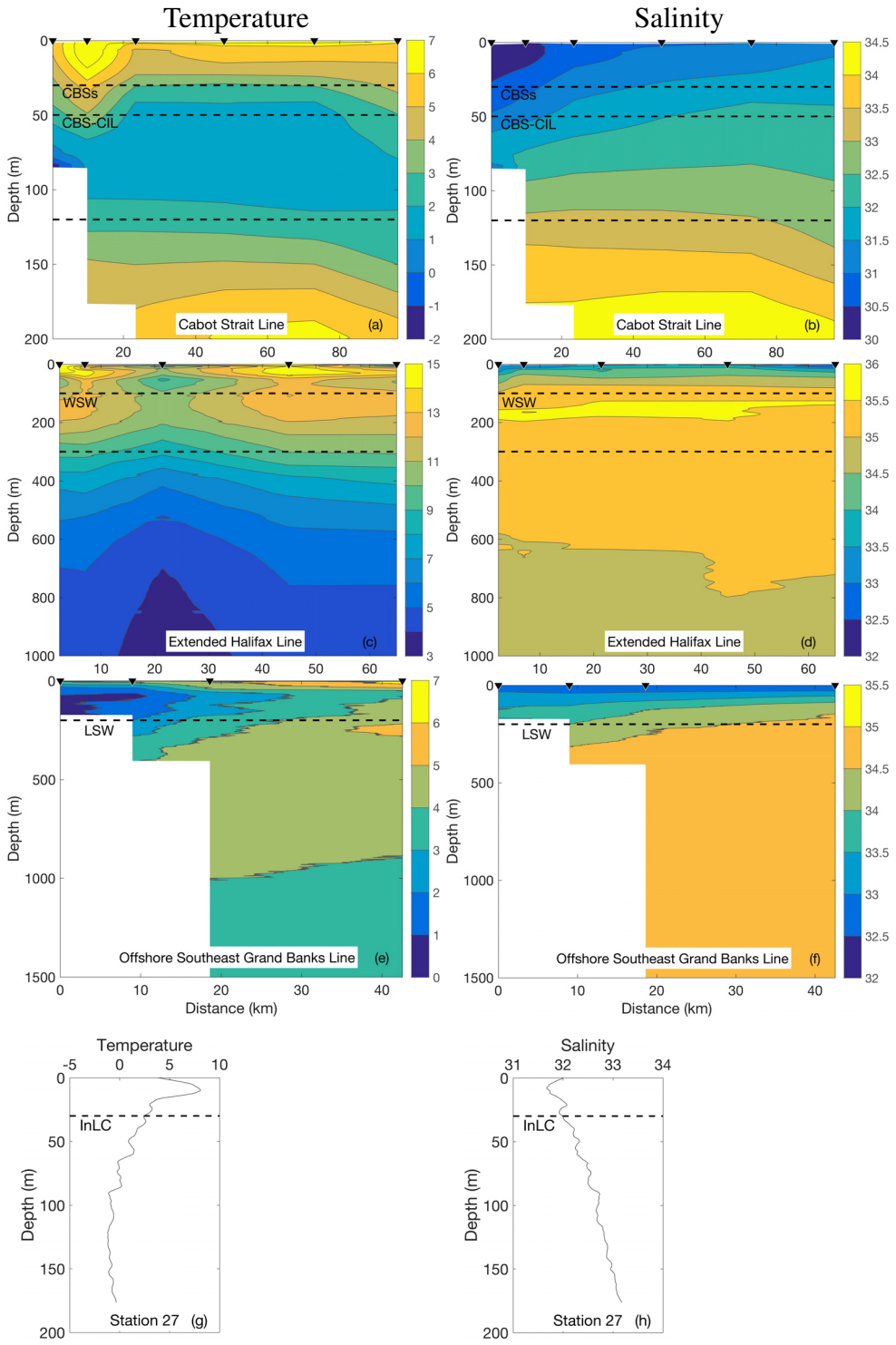


Figure 3.1: Distributions of time-mean temperature (in $^{o}$C; left panels) and salinity (right panels) averaged over the 2011-2014 period along three AZMP and AZOMP transects used to define the water mass end-members ((a) through (f)). Vertical profiles of (g) temperature and (h) salinity at Station 27 averaged over the 2011-2014 period are shown. The depth-intervals defining the different water masses (CBSs, CBS-CIL, WSW, LSW, InLC; see Section 3.1.1) are indicated with dashed lines. Downward-pointing triangles indicate sampling stations.

heat flux on the definition of end-members. While part of this water mass makes up the NSC, a portion flows along the southern bank of the Laurentian Channel to reach the Shelf break.

2. Observations at Station 27 located to the east of Newfoundland were used to define the Inshore Labrador Current Water (InLC; see Figure 2.1). Following the same reasoning as for the definition of CBSs, only observations located below 30 m were considered. The water forming the inshore branch of the Labrador Current is thought to, at least partially, enter the GSL through the northern side of Cabot Strait, recirculate within the GSL, and exit the GSL through the southern side of Cabot Strait (see Figure 1.1)

3. Hydrographic observations collected along the "Extended Halifax Line" (Figure 2.1) were used to characterize the water mass located over the continental slope off the Scotian Shelf, generally referred to as the Warm Slope Water (WSW) in the literature (*Gatien*, 1976; *Petrie and Drinkwater*, 1993). This water mass corresponds to the sub-surface water between 100 m and 300 m over the Scotian Slope and was used as an end-member to investigate the offshore slope water penetrating onto the Scotian Shelf (see Figure 4 in *Gatien*, 1976).

4. Hydrographic data collected over the offshore portion of the "Southeast Grand Banks" AZMP transect were used to describe the Labrador Slope Water (LSW). LSW is defined as the water mass located over the Newfoundland Slope at depths greater than 200 m (see Figure 2.1). This water mass is thought to flow along the continental slope and can penetrate onto the Scotian Shelf through canyons and gullies or during upwelling events at the Shelf break (see Figure 4 in *Gatien*, 1976; *Han and Loder*, 2003; *Shan et al.*, 2014a).

For each of these water masses, yearly end-members were determined over the 2011-2014 period and are represented by ellipses in Temperature-Salinity (T-S) diagrams (see

Figure 3.2). The center of each ellipse represents the average temperature and salinity of the observations over the corresponding region. The vertical and horizontal axes of each ellipse represent one standard deviation of the temperature and salinity fields, respectively. Table 3.1 summarizes the T-S characteristics of the different water masses calculated for each individual year as well as the associated standard deviation of temperature and salinity. It is important to mention that the InLC and CBS-CIL water masses have similar T-S characteristics. When considering the hydrographic observations that define these two water masses, two-sample t-tests determined that their average T-S signatures were statistically different from one another over the 2011-2014 period. Unfortunately, when considering observations collected along the HL, it was impossible to reliably infer whether a water parcel having similar T-S properties came from the CIL formed in the GSL (i.e., CBS-CIL), or from the InLC. This is reflected by the fact that the ellipses associated with the CBS-CIL and InLC end-members largely overlap (Figure 3.2). Because of this uncertainty, which cannot be avoided without a third tracer (e.g., $\delta^{18}O$; *Khatiwala et al.*, 1999), CBS-CIL and InLC together define the third vertex of the mixing triangle, for which the precise origin remains uncertain (Figure 3.2).

To examine the seasonal variability, temperature and salinity averaged over the 2011-2014 period were used as end-members (Table 3.1). However, the analysis of the inter-annual variability was based on the yearly-estimated end-members. This approach allowed us to capture the inter-annual variability in the T-S characteristics of the end-members as well, which can be quite significant. In fact, Table 1 shows that the characteristics of each end-member can vary inter-annually, with an especially warm event in 2012 (*Hebert et al.*, 2013). Such an approach allowed for a more accurate estimation of the yearly contribution of each water mass to the T-S distribution along the HL.

Temperature and salinity measured by gliders were used to describe the T-S distribution at the HL. Two mixing lines and two major axes of variability were identified when analyzing the T-S diagrams (Figure 3.2):

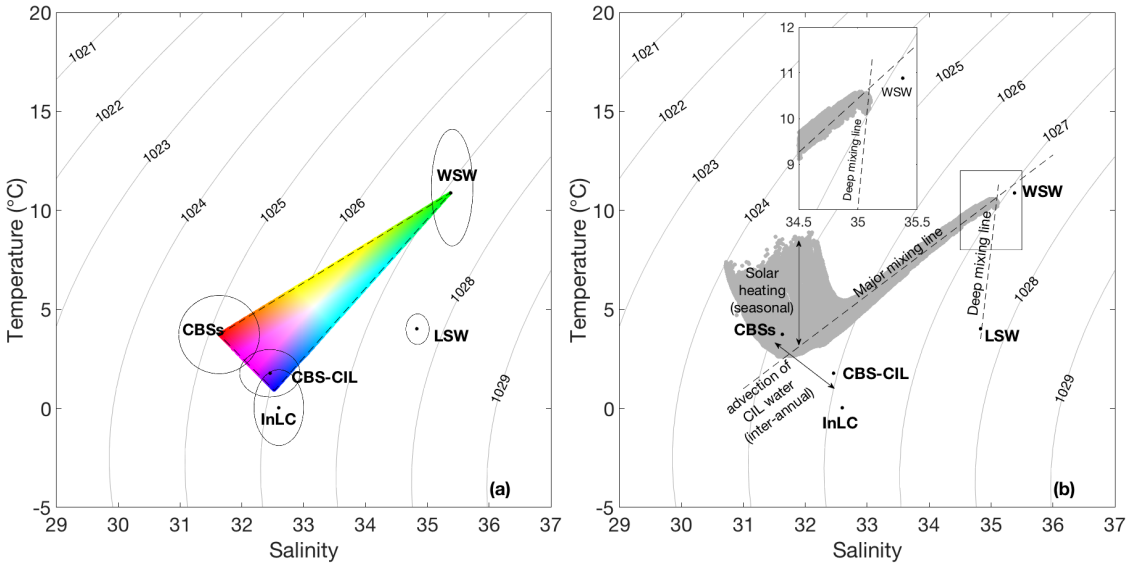


Figure 3.2: (a) Illustration of the color scheme used in the T-S space obtained by projecting Maxwell's triangle onto the mixing triangle defined by the water masses described in Section 3.1.1. End-members are determined for the 2011-2014 period and are represented as ellipses centered on the average temperature and salinity of the observations in the corresponding region. The vertical and horizontal axes represent one standard deviation of the temperature and salinity fields, respectively. (b) Example of the T-S distribution at the HL in spring that illustrates the different mixing lines and axes of variability. Inset in (b) shows a zoom-in on the tip of the T-S distribution to visualize the deep mixing line. Density contours are also indicated in both plots.

- A major mixing line connecting the WSW and the CBSs end-members.
- A "Deep mixing line" that runs from the major mixing line towards the LSW end-member and fits the warmer, and more saline, tip of the T-S distribution (see zoomed inset in Figure 3.2b).
- An axis of variability along the temperature axis (i.e., in the vertical) affecting surface water that varies on the seasonal timescale and is caused by surface heat fluxes (*Umoh and Thompson*, 1994). Most of this variability is left out of the analysis by selecting observations collected below 30 m only.
- An axis of variability that reflects the mixing between the CBSs water found in the subsurface layer and the CIL observed along the HL, and drives the inter-annual variability observed in the slope of the major mixing line.

Table 3.1: Yearly-averaged temperature (in $^{o}$C) and salinity used to describe the subsurface water from Cabot Strait (CBSs), the Cold Intermediate Layer formed in the GSL (CBS-CIL), Inshore Labrador Current (InLC) water, Warm Slope Water (WSW) and Labrador Slope Water (LSW). The averaged values over the 4-year period (2011-2014) used to study the variability at seasonal timescales are also included. Numbers inside the parentheses represents one standard deviation.

| | | 2011 | 2012 | 2013 | 2014 | Average |
|---|---|---|---|---|---|---|
| CBSs | T | 3.92 (2.67) | 3.10 (2.32) | 2.96 (2.97) | 1.99 (3.47) | 2.99 (2.86) |
| | S | 31.67 (0.56) | 31.78 (0.45) | 31.54 (0.83) | 31.57 (0.49) | 31.64 (0.58) |
| CBS-CIL | T | 2.37 (1.05) | 2.05 (0.79) | 1.55 (1.07) | 1.15 (1.40) | 1.78 (1.08) |
| | S | 32.53 (0.43) | 32.52 (0.44) | 32.35 (0.53) | 32.41 (0.52) | 32.45 (0.48) |
| InLC | T | 0.35 (1.41) | -0.62 (1.44) | -0.27 (1.21) | -0.83 (1.03) | -0.35 (1.27) |
| | S | 32.60 (0.32) | 32.78 (0.32) | 32.62 (0.31) | 32.75 (0.30) | 32.69 (0.31) |
| WSW | T | 8.15 (2.61) | 12.46 (1.35) | 13.38 (1.25) | 12.80 (1.85) | 11.70 (1.76) |
| | S | 35.03 (0.21) | 35.51 (0.13) | 35.71 (0.17) | 35.58 (0.26) | 35.46 (0.19) |
| LSW | T | 3.98 (0.47) | 4.20 (0.78) | 3.86 (0.89) | 4.09 (1.00) | 4.02 (0.78) |
| | S | 34.86 (0.14) | 34.82 (0.21) | 34.79 (0.28) | 34.86 (0.12) | 34.83 (0.19) |

Since the contribution of LSW to the water composition at the HL was relatively small and constrained to the deepest region of Emerald Basin, it was left out of the water mass analysis. A mixing triangle was defined using the CBSs and WSW end-members, with the third vertex defined as the average temperature and salinity between InLC and CBS-CIL. The definition of this third vertex reflects the uncertainty associated with the origin of water parcels with hydrographic characteristics located in that region of the T-S space.

To visualize the spatial distribution of T-S points, a two-dimensional colorbar was defined by projecting Maxwell's triangle onto the mixing triangle, therefore associating a unique color with each T-S pair located inside the mixing triangle (Figure 3.2a; *Judd*, 1935). In order to assign a color to points lying outside the mixing triangle, while ignoring datapoints located within the upper 30 m of the water column, those points were projected either:

- vertically onto the CBSs - WSW edge of the triangle. This applied to data-points located above the major mixing line and below 30 m deep. It is justified by the fact

that the variability is mainly driven by net surface heat fluxes and is therefore purely vertical in the T-S space (*Umoh and Thompson*, 1994).

- perpendicularly onto the other two sides of the mixing triangle.

The percentages ($P$) of each end-member were estimated for each datapoint by solving for the $P$'s in the following set of equations:

$$\begin{aligned} S_{obs} = &\quad P_{CBSs}S_{CBSs} &+ P_{WSW}\ \ S_{WSW} + &\quad P_{(CBS-CIL,InLC)}S_{(CBS-CIL,InLC)} \\ T_{obs} = &\quad P_{CBSs}T_{CBSs} &+ P_{WSW}\ \ T_{WSW} + &\quad P_{(CBS-CIL,InLC)}T_{(CBS-CIL,InLC)} \\ 1 = &\quad P_{CBSs} &+ P_{WSW} &+ \quad P_{(CBS-CIL,InLC)} \end{aligned} \tag{3.1}$$

### 3.1.2 Seasonal Variability

In winter (January to March), a two-layer system develops at the HL with colder and fresher water overlaying a warmer and saltier deep layer (Figure 3.3). The potential density is lowest in the upper layer over the first 30 km from the shore. This low-density water mass is associated with the GSL outflow and has a colder and fresher T-S signature compared with the ambient shelf water (*Loder et al.*, 2003). This lower-density water mass is separated from the offshore shelf water by a sharp density front located between 40 and 60 km from shore at the surface and intersects the bottom around the 100 m isobath, located approximately 25 km offshore.

In spring (April to June), the vertical temperature structure shifts towards a three-layer system as the surface water warms up and overlays the cold water located between 20 and 100 m, forming the so-called CIL (Figure 3.3d; *Loder et al.*, 2003; *Umoh and Thompson*, 1994). The CIL provides a footprint of the ocean surface temperature experienced during the previous winter and is strongest over coastal waters (less then 50 km from the shore; Figure 3.3d). The CIL is partially formed through the cooling of GSL surface water that

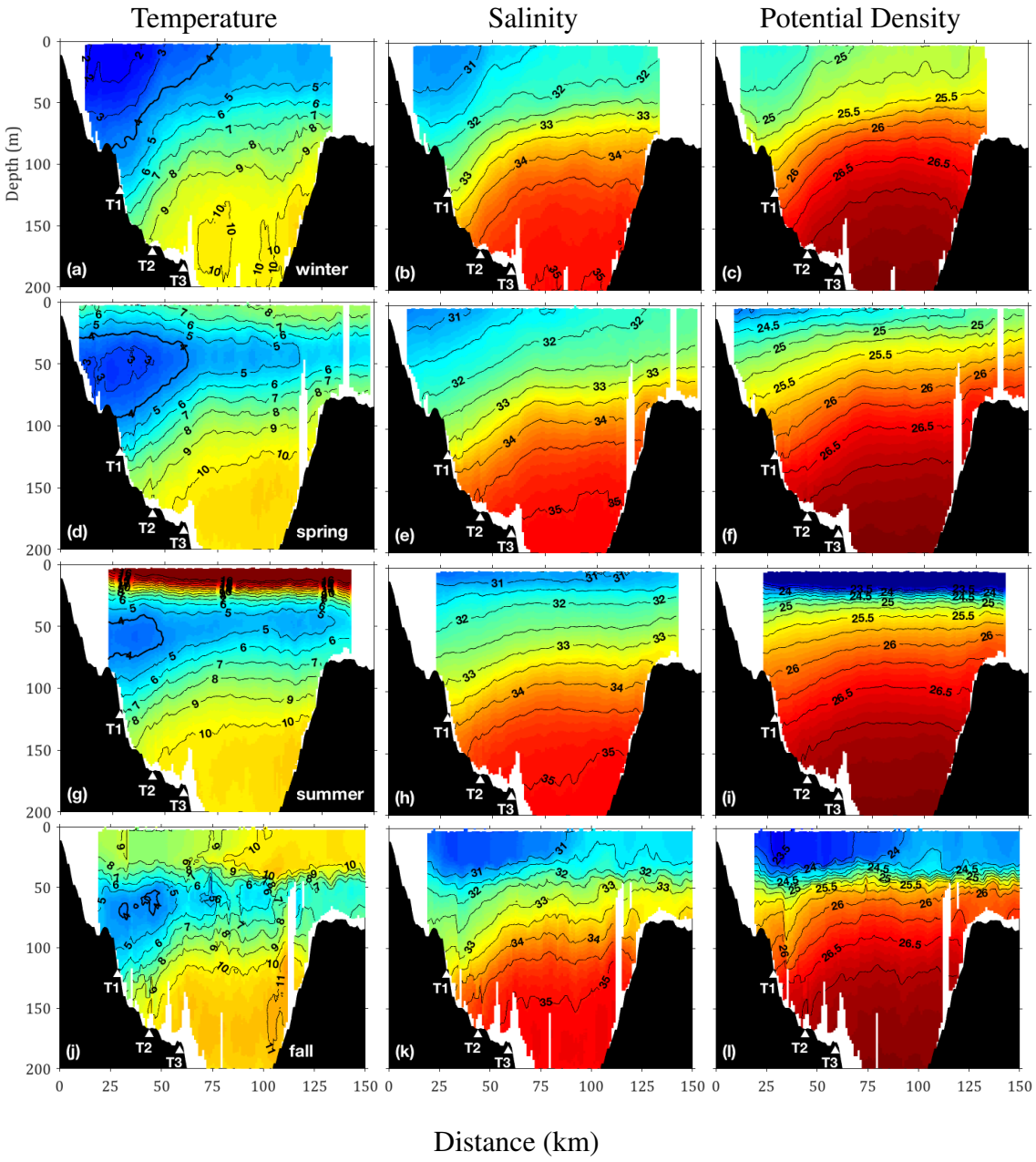


Figure 3.3: Gridded seasonally-averaged temperature in $^{o}$C (left panels), salinity (middle panels) and potential density in kg/m$^3$ (right panels) in winter (January, February, and March; $1^{st}$ row), spring (April, May, and June; $2^{nd}$ row), summer (July, August, and September; $3^{rd}$ row) and fall (October, November, and December; $4^{th}$ row) at the Halifax Line, based on glider observations over the period from June 2011 to September 2014. The 4$^{o}$C isotherm is used to define the Cold Intermediate Layer and is represented as a thick line in the temperature transects.

is advected onto the Scotian Shelf, but is mainly the result of local processes (*Umoh and Thompson*, 1994). The horizontal salinity gradient in the offshore direction in the top layer decreases from winter to spring, as shown by the flattening of isohalines above 100 m. Below 100 m, the temperature and salinity distributions are very similar to those observed in winter. The resulting density distribution features a larger horizontal density gradient close to the surface, compared to winter conditions, but a more stable water column with only slightly tilted isopycnals. The low-density signature of the NSC is still identifiable inshore in spring.

In summer (July to September), the surface temperature along the HL reaches a maximum and the water column is more stratified vertically than that in the spring months. It is worth noting that the sea surface temperature over the Shelf varies by more than 16$^o$C over the course of a year while the core temperature of the CIL experiences a comparatively small seasonal variability. The 4$^o$C isotherm, which is normally used to define the CIL over the Scotian Shelf, was used here to quantify the change in the core temperature and spatial extent of the CIL along the HL (*Hebert et al.*, 2013). When seasonally-averaged over the 2011-2014 period, the core temperature of the CIL (i.e., minimum temperature) warms up by 0.8$^o$C (from 2.6 to 3.4$^o$C) and the cross-sectional area shrinks from 2.48 to 0.68 km$^2$ from spring to summer.

In fall (October to December), the surface temperature becomes colder than in the summer due to the upward net heat flux at the sea surface and increased wind-driven vertical mixing (Figure 3.3j). A temperature drop occurs over the inner shelf ($<$ 75 km), due to the increased advection of cold and fresh water coming from the GSL in fall. The CIL experiences further erosion with a core temperature of 3.9$^o$C and a cross-sectional area of 0.13 km$^2$. The decrease in temperature over the inner shelf is accompanied by the development of a coincident body of low-salinity water (S$<$31), supporting the hypothesis that this water forms because of an increased inflow of low-salinity waters from the GSL. The inshore low salinity reaches an annual minimum, creating the basis for the large

horizontal density gradient observed in the winter. The density field in fall shows the low-density signature of the water coming from the GSL over the inner Scotian Shelf. Nevertheless, isopycnals are still flatter than in the wintertime, mainly due to the horizontal density front located at 50 m depth that is generated by the temperature distribution. It should be noted that large horizontal variations in the sub-surface (70-120 m) potential density occur at about 35 km from the coast in fall (Figure 3.3l), due mainly to large horizontal variations in the sub-surface salinity (Figure 3.3k). It was found that, in fall 2012, the glider was caught into a flow reversal event, where the currents over the inner shelf were northeastward for a few days. Because of the fewer number of transects completed in the fall of 2012 than in other years, this 2012 singular event is reflected in the seasonal average.

The seasonal distributions of the T-S characteristics at the HL show that upper water temperatures are affected by the seasonal surface warming and cooling (gray dots in Figure 3.4). Using the water masses and the color scheme described in Section 3.1.1, a water mass analysis was conducted using the high resolution glider data. The analysis demonstrates that the water in the upper layer at the HL is mainly CBSs water and therefore originates from the GSL, with the highest percentage located over the inner shelf. For deep or further offshore waters at the HL, the proportion of WSW increases, while the percentage of CBSs water decreases (Figure 3.4). Indeed, the water located below the water depth of Emerald Bank (i.e., 80 m) has T-S characteristics that resemble the WSW. The seasonal variability in the distribution of CBSs along the HL follows the same pattern as the one for the low-density water previously described. In winter, CBSs at the HL is more concentrated within the first 60 km from the shore and can penetrate as deep as 100 m. The distribution of CBSs then shallows and spreads offshore with time, to be mainly located in the upper 40 m of the water column and across the entire shelf along the HL in summer. CBSs still dominates the upper layer along the HL in the fall, although the percentage of WSW slowly increases, especially over the outer shelf ($>$70 km).

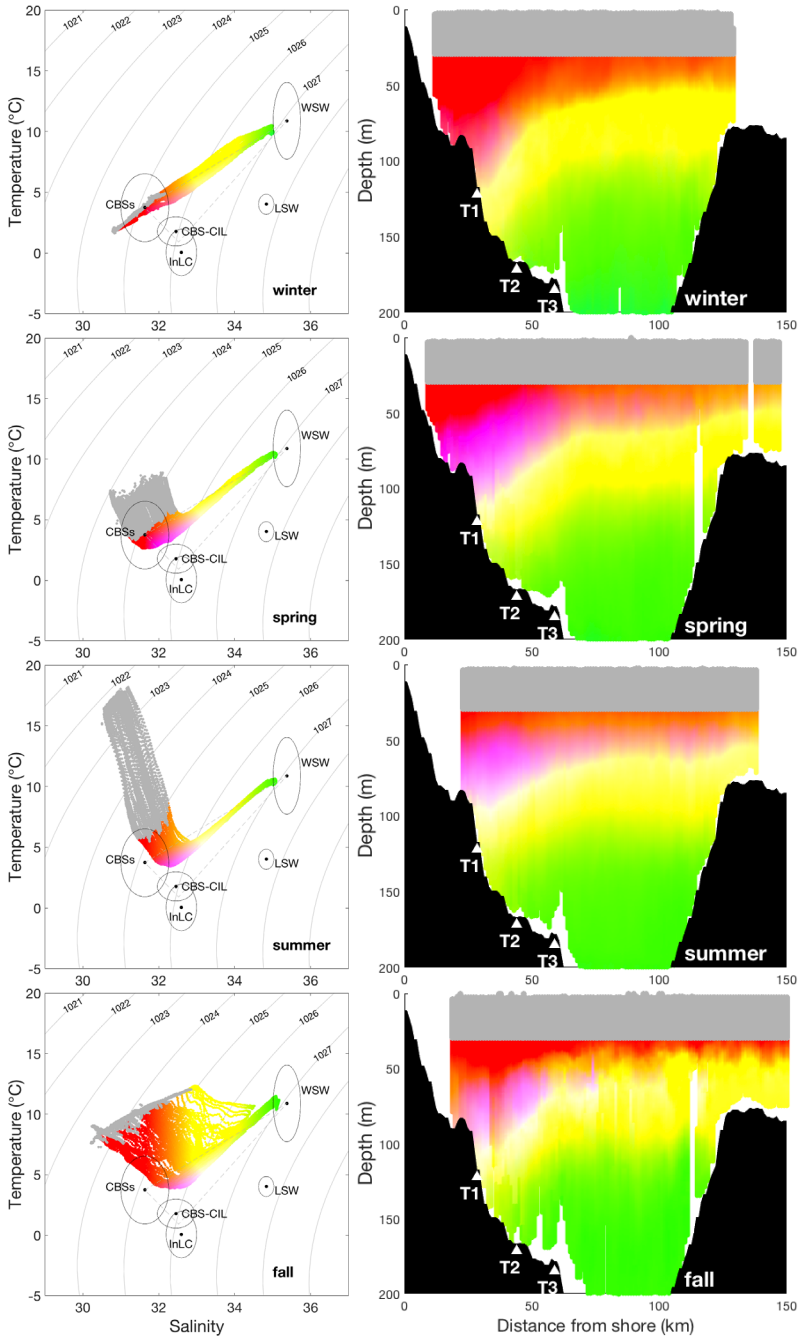


Figure 3.4: T-S diagrams based on glider observations at the Halifax Line for the 2011-2014 period (left panels) in winter (JFM; $1^{st}$ row), spring (AMJ; $2^{nd}$ row), summer (JAS; $3^{rd}$ row) and fall (OND; $4^{th}$ row). The color scheme corresponds to Maxwell's triangle (see Figure 3.2). End-members are calculated over for the 2011-2014 period and are represented as an ellipse centered on the center of gravity of the observations in the corresponding region with the main axes representing the standard deviation of the temperature and salinity fields. Right panels show the distributions along the Halifax Line using the same color scheme, for all four seasons. In all panels, the gray color has been associated to the observations collected within the upper 30 m of the water column.

As mentioned in Section 3.1.1, the origin of the water found between CBSs and WSW was difficult to identify, since it lies in a region where the CBS-CIL and InLC ellipses overlap in the T-S space (magenta in Figure 3.4). It means that water from this region can either be composed of water coming from the CIL, formed in the GSL, or of InLC water, or more likely of a combination of both. Several pathways could explain the presence of InLC water along the HL. InLC is known to penetrate the GSL through the Strait of Belle Isle as well as through the northeastern part of Cabot Strait (*Galbraith et al.*, 2013). It is possible that the InLC water residing in the GSL is advected with the CBS-CIL out of the GSL and onto the Scotian Shelf. Another possible pathway would be a shelf intrusion through canyons and gullies located along the shelf break of the Scotian Shelf (*Han and Loder*, 2003; *Shan et al.*, 2014b; *Rogers*, 2015).

Some features of the seasonal variability at the HL were previously examined using historical data (*Smith et al.*, 1978; *Loder et al.*, 2003) or numerical simulations (*Han et al.*, 1997; *Urrego-Blanco and Sheng*, 2014). The former only allows studies over decadal timescales and suffers from significant aliasing (*Mann and Needler*, 1967; *Mann*, 1969; *Petrie*, 2004). The latter is subject to all the limitations of numerical modeling techniques (e.g., parameterization, grid resolution, etc.). Hydrographic observations made by gliders thus provides the first high-resolution observational dataset resolving both the seasonal and inter-annual variability along the HL.

### 3.1.3 Inter-annual Variability

To characterize the inter-annual variability in hydrography along the HL, time series of near-bottom temperature and salinity collected at the three T-stations were combined with the glider data to improve spatiotemporal coverage (Figure 3.5).

The temperature and salinity observed at T1 exhibit a larger variability over a wide range of frequencies in comparison with the hydrographic observations at T2 and T3. This is expected since the water depth at T1 is shallower than those at the other two stations and the hydrography at T1 is therefore more affected by surface forcing than at T2 or T3. T1

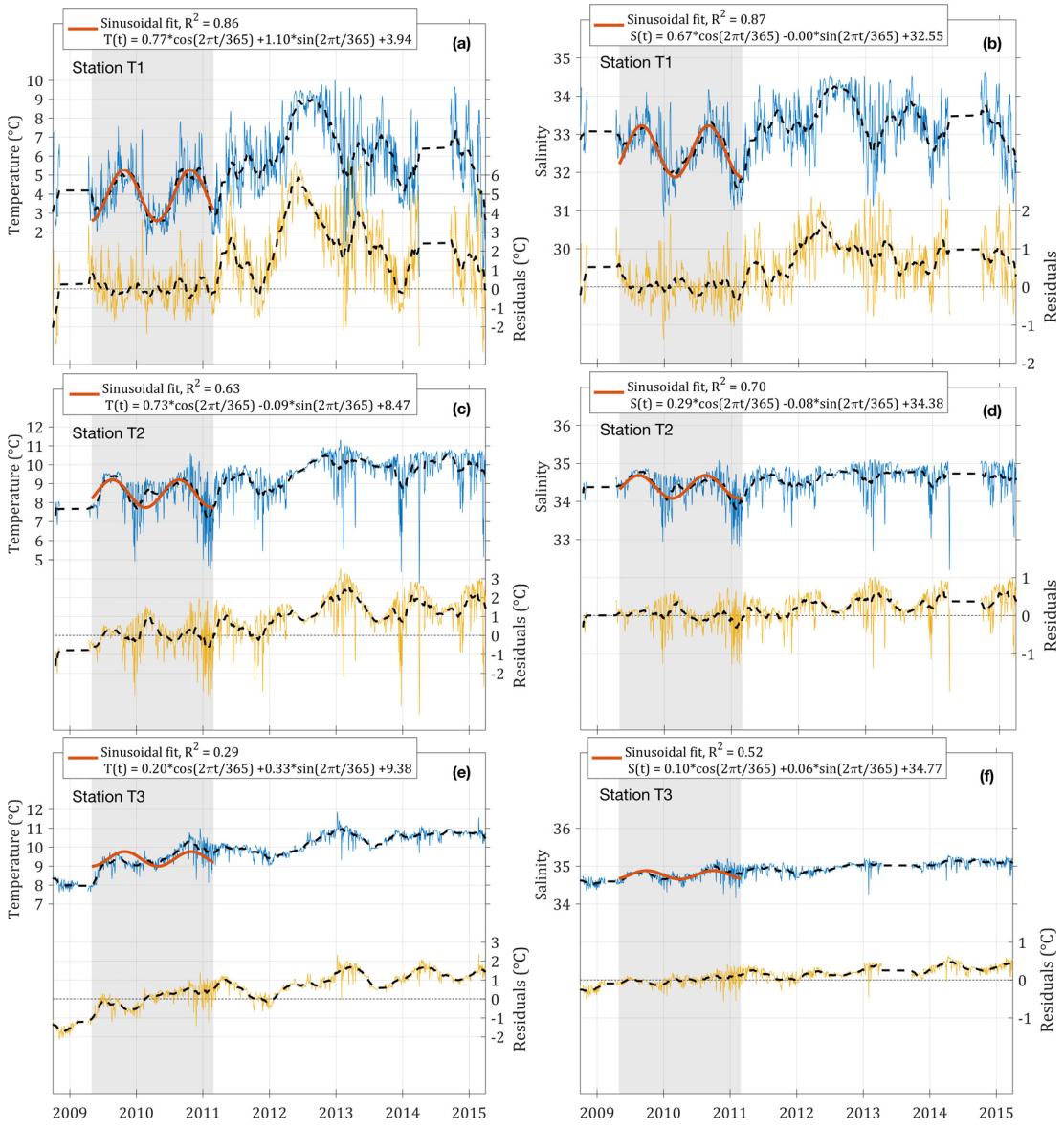


Figure 3.5: Time series (blue line) of observed near-bottom temperature (left panels) and salinity (right panels) at T1 (top), T2 (center), and T3 (bottom). In each panel, a sinusoidal function is fitted (red curve) to the data over the period represented by the shaded area. Residuals are obtained by removing the sinusoidal fit (red curve) from the observations (blue curve) and are included in each panel (yellow curve). For each time series, filtered data using a 60-day moving average (thick, dashed line) are superimposed to highlight low-frequency variability.

is also located in a frontal zone ($\sim$100 m depth), and thus observations at T1 capture the seasonal cross-shore movement of the front along the bottom (see Figure 3.3). This agrees with the observations discussed in Section 3.1.2: cold and fresh conditions were observed in the wintertime, when the foot of the density front is at its deepest and CBSs water is present as deep as the 100 m isobath (Figure 3.4). In the summer, the water is warmer and more saline than in the winter as the density front shallows and the water column stratifies, due to the increasing contribution of WSW to the water composition along the 100 m isobath.

The 7-year-long time series reveals a large temperature and salinity anomaly starting in 2011 and persisting until the end of the measurement records in 2015. To further examine the inter-annual variability, a sinusoid with a period of 365 days was used to fit the time series over the period extending from May 2009 to March 2011, where the hydrographic conditions were judged to be within one standard deviation from the climatological conditions (Figure 3.5; *Loder et al.*, 2003). The fitted seasonal cycle was then subtracted from the time series to produce temperature and salinity residuals.

The seasonal anomalies with respect to the 2009-2011 period (i.e., the residuals in Figure 3.5) feature an abnormally high temperature at all three T-stations over the 2011-2014 period, with the largest anomaly at T1 in summer, where the anomaly reached about +6 $^{o}$C during the summer of 2012. By comparison, the warm event was milder at T2 and T3 ($\sim$180 and 190 m depth), with an anomaly varying between +1 and +3$^{o}$C. A coherent anomaly occurred in the observed salinity field, with an abnormally high salinity beginning in 2011. Similar to the temperature anomaly, the salinity anomaly was largest at T1 among the three T-stations, with a maximum amplitude of +2 measured in the summer of 2012. At T2 and T3, the anomaly ranged between +0.5 and +1.

A significant positive linear trend in the observed temperature and salinity fields occurs over the length of the time series, particularly at T2 and T3. Linear regressions applied to the residuals yield a warming rate of +0.43$^{o}$C/yr ($\pm$0.02$^{o}$C/yr, $R^2$=0.20, $p<0.05$) at

T1, +0.34$^o$C/yr ($\pm$0.01$^o$C/yr, $R^2$=0.53, $p<0.05$) at T2, and +0.369$^o$C/yr ($\pm$0.005$^o$C/yr, $R^2$=0.77, $p<0.05$) at T3. At T1, the linear warming trend only explains 20% of the low-frequency variability. However, this linear trend dominates the inter-annual temperature variability observed at T2 and T3, explaining between 53% and 77% of the low-frequency variance. Similar trends were extracted from the salinity field, with a rate of +0.12 per year ($\pm$0.01/yr, $R^2$=0.12, $p<0.05$) at T1, +0.057 per year ($\pm$0.005/yr, $R^2$=0.20, $p<0.05$) at T2, and +0.081 per year ($\pm$0.001/yr, $R^2$=0.81, $p<0.05$). Again, the linear trend explains a larger part of the signal at T3 than at T1 and T2. The increasing trends in the observed near-bottom temperature and salinity differ significantly between the three T-stations, despite the small distance separating them ($\sim$16 km). This can be partially explained by the change in water depths between the three stations, since T1 is located around the 100 m isobath, and T2 and T3 are located between the 170 and 190 m isobaths. These trends are present throughout the entire time series at the three T-stations and are likely part of decadal variability (*Urrego-Blanco*, 2014).

The 2012 abnormal hydrographic anomaly was observed over the Scotian Shelf and the GoM in the past (*Hebert et al.*, 2013; *Chen et al.*, 2015; *Pershing et al.*, 2015), although the main physical mechanisms are not well understood. Combining the spatiotemporal coverage of glider missions with the long time-series collected at the T-stations provides an opportunity to discuss the main processes driving the inter-annual hydrographic variability along the HL. Especially since other long-term monitoring programs such as AZMP have a low sampling frequency and therefore suffers from aliasing (*Mann and Needler*, 1967; *Mann*, 1969; *Petrie*, 2004).

Considering the different water masses involved along the HL and their T-S signatures (see Table 3.1), different scenarios could explain the warm and saline anomaly observed in the time series:

1. a larger amount of shelf water at the HL came from a warm water mass (i.e., WSW) in 2012 than in other years,

2. a smaller amount of the water along the HL came from a colder water mass (i.e., CBS-CIL or InLC) in 2012 than in other years,

3. the relative contributions of different water masses in 2012 were similar to other years, but the temperature signature of one, or several, contributing water masses was anomalously warm (i.e., the warm anomaly was advected into the domain).

Examining seasonally-averaged time series of the relative contributions of the CBSs, CBS-CIL or InLC and WSW over the 2011-2014 period can shed light on the possible mechanisms responsible for the 2012 abnormal anomaly (Figure 3.6). The analysis for this time period confirms the features described in Section 3.1.2. In the upper-layer (30 - 50 m), CBSs dominated and represented 81% of the water mixture on average, with a higher percentage over the inner shelf (Figure 3.4). The WSW contribution was consistently low over the 2011-2014 period, varying between 3 and 24% and averaging 13%. CIL water (InLC and CBS-CIL) also contributed to the water mixture in the upper-layer, representing between 0 and 23% of the water composition.

In 2012, the CBSs percentage was higher than average (89-97%), and the contribution of CBS-CIL or InLC water was undetectable throughout the entire year. Despite this relatively small change in water composition, this result suggests that the warming observed in the upper-layer was primarily advected over the Scotian Shelf from adjacent regions. The yearly-defined end-members (Table 3.1) demonstrate that, in 2012, WSW was the only water mass that experienced a significant warming (i.e., greater than the observed standard deviation), with an increase of +4.3$^{o}$C compared to 2011. A warming of WSW is likely associated with the northward displacement of the warm slope jet flowing along the Scotian Shelf slope (*Pickart et al.*, 1999). In 2012, the warm front was indeed located approximately 80 km further north than in 2011 and penetrated onto the Scotian Shelf (Roger Pettipas, private communication). All other water masses had T-S characteristics within one standard deviation, thus not experiencing any significant changes that could

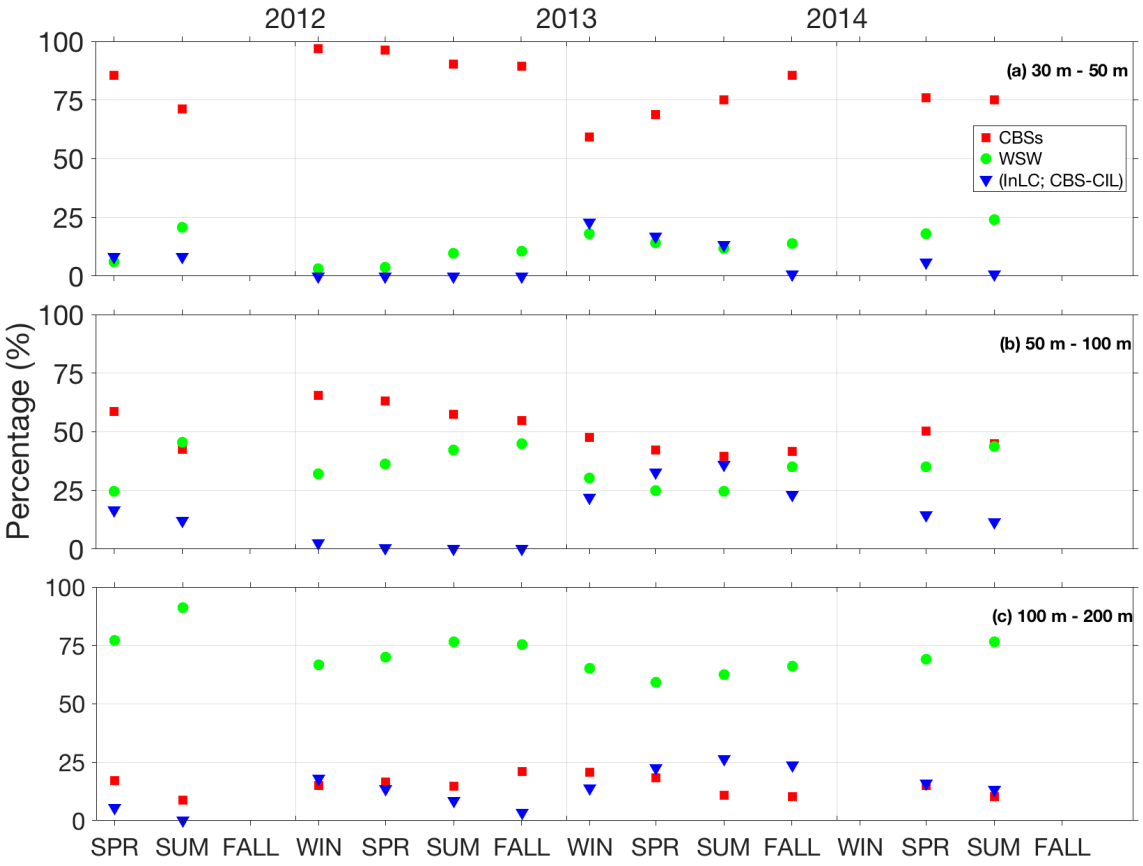


Figure 3.6: Time series of the seasonally-averaged proportion (in %) of Cabot Strait subsurface water (CBSs, red squares), Warm Slope Water (WSW, green circles) and the average between Inshore Labrador Current water (InLC) and Cabot Strait Cold Intermediate Layer water (CBS-CIL, blue triangles) between 30 and 50 m (upper panel), 50 and 100 m (middle panel), and 100 and 200 m (lower panel). The percentages are calculated using the method described in Section 3.1.1.

explain the 2012 anomaly. The major temperature anomaly in this upper-layer could therefore be partially explained by a combination of a anomalously small volume of cold water coming from CBS-CIL (or InLC), and partially by the advection of a anomalously large volume of already abnormally warm WSW.

Over the 2011-2014 period, the mid-layer (50 - 100 m) at the HL had a water mixture similar to the upper-layer (30 - 50 m); the contribution of CBSs to the water composition was fairly constant (between 40% and 66%; see Figure 3.4) and WSW contributed approximately 35% on average. As expected, the average contribution of CBS-CIL (or

InLC) in this mid-layer was larger than in the rest of the water column (14%), again with a significant decrease during the year 2012. Since CBS-CIL and InLC are responsible for the presence of colder water in this mid-layer than in the rest of the water column, a decrease in their contributions to the water composition would consequently result in an increase in water temperature. Because WSW also contributed significantly to the water composition between 50 and 100 m, it appears that the warming observed in 2012 in this mid-layer was also due to the on-shelf advection of anomalously warm WSW combined with a reduced percentage of cold water coming from the InLC and the CBS-CIL. This hypothesis is confirmed when estimating the percentage of each water mass for the time series collected near-bottom at T1 ($\sim$100 m; Figures 3.5 and 3.7). The high-temporal-resolution time series shows a significant increase of WSW in the water composition in 2012, coherent with a sharp decrease in the InLC or CBS-CIL concentration.

In the lower water column (100 - 200 m) at the HL, the water mass composition was dominated by WSW, with an average concentration of 71% over the 2011-2014 period. CBSs represented 15% of the water mass composition on average, while InLC or CBS-CIL water accounted for 15% of the water mixture. These water mass concentrations match the estimated near-bottom water mixture at T2 and T3 (Figure 3.7). The inter-annual variability in this lower-layer (100 - 200 m) does not show a change in the water composition as significant as in the upper- and mid-layers, although the increase of WSW and decrease of InLC or CBS-CIL in 2012 are also visible.

## 3.2 Circulation and Alongshore Transport

The low-frequency variability (i.e., seasonal and inter-annual) in the circulation at the HL was investigated based on in situ current observations. The analysis relied on measurements of the horizontal currents made by the bottom-moored ADCPs at a high temporal resolution over the 2008-2015 period, as well as on geostrophic currents calculated along the glider's transects completed over the 2011-2014 period. These two estimates of currents are in

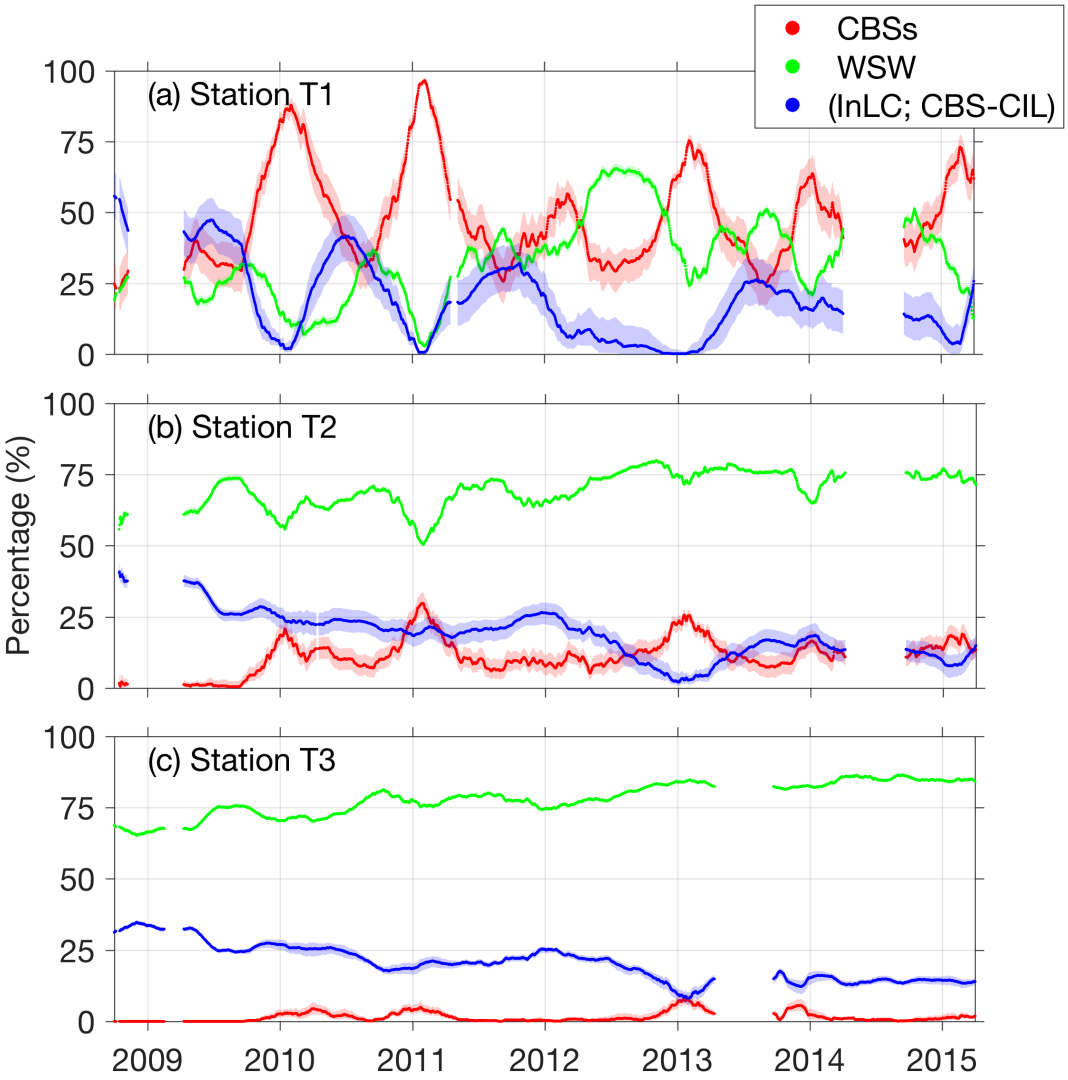


Figure 3.7: Time series of the estimated proportion (in %) of the key water masses near the bottom at stations (a) T1, (b) T2 and (c) T3. Cabot Strait subsurface water (CBSs) is represented in red, Warm Slope Water (WSW) is in green, and the average between Inshore Labrador Current water (InLC) and Cabot Strait Cold Intermediate Layer water (CBS-CIL) is in blue. The percentages are calculated using the method described in Section 3.1.1. The 99% confidence intervals are computed using a Monte Carlo method based on a 5% noise in a 1000 scenarios.

theory not equivalent since currents deduced from the gliders represent the geostrophic flow, while ADCPs measured the total currents. Thus, these two estimates cannot be directly compared but can be combined to characterize the temporal variability (using ADCPs) and the spatial variability (using gliders) of the circulation patterns at the HL. In this section, the analysis focuses on the alongshore currents and the associated transport, based on the fact that the alongshore circulation is an order of magnitude larger than the cross-shore currents.

### 3.2.1 Seasonal Variability

Based on glider measurements of temperature, salinity, and depth-averaged currents, transects of seasonal-mean alongshore geostrophic currents can be produced (Figure 3.8). The alongshore currents show that the seasonal mean alongshore circulation is largely dominated by the NSC with a strong southwestward (i.e., positive in Figure 3.8) coastal jet located in the upper 100 m and between 25 and 75 km offshore. It should be noted that the three T-stations were ideally located throughout the NSC's pathway, with T1 and T3 located near the "edges" of the average flow, and T2 located approximately at the center of the NSC. This is promising for the rest of this study, since ADCP measurements at the three T-stations provide information on the currents at a high temporal resolution.

In winter (January to March), the tilting of isopycnal surfaces over the inner section of the HL is the steepest among the four seasons (Figure 3.3c), generating a strong southwestward baroclinic flow that reaches about +0.2 m/s (positive means southwestward) at T2 (Figure 3.8a). Using the +0.05 m/s isoline as the outer edge of the NSC, the NSC spreads over 60 km and reaches a depth of 100 m over the inner part of the HL in winter. A northeastward flow of about -0.1 m/s also appears near the bottom between the 100 m and 160 m isobaths (Figure 3.8a). While a northeastward flow is also observed in the ADCP record, there is a discrepancy in their magnitude. The negative near-bottom return flow as computed from the gliders is larger than the one observed by the ADCPs. This could be due to the adjustments of geostrophic currents using the estimated depth-averaged flow

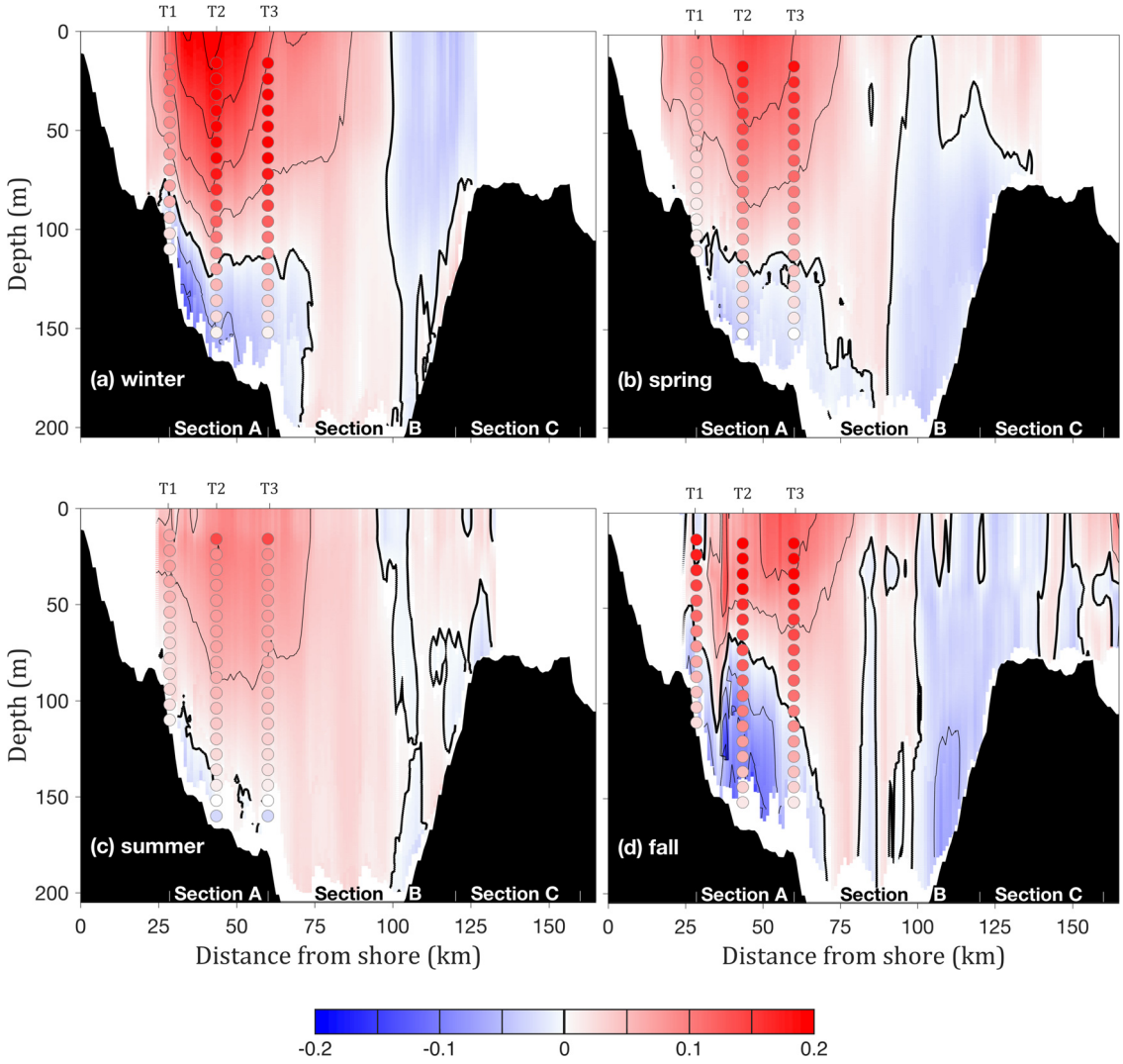


Figure 3.8: Gridded fields of alongshore geostrophic currents across the HL (in m/s) calculated from glider-based measurements of temperature, salinity and depth-averaged currents in (a) winter (JFM), (b) spring (AMJ), (c) summer (JAS) and (d) fall (OND) over the 2011-2014 period. Blue colors represent negative alongshore currents (i.e., northwestward). Red colors represent positive alongshore currents (i.e., southeastward). The thick line denotes the zero-velocity contour. Isolines are spaced by 5 cm/s. A subset of the corresponding alongshore currents measured by the ADCPs at the T-stations (colored circles) are superimposed for comparison. The extent of each section described in Section 3.2.2 is also indicated.

experienced by the glider (see Section 2.2.3). A weak (>-0.05 m/s) northeastward flow also occurs over the offshore flank of Emerald Basin in winter, which could be associated with a cyclonic flow that follows the basin's edges (*Han and Loder*, 2003).

In spring (April to June), the NSC slows down to less than 0.15 m/s, with a core still located close to T2. The NSC in spring does not spread as far offshore as in the winter, and only penetrates to about 80 m in the vertical. Both the northeastward flows previously mentioned also exist in the spring, although the bottom flow below the NSC in spring is weaker than in winter.

In summer (July to September), the alongshore flow at the HL is generally relatively weak and the NSC is at its weakest (<+0.1 m/s) compared to other seasons. It should be noted that the NSC has a spatial coverage similar to that in spring, and the near-bottom northeastward flow is weaker and occurs over a smaller area than in other seasons.

In fall (October to December), the southwestward NSC narrows and intensifies as it reaches its minimum spatial coverage with a width of about 45 km. The NSC extends down only to about 70 m in the fall, which is shallower than in summer. This coincides with the persistent summer stratification and the flatter isopycnal surfaces in the fall, compared with the wintertime conditions described in Section 3.1.2. This also explains the discrepancy between the annual salinity minimum and maximum alongshore flow. While the low-salinity water coming from the GSL is observed in the fall, the water column is still relatively stratified, flattening the density front and therefore directly impacting the computed geostrophic velocity. Both northeastward flows reach their annual maximum along the 150 m isobath, on both flanks of Emerald Basin. The sharp transition of alongshore geostrophic currents located about 35 km offshore in fall is associated with the large horizontal density gradients shown in Figure 3.3l.

A subset of the corresponding seasonally-averaged ADCP currents are superimposed in Figure 3.8. The discrepancy in the alongshore flow measured from the ADCPs and estimated from the glider data could be linked to several factors. First, ADCPs measure

total currents, as opposed to the geostrophic currents derived from the glider data. Second, the measurements were not co-located, as the glider tracks often did not exactly coincide with the location of the T-stations. Third, a large uncertainty is associated with the glider-based current estimations, as it relies on the precision of the GPS in determining the glider's positioning and the performance of the dead-reckoning algorithm, as well as on a few assumptions (e.g., linear surface drift; see Appendix A).

Due to their slow speeds and the mission durations along the HL (3 to 11 days), gliders inherently lack high temporal coverage at a given location. This issue can be resolved by using the ADCP velocity measurements recorded at the T-stations, especially since the three bottom-mounted ADCPs were ideally located to appropriately sample the NSC (Figure 3.8). The seasonal cycle of the daily alongshore transport associated with the NSC (i.e., between T1 and T3, or section A in Figure 3.8) was calculated using the currents observed by the ADCPs at 3 T-stations over the 6-year period 2008-2014 (Figure 3.9a). The daily-average alongshore transport through section A of the HL is southwestward, with a maximum amplitude in winter ($\sim$ +0.65 Sv, 1 Sv = $10^6$ $m^3/s$) and a minimum in summer ($\sim$ +0.22 Sv). The alongshore transport variability at synoptic timescales is larger in the winter than in the summer (Figure 3.9a), which may suggest that local winds played an important role in affecting the alongshore transport, since surface winds are generally stronger in winter than in summer over the Scotian Shelf.

### 3.2.2 Inter-annual Variability

The alongshore transport calculated from the ADCP measurements between T1 and T3 has significant temporal variability at synoptic timescales. Nevertheless, the transport exhibits a similar seasonal cycle throughout the 2008-2015 period (Figure 3.9b). The high frequency anomaly was obtained by subtracting the averaged annual cycle observed over the 2008-2015 period (gray line in Figure 3.9a) to the alongshore transport (gray line in Figure 3.9b). A large variability over synoptic timescales occurs on a clear seasonal pattern throughout the record with smaller anomalies in the summer than in the winter. It

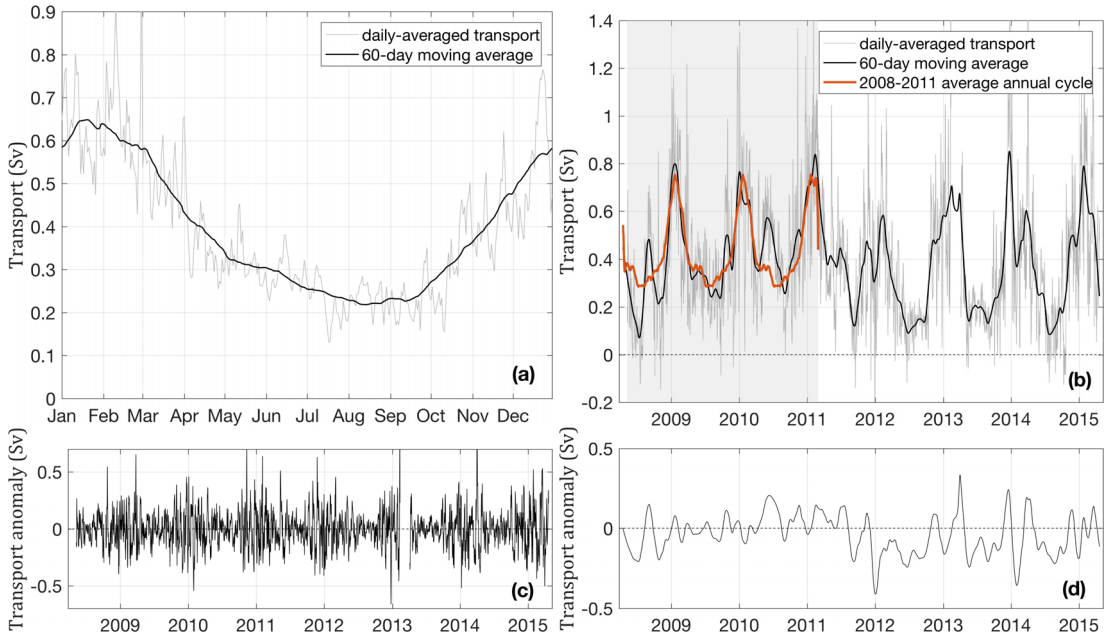


Figure 3.9: (a) Yearly time series and (b) entire time series of the daily-averaged alongshore transport (in Sv; positive means southwestward) through Section A of the HL using ADCP observations at three stations over the 2008-2015 period. In both panels, a 60-day moving average was used to smooth the high-frequency variability of the time series (thick black line). The smoothed seasonal cycle calculated from observations collected before 2012 is superimposed in (b) (red curve). (c) High-frequency transport anomalies (in Sv) are calculated by subtracting the gray curve in (a) from the gray curve in (b). (d) Low-frequency transport anomalies (in Sv) are computed by subtracting the smoothed seasonal cycle collected before the start of the 2012 anomaly (see Section 3.1.3; red line in (b)) from the smoothed transport time series (thick black line in (b)).

is also worth noting that the high-frequency variability (i.e., 1-3 days) does not seem to be affected by the 2012 abnormal anomaly (Figure 3.9c). The mechanism responsible for the seasonal cycle in the high-frequency transport anomalies (Figure 3.9c) should (1) not be directly correlated to ocean temperature (that was strongly anomalous in 2012, see Section 3.1.2), (2) be stronger in the winter compared to other seasons, (3) be relatively consistent in amplitude from year to year, and (4) exhibit large daily variability.

All these characteristics suggest that local surface winds are likely responsible for the high-frequency (i.e., 1-3 days) variability in the alongshore transport, which agrees with previous findings (*Schwing*, 1992a,b) and will be further investigated in Chapter 4.

Using the same analysis as in Section 3.1.3, the low-frequency variability (Figure 3.9d) was obtained by subtracting the smoothed seasonal cycle based on the measurements collected before the start of the 2012 anomaly (red line in Figure 3.9b) from the smoothed transport time series (thick black line in Figure 3.9b). The low-frequency anomaly of the alongshore transport exhibits two different regimes. The first half of the time series (i.e., before 2012) shows anomalies mainly centered on zero, which is expected as it is the period used to define the seasonal variability observed before the 2012 anomaly. The second half of the time series (i.e., 2012 onward) is centered on a negative anomaly (about -0.1 Sv) that indicates a slow-down of the NSC during this period, compared to conditions observed before 2012. A large negative transport anomaly is also observed in the winter of 2012, and is associated with a significant weakening of the NSC during the wintertime of that year. Other comparable anomalies are observed in the time series: the two large positive anomalies in 2013 (March and December) are related to a difference in the phase of the peak, as opposed to a difference in amplitude. This also explains why both of these anomalies are immediately followed by negative anomalies.

As mentioned earlier, the inter-annual variability of the NSC can be characterized by combining the high temporal resolution ADCP data with the high spatial resolution glider data. To see how the alongshore transport varies with distance from shore on inter-annual

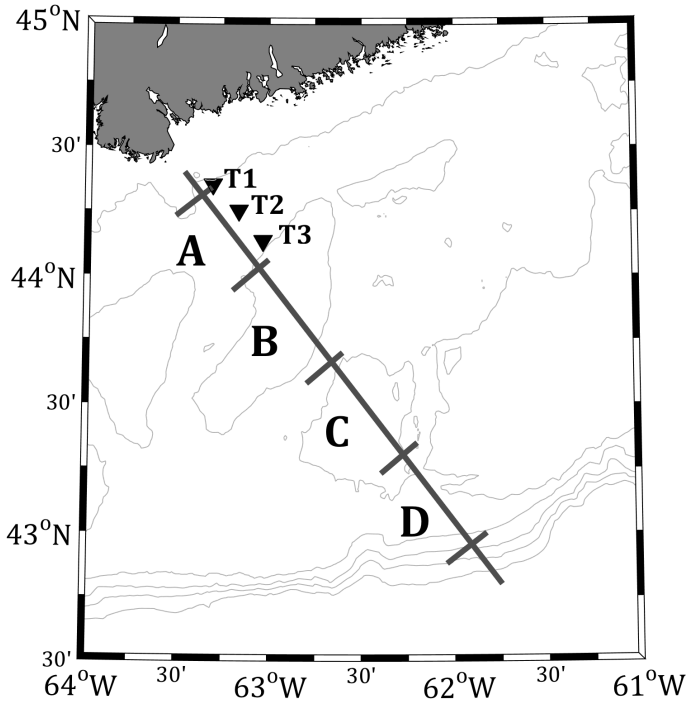


Figure 3.10: Spatial coverage of the sections defined along the Halifax Line. Section A covers the distance between T1 and T3, section B corresponds to Emerald Basin, section C is located over Emerald Bank and section D extends from Emerald Bank to the Shelf break.

timescales, the HL was divided into 4 sections (Figures 3.8 and 3.10): Section A covering the distance between T1 and T3, section B corresponding to Emerald Basin, section C being over Emerald Bank and section D extending from Emerald Bank to the Shelf break. The geostrophic transport calculated from glider data over section A shows a reasonably good agreement with the alongshore transport computed from the ADCPs ($r = 0.78$, p<0.01; see Figure 3.11). This good agreement demonstrates that the glider-based algorithm to estimate geostrophic velocities performed reasonably well. Because the glider did not always sample the entire HL, the temporal coverage of glider missions decreases from section A to section D.

Despite the larger uncertainties associated with the geostrophic alongshore transport estimated from glider data than from the ADCPs (see Figure 3.8), interesting features can be observed in Figure 3.11. While the alongshore transport can reach values as

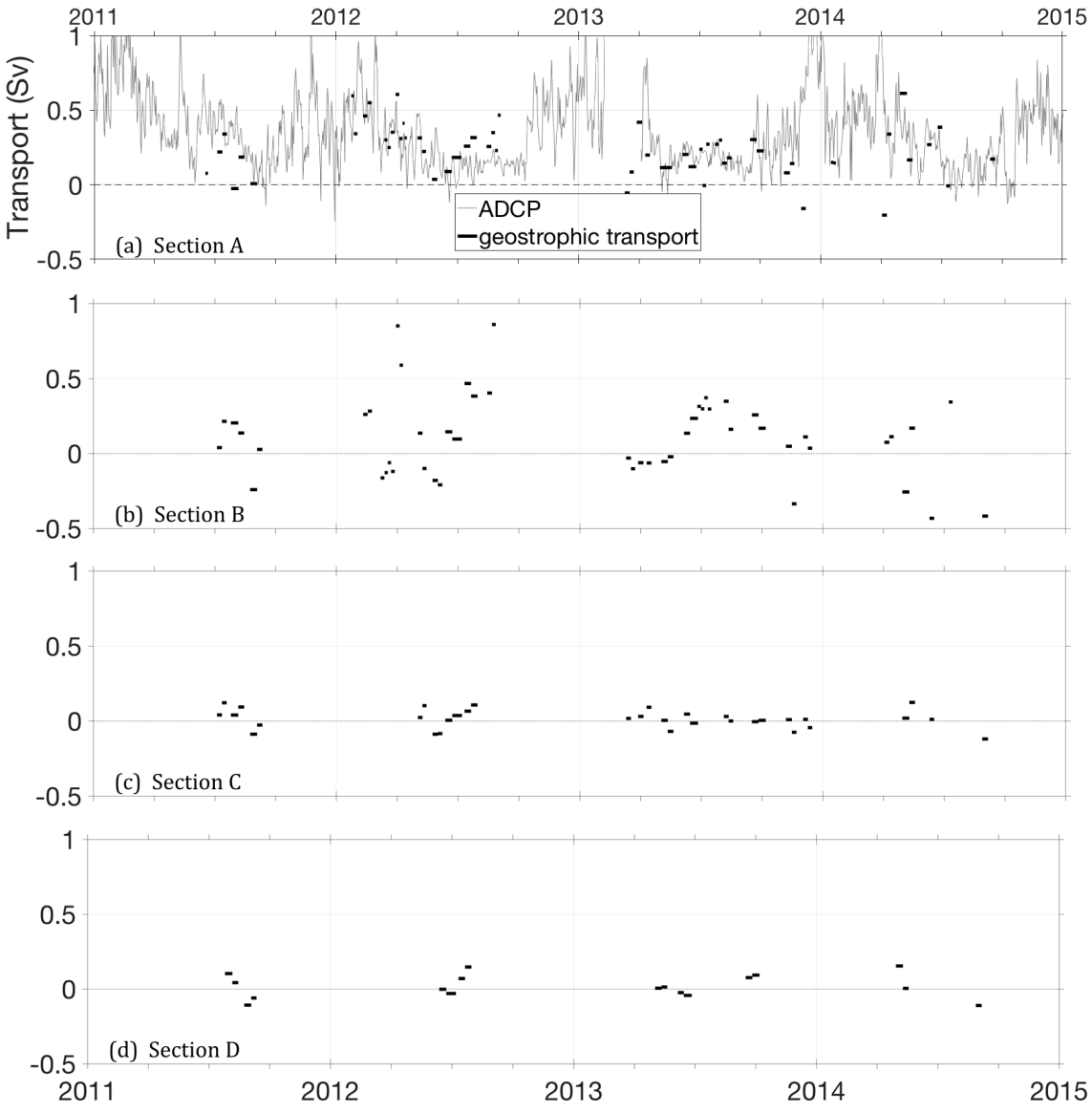


Figure 3.11: Time series of geostrophic transport (in Sv, positive means southwestward) over four different sections of the Halifax Line ((a) through (d)) computed from glider transects (thick lines). The daily averaged transport estimated from ADCP measurements between T1 and T3 is also included (solid line) in (a) and the extent of each section is depicted in Figure 3.10

large as +0.61 and +0.86 Sv over section A and B, respectively, it significantly weakens as the distance from shore increases. Over sections C and D, the alongshore transport varies between $\pm 0.12$ Sv, agreeing with the seasonal transects shown in Figure 3.8. The alongshore transport calculated within section B is sometimes larger than the transport through section A. This result suggests that, while centered on T2 on average, the core of the NSC can sometimes be displaced along the cross-shelf direction. Possible mechanisms for this cross-shelf displacement are investigated in Chapter 4.

## 3.3 Summary

The seasonal and inter-annual variability associated with the hydrography (i.e., temperature and salinity) and circulation along the HL was characterized based on CTD, ADCP, and glider observations. The analysis showed that hydrographic conditions along the HL experienced a strong seasonal cycle, as represented by the near-surface temperature field that varied by more than $16^{o}$C over the course of a year. The analysis also revealed that temperature and salinity along the HL are strongly coupled throughout the year, as the water composition is either cold and fresh water coming from the GSL and the Inshore Branch of the Labrador Current, or warm and saline water coming from offshore. However, this coupling weakens in the upper-layer in the summer, when the net surface heat flux drives the temperature field. The analysis of the inter-annual variability in the context of the 2012 warm event suggested that the anomaly was likely due to the advection of already anomalously warm water from offshore, combined with a smaller volume of cold water coming from either the GSL or the Inshore Branch of the Labrador Current.

The study of the alongshore currents characterized the location and spatial extent of the NSC, and demonstrated that the NSC predominates the alongshore circulation at the HL. The alongshore transport associated with the NSC showed a maximum in the winter and a minimum in the summer, highlighting a discrepancy between the timing of the salinity minimum and the maximum alongshore flow. The analysis of the inter-annual variability

revealed that the NSC was anomalously weak in 2012. The location of the current was shown to vary over time, while still being located within the first 100 km from shore. The next chapter focuses on the NSC and the driving mechanisms involved in the dynamics of the coastal current.

# CHAPTER 4

# DYNAMICS AND TEMPORAL VARIABILITY OF THE NOVA SCOTIA CURRENT AT THE HALIFAX LINE

The main objective of this chapter is to improve our understanding of forcing mechanisms driving the Nova Scotia Current (NSC), and how these mechanisms may vary in both space and time. A set of analytical and statistical tools are used in this chapter to examine the NSC based on high-resolution glider data.

In Section 4.1, coherency and connectivities of the NSC with adjacent regions are studied. An Hilbert Empirical Orthogonal Function (HEOF) analysis is applied to the ADCP datasets to separate the NSC into dynamical modes of variability. In Section 4.2, the buoyancy-driven and wind-driven components of the NSC are defined using the Hydrographic Wind Index (HWI), a newly-developed tool based on *Whitney and Garvine* (2005, hereafter referred to as WG05) Wind Index. The performance of the HWI is then evaluated and validated. In Section 4.3, this new approach is applied to the NSC at the HL, and results are directly compared to the approach taken by WG05. A summary is provided in Section 4.4

## 4.1 Characteristics of the Nova Scotia Current

The NSC is the dominant circulation feature at the HL (see Chapter 3). In this section, several data sources at the HL are combined to provide a comprehensive characterization of the NSC. Decorrelation scales of the NSC in the cross-shelf and along-shelf directions are quantified using three bottom-mounted ADCPs and CTDs deployed across the NSC at the HL, bottom-mounted ADCP and CTD deployed on St Anns Bank (SAB; see Figures 1.1 and 2.1), and the estimated runoff of the St. Lawrence River at Québec provided by the Maurice Lamontagne Institute (*Bourgault and Koutitonsky*, 1999; *Galbraith et al.*, 2014). The results of the HEOF analysis are used to investigate the variability of the NSC, and to examine the driving mechanisms involved in the current's dynamics. The methodology for calculating the HEOFs was provided in Section 2.3.3 (*Merrifield and Winant*, 1989; *Von Storch and Zwiers*, 2001; *Hannachi et al.*, 2007).

### 4.1.1 Cross-shelf Coherency

The cross-shelf coherency of the NSC is investigated using depth-averaged currents recorded at the three ADCPs deployed across the NSC (stations T1, T2, and T3, see Figure 2.1 for their locations). Depth-averaged velocity records at these three stations were low-pass filtered, linearly detrended, and averaged daily (see Chapter 2 for details on data processing steps). Because the NSC is, on average, centered at T2 (see Chapter 3), this station is used as the reference point, where the cross-covariance is consequently equal to unity. The cross-covariance is then calculated for cross-shore and alongshore currents, between stations T1 and T2 as well as between T2 and T3 (Figure 4.1). The cross-covariance is calculated based on observations over the entire period available (from April 2008 to April 2015), with missing values excluded and the linear trend removed. The 99% confidence intervals are determined using the bootstrapping method described in Section 2.3.2. Gaussian curves are fitted to the cross-covariance between depth-averaged currents in both the alongshore and cross-shore directions. The same analysis was applied

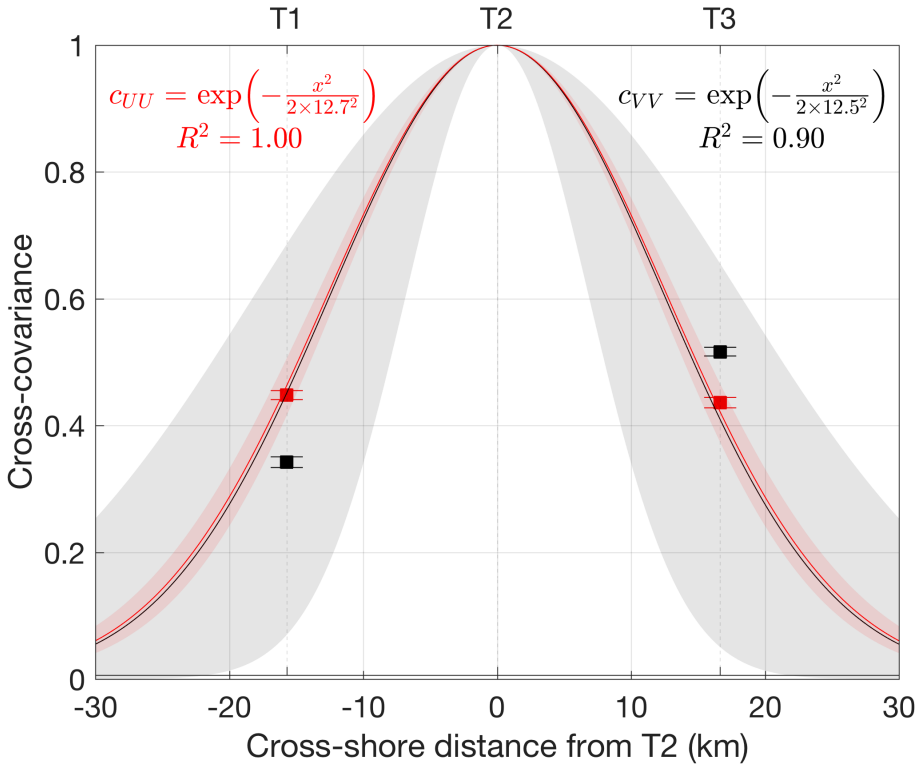


Figure 4.1: Cross-covariance of the depth-averaged currents measured at T1 and T3, referenced to the currents measured at T2. The cross-covariance is calculated for both alongshore (red, subscript $U$) and cross-shore (black, subscript $V$) currents. Gaussian fits (solid lines) and their uncertainties (shaded) are superimposed. Each fit's equation and coefficient of determination are also indicated.

to observed currents averaged in the upper water column (z>-60 m), and in the lower water column (z<-60 m), which yields very similar results to the analysis conducted with the depth-averaged currents.

The cross-covariance calculated for the depth-averaged cross-shore currents is significantly higher between T2 and T3 ($c_{V_2V_3} = 0.51 \pm 0.01$, where the second subscript is the station number) than between T1 and T2 ($c_{V_1V_2} = 0.34 \pm 0.01$). Stations T1 and T3 are almost equidistant from T2, suggesting that the cross-covariance function exhibits a negative skewness with respect to a symmetrical Gaussian fit. The decorrelation scale is therefore shorter between T2 and T1 than between T2 and T3. When considering the alongshore component of the currents, the cross-covariances calculated between T1 and T2 ($c_{U_1U_2} = 0.44 \pm 0.01$), and calculated between T2 and T3 ($c_{U_2U_3} = 0.43 \pm 0.01$) are not

statistically different. As a result, the symmetrical Gaussian fit exhibits a high coefficient of determination ($R^2 = 1.00$). This suggests that, unlike the cross-shelf currents, the decorrelation scale for the alongshore currents between T2 and T1 is identical to the decorrelation scale between T2 and T3. This result supports the findings presented in Chapter 3, wherein the core of the NSC was shown to be located, on average, near station T2 (see Section 2.3.1 and Figure 3.8). However, due to the limited number of stations considered here, it is also possible that the observed symmetry in the cross-shelf decorrelation scale is due to an offset of the core of the NSC, compensated by an asymmetric decorrelation scale. For example, if the NSC's core is located inshore (offshore) of T2, and the decorrelation scale is shorter in the inshore (offshore) direction, then the resulting distribution would fit a Gaussian curve centered on T2 as well.

Nevertheless, the above analysis demonstrates that the cross-shelf coherency of the NSC decreases over a length scale on the order of $\mathcal{O}$(10 km) from the core of the NSC, as revealed by the standard deviation of the Gaussian fits ($\sigma \sim 12.5$ km; Figure 4.1). This is an important result when considering long-term monitoring strategies for the NSC. Because the NSC's width is on the order of 35 to 50 km (see Figure 3.8), the relatively rapid decrease in the coherency of the current in the cross-shelf direction emphasizes the importance of measuring the core of the NSC. This result concurs with the good predictive skills of the linear statistical regressions used to reconstruct the alongshore transport, where 87% of the variability of the NSC's transport was resolved using measurement at T2 exclusively (see Section 2.3).

### 4.1.2 Along-shelf Coherency

The along-shelf coherency of the NSC was evaluated based on the near-bottom salinity and the depth-averaged alongshore velocity measured at the three T-stations and at SAB (Figure 4.2). At all locations, salinity and velocity records were low-pass filtered, linearly detrended, and averaged daily (see Chapter 2 for details on data processing steps). The

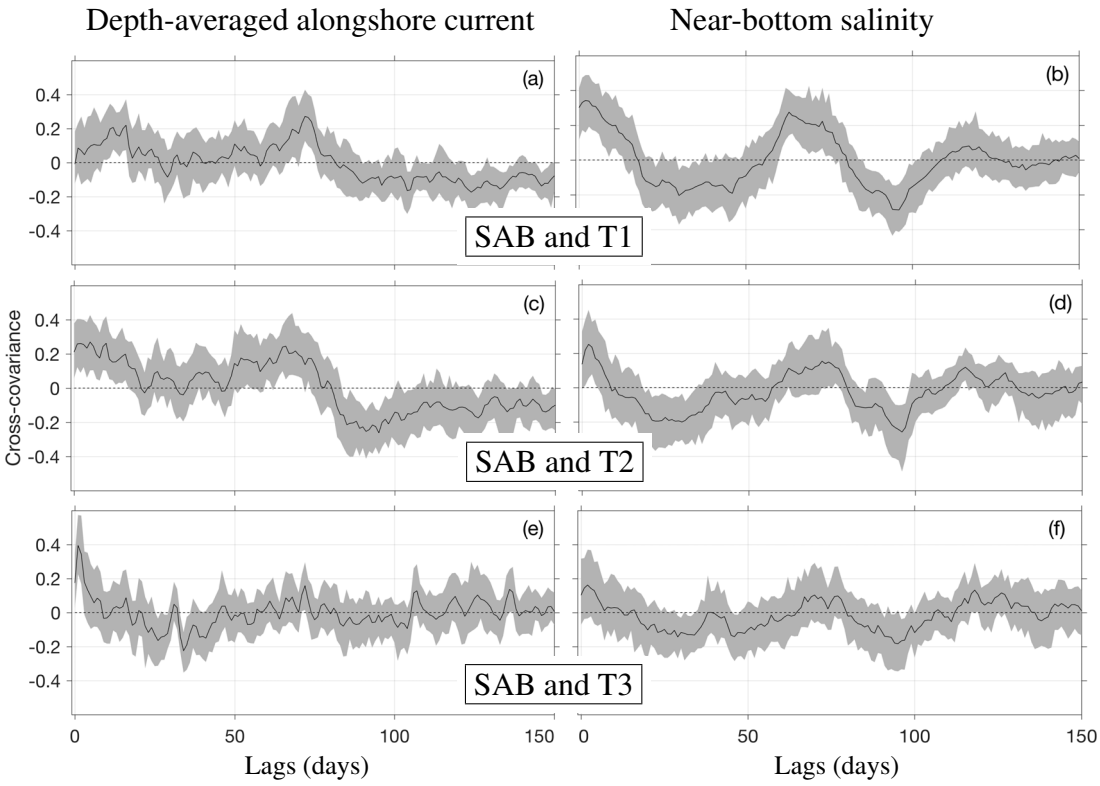


Figure 4.2: Cross-covariance function between daily-averaged alongshore currents ($c_{UU}$; left column) and near-bottom salinity ($c_{ss}$; right column) measured at the T-stations (T1, T2, and T3) and on St. Anns Bank. The 99% confidence intervals (shaded) were calculated using a bootstrapping method (see Section 2.3.2).

cross-covariance functions were calculated using the longest continuous time series available at both SAB and the HL, running from September 30, 2014 to April 20, 2015 (Figure 2.2). The cross-covariance function was calculated between SAB and each of the three T-stations. The highest correlation is expected to occur between currents (or salinity) at SAB and T1, due to the fact that those two stations were located roughly along the same isobath (110 - 120 m), in a region where topographic steering is one of the key mechanisms (*Han and Loder*, 2003). The magnitude of any significant peak provides information on the degree of correlation between the two time series, while the positive lag at which the maximum cross-covariance occurs provides information on the propagation speed of the signal from SAB to the HL.

The cross-covariance function calculated from the velocity records between SAB and T1 has two peaks: a peak ($c_{UU} = 0.21$) at short lags (10-15 days), and a larger peak ($c_{UU} = 0.26$) at lags between 68 and 75 days. The same two peaks are observed between SAB and T2, while only the first peak is observed in the cross-covariance function between SAB and T3.

These observations are consistent with the cross-covariance functions calculated from the near-bottom salinity field measured at SAB and the T-stations. At T1, the peak at a short time lag is largest and reaches $c_{ss} = 0.36$ at a 4-day lag. The second peak is located between a 61-day and 75-day lag, and reaches a maximum of $c_{ss} = 0.28$. Both peaks are also visible at T2, although the cross-covariance is smaller, with the first peak reaching $c_{ss} = 0.23$ and the second peak reaching $c_{ss} = 0.15$, which is barely significant at a 99% confidence level. At T3, none of these two peaks can be detected within the 99% confidence limit, indicating no significant correlation between the near-bottom salinity at SAB and T3. These findings are in good agreement with the dynamics of a bottom-trapped density front, where topographic steering is expected to play an important role (*Chapman and Lentz*, 1994; *Han and Loder*, 2003). As expected, a larger peak occurs in the cross-covariance function between SAB and T1 than with T2 or T3, as SAB and T1 are located on a similar isobath. However, it is not clear why the secondary peak located around the 70-day lag does not occur in the near-bottom temperature field between SAB and any of the T-stations.

The presence of the first peak in the cross-covariance function (lag of 2 to 15 days) may be related to large-scale meteorological conditions (e.g., a change in atmospheric pressure and wind patterns). Although we do not have the atmospheric data to support this hypothesis, the large-scale atmospheric forcing would explain the relatively simultaneous variability between the two locations. The second peak is likely to be generated by the down-shelf propagation of anomalies from SAB to the HL, where a lag of about 70 days is in agreement with previous estimations of about 3 months for the lag between Cabot

Strait and the HL (*Drinkwater et al.*, 1979). Similar to other buoyancy-driven coastal currents, the NSC is more coherent in the along-shelf direction than in the cross-shelf direction (*Brink*, 2015). In fact, the correlation quickly falls to $\sim$0.3 on the order of tens of kilometers in the cross-shelf direction (Figure 4.1), as opposed to hundreds of kilometers in the along-shelf direction (Figure 4.2).

The high along-shelf coherency of the NSC and the correlation with the physical oceanographic conditions flowing out of the GSL highlight the connectivity between the NSC and the GSL. This hydrodynamic connectivity can be further examined based on the cross-covariance function between the alongshore transport of the NSC at the HL and the monthly mean estimate of the St. Lawrence River runoff at Québec (i.e., RIVSUM; Figure 4.3). The alongshore transport at the HL is computed based on current measurements at the T-stations. The monthly mean river discharge of the St. Lawrence River was provided by the Maurice Lamontagne Institute (i.e., RIVSUM; *Bourgault and Koutitonsky*, 1999; *Galbraith et al.*, 2014). The peak-to-peak correlation between these two time series can be used to quantify how long the seasonal pulse in the St. Lawrence River discharge takes to reach the HL, as well as the level of correlation between the two transport estimates. The cross-covariance analysis between the St. Lawrence River discharge and the alongshore transport between T1 and T3 reveals that these two time series have significant positive covariance ($c_{xy}$ = 0.29) at a time lag of about 9 months (Figure 4.3). The correlation is relatively high considering that these two locations are more than 1,500 km apart. The estimated lag is consistent with previous estimates based on both numerical simulations (*Urrego-Blanco and Sheng*, 2014; *Shan et al.*, 2016) and in situ data (*Drinkwater et al.*, 1979).

### 4.1.3 Modes of Variability and Driving Mechanisms

To further investigate the variability associated with the NSC, the alongshore currents measured at the T-stations were separated into modes of variability using a complex decomposition technique known as the Hilbert Empirical Orthogonal Function (HEOF;

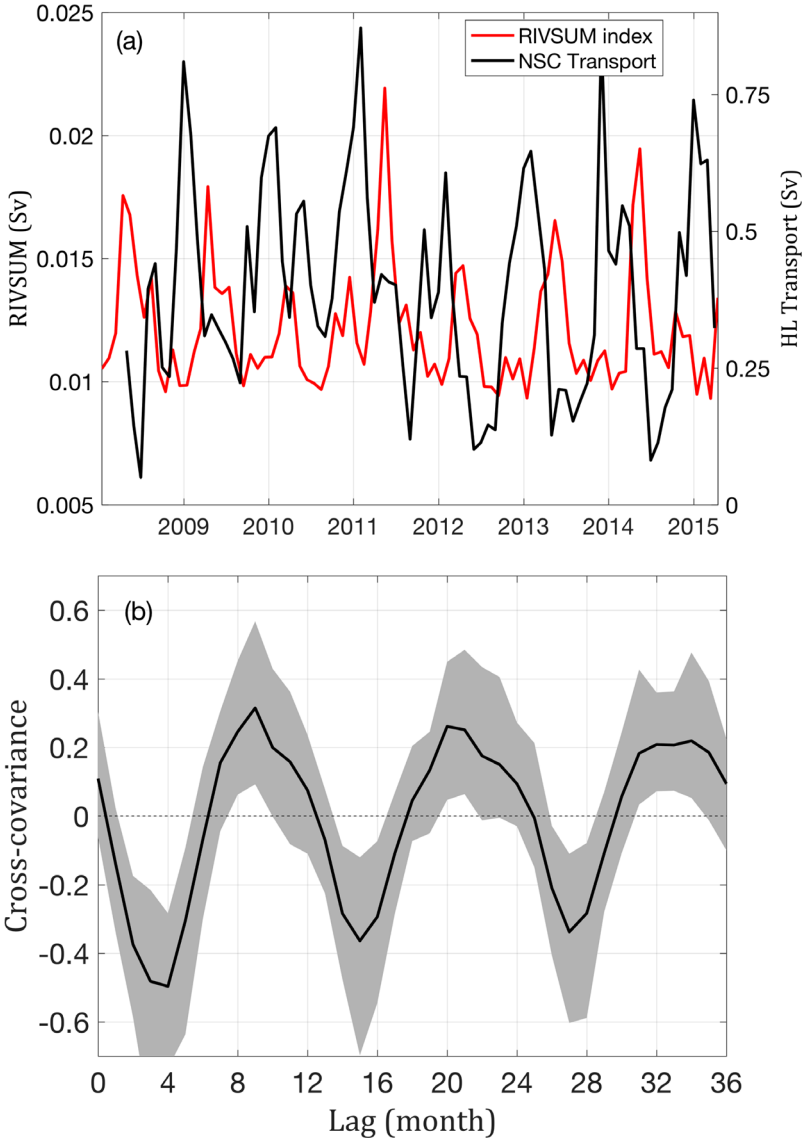


Figure 4.3: (a) Time series of transports computed from the ADCP records at the three T-stations and of the monthly mean estimate of the St. Lawrence River runoff at Québec City (RIVSUM; *Bourgault and Koutitonsky*, 1999; *Galbraith et al.*, 2014). (b) Normalized cross-covariance function between the two time series depicted in (a). The 99% confidence intervals (shaded) were calculated using a bootstrapping method (see Section 2.3.2).

*Merrifield and Winant*, 1989; *Von Storch and Zwiers*, 2001; *Hannachi et al.*, 2007; *Urrego-Blanco and Sheng*, 2012). A general description of the HEOF analysis was provided in Section 2.3.3.

The HEOF analysis was applied to the daily-averaged alongshore current anomalies (i.e., the time means of the time series were removed) at the three T-stations over the 2008-2015 period. Despite few data gaps in the daily-averaged time series, the observed alongshore current anomalies depict the NSC's annual cycle: a positive (i.e., southwestward) anomaly in the winter when the NSC is strong, and a negative anomaly during the summer when the NSC is weaker (Figure 4.4c). The vertical distribution of the current variance is similar across the T-stations, and is mostly contained in the top 50 m of the water column, where the NSC is stronger (Figure 4.5b). According to the HEOF analysis, the first mode of variability explains about 72% of the total variance of the signal, and the second and third modes of variability represents about 19% and 6%, respectively (Figure 4.5). Together, the first two modes of variability explain about 91% of the variance observed in the alongshore currents. These two modes of variability only are therefore considered in the rest of this chapter.

The first mode of variability, HEOF1, is characterized by a near-surface maximum amplitude centered at T2 (Figure 4.6a). The depth-averaged spatial amplitude decreases as one moves away from T2 ($\bar{S}_1$ = 0.084 at T2). This shows that the spatial amplitude decreases faster in the offshore direction ($\bar{S}_1$ = 0.058 at T3), than in the onshore direction ($\bar{S}_1$ = 0.072 at T1). The spatial phase function shown in Figure 4.6b exhibits that the signal associated with the HEOF1 propagates downward and in the offshore direction.

The time series of the temporal amplitude of HEOF1 shows a seasonal cycle, with a higher amplitude in the winter than in the summer (Figure 4.6c). A peak occurs in the temporal amplitude between January and March for the years 2009, 2010, 2014, and 2015. However, no apparent peaks can be seen in 2011, 2012, and 2013. The absence of a winter maximum in 2012 could be explained by the anomalous conditions that year, where the

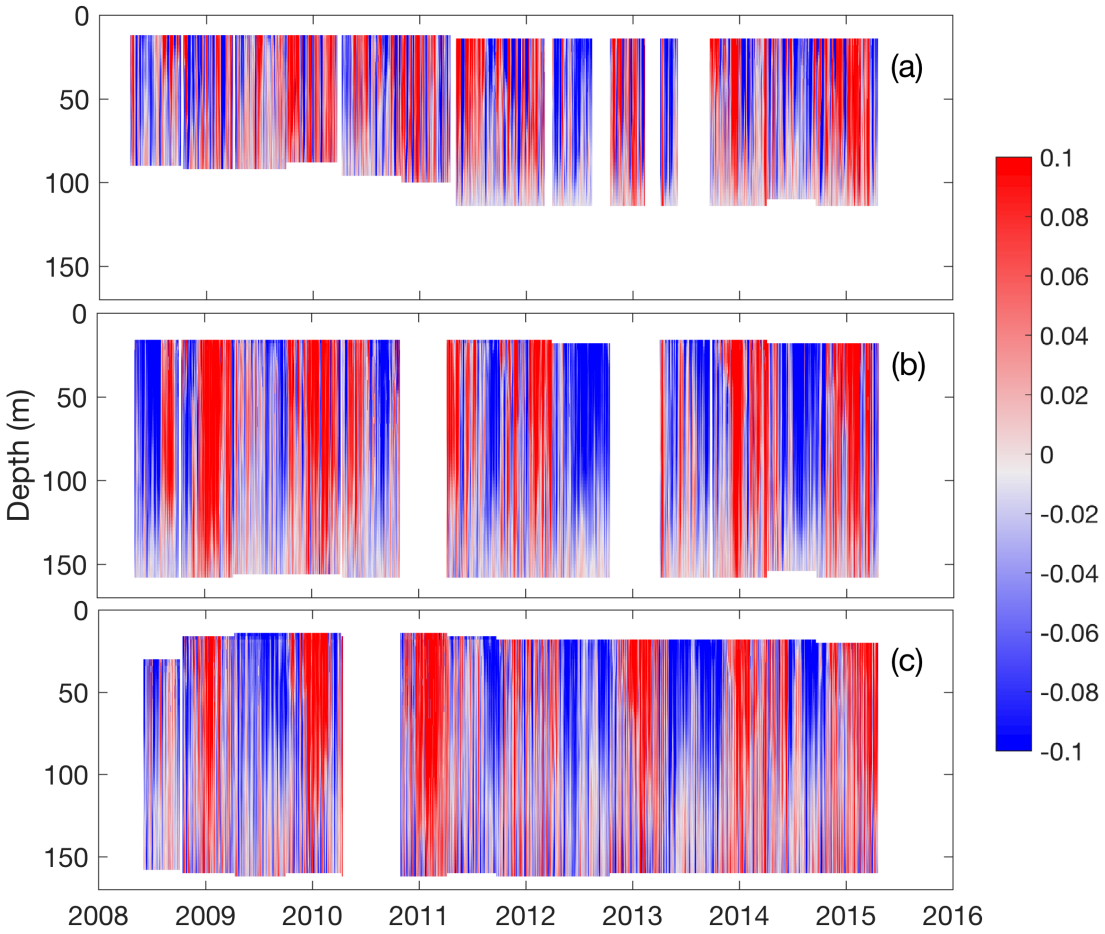


Figure 4.4: Daily-averaged alongshore current anomalies measured at (a) T1, (b) T2, and (c) T3 (in m/s). Positive means southwestward.

NSC was weaker than other years (see Chapter 3). This anomaly is also represented by the weaker positive anomaly in the alongshore flow in 2012 compared to any other year (Figure 4.4). In 2011 and 2013, the ADCP at station T2 failed to operate during the winter deployment. Because the amplitude of the HEOF1 is maximum at T2, these instrument failures are likely to be responsible for the lack of a winter maximum in 2011 and 2013 in the temporal amplitude function of HEOF1. The low-frequency temporal phase function shows a quasi linear trend over the $2\pi$ (i.e., $360^o$) range, with a full cycle completed over approximately one year (Figure 4.6d). For six of the seven winters sampled, the temporal phase function had the same phase ($\phi_1 \sim$ -$120^o$), indicating that the phase is locked to the

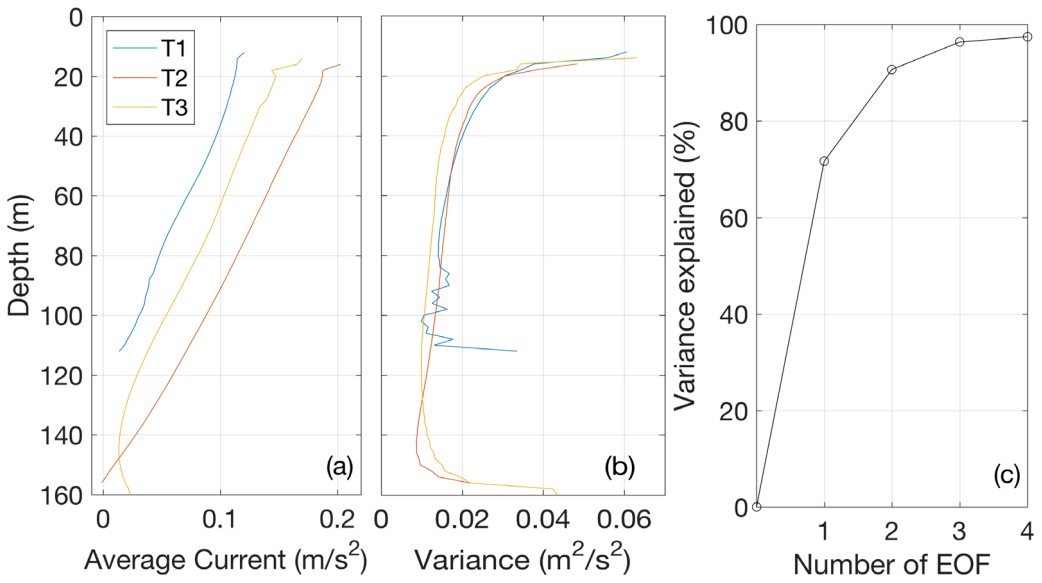


Figure 4.5: Depth profiles of (a) time-averaged alongshore currents (in m/s) and (b) current variance (in $m^2/s^2$) based on current measurements collected at the T-stations. (c) Cumulative total variance explained by the EOFs (in %). The first four modes explain about 72%, 19%, 6%, 1% of the total variance, respectively.

seasonal cycle. This result, combined with the repeated winter maximum in the temporal amplitude function, supports the presence of a cyclostationary process at the HL with a periodicity of about one year.

The first mode of variability has characteristics highly similar to the buoyancy-driven geostrophic flow described in Chapter 3 (see Figure 3.8) including: (1) an annual cycle, (2) a winter maximum, and (3) a maximum amplitude that is both contained in the upper-water column and highest at T2 among the three stations. The percentage of the total variance resolved by this mode (about 72%) explains why geostrophic currents are a good first-order approximation to the total alongshore currents at the HL. When the HEOF analysis was applied to monthly-averaged current anomalies, HEOF1 explained about 87% of the total variance, showing that geostrophic currents are not only representative of the alongshore circulation on daily timescales, but are an even better approximation when considering lower frequencies (i.e., longer timescales).

The second mode of variability, HEOF2, is characterized by a spatial amplitude

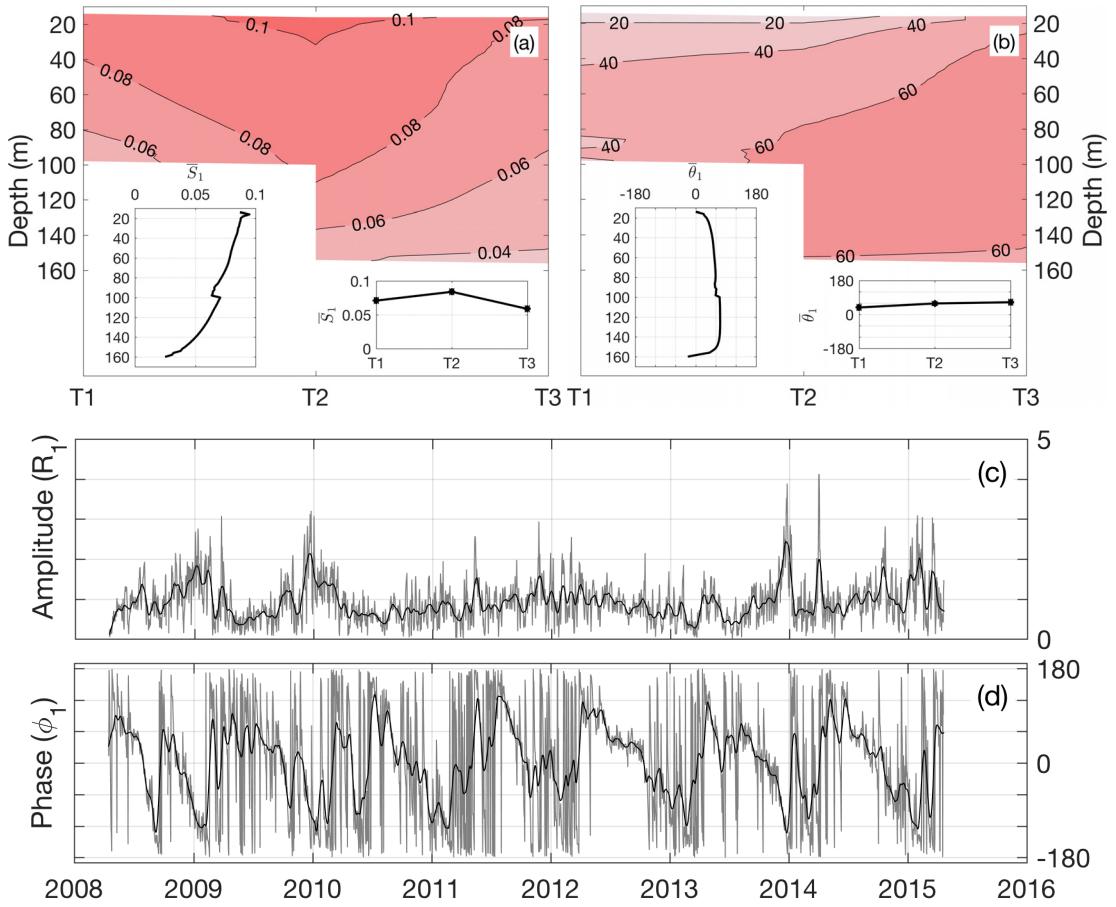


Figure 4.6: First HEOF (HEOF1; explains about 72% of the total variability) calculated from daily-averaged current anomalies at the three T-stations over the 2008-2015 period. (a) Spatial amplitude function $S_1$ (relative units), together with its averaged depth profile and cross-shelf distribution (see insets). (b) Spatial phase function $\theta_1$ (in degrees), together with its averaged depth profile and cross-shelf distribution (see insets). (c) Temporal amplitude ($R_1$, relative units) and (d) temporal phase ($\phi_1$, in degrees) functions, where a 30-day moving average (thick line) is plotted on top of the daily time series (thin line).

function that is maximum near the surface at T1 (Figure 4.7a). While HEOF1 decreases linearly with depth, the spatial amplitude of HEOF2 decreases rapidly with depth within the first 60 m of the water column, is relatively constant in the mid-water column, and increases back to its near-surface value near the bottom. The spatial amplitude function is weakest at T2, where the depth-averaged amplitude is about half as large as at T3 or T1. This mode of variability has a downward and offshore propagation pattern from the near-surface at T1 to the near-bottom at T3, where the signal is almost in phase (Figure 4.7b). This is represented by the spatial phase function, that shows an almost complete cycle over the 32 km separating T1 and T3.

The temporal amplitude function for HEOF2 has a consistently larger magnitude and variance in the winter than in the summer (Figure 4.7c). The temporal phase function does not show a consistent trend like in $\phi_1$ and does not seem to be locked to a specific cycle, suggesting the absence of a cyclostationary process in this mode (Figure 4.7d). When the HEOF analysis was applied to monthly-averaged current anomalies, the percentage of variance explained by HEOF2 decreases from 19% to 9%, suggesting that the mechanisms involved in HEOF2 have more energy at higher frequencies.

The fact that the spatial amplitude function decreases exponentially in the vertical over a depth-range that is similar to the mixed layer depth, combined with the high temporal amplitude and variance during the winter, suggest that HEOF2 is likely linked to surface winds. This is confirmed by the fact that the variance explained by HEOF2 decreases when higher-frequencies are further smoothed out from the original time series from which HEOFs are calculated. However, the heterogeneity of HEOF2's amplitude in space and the offshore propagation of the signal suggest that surface winds alone cannot be attributed to this mode. A combination of processes are likely to be driving this mode of variability, preventing a direct mechanistic interpretation.

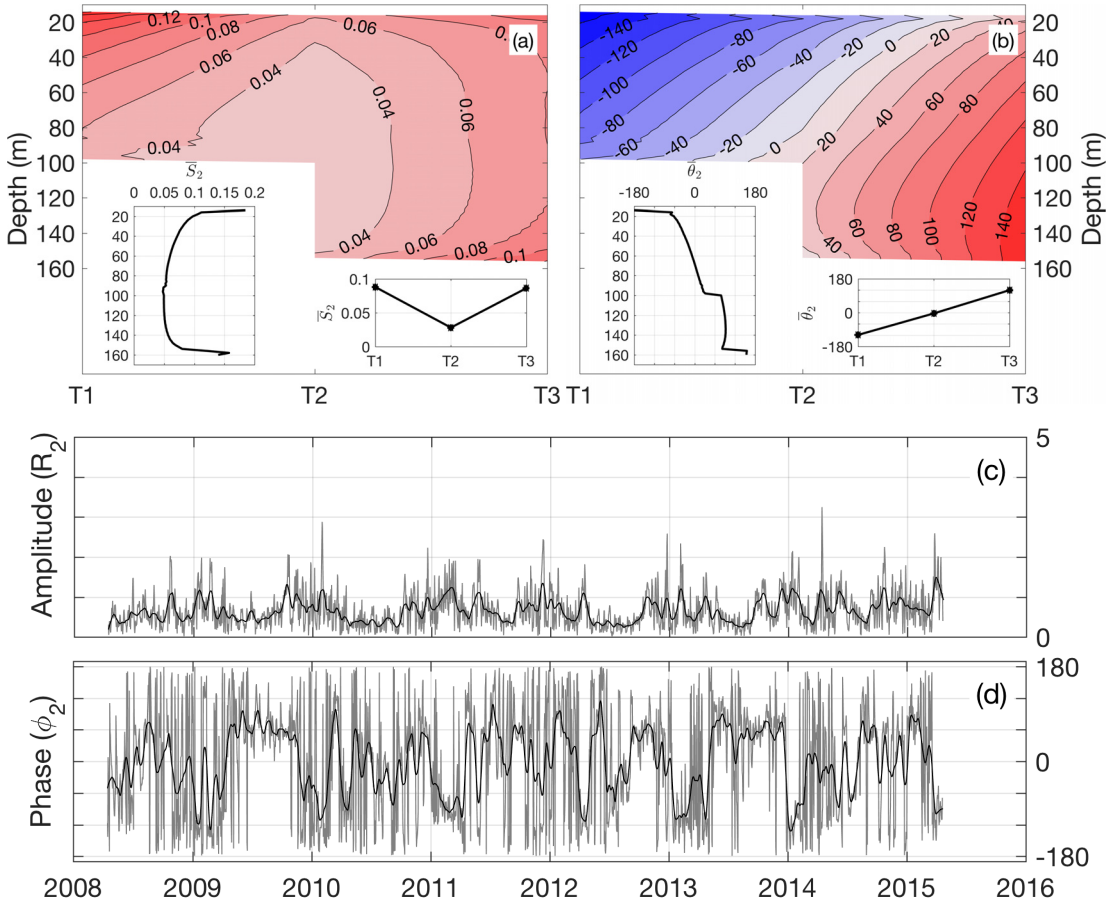


Figure 4.7: Same as in Figure 4.6, but for the second HEOF (HEOF2; explains about 19% of the total variability).

## 4.2 The Wind Index

The Wind Index (WI) was defined by WG05 as the dimensionless ratio of the estimated alongshore wind-driven depth-averaged current ($U_{wind}$) and the alongshore buoyancy-driven depth-averaged current ($U_{geo}$), associated with the discharge of buoyant water over a continental shelf:

$$WI = \frac{U_{wind}}{U_{geo}} \tag{4.1}$$

where $U_{geo}$ and $U_{wind}$ are defined as positive southwestward (Figure 4.8). This index quantifies the relative contributions of geostrophy and alongshore wind stress to a density-driven coastal current. WG05 used a set of assumptions to derive their definition of the Wind Index, hereinafter referred to as the TWI. While appropriate in WG05's study, these assumptions present some important limitations that restricts the use of the TWI in other studies of buoyancy-driven coastal currents. In lieu of these limitations, this study presents the Hydrographic Wind Index (HWI), which is a generalized version of the TWI based on a conceptual model applicable to any buoyancy-driven coastal current. The reliability of this new index is first tested using a scaling analysis in an idealized 2-layer case, and then validated using independent current velocity measurements collected along the HL. Finally, the HWI is estimated for the NSC at the HL, and directly compared to the TWI.

### 4.2.1 Equations of Motion

The scaling of the general equations of motion for a rotating fluid parcel (see *Gill*, 1982) requires the use of three dimensionless numbers: (1) the Reynolds number, (2) the Rossby number, and (3) the Ekman number (*Cushman-Roisin and Beckers*, 2009).

Assuming a high Reynolds number (Re $\gg$1; i.e., advection $\gg$ molecular friction), a small Rossby number (Ro $\ll$1; i.e., rotation $\gg$ advection) and small horizontal mixing, the equations of motion in the horizontal for a rotating fluid under the Boussinesq

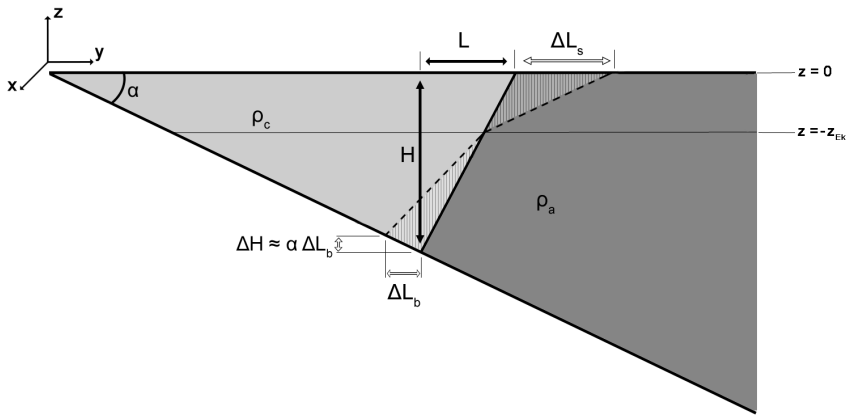


Figure 4.8: Schematic of a buoyancy-driven coastal current. The parameters from Equation 4.12 are indicated in the figure: the frontal width $L$, the frontal depth $H$ and the average densities of coastal water $\rho_c$ and ambient shelf water $\rho_a$. The change in frontal width ($\Delta L$) and frontal depth ($\Delta H$) associated with the tilting of the density front under upwelling-favorable winds are also indicated (Equations 4.19, 4.21, and 4.22). The tilting occurs at the Ekman depth ($z_{Ek}$). The bottom horizontal displacement $\Delta L_b$ is estimated based on the fact that the offshore transport in the upper layer ($z > -z_{Ek}$) should be equal to the onshore transport in the rest of the water column ($z < -z_{Ek}$; hatched regions). The bottom slope $\alpha$ is also shown.

approximation can be simplified to:

$$\frac{\partial u}{\partial t} - fv = -\frac{1}{\rho_0}\frac{\partial P}{\partial x} + \frac{\partial}{\partial z}\left(A_V \frac{\partial u}{\partial z}\right) \qquad \text{(x-comp)} \qquad (4.2a)$$

$$\frac{\partial v}{\partial t} + fu = -\frac{1}{\rho_0}\frac{\partial P}{\partial y} + \frac{\partial}{\partial z}\left(A_V \frac{\partial v}{\partial z}\right) \qquad \text{(y-comp)} \qquad (4.2b)$$

where the symbol $\partial$ denotes partial derivatives, ($u$, $v$) are the current speeds in the $x$ and $y$ directions respectively, $f$ is the Coriolis parameter, $\rho_0$ is a reference water density (Boussinesq approximation), $P$ is the pressure and $A_V$ is the vertical eddy viscosity.

In a steady-state, the geostrophic flow ($u_{geo}$, $v_{geo}$) can be written as the balance between the Coriolis term and the pressure gradient. The vertical mixing term in Equation 4.2b

is at least one order of magnitude smaller than the other terms when considering the alongshore geostrophic flow in a steady-state as the geostrophic velocity shear in the cross-shelf direction $\partial v_{geo}/\partial z$ is expected to be of the order of $\mathcal{O}(10^{-4})$. Equation 4.2b for the alongshore geostrophic flow in a buoyancy-driven coastal current can therefore be simplified to:

$$f u_{geo} = -\frac{1}{\rho_0}\frac{\partial P}{\partial y} \tag{4.3}$$

By assuming that the horizontal length scale of circulation is much larger than the vertical length scale, the hydrostatic approximation can be made, yielding a balance between the vertical pressure gradient and the water density multiplied by the gravitational acceleration $g$:

$$\frac{\partial P}{\partial z} = -g\rho \tag{4.4}$$

Substituting Equation 4.4 into the vertical derivative of Equation 4.3, we obtain the so-called thermal wind equations (*Gill*, 1982):

$$\frac{\partial (u_{geo})}{\partial z} = \frac{g}{f\rho_0}\frac{\partial \rho}{\partial y} \tag{4.5}$$

Under the Boussinesq approximation, the one-and-a-half layer geostrophic flow (i.e., two-layer flow with quiescent bottom layer; see Figure 4.8 and Appendix B) can be deduced from the Margules equations (*Margules*, 1906):

$$u_{geo} = \frac{g}{f}\frac{\rho_a - \rho_c}{\rho_a}\frac{\partial h_f}{\partial y} \tag{4.6}$$

where $h_f$ is the $z$-coordinate of the interface between the two layers, $\rho_a$ is the density of the lower, stagnant layer (i.e., ambient shelf water in this study) and is used as the reference density ($\rho_0 = \rho_a$), and $\rho_c$ is the density of the upper layer (i.e., coastal water in this study; see Figure 4.8).

In a steady-state, the flow driven by frictional forces such as surface winds ($u_{wind}$,

$v_{wind}$) can be deduced from the steady-state Ekman theory. In this case, the appropriate length scale is the Ekman depth ($\mathcal{O}$(10 m)). The Ekman number is therefore on the order of 1, leading to a balance between the rotation and vertical mixing terms:

$$-fv_{wind} = \frac{\partial}{\partial z}\left(A_V \frac{\partial u_{wind}}{\partial z}\right) \tag{4.7a}$$

$$fu_{wind} = \frac{\partial}{\partial z}\left(A_V \frac{\partial v_{wind}}{\partial z}\right) \tag{4.7b}$$

This balance is based on the assumption that the pressure gradient terms from Equations 4.2a and 4.2b are small in comparison to the other terms. The depth-averaged alongshore flow $U_{wind}$ can be obtained by integrating Equation 4.7b over a water column with water depth $h$:

$$fU_{wind} = \frac{1}{h} A_V \frac{\partial v_{wind}}{\partial z}\bigg|_{surface} - \frac{1}{h} A_V \frac{\partial v_{wind}}{\partial z}\bigg|_{bottom} \tag{4.8}$$

Considering the following boundary conditions:

$$A_V \frac{\partial v_{wind}}{\partial z}\bigg|_{surface} = \frac{\tau_{sy}}{\rho_0} \tag{4.9a}$$

$$A_V \frac{\partial v_{wind}}{\partial z}\bigg|_{bottom} = \frac{\tau_{by}}{\rho_0} \tag{4.9b}$$

where $\tau_s$ and $\tau_b$ are the surface and bottom stresses, respectively. The depth-averaged, friction-driven flow can be expressed as:

$$fU_{wind} = \frac{\tau_{sy} - \tau_{by}}{\rho_0 h} \tag{4.10}$$

Equations 4.6 and 4.10 form the set of key equations on which the Wind Index approach is based, as shown in the next section.

### 4.2.2 The Traditional Wind Index

#### 4.2.2a Buoyancy-Driven Alongshore Flow

WG05's estimation of $U_{geo}$ is based on the assumption that the buoyancy-driven coastal current is wedge-shaped and follows thermal wind dynamics (Figure 4.8 and Equation 4.5; *Gill*, 1982). The alongshore velocity due to buoyancy forcing can be estimated based on thermal wind dynamics for a two-layer system (Equations 4.6; *Margules*, 1906):

$$u_{geo} = \frac{g'}{f}\frac{dh_f}{dy} \tag{4.11}$$

where $dh_f/dy$ represents the slope of the interface separating the two layers (i.e., the density front) and $g'$ is the reduced gravity based on the density difference between the fresher, less dense coastal water ($\rho_c$) and the more saline, denser ambient shelf water ($\rho_a$) and is defined by $g' = g(\rho_a - \rho_c)/\rho_a$.

Assuming a wedge-shaped current, the slope of the front is the ratio of the frontal depth ($H$) to the frontal width ($L$; see Figure 4.8):

$$U_{geo} = \frac{g'H}{fL} \tag{4.12}$$

The transport associated with the buoyancy-driven coastal current within the wedge-shaped cross-section can then be written as:

$$Q_{geo} = U_{geo}\frac{HL}{2} = \frac{g'H^2}{2f} \tag{4.13}$$

In WG05, the length scale $L$ in Equation 4.12 is represented by $KR_b$, where $K$ is a scaling coefficient linking the current width to the Rossby radius of deformation $R_b = \sqrt{g'H}/f$. Using Equation 4.13 to define $H$, Equation 4.12 becomes:

$$U_{geo} = \frac{1}{K}(2g'Q_{geo}f)^{1/4} \tag{4.14}$$

Estimating $g'$ and $Q_{geo}$ requires information on the density and velocity fields within the coastal current. These variables are, however, very difficult to determine, especially as they greatly vary in space and time. For these reasons, WG05 links the transport and reduced gravity terms to the river discharge ($Q_r$) and reduced gravity of the river ($g'_r$), yielding the following equation:

$$U_{dis} = \frac{1}{K}(2g'_r Q_r f)^{1/4} \tag{4.15}$$

where $U_{dis}$ is the alongshore geostrophic current calculated from the river discharge $Q_r$. $g'_r = g(\rho_a - \rho_r)/\rho_a$, where $\rho_r$ is the density of the river water. This approach assumes that the only process occurring between the source of buoyant water and the study region is the mixing between river water and ambient shelf water. The applicability of this assumption to the NSC will be discussed in Section 4.2.2c.

#### 4.2.2b Wind-Driven Flow

An estimate of the barotropic response to local surface winds (i.e., wind-driven flow) can be established based on Equation 4.10. The analysis of observed currents at the HL showed that the alongshore currents are approximately two orders of magnitude larger than the cross-shelf currents. The left-hand term in Equation 4.10a is assumed to be small near the coast, leading to a simple balance between the alongshore surface wind stress ($\tau_{sx}$) and the alongshore bottom stress ($\tau_{bx}$). This approximation is consistent with previous results obtained in both observational and modeling studies conducted over the Scotian Shelf, which demonstrated that this assumption is valid over the inner Scotian Shelf for waters as deep as 100 m (*Sandstrom*, 1980; *Schwing*, 1992a,b). This balance between alongshore surface wind stress and bottom friction was also used when studying the impact of winds over continental shelves other than the Scotian Shelf, for water depths comparable to the one in this study (*Whitney and Garvine*, 2005; *Lentz and Largier*, 2006; *Mazzini et al.*,

2014). Both surface and bottom stresses are expressed using a quadratic law:

$$\begin{aligned} \tau_{sx} &= \rho_{air} C_{10} |U_{10}| U_{10} \\ \tau_{bx} &= \rho_0 C_{Da} |U_{wind}| U_{wind} \end{aligned} \tag{4.16}$$

where $\rho_{air}$ is the air density (1.2 kg/m$^3$), $C_{10}$ is the surface drag coefficient (1.2 x $10^{-3}$), $U_{10}$ is the alongshore wind speed at 10 m above the sea surface, and $U_{wind}$ is the depth-averaged, wind-generated alongshore current velocity. Because depth-averaged velocities are considered, the traditional bottom drag coefficient $C_D$ is adjusted to its depth-averaged equivalent using $C_{Da} = (8 + 1/\sqrt{C_D})^{-2}$ (***Csanady***, 1982). This approach is identical to the one discussed in *Whitney and Garvine* (2005). By setting $\tau_{sx} = \tau_{bx}$, the two equations in Equation 4.16 can be combined to estimate the wind-forced alongshore depth-integrated current:

$$U_{wind} = \sqrt{\frac{\rho_{air}}{\rho_0} \frac{C_{10}}{C_{Da}}} U_{10} \tag{4.17}$$

$U_{wind}$ is therefore directly proportional to the alongshore wind speed and follows the same sign convention as $U_{geo}$: a positive $U_{wind}$ means a downstream flow (i.e., downwelling conditions), while a negative $U_{wind}$ represents an upstream flow (i.e., upwelling conditions).

#### 4.2.2c Shortcomings of the Traditional Wind Index

Although elegant, WG05's definition for TWI presents some important limitations, principally in the definition of the buoyancy-driven term based on the river discharge driving the coastal current (see Equation 4.15), that prevents the TWI from being generally applicable to buoyancy-driven coastal currents. Relating the alongshore geostrophic flow to the river discharge eliminates the need for information on the shape of the density front (as opposed to $U_{geo}$ in Equation 4.12), or on the "local conditions" (i.e., $\rho_c$, $\rho_a$, and $Q_{geo}$ in Equation 4.14). However, it relies on several important assumptions. The first assumption is that the only process taking place as the buoyant plume moves downstream is the "mixing

between river water (with density $\rho_r$) and ambient shelf water" (WG05). While that might be reasonable over short spatial scales ($\mathcal{O}$(10 km)), this assumption is not valid when considering scales on the order of $\mathcal{O}$(100 km), where many other processes affect the density field. The second assumption concerns the length scale associated with the density front ($K$ in Equation 4.15), defined in WG05 as a constant linking the width of the current to the Rossby radius of deformation. As demonstrated in the thesis, the width of the current varies greatly with time and space, and should not be assumed to be constant within a single system. Furthermore, by exclusively using the upstream conditions ($Q_r$ and $\rho_r$), the time lag associated with the downshelf propagation of the signal coming from the source of buoyant water to the study region is overlooked. As demonstrated in Section 4.1, this lag can be significant (e.g., months) when investigating a buoyancy-driven coastal current over spatial scales on the order of hundreds of kilometers.

Although most of the assumptions for Equation 4.15 are acceptable over spatial scales of the order of $\mathcal{O}(10km)$ and are therefore suitable for the study of the Delaware Current (WG05), a general definition for the alongshore buoyancy-driven flow is required for this approach to be applicable to other buoyancy-driven coastal currents such as NSC. This is especially true for density-driven currents forced by multiple freshwater sources. For multi-source buoyancy-driven coastal currents, the use of upstream conditions in Equation 4.15 is difficult to justify given the presence of several freshwater sources with potentially overlapping plumes. Estimating $U_{geo}$ using local conditions not only provides the opportunity to assess spatial variability in the buoyancy-driven flow, but also expands the applicability of the approach to both single-source and multi-source buoyancy-driven coastal currents.

### 4.2.3 The Hydrographic Wind Index

#### 4.2.3a Frontal Characteristics and Buoyancy-Driven Flow

The analysis to be made in this section relies on the relatively high spatial resolution of glider data. As a result, the frontal depth $H$ and frontal width $L$ are determined with enough

confidence to reliably estimate the alongshore, buoyancy-driven flow ($U_{geo}$) directly from Equation 4.12, thus removing the need to define upstream conditions.

The calculation of $U_{geo}$ requires four key parameters that can be determined from each density distribution across the buoyancy-driven coastal current (Figure 4.8): the average density of the buoyant plume $\rho_c$, the average density of the ambient water $\rho_a$, the frontal width $L$, and the frontal depth $H$. These parameters are computed for each density transect collected along the HL, using the following algorithm:

1. The offshore density gradient is computed from the glider data (Figure 4.9a).

2. The cumulated density gradient is estimated along each isopycnal, and the isopycnal experiencing the largest cumulated offshore density gradient in the top 20 m is used to define the density front. Applying this criteria to the upper water column guarantees that the density front detected by the algorithm intersects the ocean surface. This approach improves the reliability of the algorithm by discriminating other sub-surface density fronts that might be present throughout the water column (e.g., density front between ambient shelf water and deeper Warm Slope Water discussed in Section 3 and visible around 70 m in Figure 4.9).

3. The frontal characteristics ($\rho_c$, $\rho_a$, $L$, and $H$) required by Equation 4.12 are computed and extracted from the transect, and the isopycnal selected to define the density front is recorded.

#### 4.2.3b Isopycnal Tilting and Wind-Driven Flow

Alongshore winds generate a cross-shore Ekman transport, resulting in isopycnal tilting (Figure 4.8). An upwelling (downwelling) favorable wind stress will increase (decrease) the width of the density-driven coastal current by advecting the density front offshore (onshore) in the upper layer. At the bottom, the density front will shoal (deepen) due to the pumping (sinking) of water along the bottom slope. Because the geometry of the current

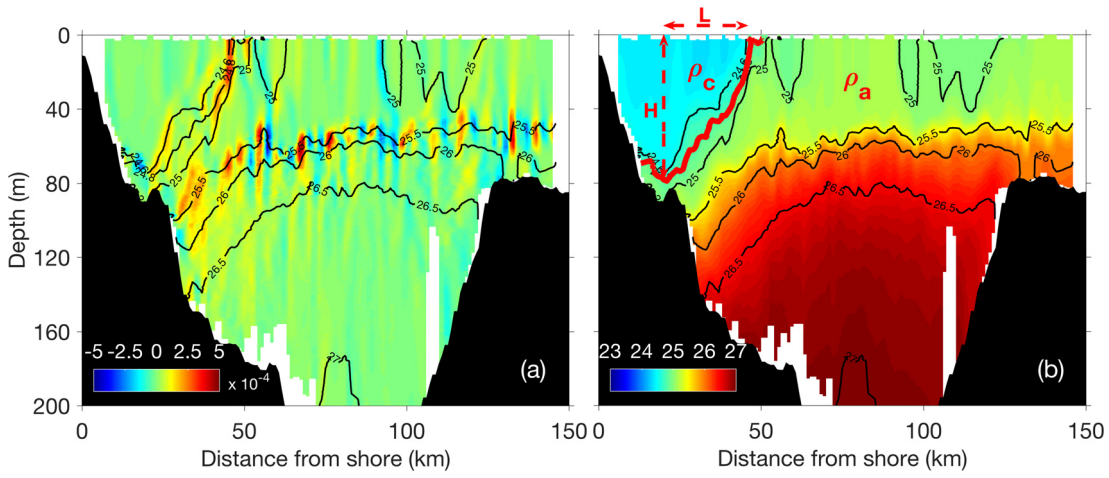


Figure 4.9: Example of the detection of the density front using the algorithm described in Section 4.2.3a, based on a transect of potential density completed between February 9th and 17th, 2012. (a) Offshore density gradient (in kg/m$^3$/m). (b) Potential density field (in kg/m$^3$), with the isopycnal selected by the algorithm to describe the density front (thick red line), as well as the four parameters extracted from the transect ($L$, $H$, $\rho_c$, and $\rho_a$).

directly – and only – affects the estimate of $U_{geo}$ through Equation 4.12, part of $U_{geo}$ is due to the interaction of the density front with the surface winds. Neglecting wind-driven isopycnal tilting would therefore bias the HWI towards the buoyancy-driven component and underestimate the role of local winds.

Here, the role of local winds is accounted for by considering the change in the geometry of the front generated by surface winds ($\Delta H$, $\Delta L_s$, and $\Delta L_b$ in Figure 4.8). The frontal displacement associated with the wind forcing can be reconstructed if both the original geometry of the front and the surface wind stress are known. Assuming that isopycnals tilt at the Ekman depth $z_{Ek}$ (Figure 4.8), the change in the width of the current at the surface ($\Delta L_s$) can be calculated using:

$$\Delta L_s = -\int \frac{2\tau_{sx}}{\rho f z_{Ek}} dt \tag{4.18}$$

which is equivalent to integrating the Ekman transport over time. The negative sign means that the front widens ($\Delta L_s > 0$) when surface winds are upwelling-favorable ($\tau_{sx} < 0$). The factor 2 arises from the assumption of a linear velocity profile throughout the Ekman

layer, with a maximum flow at the surface and no flow at the Ekman depth. The front is assumed to tilt at its mid-point (i.e., $H/2$), unless the water column is deeper than 50 m, in which case the Ekman depth is set to 25 m. This depth corresponds to the average Ekman depth scaled using the vertical eddy viscosity parameter used in the submodel L2 presented in Section 2.1.3 ($\sim 3{\times}10^{-3}$ m$^2$/s; *Shan et al.*, 2016). Assuming that the integrand is constant over one time step $\Delta t$, Equation 4.18 can be discretized:

$$\Delta L_s = -\sum_i \frac{2\tau_{sx_i}}{\rho f z_{Ek}} \Delta t \tag{4.19}$$

where $i$ is the number of time steps. The timescale $\Delta t$ is chosen to correspond to the "frictional adjustment time" (see Section 1.2), as it is the time required for the ocean to respond to surface winds and reach the frictionally adjusted state (i.e., $\tau_{sx} = \tau_{bx}$; see Equation (35) in *Csanady*, 1974). This timescale depends on the water depth and the surface wind stress, and can be expressed as (*Csanady*, 1974):

$$\Delta t = \frac{H}{2\sqrt{\frac{\tau_{sx} C_{Da}}{\rho}}} \tag{4.20}$$

Using realistic wind stress observed over the Scotian Shelf, the adjustment time is estimated to be less than 3 days on average, for water depths shallower than 100 m. A Butterworth filter with a cut-off period of 72 hours is therefore used to filter out variability in the wind signal at higher frequencies. For mass conservation, the cross-shore Ekman transport in the surface Ekman layer ($z > -z_{Ek}$) is compensated by an equal transport in the opposite direction over the lower part of the water column ($z < -z_{Ek}$). The horizontal displacement of the front at the bottom ($\Delta L_b$) can thus be computed using:

$$\Delta L_b = -\sum_i \frac{2\tau_{sx_i}}{\rho f (H_{i-1} - z_{Ek})} \Delta t \tag{4.21}$$

The change in the frontal depth can then be deduced by scaling $\Delta L_b$ with the bottom slope

$\alpha$ (Figure 4.8):

$$\Delta H = -\Delta L_b tan(\alpha) \sim -\alpha \Delta L_b \,, \quad \text{for } \alpha \ll 1 \tag{4.22}$$

Two limiting cases are imposed to the change in the frontal width due to isopycnal tilting. The first one prevents the density front from spreading further than 170 km from shore, which corresponds to the width of the Scotian Shelf at the HL. This is based on the maximum frontal width measured over the observation period and is justified by the fact that other mechanisms come into play when approaching the shelf break, preventing further widening of the coastal front (e.g., shelf break jet and front; *Pickart et al.*, 1999). The second limiting case is to prevent an "inshore" tilting of the front, that is when the density front has a negative slope. While downwelling winds could theoretically generate a negatively sloped density front, this would in turn lead to convective mixing, homogenizing the water column.

Once the wind-driven isopycnal tilting is known, the observed current geometry at any given time can be corrected by eliminating the wind-driven component:

$$U^c_{geo} = \frac{g' H^c}{f L^c} \quad \text{, where} \quad \begin{cases} H^c = H - \Delta H \\ L^c = L - (\Delta L_s + \Delta L_b) \end{cases} \tag{4.23}$$

where the superscript $c$ denotes the corrected estimates. While $U_{geo}$ provides an estimation of the buoyancy-driven flow, $U^c_{geo}$ estimates the magnitude of the buoyancy-driven flow in the absence of winds. The difference between $U_{geo}$ and $U^c_{geo}$ corresponds to the baroclinic flow resulting from the isopycnal tilting induced by surface winds. This velocity difference is also used to modify the wind-driven flow based on:

$$U^c_{wind} = U_{wind} + (U_{geo} - U^c_{geo}) \tag{4.24}$$

where the first term on the right-hand-side corresponds to the wind-driven flow estimated

using Equation 4.17, and the second term results from the change in the alongshore velocity due to the wind-driven isopycnal tilting. While this correction is re-attributed to the wind component, it only exists because of the interaction between the density front and the surface winds. The corrected HWI can now be defined as:

$$HWI^c = \frac{U^c_{wind}}{U^c_{geo}} \tag{4.25}$$

#### 4.2.3c Method Validation

The performance of this new methodology in quantifying the buoyancy-driven and wind-driven components of the density-driven coastal current is assessed by comparing velocity estimates for the NSC from Equations 4.12 and 4.17 using concurrent ADCP measurements (see Section 2.1).

Both the buoyancy-driven and wind-driven transports are estimated using the modal value of each parameter for the NSC at the HL, based on the glider data. The estimated total transport can then be directly compared to the independently computed transport associated with the NSC and determined from the ADCP records described in Section 2.1.

The baroclinic flow is estimated using Equation 4.12. Using the mode of each parameter at the HL, we take $g = 9.81$ m/s$^2$, $\rho_a = 1025.4$ kg/m$^3$, $\rho_c = 1024.5$ kg/m$^3$, $H = 87$ m, $L = 50$ km, and $f = 1.02 \times 10^{-4}$ s$^{-1}$ (Figure 4.10). The buoyancy-driven flow at the HL therefore scales to:

$$U_{geo} = 0.15 \pm 0.01 \text{ m/s}$$

where the measurement error is estimated using the standard deviation of each parameter and the error propagation formula detailed in Appendix C. The geostrophic transport ($Q_{geo}$) can be calculated by multiplying the geostrophic flow by the cross-sectional area $HL/2$:

$$Q_{geo} = 0.32 \pm 0.01 \text{ Sv}$$

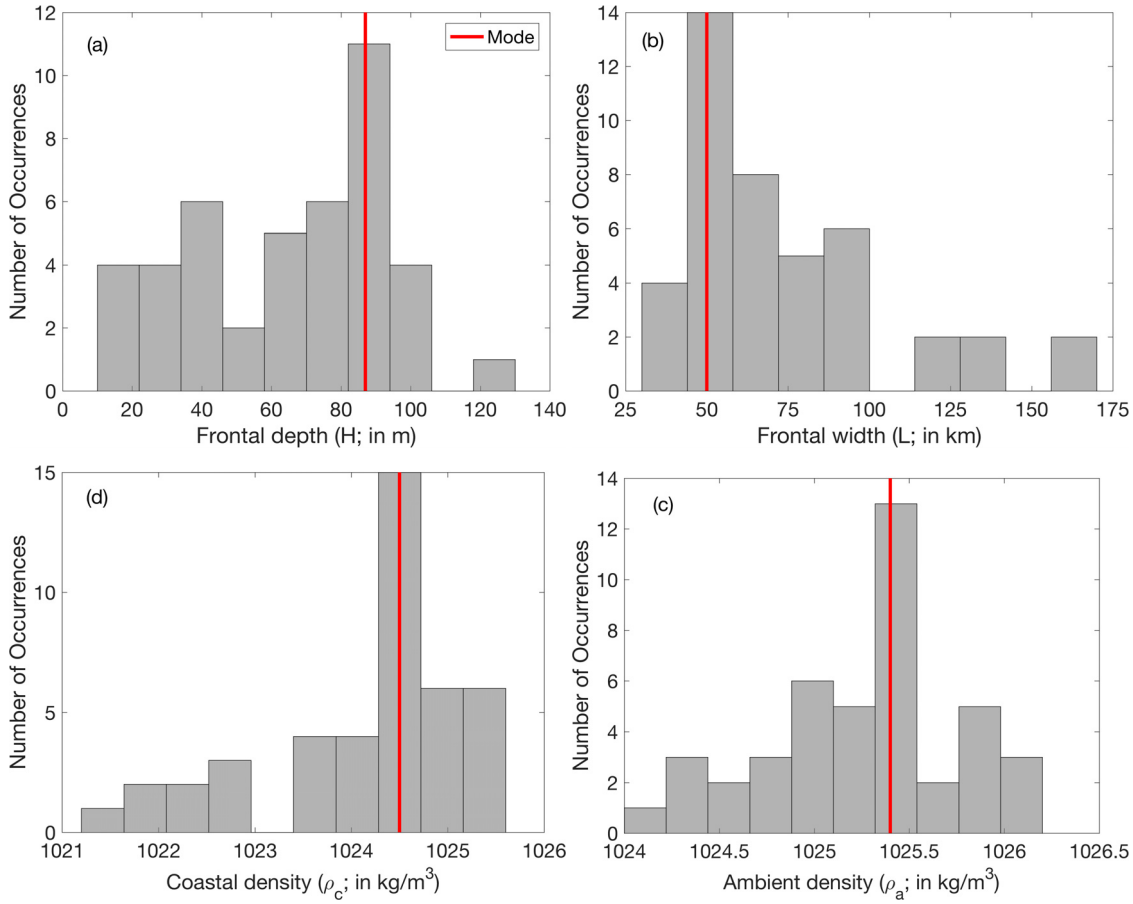


Figure 4.10: Number of occurrences per bin for (a) the frontal depth ($H$; in m), (b) the frontal width ($L$; in km), the coastal density ($\rho_c$; in kg/m$^3$), and (d) the ambient shelf water density ($\rho_a$; in kg/$^3$) determined from the glider observations. In each panel, the mode is indicated by the red line.

where the positive sign means southwestward. The wind-driven flow can be estimated at the HL using $\rho_{air} = 1.2$ kg/m$^3$, $\rho = 1025$ kg/m$^3$, $C_{10} = 1.1 \times 10^{-3}$, and $U_{10} = -2.28$ m/s in Equation 4.17 (*Whitney and Garvine*, 2005). While bottom drag values $C_D$ usually range from 1 to $5 \times 10^{-3}$, the bottom drag is chosen to be $C_D = 5 \times 10^{-3}$ in this study, to be consistent with *Whitney and Garvine* (2005). The wind-driven flow at the HL therefore scales to:

$$U_{wind} = -0.06 \text{ m/s}$$

The wind-driven transport within the upper layer is therefore,

$$Q_{wind} = -0.12 \pm 0.003 \text{ Sv}$$

where the negative sign means northeastward.

The total alongshore transport within the NSC ($Q_{geo} + Q_{wind}$) is therefore estimated to be 0.20 $\pm$ 0.01 Sv, which is comparable to the modal value of 0.23 Sv determined directly from the ADCP current records collected at the HL.

The same ADCP current records can also be used to further evaluate the reliability of the newly defined index, by comparing the time series of the total alongshore flow ($U_{wind}$ + $U_{dis}$) estimated using Equations 4.12 and 4.17, with the average alongshore flow measured by the three ADCPs during each glider deployment (Figure 4.11). The two time series present a high correlation coefficient ($r$ = 0.90, $p$ <0.01). On average, the residual $\Delta_{res} = U_{ADCP} - (U_{wind} + U_{geo})$ is about $4 \times 10^{-3}$ m/s, which represents approximately 7% of the coastal current mean velocity. This result is both promising and not surprising: as suggested by the HEOF analysis in Section 4.1.3, since most of the NSC's variability (91%) can be explained by only considering the wind-driven and buoyancy-driven flows. The good agreement shown in Figure 4.11 is therefore consistent with the fact that the NSC seems to be principally driven by the geostrophic component of the flow, as suggested by the HEOF analysis. It should be noted that the high spatial resolution of the glider data allows us to determine the frontal characteristics with relatively high confidence. Despite the simplicity of this new method, it is able to provide a good first-order approximation of the buoyancy-driven coastal current. It is important to note that correcting for the wind-driven isopycnal tilting will not affect this result as it only redistributes a portion of $U_{geo}$ to $U_{wind}$, leaving the sum unchanged.

This validation demonstrates that the set of assumptions made to estimate the HWI, such as the frictionally adjusted flow and the wedge-shape of the current, are reasonable

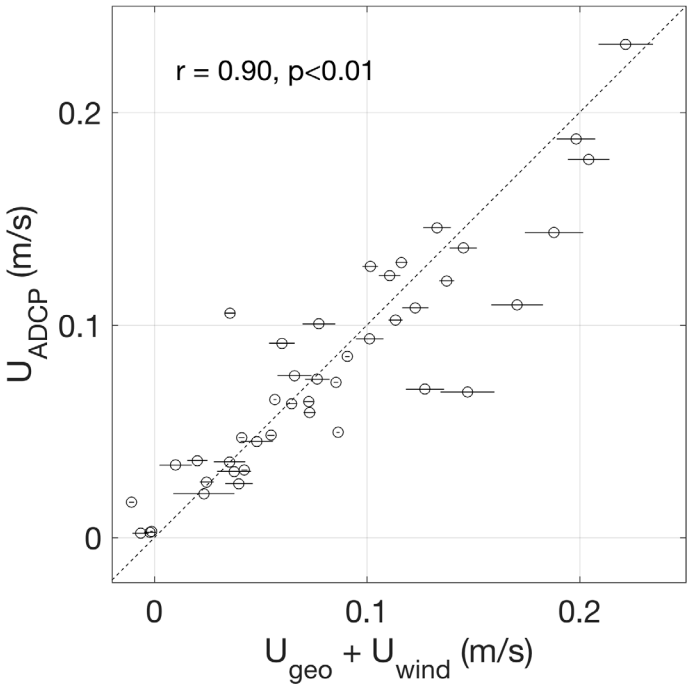


Figure 4.11: Comparison between the alongshore flow computed from ADCP observations ($U_{ADCP}$) and obtained by combining the buoyancy-driven ($U_{geo}$) and wind-driven ($U_{wind}$) currents obtained from the conceptual model described in Section 4.2. The dashed line represent the 1:1 line. The correlation coefficient and the associated p-value are indicated. The uncertainty associated with each alongshore current estimation from the conceptual model are indicated with error bars (see Appendix C).

and yield good results. In the next section, the HWI is characterized at the HL, and directly compared to the traditional approach taken by WG05.

## 4.3 The Wind Index along the Halifax Line

In this section, the monthly-averaged characteristics of the density front associated with the NSC at the HL are analyzed to gain good understanding of the mechanisms driving the seasonal cycle of the buoyancy-driven flow. The resulting $U_{geo}$ is then corrected for the wind-driven isopycnal tilting, and directly compared to WG05's traditional approach. $U_{wind}$ is also computed and the seasonal cycle of the HWI characterized.

### 4.3.1 Datasets

The estimation of the HWI for the NSC is made based on density distributions at the HL collected by the gliders over the 2011-2014 period and time series of surface winds. Glider data used to determine $U_{geo}$ are described in Section 2.1 (See Equation 4.12). Surface wind speeds used to determine $U_{wind}$ (See Equation 4.17) are extracted from the ECMWF ERA-interim reanalysis product that offers a resolution of 1/8 of a degree (*Dee et al.*, 2011). Similarly to the current observations, the wind speed is rotated by an angle of $212^o$ to obtain the alongshore component and averaged daily over the grid points located within the NSC (Figure 4.12). A 5th-order, low-pass, squared Butterworth filter with a cut-off period of 72 hours was applied to the time series (Section 4.2.3b). A direct comparison between the ECMWF ERA-Interim alongshore winds and the alongshore wind speed observed at a buoy located on the inner Scotian Shelf (C44258) shows that the observed wind pattern is reasonably well represented by the ECMWF product ($r = 0.92$, $p < 0.01$).

In order to directly compare the TWI to the HWI, information on the discharge of buoyant low-salinity water from the GSL $Q_r$ and the density of the outflow $\rho_r$ is required (see Equation 4.15). We considered the conditions at Cabot Strait to represent the upstream conditions for the NSC. As mentioned in previous chapters, the NSC is generated by a combination of river outflows (e.g., the St. Lawrence River) and Inshore Labrador Current water leaving the GSL (see Chapter 3). Choosing Cabot Strait as the upstream boundary simplifies the analysis, as it allows us to not consider the complex dynamics in the GSL. Unfortunately, no direct observations were available to estimate $Q_r$ and $\rho_r$ at Cabot Strait over the period sampled by gliders (i.e., 2011 to 2014). As a result, numerical simulations using the circulation model described in Section 2.1 (*Shan et al.*, 2016) were used to estimate the discharge of low-salinity waters and the water density at Cabot Strait (Figure 2.1).

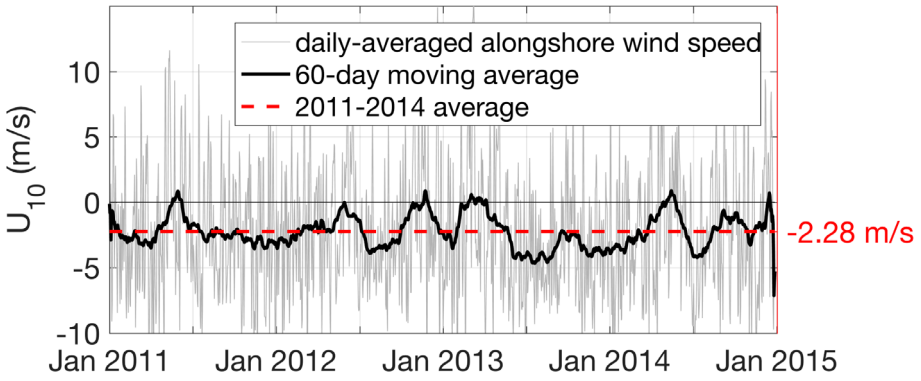


Figure 4.12: ECMWF ERA-Interim alongshore wind speed ($U_{10}$) averaged over the Nova Scotia Current at the Halifax Line over the 2011-2014 period (in m/s). The time series average is indicated by the red dashed line, along with a 60-day moving average (thick black line). Negative means northeastward.

### 4.3.2 Frontal Characteristics and Buoyancy-Driven Flow

The buoyancy-driven flow (i.e., the NSC) over the inner Scotian Shelf is predominantly southwestward with speeds ranging between 0.06 m/s in summertime to 0.20 m/s during the winter months (Figure 4.13). This result agrees with the observed seasonally-averaged flow (see Figure 3.8), as well as with the current speeds reported in the literature (*Drinkwater et al.*, 1979; *Smith and Schwing*, 1991; *Urrego-Blanco and Sheng*, 2014; *Dever et al.*, 2016). It is interesting to note that this non-corrected $U_{geo}$ tends to follow the seasonal cycle of the frontal dimensions ($H$ and $L$), as opposed to the one of the density gradient (Figure 4.13). Despite the reduced gravity reaching its maximum in the summer and fall, when the density difference between buoyant coastal water and ambient shelf water is the largest, the buoyancy-driven flow in summer and fall is weakest. This can be explained by the wide and shallow (i.e., flat) density front observed in this season, representing a stratified water column. By comparison, the density front is narrowest and deepest (i.e., steep) in the wintertime, leading to the strong buoyancy-driven flow calculated in late winter. This result suggests that the variability in the ratio $H/L$ in Equation 4.12 modulates the variability in $U_{geo}$, as opposed to the reduced density $g'$.

The impact of correcting for the isopycnal tilting due to wind forcing can be examined

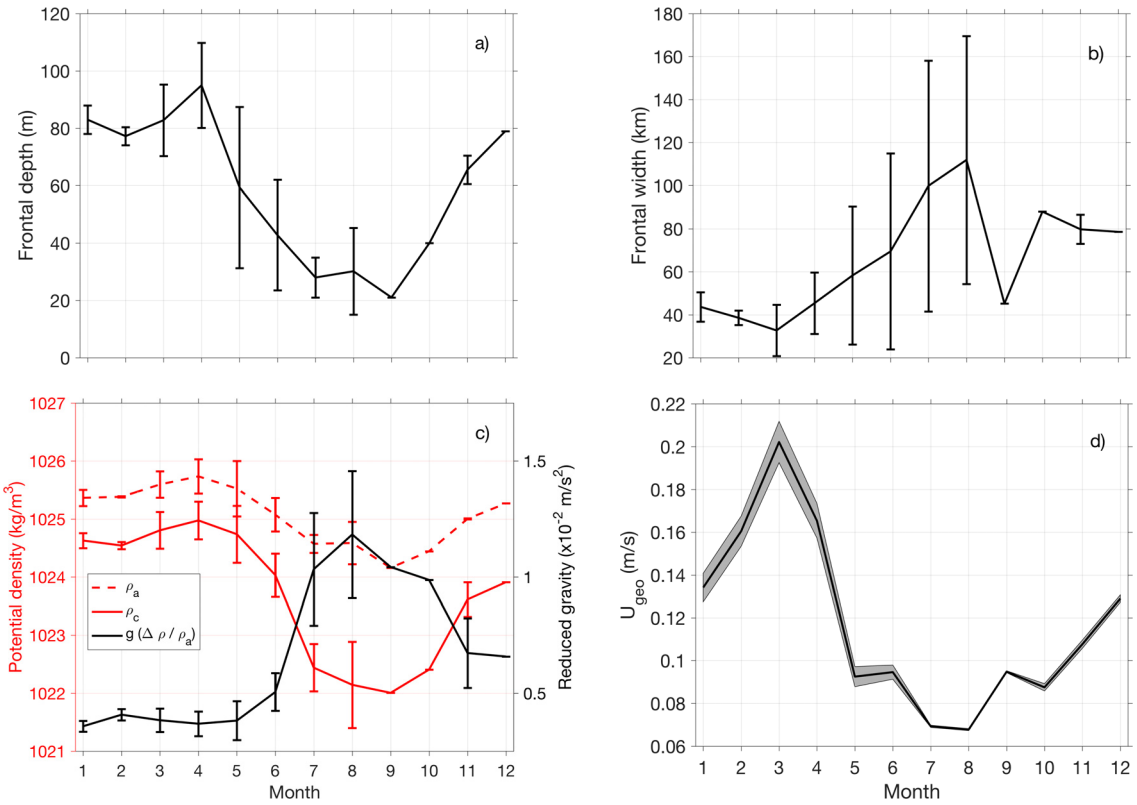


Figure 4.13: Monthly-averaged frontal characteristics extracted from density transects along the Halifax Line using the algorithm described in Section 4.2.3a: (a) the frontal depth (in m), (b) the frontal width (in km), (c) the average potential density within the buoyant plume ($\rho_c$, in kg/m$^3$), the average potential density of ambient shelf water ($\rho_a$, in kg/m$^3$), and the value of the corresponding reduced gravity $g'$ (in m/s$^2$). The error bars showed in these three panels correspond to one standard deviation of the observations. (d) the resulting $U_{geo}$ (in m/s) along with the estimated error (shading; see Appendix C).

by comparing $U_{geo}$ to the corrected $U^c_{geo}$ (Figure 4.14). The magnitude of $U_{geo}$ increases when correcting for wind-driven isopycnal tilting, which can be explained by the fact that monthly-averaged alongshore winds are dominantly upwelling-favorable at the HL. The maximum buoyancy-driven flow does not occur in the winter, but during the fall (Figure 4.14). This new seasonal cycle coincides with the time of year when the reduced gravity is relatively high and the density front starts steepening. The phase shift in the seasonal cycle therefore suggests that correcting for the wind-driven isopycnal tilting seems to increase the role of the density gradient in modulating the alongshore buoyancy-driven flow.

The corrected $U^c_{geo}$ is, in theory, equivalent to the buoyancy-driven flow computed

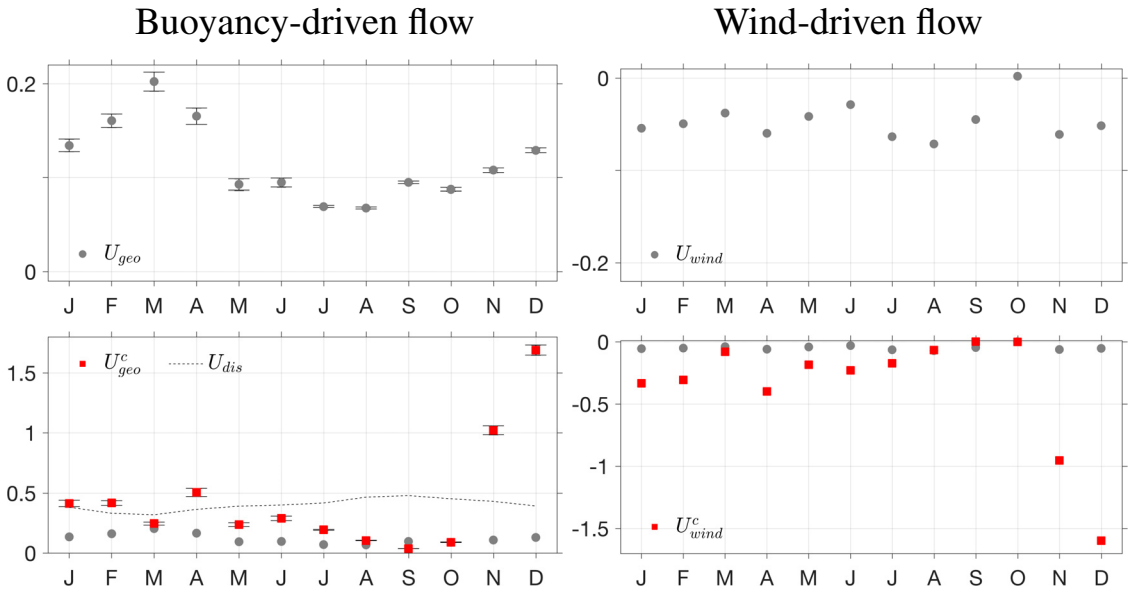


Figure 4.14: Monthly-averaged non-corrected (grey circles) and corrected (red squares) buoyancy-driven flow and wind-driven flow along the HL (in m/s). Positive means southwestward. Error bars indicate measurement errors on the computation of $U_{geo}$ (see Appendix C). The buoyancy-driven flow $U_{dis}$ computed using the traditional approach is superimposed (dashed line, see Equation 4.14).

from the river discharge used in WG05 ($U_{dis}$; using $K = 4$ in Equation 4.15). However, a comparison between the two estimates yields significant differences between them (Figure 4.14). Applying WG05's approach to the NSC fails to reproduce both the amplitude and the phase of the seasonal cycle of $U^c_{geo}$. Additionally, the buoyancy-driven flow derived from the upstream conditions ($U_{dis}$) is overestimated for most of the year, and peaks about 3 months earlier in the year (August-September vs. November-December). This phase difference corresponds to the time lag associated with the downshelf propagation (in terms of alongshore propagation of Kelvin waves) of the pulse of freshwater from Cabot Strait to the HL estimated in Section 4.1.2 and in the literature (*Drinkwater et al.*, 1979; *Smith and Schwing*, 1991). This discrepancy illustrates the previously mentioned shortcomings of using the upstream conditions to determine the buoyancy-driven flow at a location far from the source (i.e., $\mathcal{O}$(100 km)).

### 4.3.3 Isopycnal Tilting and Wind-Driven Flow

As shown in Equation 4.17, $U_{wind}$ is directly proportional to the alongshore wind speed. Analyzing the non-corrected $U_{wind}$ therefore provides information on the alongshore wind speed (Figure 4.14). Figure 4.14 shows that the monthly-averaged alongshore wind stress is mostly upwelling-favorable (i.e., negative or northeastward) at the HL. The monthly-averaged alongshore wind stress exhibits two peaks of similar amplitude throughout the year. The fall and winter maximum is due to strong winds, logically increasing the magnitude of the alongshore component. In summertime, winds tend to be weak but are oriented in a more upwelling-favorable direction, also increasing the alongshore component.

Due to the upwelling-favorable monthly winds, correcting for the isopycnal tilting tends to decrease the amplitude of $U_{wind}$ (i.e., more negative, Figure 4.14). This can be explained by the fact that the decrease in $U_{geo}$ due to shoaling and widening of the front caused by the upwelling-favorable winds is re-attributed to $U_{wind}$. Although the monthly-averaged wind direction provides information on the sign of the correction on $U_{geo}$ (i.e., increase or decrease), no information on the amplitude of this correction can be deduced from the average wind direction and velocity. The amplitude of the correction for the wind-driven isopycnal tilting is contained in the variability of the wind stress at timescales close to the adjustment timescale (Equation 4.20); a larger, rapidly oscillating, wind stress will not drive the same isopycnal tilting as a constant, weaker, wind stress.

### 4.3.4 The Hydrographic Wind Index

Both the sign and the magnitude are important when interpreting the HWI. There are four possible outcomes for HWI:

1. If HWI $> 1$, $U_{wind}$ dominates and is reinforced by $U_{geo}$, as they both have the same direction.

2. If 0 $<$ HWI $<$ 1, $U_{geo}$ dominates and is reinforced by $U_{wind}$, as they both have the same direction.

3. If -1 $<$ HWI $<$ 0, $U_{geo}$ dominates and is slowed down by $U_{wind}$, as they act in opposite directions.

4. If HWI $<$ -1, $U_{wind}$ dominates the current's dynamics and is slowed down by $U_{geo}$, as they act in opposite directions. This situation leads to a flow reversal, which occurs when the coastal current flows "upstream" (i.e., in the opposite direction to shelf wave propagation). Such flow reversals have previously been observed and documented (*Sanders and Garvine*, 2001; *Whitney and Garvine*, 2005, see Section 3.1.2).

The difference between HWI and HWI$^c$ provides information on the impact of wind-driven isopycnal tilting on the alongshore current (Figure 4.15). While the isopycnal tilting correction significantly affects the magnitude of $U_{geo}$ and $U_{wind}$ at the HL, it has a limited effect on the ratio of the two quantities, with the total alongshore flow dominated by the buoyancy-driven component most of the year.

Correcting for the wind-driven isopycnal tilting decreases the HWI in every month except for August and September. The corrected HWI$^c$ has two yearly maxima, indicating times when the buoyancy-driven flow modulates the NSC; the first local maximum is reached in winter, with HWI $= -0.32$ in March, indicating that the buoyancy-driven flow is about 3 times as large as the wind-driven flow. The second local maximum is reached in the fall (HWI $\approx$ 0), showing that the buoyancy-driven flow almost entirely drives the NSC at that time of year. During the rest of the year, the wind-driven component plays a greater role in driving the NSC and at certain times almost balances the buoyancy-driven term, leading to HWI $\approx$ -1.

The alongshore transport $Q$ obtained by summing the buoyancy-driven and wind-driven flows ($Q = (U_{wind} + U_{geo}) \times HL/2$) is compared to the alongshore transport computed

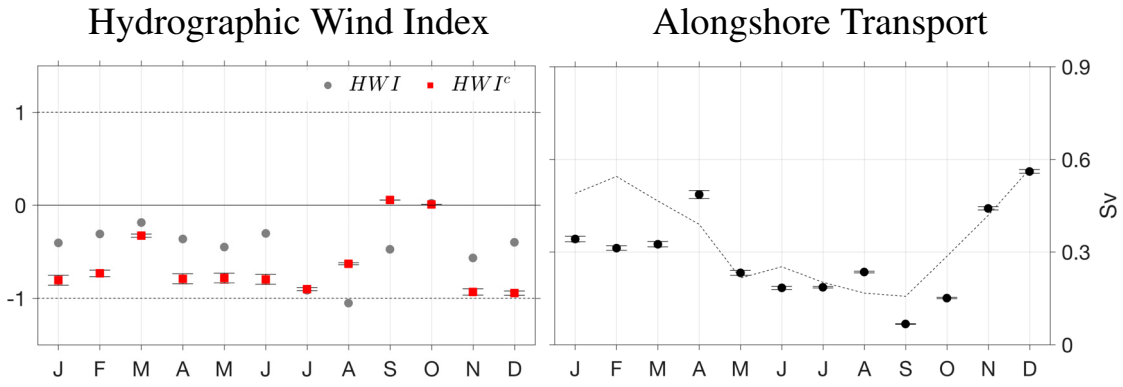


Figure 4.15: Monthly-averaged non-corrected (grey circles) and corrected (red squares) Hydrographic Wind Index along the Halifax Line. The monthly-averaged alongshore transport $Q = (U_{geo} + U_{wind})(HL/2)$ within the buoyant plume (in Sv, black circles) is shown with the transport computed from the three ADCPs (dashed line) (See Figure 3.9 and *Dever et al.*, 2016).

from the velocity records collected at the T-stations (Section 3.2). These two estimates of the alongshore transport are not identical and cover slightly different areas: the former is estimated within the wedge-shaped current, which dimensions vary with time, while the latter is computed between fixed locations (i.e., the T-stations). The two transport estimates nevertheless exhibit a similar seasonal cycle, where both the amplitude and phase are in good agreement. In both time series, the minimum transport is reached in the summer ($\sim$0.20 Sv), while the maximum occurs in winter ($\sim$0.60 Sv). The largest discrepancy between the two estimates occurs in the months of January, February, and March, where the alongshore transport computed between T1 and T3 is consistently larger than the transport deduced from the conceptual model. A possible explanation for this discrepancy is that the front outcrops around station T2 at this time of year (see Figures 3.8 and 4.9). The alongshore transport determined from the wind-driven and buoyancy-driven terms is therefore logically underestimated, compared to the alongshore transport estimated from the ADCPs between T1 and T3. Nevertheless, the generally good agreement between the two estimates confirms the reliability of the Wind Index algorithm, as well as the validity of the key assumptions associated, in capturing most of the alongshore transport's variability.

## 4.4 Summary

This chapter focused on characterizing the NSC, which is one of the dominant circulation features over the Scotian Shelf. The coherency of this buoyancy-driven coastal current was characterized in both the along-shelf and cross-shelf directions, highlighting the connectivity between the St. Lawrence River, the GSL, and the NSC. The HEOFs were also used to study the first two modes of variability of the NSC. It revealed that the NSC's variability can be explained by considering geostrophy, associated with the first mode of variability, and wind forcing, partially associated to the second mode of variability. A conceptual model was then developed to both separate the buoyancy-driven and wind-driven flows within the NSC at the HL, and to study their relative contributions. This approach relied on local conditions (i.e., density transects and winds), as opposed to the traditional approach that relied on upstream conditions only (i.e., river discharge and river density). We demonstrated that the new approach yields better results than the traditional approach while being generally applicable to buoyancy-driven currents. In the next chapter, we explore the spatial variability associated with the HWI and the main driving mechanisms for the NSC over the Scotian Shelf.

# CHAPTER 5

# SPATIAL VARIABILITY OF THE NOVA SCOTIA CURRENT OVER THE SCOTIAN SHELF

In this chapter, we explore the spatial variability associated with the major forcing mechanisms driving the NSC using the approach presented in Chapter 4. Due to the lack of observational datasets with satisfactory spatiotemporal coverage in this region, numerical results produced by a nested-grid ocean circulation modeling system mentioned in Section 2.1.3 are used in the analysis.

The main objective of this chapter is to characterize the spatial variability in the role played by buoyancy and wind forces in driving the NSC over the Scotian Shelf. The Wind Index presented in Chapter 4 is applied to four different transects crossing the Scotian Shelf (Figure 5.1). The density, surface winds, and current velocity fields are extracted along these transects from a numerical simulation covering the 2011-2012 period to estimate the key variables (see Figures 2.4 and 2.5): the buoyancy-driven flow ($U_{geo}$), the wind-driven flow ($U_{wind}$), the HWI, and the total alongshore transport (for information on the numerical model, see Section 2.1 and *Shan et al.*, 2014b).

In Section 5.1, we compare the results obtained at the HL from the numerical simulation and from the observations presented in Chapter 4. Model outputs are then used in Section 5.2 to explore the spatial variability associated with the driving mechanisms of the NSC.

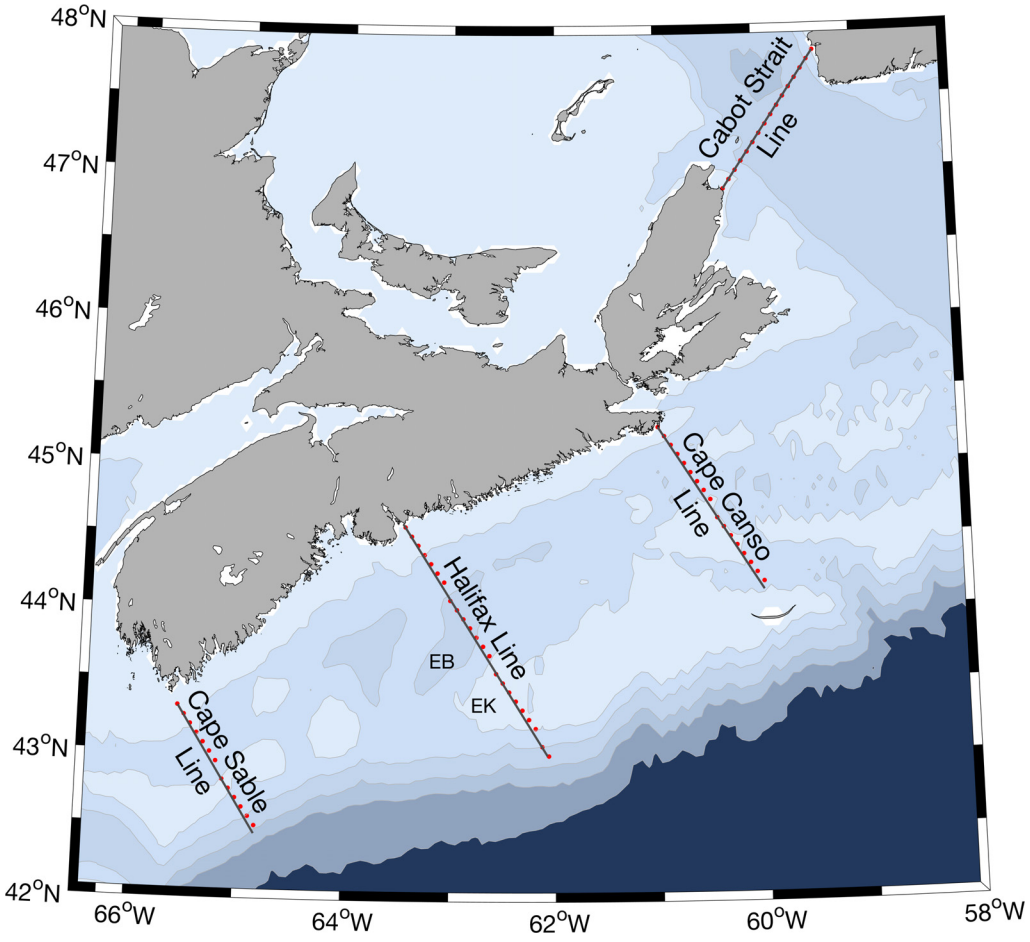


Figure 5.1: Map of the Scotian Shelf showing four transects along which the buoyancy-driven current ($U_{geo}$), the wind-driven current ($U_{wind}$) and the HWI are computed using numerical model results (see Section 2.1). The red dots show the dynamical model grid points used to extract the frontal parameters ($H$, $L$, $\rho_a$, $\rho_c$) necessary for the computation of $U_{geo}$. The shading shows the topography used in the numerical model (isobaths 100, 200, 500, 1000, and 2000 m). Emerald Basin (EB) and Emerald Bank (EK) are also identified.

Insights into the wind-driven isopycnal tilting and coastal detachment mechanisms are also included in this section. A summary is provided in Section 5.3.

## 5.1 Comparison Between Model Results and Observations

The quantities $U_{geo}$, $U_{wind}$, and the HWI were computed at the HL using the dynamical model results and compared to the results obtained using the glider-based observations (Figure 5.2). In this section, we assess if (1) the dynamical model results can reproduce the amplitude and phase of the seasonal cycle in $U_{geo}$ and $U_{wind}$ determined from the glider data, and (2) if the HWI and the estimated alongshore transport determined from the numerical model results match the HWI and alongshore transport estimated from observations. To achieve this, we consider the non-corrected $U_{geo}$ and $U_{wind}$ to remove the layer of complexity added by the wind-driven isopycnal tilting correction (see Chapter 4). The buoyancy-driven flow $U_{geo}$ is determined in the same way as in Chapter 4. The wind-driven flow $U_{wind}$ is based on the same assumptions presented in Section 4.2.2b (i.e., small cross-shelf flow and balance between bottom and surface alongshore wind stress). The model-based $U_{wind}$ is determined from the alongshore surface wind stress used to force the dynamical ocean model. Equation 4.17 can therefore be modified to estimate $U_{wind}$ from the surface wind stress:

$$U_{wind} = \mathrm{sgn}(\tau_{sx})\sqrt{\frac{|\tau_{sx}|}{\rho C_{Da}}} \tag{5.1}$$

where the function $\mathrm{sgn}$ is the signum function, $\rho$ is the average water density, and $C_{Da}$ is the depth-averaged bottom drag coefficient (see Section 4.2.2b). It is worth noting that differences between the model-based and observation-based $U_{wind}$ are due to differences in the reanalysis product used to estimate $U_{wind}$.

The numerical circulation model is capable of reproducing the seasonal cycle in the

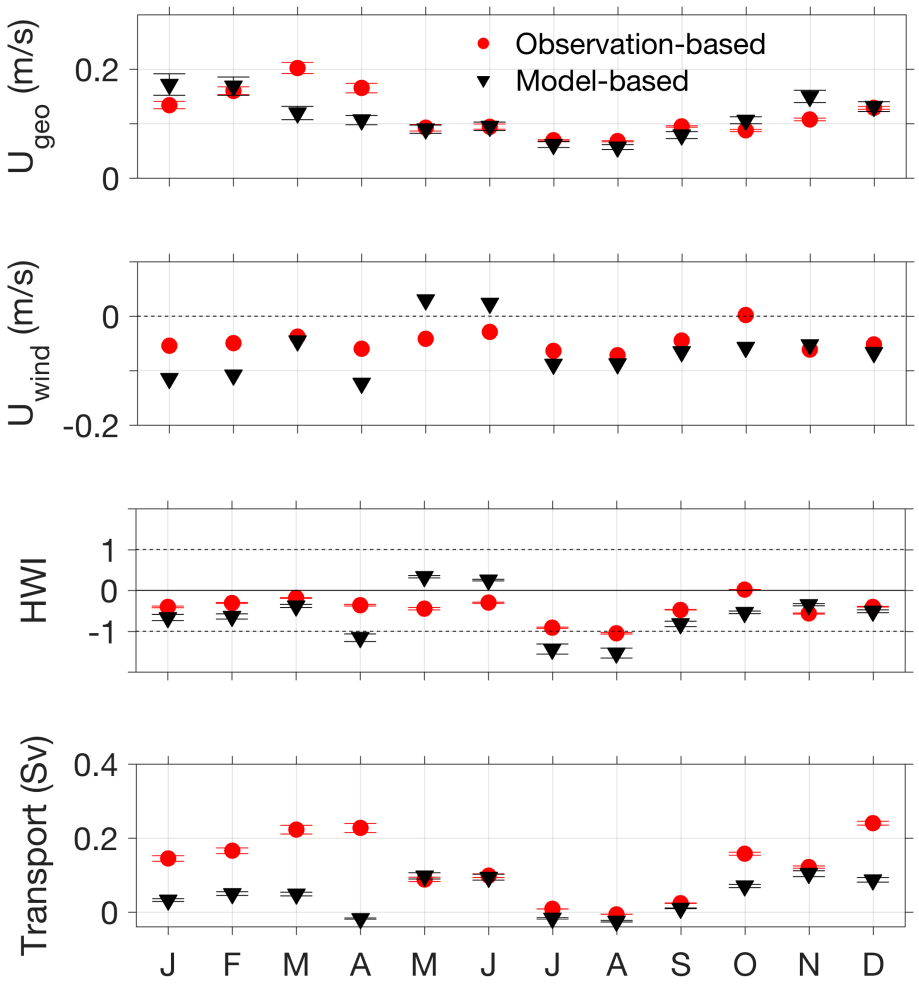


Figure 5.2: Comparison of the buoyancy-driven flow ($U_{geo}$; estimated using Equation 4.12), the wind-driven flow ($U_{wind}$; estimated using Equation 5.1), the HWI, and the alongshore transport estimated from the observations (red circles) and in the dynamical model (black triangles).

buoyancy-driven flow quite accurately, with a maximum in the winter and a minimum in the summer (Figure 5.2). A slight difference in phase can be found between the two data sources for the buoyancy-driven flow: the observation-based buoyancy-driven flow is maximum in March, while the model-based buoyancy-driven flow peaks in January. The wind-driven component of the NSC is also reasonably well-captured in the dynamical model, with a similar order of magnitude between the two time series. The most noticeable difference occurs in the wind direction during the months of May and June. While both time series show weak winds during these two months, winds are upwelling-favorable in the re-analysis product used in combination with the observations, and downwelling-favorable in the forcing used to drive the ocean circulation modeling system. Because the monthly-averaged wind speed is slow in both cases, this difference has little repercussions on the HWI and is not expected to impede our study of the spatial variability over the Scotian Shelf.

The model-based HWI shows similar features as the HWI computed from observations (Figure 5.2), with a buoyancy-driven NSC over the course of the year, except for July and August when the wind-driven flow balances the buoyancy-driven flow, leading to flow reversal events. The southwestward direction of the alongshore winds forcing the dynamical model in May and June is logically reflected in the HWI, with HWI$>0$ in May and June. It can also be seen that the model-based wind-driven flow is larger than the observation-based wind-driven flow, as the absolute magnitude of the model-based HWI is larger than the observation-based HWI. The total alongshore transport is calculated across the wedge shape current using the following equation (see Appendix C for associated measurement error):

$$Q = (U_{geo} + U_{wind})\frac{HL}{2} \tag{5.2}$$

The transport is generally weaker when computed from the dynamical model than using

the observations, particularly in the winter. This discrepancy can be explained by two different factors: firstly, the upwelling-favorable alongshore winds used to force the dynamical model tend to be stronger than the reanalysis product used in combination with the observations, therefore decreasing the southwestward (i.e., positive) alongshore transport. Secondly, the modeled density front is consistently shallower than the observed front, especially in the wintertime (blue and gray lines in Figure 5.3c). This deficiency of the numerical model would affect the estimate of the alongshore transport in two ways: by reducing the cross-sectional area of the NSC, therefore decreasing the alongshore transport estimate, and through Equation 4.12, where a shallower front would result in a decrease in $U_{geo}$, and in turn a decrease in the alongshore transport. The latter feedback is not directly visible in the comparison of $U_{geo}$, as it is compensated by a larger density gradient between coastal and ambient shelf water (blue and gray lines in Figure 5.3b).

Despite these limitations we argue that the dynamical model outputs are useful to study the spatial variability of the mechanisms driving the NSC as the current travels across the Scotian Shelf. It should be noted that not only do the modeled $U_{geo}$ and $U_{wind}$ compare relatively well to their observation-based counterparts, but the total alongshore transport estimated from $U_{geo}$ and $U_{wind}$ is similar to the alongshore transport computed from the simulated velocity field.

## 5.2 Frontal Characteristics and Buoyancy-Driven Flow

To characterize the spatial variability in model-based observations of $U_{geo}$ and $U_{wind}$ over the Scotian Shelf, we consider four transects: the Cabot Strait Line, the Cape Canso Line, the HL, and the Cape Sable Line (Figure 5.1). The Cabot Strait Line is considered to characterize the upstream conditions of the NSC. The three other lines are parallel to the HL ($148^o$ from true north; see Section 2.2) and are separated by approximately 200 km.

We first focus on the spatial variability of the key variables determining $U_{geo}$ in Equation 4.12: the average ambient and coastal densities ($\rho_a$ and $\rho_c$, respectively) used in

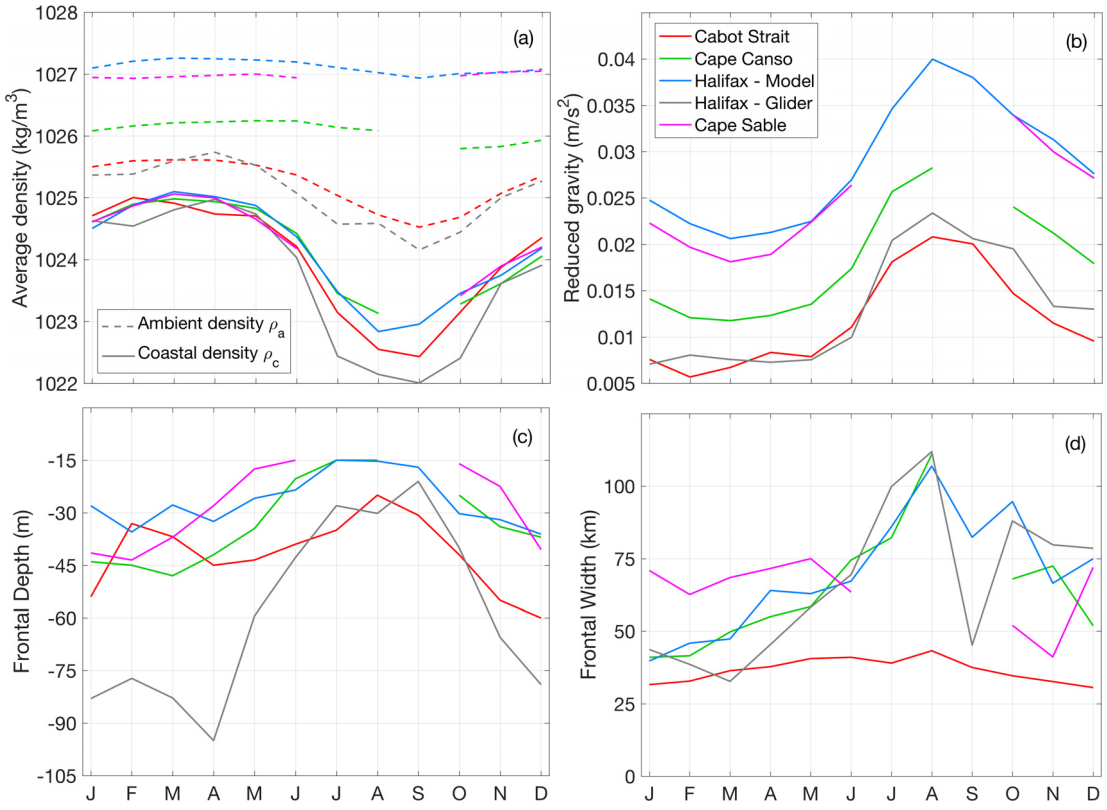


Figure 5.3: Model-calculated seasonal cycle of (a) the average coastal (solid) and ambient (dashed) water density (kg/m$^3$), (b) the reduced gravity (in m/s$^2$), (c) the frontal depth (in m), and (d) the frontal width (in km) at the four lines shown in Figure 5.1: the Cabot Strait Line (red), Cape Canso Line (green), Halifax Line (blue), and Cape Sable Line (magenta). Observations from gliders at the Halifax Line are also shown (gray line).

the calculation of the reduced gravity $g'$, as well as the frontal characteristics ($H$, $L$; Figure 5.3). Figure 5.3 demonstrates that, on the four transects, the coastal density produced by the circulation model follows a very similar seasonal cycle, with water slightly less dense across Cabot Strait from spring to fall. The density of coastal water is very uniform in the alongshore direction over more than 600 km, which provides yet another example of the high degree of coherency of the NSC in the alongshore direction (see Section 4.1). It also supports the hypothesis that coastally-trapped density fronts act as barriers for cross-frontal mixing, and therefore limit exchanges between coastal and ambient shelf waters. This has important implications for our understanding of the distribution of both physical (e.g., freshwater) and biological properties (e.g., fish larvae, nutrients, pollutants) over the

Scotian Shelf. In comparison, the ambient shelf water density differs significantly between the four transects. As the NSC propagates downshelf, the yearly-averaged ambient water density increases, from $\rho_a \approx 1025.2$ kg/m$^3$ at Cabot Strait, to $\rho_a \approx 1026.1$ kg/m$^3$ at Cape Canso, and to $\rho_a \approx 1027.1$ kg/m$^3$ at the HL. The ambient shelf water density then remains relatively constant from the HL to Cape Sable, with only a slight decrease to $\rho_a \approx 1027.0$ kg/m$^3$. This large change in the ambient shelf water density between the Cabot Strait Line and the HL can be explained by the intrusion of dense slope water onto the Scotian Shelf through gullies and channels located at the shelf break (e.g., Sable Gully), or around Emerald Bank, south of Emerald Basin (Figures 1.1 and 5.1; *Han and Loder*, 2003; *Shan et al.*, 2014b; *Rogers*, 2015).

This downshelf increase in the ambient shelf water density is reflected in the reduced gravity term, which is directly proportional to $U_{geo}$ (Equation 4.12 and Figure 5.3). The seasonal cycle of the reduced gravity is in phase at the four transects, with a maximum $g'$ reached in the summer. As the NSC propagates downshelf, the yearly-averaged reduced gravity of the coastal current increases from 0.118 m/s$^2$ at Cabot Strait, to 0.180 m/s$^2$ at Cape Canso, and 0.286 m/s$^2$ at the HL. The reduced gravity is similar at the HL and Cape Sable, and about 0.243 m/s$^2$.

The frontal width and depth at Cabot Strait have a relatively weak seasonal cycle compared to those at other lines located over the Scotian Shelf, although a small flattening of the front (i.e., widening and shoaling) can be seen in the summer. The frontal dimensions at the other three transects exhibit similar seasonal cycles, with a wider ($\sim$ 90 - 120 km) and shallower ($\sim$ 15 m) front in the summer than in the winter, where the frontal depth is at a maximum ($\sim$ 45 m) and the frontal width is at a minimum ($\sim$ 50 km). There are no large differences between the three transects located over the Scotian Shelf, as the month-to-month variability can be relatively large. This is partially due to the limited temporal coverage of the dynamical model outputs (i.e., 2011-2012); a longer time series would certainly provide a smoother seasonal cycle, as is the case in Chapter 4 when

using glider data over the 2011-2014 period. Gaps in the time series at Cape Canso and Cape Sable in the summer correspond to times where the NSC was coastally-detached, meaning that the density front is no longer bottom-trapped (Figure 5.3). Our conceptual model is based on assumptions that are no longer valid once the current detaches from the coast (e.g., current shape, frictionally-adjusted flow, etc.). Transects where the NSC is coastally-detached were therefore left out of the analysis. Coastal detachment and the limitations of our conceptual model in representing this process will be further discussed in Section 5.2.2.

### 5.2.1 Buoyancy-Driven and Wind-Driven Flows

The buoyancy-driven term was calculated from dynamical model results using Equation 4.12 at each transect. The monthly-mean buoyancy-driven flow ($U_{geo}$) at Cabot Strait differ significantly from its counterparts at the other three transect (Figure 5.4). The buoyancy-driven flow at Cabot Strait follows a cyclical seasonal cycle, with a minimum in February ($U_{geo}$ = 0.057 $\pm$ 0.008 m/s) and a maximum in November ($U_{geo}$ = 0.191 $\pm$ 0.027 m/s). The buoyancy-driven flow $U_{geo}$ at Cape Canso is slightly weaker than at Cabot Strait and demonstrates a different seasonal cycle. At Cape Canso, $U_{geo}$ peaks in January ($U_{geo}$ = 0.154 $\pm$ 0.017 m/s) and reaches its minimum in August ($U_{geo}$ = 0.038 $\pm$ 0.003 m/s). At the HL, the seasonal cycle's phase is similar to Cape Canso, with a maximum reached in January and a minimum in August. The amplitude is, however, consistently larger at the HL than at Cape Canso, by 5 to 17%. This is the result of the increase in ambient shelf water density between the Halifax and Cape Canso lines described in the previous section (Figure 5.3). There is a noticeable weakening of the buoyancy-driven flow at Cape Sable, particularly in the winter. The yearly maximum is now in November ($U_{geo}$ = 0.161 $\pm$ 0.019 m/s), and the minimum is in May ($U_{geo}$ = 0.052 $\pm$ 0.004 m/s). While the buoyancy-driven flow is likely further weakened in the summer, our conceptual model does not allow an estimation of $U_{geo}$ at Cape Sable during that time of year, due to a coastally-detached NSC (see Section 5.2.2).

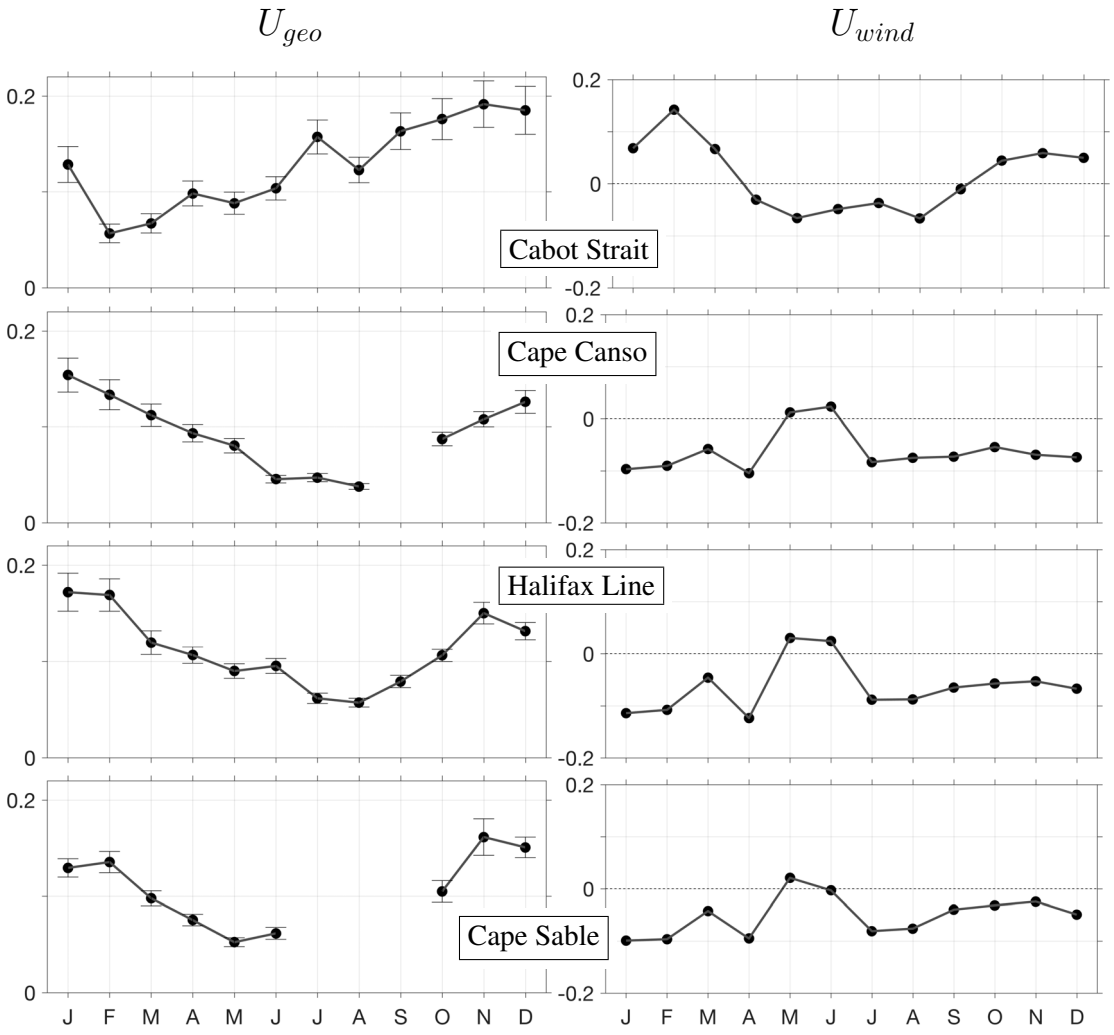


Figure 5.4: Monthly-averaged buoyancy-driven flow (left panels; see Equation 4.12) and wind-driven flow (right panels; see Equation 4.17) at Cabot Strait, Cape Canso, Halifax Line, and Cape Sable over the 2011-2012 period from numerical simulations. Positive means southwestward.

The seasonal cycle in the buoyancy-driven flow produced by the dynamical model at Cabot Strait agrees with the seasonal cycle in freshwater discharge within the GSL. As spring comes, freshwater discharges of the rivers flowing into the GSL increase, leading to a freshening of the coastal water (Figure 5.3). The increasing trend in $U_{geo}$ at Cabot Strait through the summer and fall is likely due to the effect of a large freshwater input from the St. Lawrence River. The freshwater pulse associated with the St. Lawrence River, which is the dominant source of freshwater in this region, is expected to reach Cabot Strait in the fall (*Sutcliffe et al.*, 1976; *El-Sabh*, 1977). The downshelf propagation of this pulse, however, is not clearly visible in the buoyancy-driven component of the flow. The expected lag due to the downstream propagation of freshwater runoff between Cape Canso and the HL, as well as between the HL and Cape Sable, is approximately one month. This estimation is based on the distance separating the two transects (i.e., $\sim$ 200 km) and the propagation speed estimated in Chapter 4 (i.e., $\sim$ 5.5 km/day). This expected one-month lag, however, does not occur in the time series shown in Figure 5.3, which is mostly due to large month-to-month variability in $U_{geo}$ at these two transects. Nevertheless, a lag in the maximum geostrophic flow can be found when comparing the upstream and downstream conditions; while $U_{geo}$ peaks in November at Cabot Strait, it reaches a local maximum in February at Cape Sable, therefore yielding the expected 3-month lag between the two transects. This lag is not visible in the yearly minimum geostrophic flow occurring in the summer for all locations over the Scotian Shelf. This in-phase minimum is related to the local net heat flux; during the summer, the upper water column warms due to a downward net heat flux at the sea surface (see Figure 3.3). The density field becomes temperature-driven in the summer, as opposed to salinity-driven during the rest of the year. The upper-water column therefore stratifies in the summer and the water density becomes more uniform across the Shelf. This stratification occurring in the summer flattens the isopycnals and thus corresponds to a weakening of the NSC. The net surface heat flux is, therefore, responsible for skewing the seasonal minimum towards the summer, suppressing

the expected downshelf propagation of the signal minimum.

The important information to be extracted from the wind-driven component of the flow is the change of direction with seasons. This is especially important at Cabot Strait, where alongshore winds are downwelling-favorable (i.e., positive) from October through March, and upwelling-favorable (i.e., negative) for the rest of the year. Downwelling winds tend to be stronger ($U_{wind} = 0.14$ m/s in February) than upwelling-favorable winds ($U_{wind}$ = -0.07 m/s in May and August). The alongshore winds at the three other transects on the Scotian Shelf are noticeably similar. The seasonal cycle is characterized by upwelling-favorable winds throughout the year, with the exception of May and June, when winds are weakly downwelling-favorable ($U_{wind} \approx 0.02$ m/s). The two yearly upwelling-favorable maxima discussed in Section 4.3.3 are also visible, with a winter peak at approximately -0.10 m/s, and a summer peak around -0.08 m/s. The large discrepancy observed between Cabot Strait and the other three lines located over the Scotian Shelf is due to the changing coastal orientation, affecting the alongshore component of the wind (see Figure 5.1).

The HWI and total alongshore transport estimated from dynamical model results are shown in Figure 5.5. At Cabot Strait, the NSC is mostly buoyancy-driven from March to January, with the absolute value of the HWI to be less than 1. The minimum absolute magnitude in the HWI is in September, where the total current is almost exclusively driven by the buoyancy-driven flow (|HWI| = 0.06 $\pm$ 0.01). $U_{geo}$ dominates from April to January of the next year, where the wind-driven flow is responsible for at most 25% of the total flow. However, the NSC seems to be mostly driven by the downwelling-favorable winds in February (HWI = +2.52 $\pm$ 0.35). In March, the wind and buoyancy components have similar magnitudes, leading to HWI $\approx$ 1. The total alongshore transport at Cabot Strait peaks in November and December (0.279 $\pm$ 0.039 Sv) and is at a minimum in May (0.023 $\pm$ 0.002 Sv). The period where the alongshore transport is weakest (i.e., from May to August) corresponds to the time where the HWI is negative. This indicates that $U_{wind}$ is in the opposite direction as $U_{geo}$, logically slowing the NSC down.

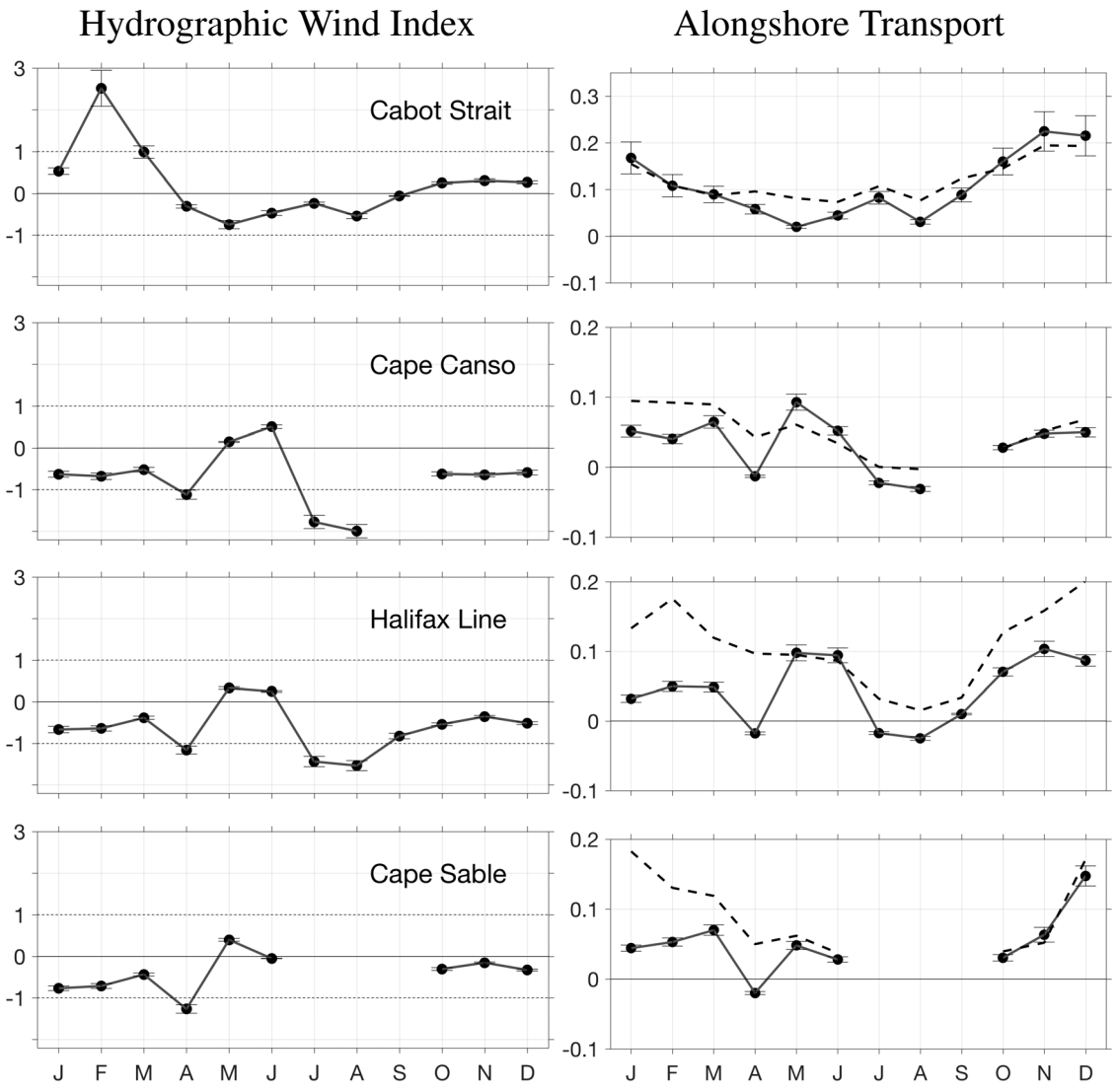


Figure 5.5: Monthly-averaged HWI (left panels) and alongshore transport (in Sv; right panels) at Cabot Strait, Cape Canso, HL, and Cape Sable over the 2011-2012 period from numerical simulations. Alongshore transport computed from the simulated velocity field is superimposed for comparison (dashed lines).

The seasonal cycle in the HWI is noticeably similar at three transects on the Scotian Shelf (Figure 5.5). This is due to similarities of both the buoyancy-driven and wind-driven flows at these three transects (Figure 5.4). From October to March, the HWI varies between -1 and 0 at these three transects on the Scotian Shelf, demonstrating that $U_{geo}$ dominates over $U_{wind}$ during this period. Wind and buoyancy forces tend to act in opposite directions over the Scotian Shelf (HWI $<$0). This partly explains why the alongshore transport is generally weaker at locations over the Scotian Shelf compared to Cabot Strait. This weakening alongshore transport can also be explained by the separation of the NSC into two branches near SAB; while one branch veers southwest to follow the Nova Scotian coastline, a portion of the alongshore current flows southeastward along the slope of the Laurentian Channel (see Figure 1.1; *Ohashi and Sheng*, 2013; *Urrego-Blanco and Sheng*, 2014).

The change in direction of the alongshore winds in May and June over the Scotian Shelf is reflected in the HWI (Figures 5.4 and 5.5). While the NSC remains dominated by the buoyancy-driven term, the current is intensified by the downwelling-favorable winds generating a positive $U_{wind}$. Although the wind contribution is small when southwestward (2 to 4 times smaller than $U_{geo}$), it leads to a larger alongshelf transport at that time of year than during the rest of the year (Figure 5.5). Conversely, upwelling-favorable winds generate an upstream current exceeding the downstream buoyancy-driven flow in April along the three transects crossing the Scotian Shelf (HWI$<$-1). This logically leads to a negative alongshore transport at that time (Figure 5.5).

The alongshore transport obtained by summing the buoyancy-driven and wind-driven flows based on observations (Equation 5.2) is directly compared to the model-based alongshore transport computed from the simulated velocity field within the NSC (Figure 5.5). The comparison of these two estimates allows an assessment of the reliability of the Wind Index approach in resolving the alongshore current. The good agreement between these two estimates is once again a clear indication that the assumptions on which the

Wind Index is developed are suitable for this current system. At all four transects, the phase of the alongshore transport is properly captured by the model-based Wind Index approach, with a minimum transport in spring and summer. The seasonal cycle of the alongshore transport estimated from the Wind Index approach compares very well to the alongshore transport computed from the simulated velocity field across Cabot Strait ($r$ = 0.97). The correlation coefficients between the two transport estimates at the Cape Canso Line ($r$ = 0.73), HL ($r$ = 0.66), and Cape Sable Line ($r$ = 0.61) illustrate the relatively good agreement between these two time series. A discrepancy can however be consistently observed across these last three locations; the transport calculated from the Wind Index method underestimates the alongshore transport in the wintertime. This result is consistent with what was discussed in Section 4.3.4 when comparing alongshore transport estimates from the HWI and computed using the ADCPs at the T-stations. The alongshore transport calculated from Equation 5.2 also suggest the presence of flow reversals in July and August at the Cape Canso line and HL, that is not represented in the transport computed directly from the simulated velocity field.

The change in coastal orientation from the Cabot Strait Line (+50$^o$) to the Cape Canso Line (+148$^o$) generates the largest spatial variability in the NSC's dynamics. The uniformity of the conditions over the Scotian Shelf demonstrates that the distance from the buoyant source of freshwater does not introduce significant spatial variability in the NSC's driving mechanisms. Despite that, a lag can be observed in $U_{geo}$'s maximum as the freshwater pulse from the GSL travels southwestward. This constancy in the dynamics over the Scotian Shelf is more evidence of the alongshore coherency of the NSC over large distances ($\mathcal{O}$(100 km)).

### 5.2.2 Wind-Driven Isopycnal Tilting and Coastal Detachment

A comparison between $U^c_{geo}$ and $U_{geo}$ provides insights into the importance of the interaction between the density front and the alongshore winds in driving the NSC (Figure 5.6). At Cabot Strait, this correction leads to a decrease in the amplitude of the buoyancy-driven

component. Because the total flow ($U_{geo} + U_{wind}$) must remain unchanged, any decrease in the amplitude of $U_{geo}$ due to the isopycnal tilting correction is compensated by an intensification of the wind-driven flow $U_{wind}$, and vice versa. This weakening in $U_{geo}$ at Cabot Strait is therefore reflected in the corrected HWI$^c$. The largest difference can be seen in January, where the role of alongshore winds is amplified (HWI$^c = 4.10 \pm 0.56$). This is due to the downwelling-favorable winds in the winter that steepen the density front (Figures 5.3 and 5.4).

At Cape Canso, $U^c_{geo}$ is consistently larger than $U_{geo}$ (Figure 5.6). This is due to the dominant upwelling-favorable winds along the Scotian Shelf. These winds tend to flatten the density front, leading to an underestimation of the geostrophic flow that would occur in the case of no wind. The smallest correction is seen in the summertime; this can be explained by the already flat density front in this season, due to the local net surface heat flux stratifying the upper water column. Because of the constraint imposed on the maximum surface spreading of the density front included in the conceptual model, the correction for wind-driven isopycnal tilting in summer is weak. This is because the frontal width is already close to the maximum width allowed in the conceptual model. HWI$^c$ at Cape Canso shows that the wind and buoyancy forces act in opposite directions and contribute almost equally to the NSC. With a magnitude consistently above -1 from October through June (between -0.6 and -0.9), HWI$^c$ shows that the buoyancy-driven flow remains the dominant driving mechanism most of the year. In July and August, HWI$^c$ has the same characteristics as HWI, where the alongshore flow is dominated by the wind-driven circulation and is directed northeastward.

The model-based wind-driven isopycnal tilting correction at the HL estimated from the dynamical model results is similar to its counterpart at the Cape Canso Line. Again, the winds are dominantly upwelling-favorable and therefore tend to flatten the density front, resulting in a larger $U^c_{geo}$ than $U_{geo}$. Similar to Cape Canso, the correction is weakest in the summer due to the already wide and shallow density front, preventing any further

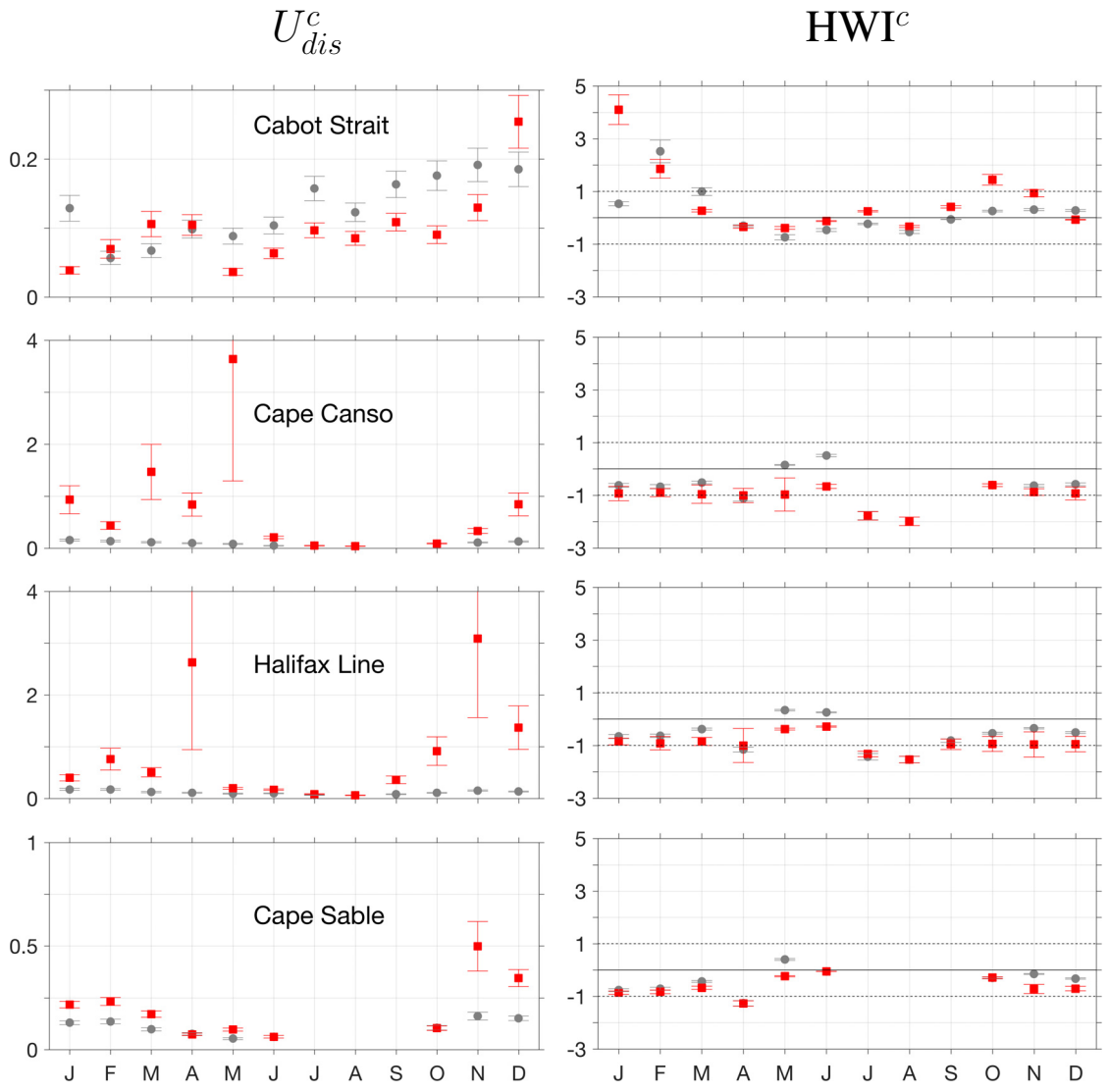


Figure 5.6: Monthly-averaged buoyancy-driven current (left panels) and HWI (right panel) before (gray dots) and after (red squares) correcting for the wind-driven isopycnal tilting. Both variables are estimated from numerical simulations of the oceanographic conditions over the 2011-2012 period at the Cabot Strait Line, the Cape Canso Line, the HL, and the Cape Sable Line.

wind-driven flattening. The resulting HWI$^c$ at the HL is also similar to the one estimated at Cape Canso. As expected, the NSC remains mostly buoyancy-driven, excluding the months of July and August where the northeastward wind-driven flow exceeds the southwestward buoyancy-driven current.

The impact of the wind-driven isopycnal tilting correction is different at the Cape Sable Line than at the Cape Canso Line or the HL. While the correction is once again larger in fall and winter than in summer, the amplitude of the correction is considerably smaller at Cape Sable than at the other locations. This can be explained by the narrowing of the Scotian Shelf at Cape Sable ($\sim$ 120 km), where the continental shelf is almost half as wide as along the HL or the Cape Sable Line. The constraint imposed on the maximum surface spreading of the density front in our conceptual model therefore limits the impact of the wind-driven isopycnal tilting on the estimation of $U_{geo}$.

This constraint was included in the HWI conceptual model to avoid an unrealistic offshore spreading of the density front at the HL (Chapter 4). However, extending the analysis to the entire Scotian Shelf demonstrated that this constraint constitutes a weakness of the conceptual model; while it provides bounds for the wind-driven isopycnal tilting, it also prevents the conceptual model from resolving the coastal detachment of the buoyancy-driven coastal current. Such coastal detachments are observed along both the Cape Canso and Cape Sable Lines in the summer (Figure 5.7). Using a conceptual model, *Fong and Geyer* (2001) discussed the conditions under which sustained upwelling-favorable winds can generate the detachment of a buoyancy-driven coastal current. The coastal current therefore becomes surface advected, as opposed to bottom-trapped. In this situation, the assumptions on which our conceptual model was developed are no longer valid, making the estimation of $U_{geo}$ and $U_{wind}$ impossible.

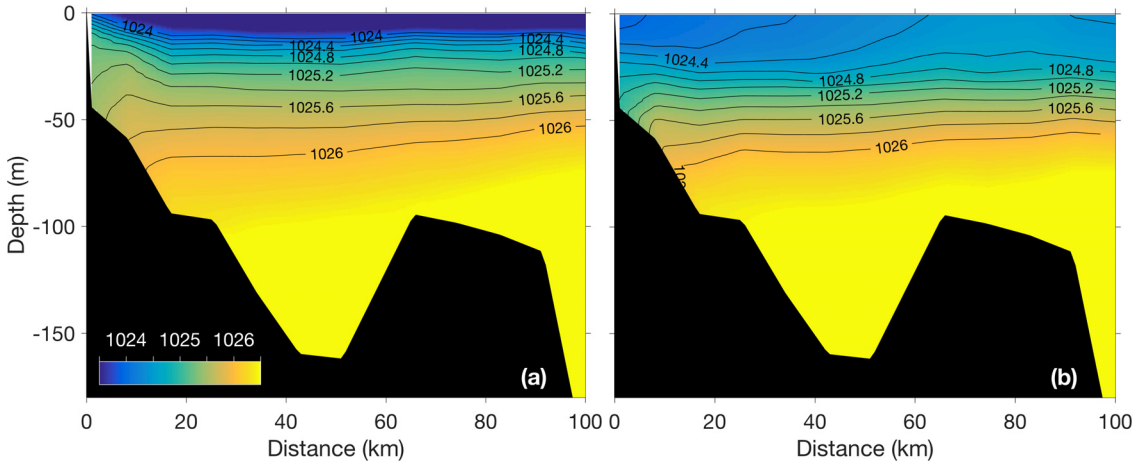


Figure 5.7: Density transect at Cape Sable extracted from the numerical model in (a) July 2012 and (b) December 2012 (in kg/m$^3$). The coastal detachment of the current is visible in (a), where isopycnal are tilted upwards near the coast.

## 5.3 Summary

In this chapter, we took advantage of the spatial dependency of the newly-defined HWI to apply the analysis to four different locations over the Scotian Shelf using a dynamical ocean model. It revealed that some key characteristics of the NSC can significantly vary as it propagates downshelf; for example, the density difference between coastal and ambient shelf water that contributes to the buoyancy-driven component of the flow varies by a factor of 2. This further supports the argument that using local observations to analyze the NSC is more suitable than relying on upstream conditions. This chapter demonstrated the effects of a change in coastal orientation on the driving mechanisms of the NSC. Due to the small variability in alongshore winds over the Scotian Shelf, small spatial variability occurs in the processes driving the NSC once it has veered southwestward over SAB. Correcting for the wind-driven isopycnal tilting revealed the importance of the interaction between the density front arising from the input of buoyant water, and the local winds modulating the frontal shape. Finally, the coastal detachment of the NSC simulated by the dynamical model drew attention to the limitations of the conceptual model used to describe the wind-driven isopycnal tilting, providing interesting prospects for future work.

# CHAPTER 6

# CASE STUDY: LINKAGES BETWEEN COASTAL CONDITIONS AND MIGRATION OF ATLANTIC SALMON POSTSMOLTS OVER THE SCOTIAN SHELF

In this chapter, we combine acoustic detections of Atlantic salmon postsmolts with oceanographic conditions to characterize the seascape through which these fish migrate. The main objectives of this chapter are: (1) to describe the spatial and temporal detection patterns of the salmon postsmolts along the HL, (2) to investigate cross-shelf movements during the migration, and (3) to examine the effects of marine physical environmental conditions on migratory behavior of salmon postsmolts, including estimating the migration heading.

The oceanographic datasets to be used in this chapter have been introduced in previous chapters. Section 6.1 describes the acoustic dataset used for this study specifically. Section 6.2 characterizes the distribution in space and time of the Atlantic salmon postsmolts along the HL, as well as cross-shelf movements and migratory behavior. These patterns are linked to oceanographic conditions using temperature, salinity and current velocity. In Section 6.3, the results are discussed and put in perspective with the existing literature. Section 6.4 summarizes the main conclusions of this chapter.

## 6.1 Methods

### 6.1.1 Tagging and Release of Smolts

During the 2008-2014 period, 2,671 Atlantic salmon smolts were surgically tagged with Vemco V9 transmitters (as described in *Kocik et al.*, 2009 and *Holbrook et al.*, 2011) and released in the Penobscot River (Figure 6.1). Tagging was made from April to May for both female and male smolts (undetermined), as well as both wild and hatchery fish. The primary objectives for these tagging and release were to assess in-river management questions such as dam impacts (*Holbrook et al.*, 2011; *Stich et al.*, 2014) and estuary survival, path choice, and behavior (*Stich et al.*, 2015). Smolts were released at various points in the Penobscot river, with some passing as many as six dams, while others had no dams obstructing their seaward migration. The transmitters were programmed to transmit at random intervals between 20 and 40 s for the first 35 days and between 60 and 80 s afterwards (to preserve battery life and increase the probability of detecting the transmitter over longer periods).

### 6.1.2 Receiver Network

The array of receivers at the HL (referred to as the OTN-HL) included up to 256 acoustic receivers, deployed about 800 m apart over the 2008-2014 period (Table 6.1; Figure 6.1). Each station within the OTN-HL was equipped with a bottom-mounted Vemco VR3 or VR4 acoustic receiver depending on the station. To minimize interactions with local commercial fisheries, the OTN-HL changed direction at stations HFX073 and HFX164, and can therefore be separated into three sections:

1. Inner Section; which is defined between stations HFX001 and HFX073, covering 60 km at an angle of $141^o$ from True North, with a depth ranging between 45 and 200 m.

2. Middle Section; which is defined between stations HFX074 and HFX164, covering

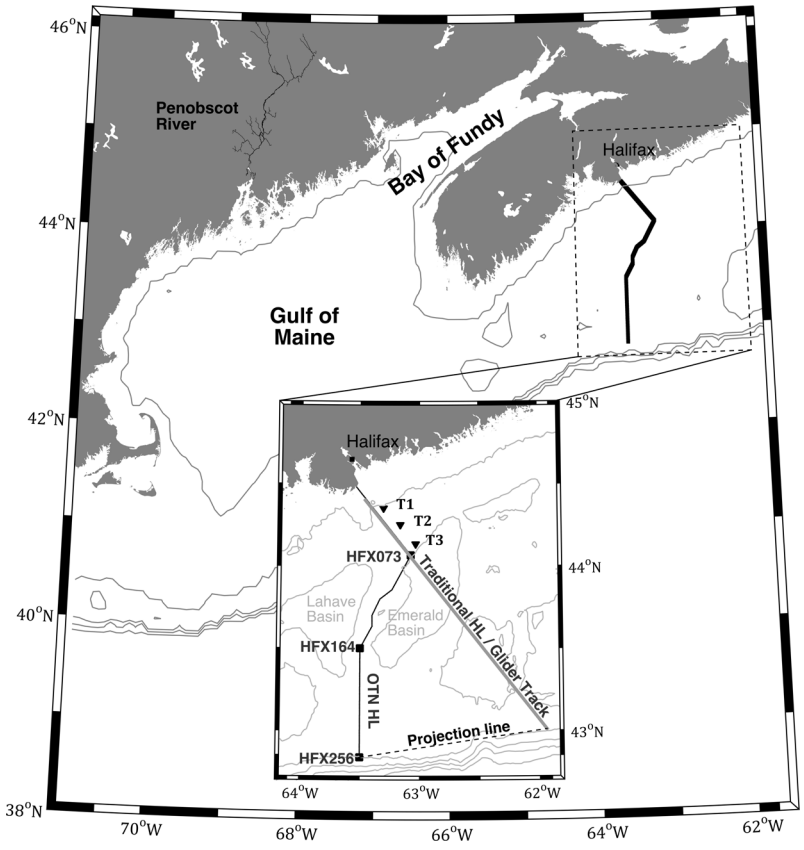


Figure 6.1: Map of the region connecting the Penobscot River System to the Halifax Line on the Scotian Shelf. Inset shows the traditional Halifax Line, which corresponds to the average glider track, the OTN-HL defined by the 256 receivers (black dots) with the station numbers where the OTN-HL changes direction (black squares), as well as the projection line used for the spatial analysis (see Section 6.1). The locations of three ADCP stations (T1, T2 and T3) are marked by black triangles. Bathymetric contours are shown for the 100, 500, 750, and 1000 m isobaths (for inset - the 100, 200, 500, 750, and 1000 m).

72 km at an angle of 208$^o$ from True North, with a depth ranging between 95 and 210 m.

3. Outer Section; which is defined between stations HFX165 and HFX256, covering 73 km at an angle of 180$^o$ from True North, with a depth ranging between 140 and 190 m.

The OTN-HL array was installed incrementally over several years. From 2008 to 2010, only the shoreward half of the Inner Section was deployed (up to HFX028). In 2011, the

Table 6.1: Number of Atlantic salmon smolts tagged and released in the Penobscot River, and detected at the OTN-HL over the 2008-2014 period.

| | Year | | | | | | |
|---|---|---|---|---|---|---|---|
| | 2008 | 2009 | 2010 | 2011 | 2012 | 2013 | 2014 |
| Smolts released | 157 | 420 | 593 | 597 | 359 | 313 | 232 |
| Individuals detected | 24 | 29 | 20 | 72 | 64 | 70 | 60 |
| Detection sequences | 26 | 29 | 20 | 88 | 124 | 113 | 72 |
| OTN-HL receivers | 28 | 29 | 38 | 72 | 256 | 256 | 256 |

remainder of the Inner Section was deployed (up to HFX073), and the entire line was completed in May 2012 (up to HFX256; Table 6.1). Detection data were acoustically downloaded from the receivers. If a receiver was unresponsive, the acoustic release was triggered, the receiver was recovered and replaced. In those cases, the data were then downloaded directly from the receiver once on land. Receivers were conservatively assumed to have failed immediately after the last logged detection. Less than 4% of the stations had failed at any given time, with no adjacent stations failing simultaneously. Station failures, therefore, were assumed to have negligible effects on observed detection patterns.

### 6.1.3 Transmitter Detections

Of the 2,671 smolts released for the Penobscot River studies, 339 fish were detected as postsmolts at the OTN-HL. These postsmolts are the study population in our analysis. For V9 transmitters, the detection range is reported to be about 900 m in calm oceanographic conditions but can be affected by variables that increase the level of ambient noise (*Kessel et al.*, 2014), such as environmental factors (e.g., rain, wind, wave action, currents, hydrography), anthropogenic factors (e.g., boats and sonars), and biological factors (e.g., biofouling). However, under optimal conditions a single tag could theoretically be detected

at two receivers simultaneously.

For this reason, individual detections were pooled into "sequences" to characterize distinct encounters as opposed to treating each detection independently (*Furey et al.*, 2015). Detection sequences were defined as a set of detections of a unique transmitter that occurred within one hour and were not separated by more than two receivers along the OTN-HL. For each detection sequence, the location and time stamp associated with the first detection was used to define the arrival of the fish.

### 6.1.4 Oceanographic Variables

Temperature, salinity, current strength, and current direction were measured from a variety of instruments along the HL over the 2008-2014 period. These field data were combined to better characterize the seascape during the ocean migration phase of Atlantic salmon postsmolts.

The oceanographic datasets used in this chapter were described in Chapter 2:

1. Currents records measured continuously from April 2008 to October 2014 at stations T1, T2 and T3, with some data gaps (10 to 15%) due to either instrument failures or deployment delays. As a reminder, observed currents were rotated clockwise by an angle of $148^o$ from True North to obtain the alongshore and cross-shore directions (see Section 2.2). The stations T1, T2 and T3 correspond to the stations HFX028, HFX048, and HFX069 on the OTN-HL line, respectively.

2. Gridded temperature, salinity and current velocity, based on measurements made by underwater gliders along the HL over the 2011-2014 period (see Section 2.2.3).

To directly compare hydrographic data collected by the gliders along the Traditional HL (Figure 6.1) to acoustic detections as a function of distance from shore, the Traditional HL was projected onto the OTN-HL occupied by acoustic receivers so that HFX256 coincides with the offshore end of the traditional HL at a similar depth (see Figure 6.1). Because

of this projection, and for simplicity, the acronym HL will be used hereinafter to denote the OTN-HL. The distance from shore is calculated for both datasets based on a reference point located on Sambro Head (63.534$^o$W, 44.482$^o$N).

### 6.1.5 Analysis of Arrival Timing at the HL

To analyze the temporal variability of the transmitters' first detections, a seven-day moving average was calculated and a Gaussian distribution fitted to the smoothed temporal distribution based on:

$$D_m = a \times exp\left(-\left(\frac{t-\mu}{2\sigma}\right)^2\right) \tag{6.1}$$

where $D_m$ is the modeled detection percentage, $t$ is the detection date and $a$, $\mu$ and $\sigma$ are the regression coefficients and represent the amplitude, mean and standard deviation of the Gaussian distribution, respectively.

### 6.1.6 Analysis of Spatial Patterns of Detection and Environmental Factors

Because the network of receivers along the HL was not complete until the 2012 salmon migration period, only data during the years 2012-2014 are used to analyze the spatial variability of the detections. The average distribution of detection sequences along the HL was calculated based on the 309 detection sequences logged over the years 2012-2014.

To quantify the relationship between the spatial detection patterns and oceanographic variables, a multiple regression analysis was applied to the detection count. Observations made in the top 20 m of the water column were averaged to obtain the vertically mean temperature, salinity, and alongshore currents in the surface layer. The variables were then normalized by subtracting the average for all years and scaling by the standard deviation. The linear regression model can be written as:

$$D_{m,i} = \beta_o + \beta_1 \bar{T}_i + \beta_2 \bar{S}_i + \beta_3 \bar{U}_i \tag{6.2}$$

where $D_{m,i}$ is again the detection percentage (predictand), and $\bar{T}_i$, $\bar{S}_i$, and $\bar{U}_i$ are the

normalized average temperature, salinity and alongshore flow anomalies (predictors), over the top 20 m for each observed detection sequence $i$. A t-test was applied to provide information on the level of confidence that a coefficient is different than zero (i.e., the null hypothesis). The p-value was also computed, which provides an estimate of the smallest value at which the null hypothesis can be rejected for the corresponding coefficient.

The multiple regression analysis discussed above has strengths and limitations. Firstly, oceanographic variables alone cannot be expected to explain all the observed spatial variability in the acoustic detections. Other parameters such as fish size (*Handeland et al.*, 2008), the chemical signal of water masses (*Døving and Stabell*, 2003), and navigation and orientation of marine species (*Burke et al.*, 2014; *Byron and Burke*, 2014) are likely to play a role in the fish migratory behavior. Secondly, glider-based measurements were not necessarily concurrent to the acoustic detection data. The regression model presented in Equation 6.2 only investigates statistically the linear relation between the detection patterns and the physical environmental conditions. Furthermore, the temporal variability of the predictors over the duration of a transect is assumed to be smaller than their spatial variability across the Shelf, compensating for the time difference between glider and detection observations. Finally, the regression model assumes that the predictors are independent. This assumption is not true in general since temperature and salinity are strongly correlated on the Scotian Shelf, with the presence of coastal water both colder and fresher than ambient shelf water (*Loder et al.*, 1997; *Dever et al.*, 2016). However, we treat temperature and salinity variables independently in the regression model because these two variables are less correlated in the upper water column during spring and summer when the temperature field is primarily driven by the net heat flux at the ocean surface (*Umoh and Thompson*, 1994). Because Atlantic salmon postsmolts are detected in spring in the upper water column, temperature and salinity can be considered as two independent variables. The sign and relative amplitude of $\beta_i$, as well as the error associated with the coefficients, provide insights into the environmental preferences of Atlantic salmon postsmolts.

### 6.1.7 Migratory Behavior and Cross-shelf Movements

Detection sequences of salmon postsmolts were considered individually to investigate their migratory behavior when crossing the HL. Assuming that the first and last detections of each detection sequence correspond respectively to the arrival and departure of individual fish, estimates of the time spent, the ground covered, and the net cross-shelf movements of the animals along the HL can be evaluated. It is important to note that the estimations of distances covered by salmon postsmolts are only approximate since tagged fish could be located anywhere within the receiver's detection radius, which is approximately 450 m but varies in time and space (*Kessel et al.*, 2014). To illustrate, a fish detected at two adjacent stations could have covered any distances from 900 m to only a few meters, by simply switching from one detection sphere to another between individual detections. Nevertheless, the results provided valuable insights into fish behavior.

A Sinuosity Index (SI) was also developed to evaluate whether a marine animal swims back-and-forth between two receivers, or demonstrates a more substantive cross-line movement. In this study, the SI is defined as the net difference in the station number between the first and last detections (i.e., "net station change") divided by the total number of station changes:

$$\text{SI} = \frac{\text{net station change}}{\text{total number of station changes}} \tag{6.3}$$

SI is therefore only defined for detection events covering more than a single station (total number of station changes $> 0$), and can be interpreted as follows (See Figure 6.2):

1. SI = 0; the fish left the HL at the same location it was first detected, therefore exhibiting no net cross-line movement

2. SI $< 1$; the fish principally zigzagged, with some small cross-shelf movement

3. SI = 1; the fish completed a cross-shelf movement along the HL and has been detected consecutively at each station along the way

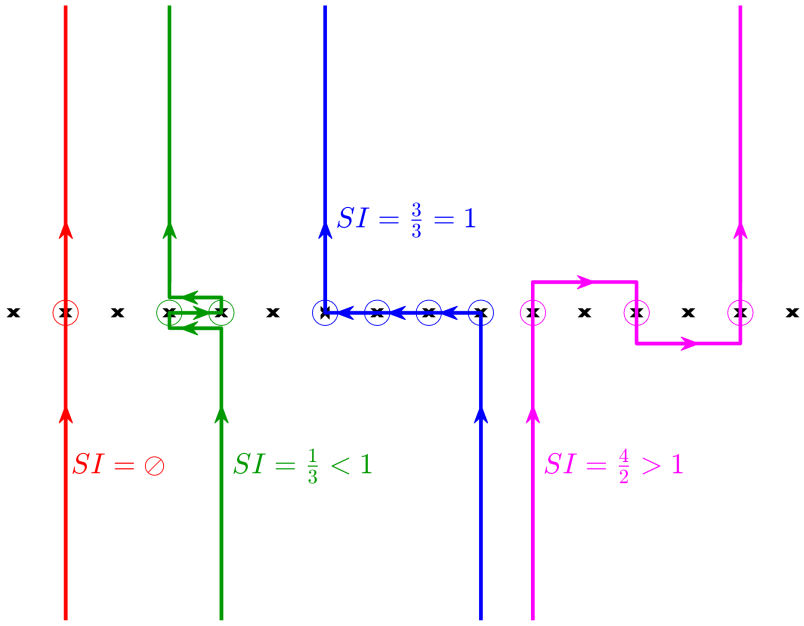


Figure 6.2: Schematic of the possible scenarios for the Sinuosity Index (SI; see Equation 6.3), depending on the migratory behavior of the fish. The acoustic receivers array is represented by the black crosses. Stations where the fish was detected are marked by a colored circle.

4. SI $> 1$; the fish completed a significant cross-shelf movement away from the HL, and has therefore not been consecutively detected along the array

The averaged direction of the total cross-shelf currents measured in the top 20 m of the water column at the three T-stations was compared to the observed cross-shelf movement of the fish over the Inner Section. This analysis aims at assessing a possible correlation between the along-line movements recorded for fish detected over the Inner Section, and the directionality of the flow. The hypothesis that postsmolts swim in the same direction as local currents is tested over a range of current speeds to ensure that the relationship between swimming and current direction does not depend on the current speed considered. This hypothesis was only tested over the Inner Section, due to the lack of total currents measurements over the Middle and Outer Sections.

## 6.2 Results

### 6.2.1 Analysis of Arrival Timing at the HL

The spatiotemporal distribution of the transmitters' first detections along the completed HL over the 2012-2014 period revealed no correlation between the distance from shore and the timing of salmon arrival at the HL. This means that although only the receivers over Inner Section of the HL were deployed from 2008 to 2012 (see Table 6.1), these years can still be considered to study the timing of Atlantic salmon postsmolts arrival at the HL.

The overall mean date of detection ($\mu$) over the 2008-2014 period, as estimated by the Gaussian model ($R^2 > 0.96$), was June 6 (week 23, $\sigma$ = 9.6 days), with detection dates varying from May 15 (week 20) to July 1 (week 26). Figure 6.3 demonstrates that the Gaussian distribution performed reasonably well for describing annual distributions of postsmolts arrival ($R^2$ between 0.88 and 0.99). There is however a high degree of inter-annual variability in the detection dates of arrival at the HL. It should be noted that variability on daily timescales might not be representative of the actual migratory behavior, but rather associated with poor detection efficiency due to environmental conditions. For example, the bimodal distribution observed in 2011 and 2014 was likely due to a short period of high winds (Figure 6.4) affecting the detection efficiency.

Yearly detection periods of salmon postsmolts at the HL revealed two different modes (Figure 6.3): early arrivals in 2010, 2012 and 2013 and later arrivals in 2008, 2009, 2011 and 2014. Early arrivals usually occurred on the last few days of May, while late arrivals occurred between June 12 and June 17. The yearly standard deviations for detections estimated by the Gaussian distributions varied between 3 and 6.8 days, but were not correlated with the timing of arrival. Although the detection peak appeared earlier in 2014 (June 9), this year was considered as a "late year" as there were no detections recorded before June 1, similarly to other "late years". Furthermore, the detection efficiency (and thus numbers of detections recorded) after June 15, 2014 was most likely due to strong winds recorded at a nearby weather station between June 15 and June 21. A similar event

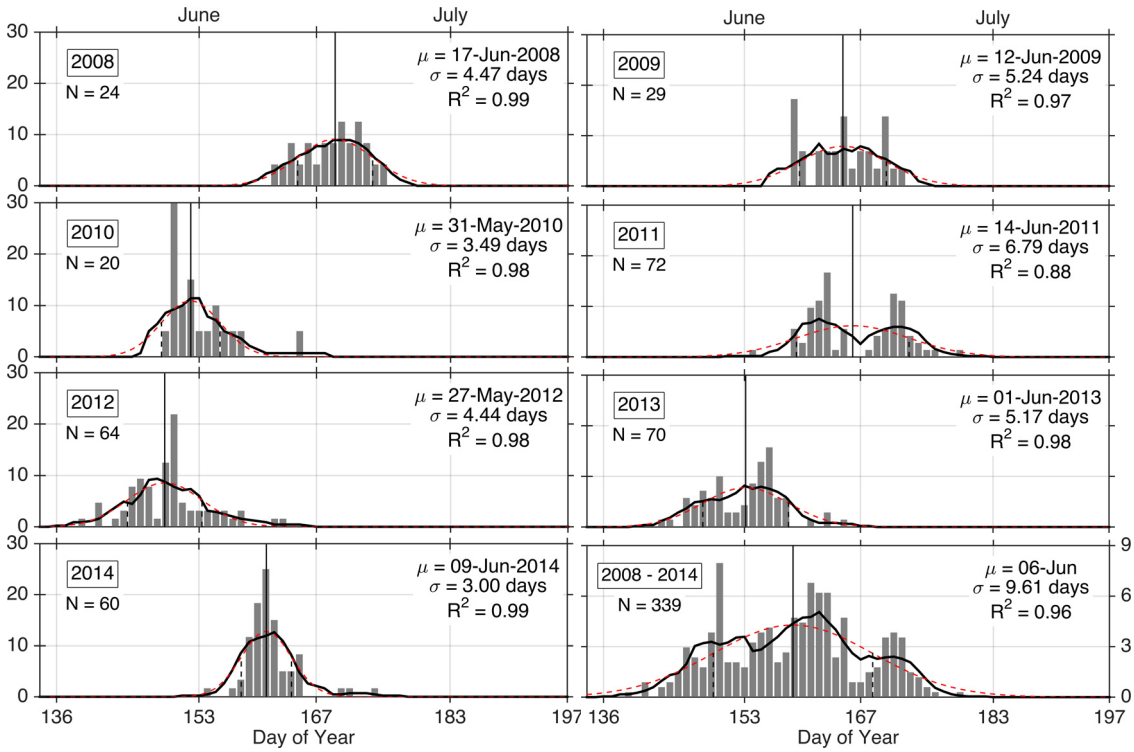


Figure 6.3: Daily counts of first detections of Atlantic salmon postsmolts along the HL for individual years, as well as averaged over the 2008-2014 period. The Gaussian model fitted to the 7-day moving average (thick black line) using Equation 6.1 is represented by a red dashed line. The model's average ($\mu$; vertical black line) and standard deviation ($\sigma$) are provided for each year. The sample size (N) and the coefficient of determination ($R^2$) of the model are also indicated in each panel. Note the change in scale in the last panel.

can be seen around June 15, 2011, where the number of detections decreased, likely due to the strong winds recorded during that time (Figure 6.4).

### 6.2.2 Oceanographic Variables

The temperature and salinity distributions in the upper 50 m collected along the HL before, during, and after the detection period of salmon postsmolts were analyzed to identify changes in the seascape that could be related to the arrival of the Atlantic salmon postsmolts (Figures 6.5, 6.6, and 6.7). A substantial difference in the upper water temperature occurred in the years 2011-2014 before and during the detection period (Figure 6.5). During these four years, water temperature in the top 20 m of the water column (i.e., where postsmolts spend most of their time) was about 7$^o$C before the postsmolts' arrival and 10$^o$C during

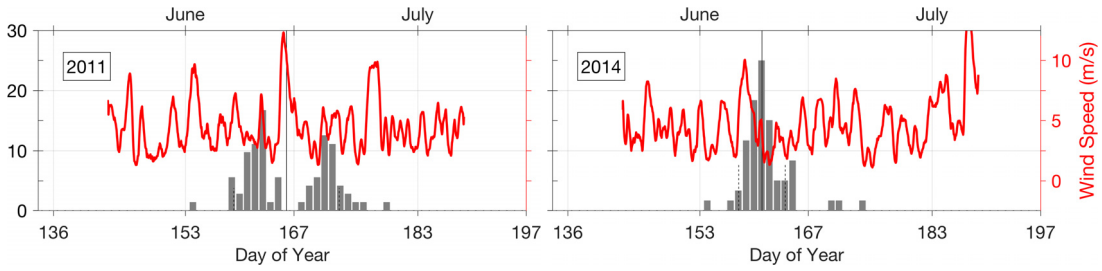


Figure 6.4: Daily counts of first detections of Atlantic salmon postsmolts along the HL in 2011 and 2014 (same as in Figure 6.3). The red line represents concurrent surface wind speeds measured at a near-by buoy (63.4$^o$W, 44.5$^o$N) after smoothing using a 6-hour moving average.

the detection period. As the net sea surface heat fluxes increase with time, a vertical stratification develops in the temperature field. Before the detection periods, the upper water column is weakly stratified compared to during and after the detection periods, with a strong thermocline located at about 20 m deep. This warming of the upper water column at the time of postsmolts detection periods occurs every year for the years 2008-2014. By comparison, no significant changes occurred in the salinity field in the periods before, during, and after the detection periods (Figure 6.6).

Low-frequency differences in the strength or position of the glider-based geostrophic currents were small and does not seem to correlate with the timing of crossing of the HL by the postsmolts (Figure 6.7; see Chapter 2). Daily detections logged over the Inner Section of the HL were also compared to the alongshore transport associated with the NSC computed from the three ADCP stations (not shown). The results confirmed that the alongshore transport associated with the NSC varies significantly over timescales ranging from daily to inter-annually, indicating that the variability in the NSC was not correlated with the timing of arrival of the postsmolts.

When comparing the hydrography along the HL during the detection period, we see that the distribution of low-salinity water across the HL varied between years during the 4-year period (see middle panels in Figure 6.6). Low-salinity water at the surface was more widely distributed in 2013 than in 2012 or 2014 when the low-salinity water was

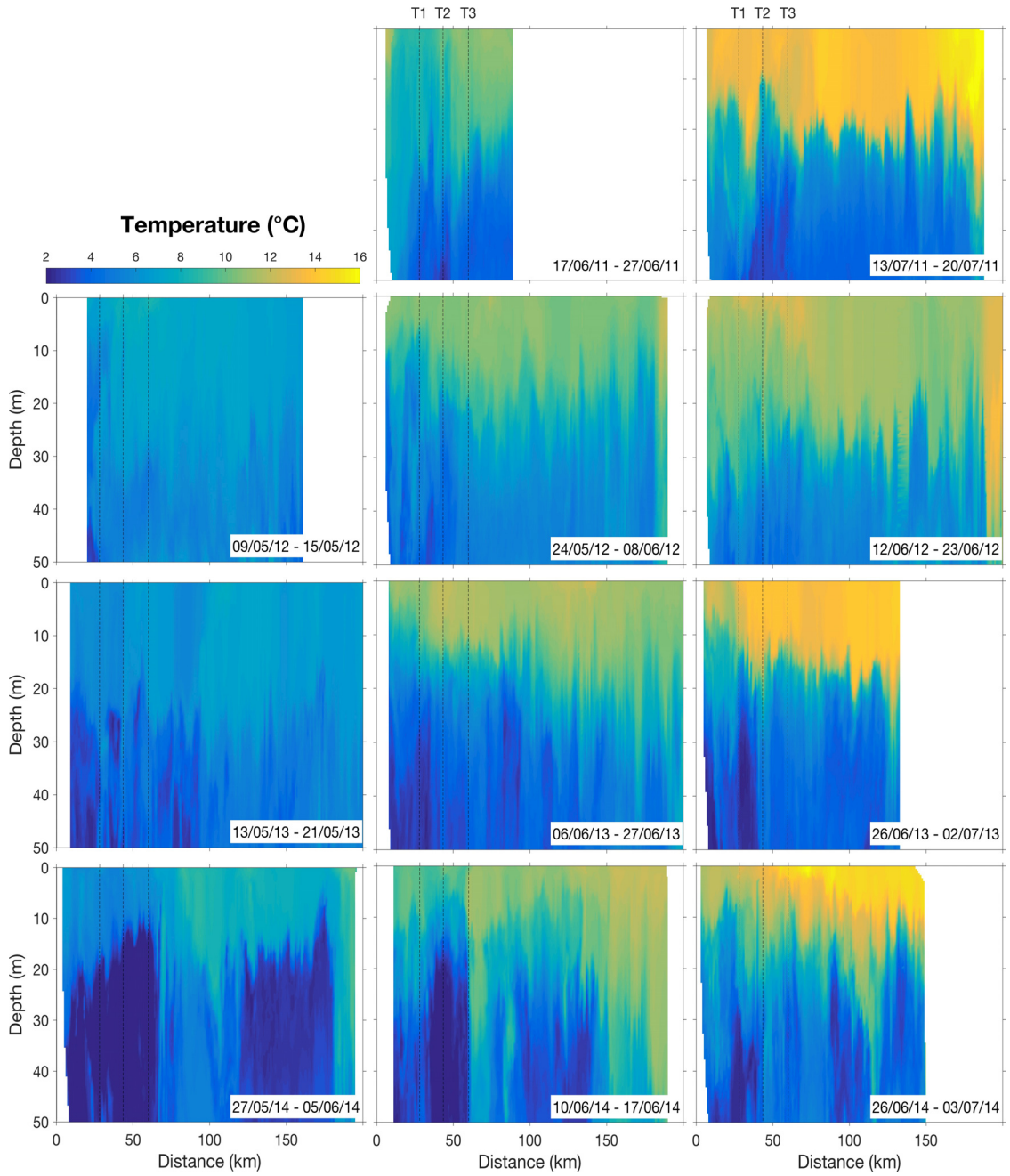


Figure 6.5: Vertical distributions of temperature (in $^{o}$C) collected by underwater gliders along the Halifax Line before (left panels), during (middle panels) and after (right panels) the Atlantic salmon postsmolts detection period in 2011 (1st row), 2012 (2nd row), 2013 (3rd row) and 2014 (4th row). The positions of the ADCP stations are indicated by vertical dashed lines.

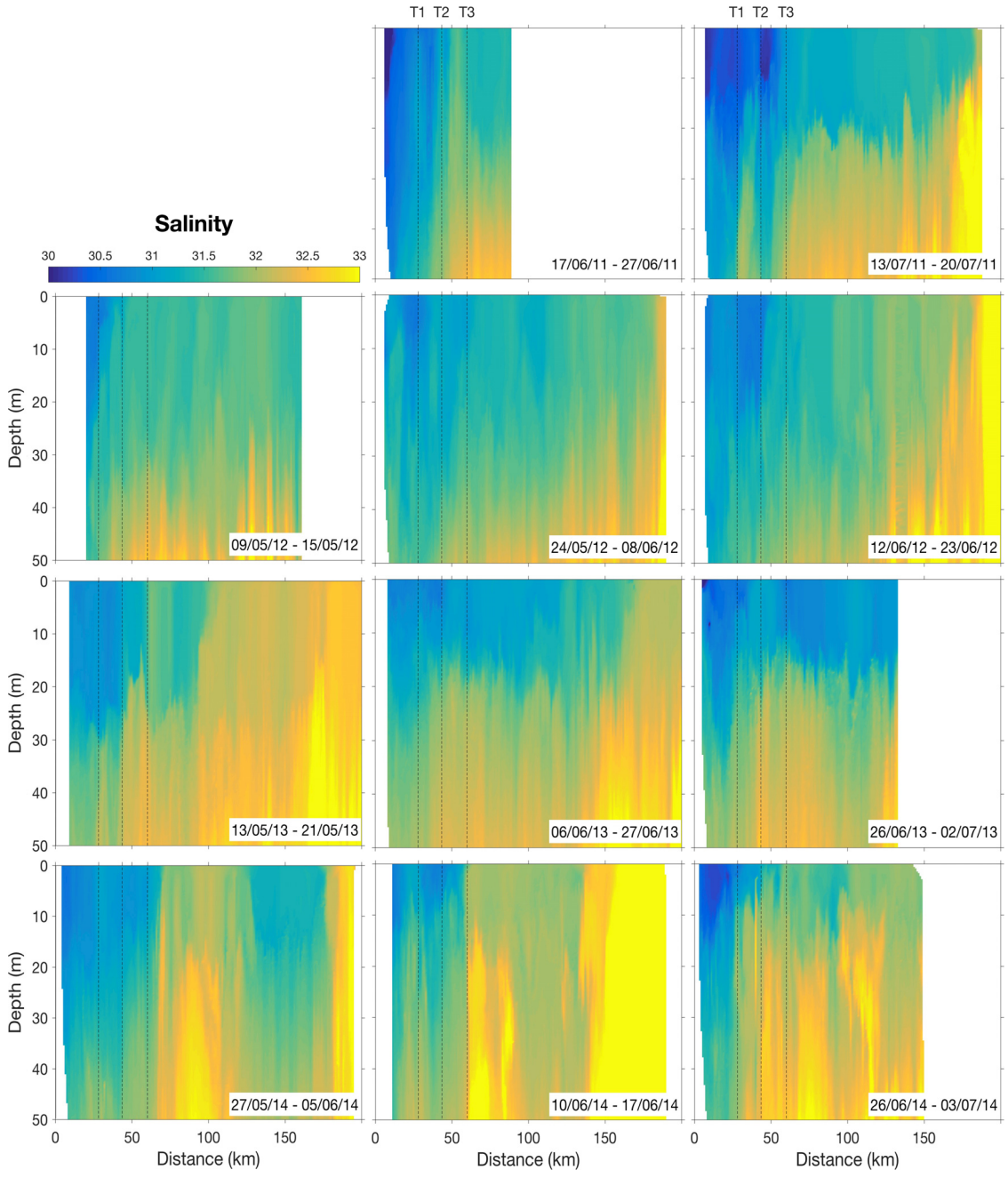


Figure 6.6: Same as in Figure 6.5 except for salinity.

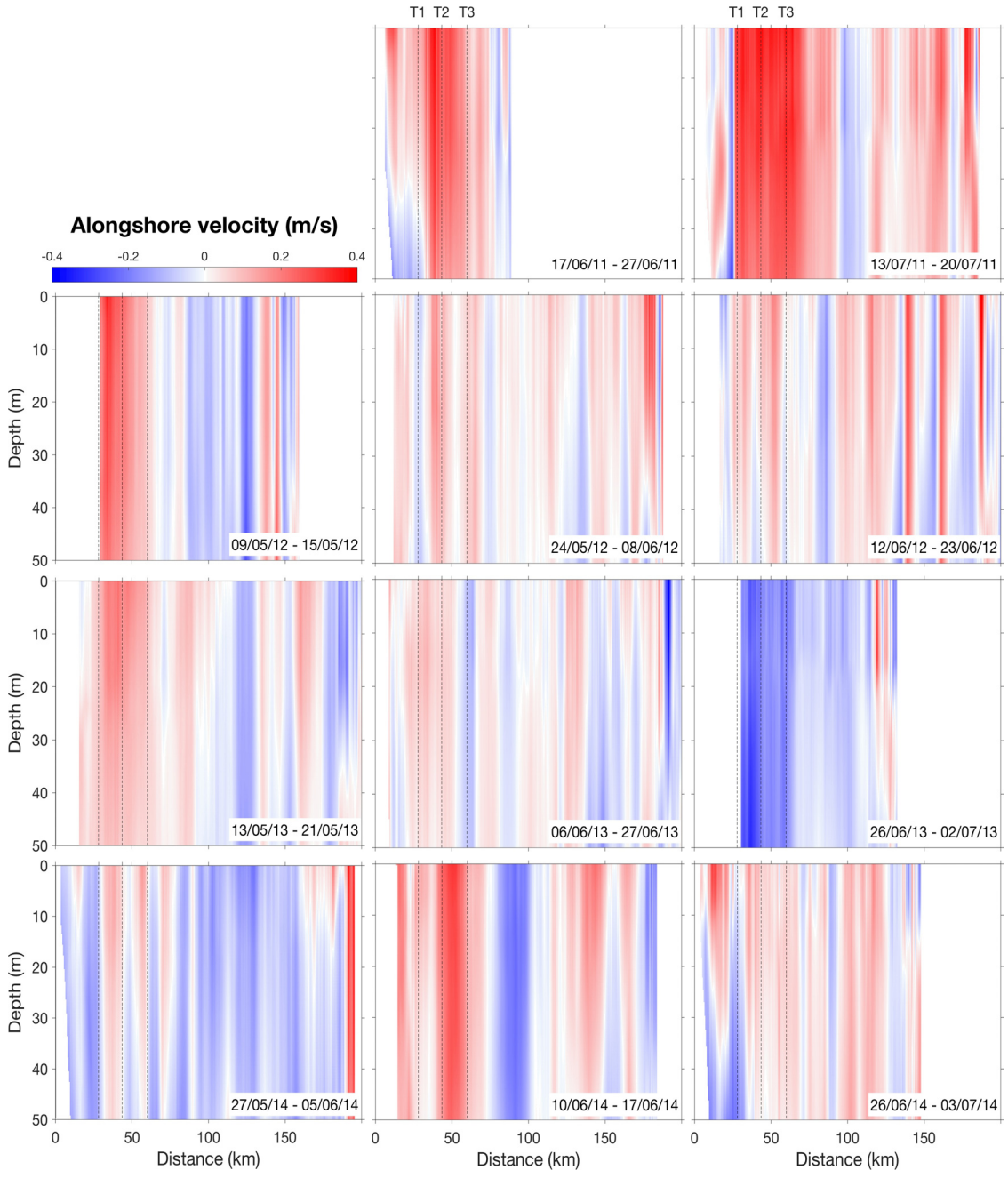


Figure 6.7: Same as in Figure 6.5 except for alongshore current velocity (in m/s).

Table 6.2: Coefficients of the multiple regression analysis linking the detection percentage of Atlantic salmon postsmolts to the temperature, salinity, and current speed (Equation 6.2)

| Variable | Coefficient | Value | Standard error | $t$ | p-value |
|---|---|---|---|---|---|
| - | $\beta_0$ | 0.00 | 0.02 | 0.00 | 1.00 |
| Temperature | $\beta_1$ | -0.12 | 0.03 | -4.19 | $\ll 0.0001$ |
| Salinity | $\beta_2$ | -0.28 | 0.03 | -10.16 | $\ll 0.0001$ |
| Current velocity | $\beta_3$ | +0.03 | 0.03 | -0.92 | 0.36 |

more confined to the Inner Section.

The magnitude, standard error, t-test, and p-value for each coefficient in the multiple regression analysis (Equation 6.2) are listed in Table 6.2. The value of $\beta_0$ is consistent with the fact that the regression model is applied to anomalies and the intercept should therefore be 0. The coefficients $\beta_1$ and $\beta_2$ are significant and have a standard error smaller than their estimated values. This indicates that the percentage of postsmolts detections on the HL was related to temperature and salinity. The value of $\beta_3$ has the same order of magnitude as the standard error and presents a large p-value, which means that the regression model failed to detect a correlation between detections and alongshore flow. Overall, the linear regression model explained about 27% of the observed variance in the distribution of postsmolt detections ($R^2$ = 0.27, df = 539 , p $\ll$ 0.01).

### 6.2.3 Analysis of Spatial Patterns of Detection and Environmental Factors

The analysis of spatial patterns in postsmolts detection revealed that 53% (163/309) of the detection sequences were located over the Inner Section of the HL with 25% (76/309) inshore of T1 (station 28, <26 km from shore). About 38% (118/309) of the detections were logged over the Middle Section, and only 9% (28/309) over the Outer Section, even though the Outer Section covered more distance than the other sections (Figure 6.8). The average distribution also exhibited a local minimum in the detection percentage around T2 (station HFX050; 45 km offshore) for all years, which coincides with the averaged

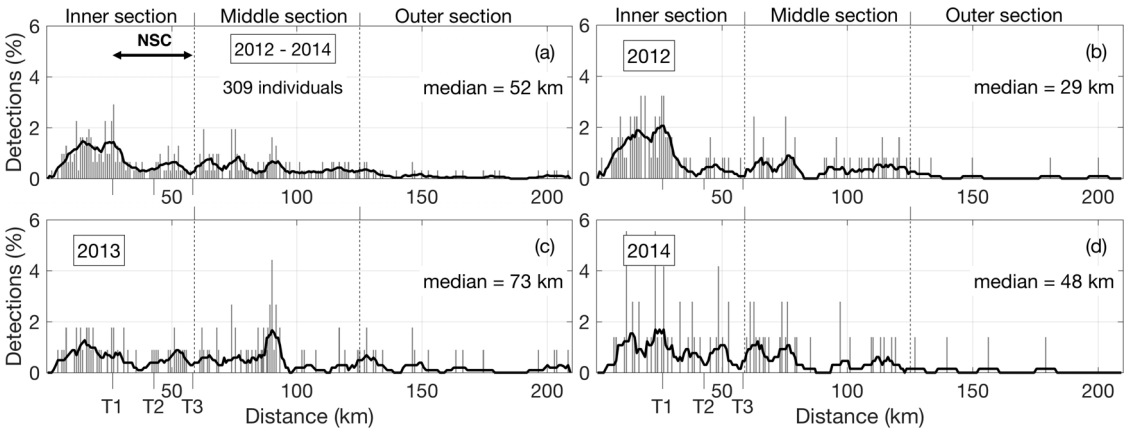


Figure 6.8: Spatial distributions of Atlantic salmon postsmolts detection sequences along the Halifax Line (a) over the 2012-2014 period, as well as for each individual year ((b) through (d)). In each panel, the 10-km moving average (thick line) is super-imposed and the median distance from shore is indicated. The approximate location of the NSC is also indicated in (a).

location of the maximum flow associated with the NSC (see Chapter 3).

Figure 6.8 demonstrates that the detection sequences had significant spatial and temporal variability in the years 2012-2014 along the HL. Distributions of detections at the HL were similar in 2012 and 2014, with 56-62% over the Inner Section, 33-39% over the Middle Section, and 5-6% over the Outer Section. Furthermore, large differences occurred within the Inner Section. In 2012, most of the detections were located onshore of station T1, that is shoreward of the NSC. In 2014, detections were evenly spread out throughout the Inner Section, as indicated by a median distance of 48 km in 2014 vs. 29 km in 2012 ($p < 0.01$). This increase in detection percentage within the NSC (i.e., between T1 and T3) is intriguing given that the NSC transport averaged over the detection period was 0.30 Sv in 2014 compared to 0.21 Sv in 2012 ($p < 0.01$). In 2013, fewer detections were logged over the Inner Section than in the other years (41%; 46/113). However, the number of detections over the Middle Section accounted for 43% (49/113) of the detections and the Outer Section 16% (18/113), which is higher than for the years 2012 and 2014 (Figure 6.8. A local minimum was measured between the stations T1 and T2, even though the transport associated with the NSC was weaker in 2013 (0.17 Sv) than in 2012 (0.21 Sv; $p<0.01$). .

### 6.2.4 Migratory Behavior and Cross-shelf Movements

The majority of postsmolts (92%) were detected more than once, with an average of 18 detections per detection sequence. This was an encouraging sign that the detection efficiency of the acoustic curtain at the HL was reasonably reliable. While 60% (281/472) of detection sequences were logged over a single station, 28% (134/472) were detected over two adjacent receivers and 12% (57/472) were recorded at more than 2 adjacent stations.

The average time spent by each postsmolt at the HL was relatively short and about 21 min, but varied greatly from 32 s to 4.3 h (Figure 6.9). Almost 75% of the animals spent less than 25 min at the HL, and half of the multi-detected postsmolts passed the HL within 12 min of their initial detections. As expected, sequences detected over several receivers (i.e., Multi-Station Sequences (MSS), representing 40% of the population) corresponded to longer residence times at the HL. The average residence for MSS was 37 min, with 75% of the MSS spending less than 36 min at the HL and 50% leaving the HL within 24 min of their initial detection.

Considering all 472 detection sequences of postsmolts, the average distance traveled along the HL was about 500 m, ranging from within 400 m (i.e., fish detected at a single station) to 5.6 km ($\sim$ 7 stations). The median value is logically less than 400 m, as more than half the detection sequences were logged over a single station (60%). This skews the probability distribution towards lower values so descriptive statistics were calculated for MSS fish only (N=191, Figure 6.9). The average distance covered increased to 1.2 km in this group, with half of the individuals covering no more than 850 m. This indicates that most of the observed cross-shelf movements occur over two to three adjacent stations.

When estimated for all 472 detection sequences, the SI varied from 0 to 1, with an average of 0.6 (25th percentile = 0.20, median = 0.5, 75th percentile = 1.00). As previously mentioned in Section 6.1, the SI is only defined for detection events covering more than a single station (191/472). The SI cannot be greater than 1 due to the condition that a fish

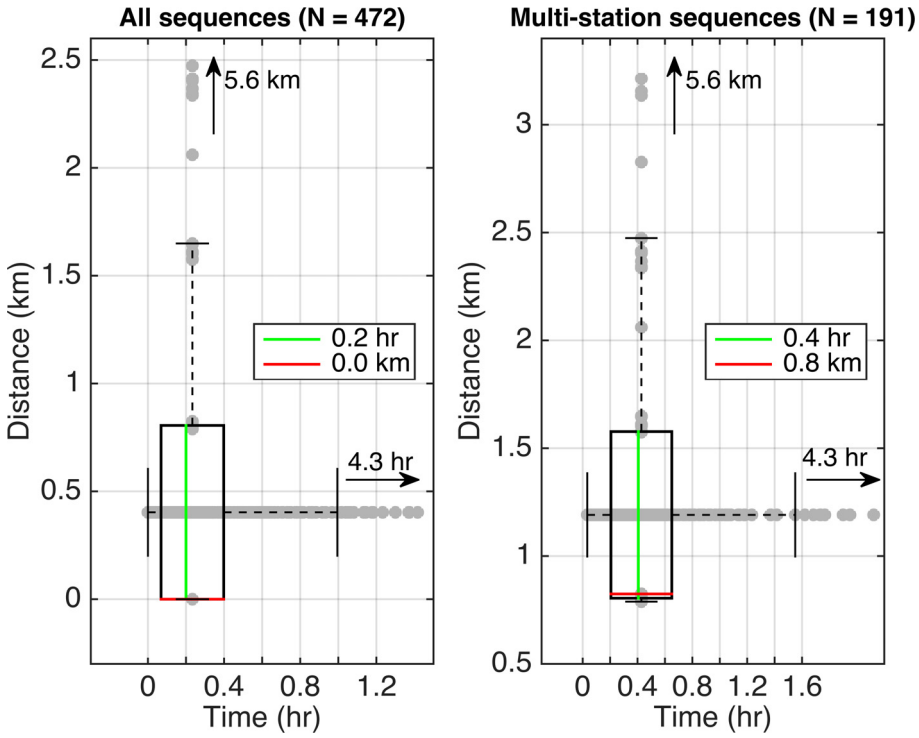


Figure 6.9: Bi-dimensional boxplots showing the distributions of the time spent (in h) and the total distance covered (in km) along the Halifax Line for (a) all the detection sequences and (b) the detection sequences that spread over at least two stations (i.e., multi-station sequences).

detected more than 2 stations away from the previous detection constitutes a new detection sequence. For this reason, it is also important to calculate the SI on an individual basis as opposed to detection sequences because it characterizes the migratory behavior of the fish as an animal. It therefore allows the SI to be greater than 1. When estimated for all 339 fish detected along the HL, the SI varied from 0 to 111, averaging 3.8 (25th percentile = 0.27, median = 1.00, 75th percentile = 1.10).

An analysis of cross-shelf movements of Atlantic salmon postsmolts was conducted to detect any significant patterns that would provide more information on the postsmolts' migratory behavior. These data include 34, 29 and 4 fish detected over the Inner, Middle, and Outer Sections of the HL. A clear pattern was found in cross-shelf movement patterns of postsmolts that migrated through different sections of the HL (Figure 6.10). About 76% (26/34) of the fish detected over the Inner Section of the OTN line moved in an offshore

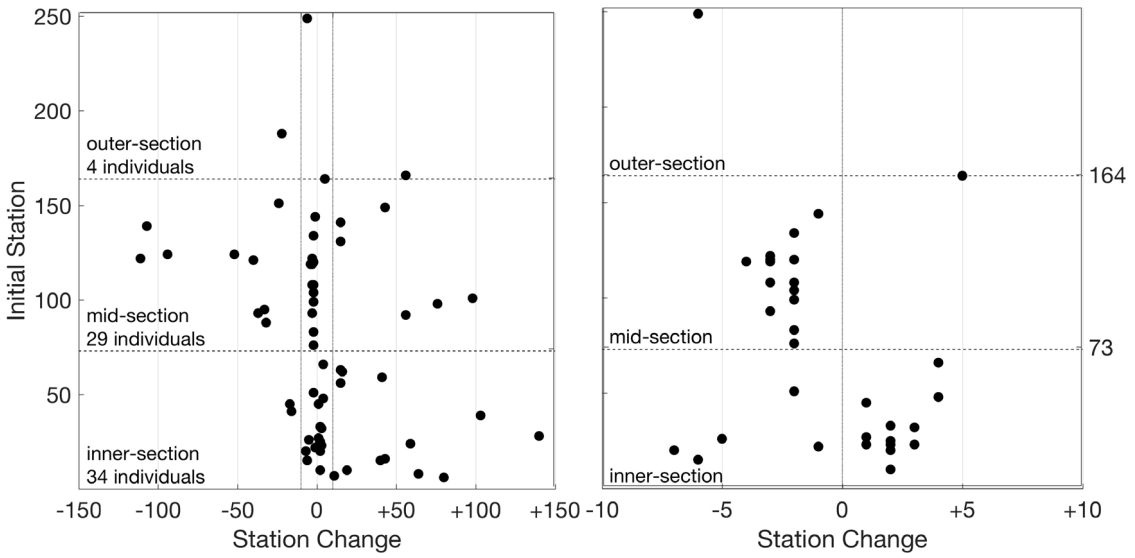


Figure 6.10: Left panel shows differences in the station number between the first and last detection recorded for animals logged over at least three adjacent or two non-adjacent receivers over the 2008-2014 period (N = 67). A negative (positive) station change is indicative of an onshore (offshore) movement. Horizontal dashed lines indicate where the HL changes direction. The right-hand-side panel shows a zoom-in of the distribution over the first 10 stations.

direction (i.e., increasing station number), while 80% (23/29) of the postsmolts detected over the Middle Section moved onshore (i.e., decreasing station number). Too few fish (N=4) were detected over the Outer Section of the HL to allow for a reliable interpretation.

Since postsmolts typically spent less than 1 hour around the HL (Figure 6.9), the next logical step was to test the hypothesis that these cross-shelf movements were driven by local total currents experienced by the fish at the time of crossing. This hypothesis was tested using the ADCP measurements at the three T-stations located over the Inner Section. No statistically significant correlations between cross-shelf movements and current direction were detected. As strong swimmers, salmon swimming direction is likely not affected by weak currents. Episodic strong currents might, however, influence the along-array movements of the detected fish. The same analysis was therefore applied to fish experiencing strong currents only. The result persists: along-array movements were not correlated to the flow direction and occurred independently of the current speed.

## 6.3 Discussion

### 6.3.1 Temporal Variability of Detections

The arrival of Atlantic salmon postsmolts at the HL appeared to be largely under the control of the seasonal change in temperature in spring. Atlantic salmon postsmolts were only detected at the HL once the surface warming has started in spring (Figure 6.5). Temperatures in the top 20 m of the water column increased from an average temperature of about $7^{o}$C with a weak thermocline before the detection period, to a temperature of about $10^{o}$C and a better-defined thermocline during the detection period. Our findings are consistent with the extensive evidence in the freshwater migration literature that salmon smolts migration is modulated by the onset of a $10^{o}$C threshold temperature (*Hayes and Kocik*, 2014; *Zydlewski et al.*, 2005, , and references therein). It also corresponds to the estimates of optimal temperature for postsmolts growth and food conversion efficiency (*Handeland et al.*, 2008; *Minke-Martin et al.*, 2015). More importantly, the temperature-dependence of the detection period of Atlantic postsmolts is consistent over the years 2011-2014, independent of whether the migration timing was classified as a late or an early year. This is strong evidence that some of the inter-annual variability observed in the arrival of postsmolts at the HL is influenced by the temperature in the upper water column, where the fish are present.

No similar trends were found when comparing transects of salinity collected before, during, and after the detection period. The salinity variability at the HL Atlantic salmon postsmolts transit is relatively small compared to the range of salinities experienced by the salmon during the migration from a freshwater to a saltwater environment. This suggests that salinity is not an important variable when defining ocean habitat for salmon, although it could have an impact on their swim speed (*Byron and Burke*, 2014).

Previous research demonstrated correlations between ocean currents and adult return rates of Atlantic salmon over inter-annual timescales (*Thomson et al.*, 1992; *Byron and Burke*, 2014). However, no significant changes were observed in the alongshore ocean

currents at the HL that could explain the temporal variability of migration timing in postsmolts. The alongshore transport associated with the NSC, used as a proxy for the currents experienced by the postsmolts, was observed to be highly variable over timescales ranging from daily to inter-annually. However, the transport was always southwestward at the time of detection, indicating that Atlantic salmon may use positive rheotaxis during migration, even in the marine environment, although the nature of the present study does not permit investigation of such causative mechanisms. Studies indicate that salmon migration may (*Booker et al.*, 2008; *Mork et al.*, 2012) or may not (*Burke et al.*, 2014; *Byron and Burke*, 2014) be affected by ocean currents, suggesting a population-specific migratory behavior (*Døving and Stabell*, 2003).

Our findings confirm the importance of ocean temperature as an important environmental cues influencing Atlantic salmon postsmolts during their oceanic migration (*Friedland et al.*, 2000, 2005; *Handeland et al.*, 2008; *Minke-Martin et al.*, 2015). The results suggest that Atlantic salmon postsmolts migrate once surface water has warmed in the spring, and may follow this surface heating as it propagates to higher latitudes. This hypothesis is supported by findings of *Minke-Martin et al.* (2015), who found that salmon captured west of Greenland experienced a relatively constant temperature throughout their ocean migration. Our findings are also consistent with the fact that the temperature, salinity, and alongshore velocity fields observed after the detection period did not present any major differences to those measured during the detection period. This indicates that postsmolts migrate as conditions are ideal, not "before they get inhospitable".

### 6.3.2 Spatial Variability of Detections

Distribution of postsmolts along the HL showed significant inter-annual variability, but was consistently relatively low near the maximum of the NSC (*Dever et al.*, 2016). The important role of oceanic fronts in shaping large ecosystems has been previously recognized by *Le Fevre* (1986) and *Belkin et al.* (2009). Biomass was also found to accumulate along oceanic fronts due to converging flows (*Houghton and Marra*, 1983; *Franks*, 1992).

Conversely, studies focusing on Pacific salmon found that fish prefer specific thermal and halo-limits, and are not more abundant within a riverine plume front, despite the relatively larger concentration of prey organisms (*Robertis et al.*, 2005; *Azumaya et al.*, 2007). Two possible mechanisms could explain the local minimum in transmitter detections: either postsmolts tend to avoid the NSC and the associated front located between T1 and T3, or they have a preference for the colder and fresher inshore water associated with the outflow coming from the GSL (*Loder et al.*, 1997; *Dever et al.*, 2016).

Results suggest that Atlantic salmon postsmolts prefer cold and fresh water during this phase of their migration. However, these results should be interpreted with caution, as colder and fresher water corresponds to the previously described inshore water mass emanating from the GSL (*Loder et al.*, 1997; *Dever et al.*, 2016). While the preference of the postsmolts for this water mass can be observed in the temperature and salinity fields, postsmolts might also be responding to other characteristics associated with this water mass such as the presence of prey organisms or a more suitable chemical signature (*Le Fevre*, 1986; *Døving and Stabell*, 2003; *Robertis et al.*, 2005). Unfortunately, no concurrent observations of food availability were made along the HL to investigate this further.

No statistically significant correlation could be found between postsmolt detection and alongshore currents variability. This suggests that the migratory behavior of postsmolts is not affected by changes in the ocean currents, and that the decrease in detections between T1 and T3 might be linked to the change in water properties rather than related to the NSC. A similar observation was made by *Robertis et al.* (2005), where more fish were localized in the Columbia River plume region than in the marine shelf waters. However, the multiple regression analysis is used to investigate the relationship between the variability in alongshore currents and acoustic detection. While variability from the mean state might not be correlated to detection patterns of Atlantic salmon, the mean circulation patterns might influence the spatial distribution of the salmon along the HL.

### 6.3.3 Migratory Behavior and Cross-shelf Movements

The time spent and the area covered along the HL during each detection sequence reveal that the migratory behavior of Atlantic salmon postsmolts is characterized by a rapid migration, as opposed to a lingering foraging behavior that would be indicated by relatively long residency times. This conclusion is further supported by the Sinuosity Index that demonstrated that a large majority of the fish crossed the HL over a relatively small area and that the habitat covered by the fish can be explained by a generalized back-and-forth movement over a limited number of receivers.

Nevertheless, a portion of the detected fish exhibit significant cross-shelf movements, characterized by SI$>$1. When the direction of the cross-shelf movement is compared to the station where the fish was first detected, it shows that a large majority of the fish moved offshore when they were migrating over the Inner Section, and onshore when migrating through the Middle Section. This convergence towards the edge of the NSC suggests that Atlantic salmon postsmolts may use positive rheotaxis and the NSC to both orient and navigate. Because these cross-shelf movements were not correlated with ocean currents, the different orientation of the two sections of the line can be used to define a general heading of the migration. Using the orientation of the Inner Section ($141^o$) and the Middle Section ($208^o$), and assuming that postsmolts are heading northeastward at the HL, the migration heading ranged between $51^o$ and $118^o$ from True North. Unfortunately, too few detections were made over the Outer Section of the line to reduce the heading range any further.

## 6.4 Conclusions

Analyses in this chapter provided evidence on the physical oceanographic conditions experienced by Atlantic salmon postsmolts from the Gulf of Maine during their ocean migration. We found that the postsmolts arrival at the HL significantly varied from year-to-year, and that much of the variability was modulated by the warm-up of the surface layer

through solar heating in spring. The ocean temperatures observed along the HL at the time of crossing ($>10^{o}$C) were slightly warmer than previously reported for Atlantic salmon habitat (4 - 8$^{o}$C, *Reddin and Shearer*, 1987; 3.9 - 9.7$^{o}$C, *Minke-Martin et al.*, 2015). Our study also demonstrated the salmon preference for cold and fresh water, while avoiding the frontal region, despite evidence that high concentrations of prey organisms are usually present along ocean fronts (*Le Fevre*, 1986; *Franks*, 1992; *Robertis et al.*, 2005). The observed cross-shelf movements of the fish was not correlated with local ocean currents and can therefore be attributed to the migratory behavior and migration routes of the salmon. This work led to the hypotheses that (1) inter-annual variability in postsmolts migration timing is driven by the increase of the net surface heat flux associated with spring; (2) postsmolts favor the cold and fresh river plume water; and (3) local oceanic currents have minimal impact on the migratory behavior of the postsmolts. These hypotheses could be tested with refined arrays deployed in key regions such as Browns Bank, where the Atlantic salmon postsmolts are expected to change their migratory heading from eastward to northeastward as they migrate around the southern tip of Nova Scotia. The acoustic array could be deployed during the migration period of the postsmolts only (April to July), established from the results of this study. The use of depth tags providing more information on the vertical movement of the fish would also be beneficial. Finally, an extensive study of the variability in detection efficiency using sentinel tags would provide more added confidence in the representativeness of observed fish detection patterns.

Our study highlighted the potential of combining animal tracking and oceanography to better understand the factors driving postsmolts ocean migration and affecting their marine survival. Networks like these would not only benefit salmon, but any other highly migratory species. They also provide valuable observations to further inform models that use temperatures and ocean currents to simulate migratory behaviors.

# CHAPTER 7

# CONCLUSIONS

The overall goal of this work was to characterize aspects of the hydrography and circulation over the Scotian Shelf to further improve our understanding of the important dynamics driving the Nova Scotia Current (NSC). The objectives were threefold. Firstly, the thesis aimed at providing a comprehensive characterization of the physical oceanographic conditions along the Halifax Line (HL) relying on complementary observational datasets. Secondly, this work intended to analyze the main forcing mechanisms driving the Nova Scotia Current, and study their spatiotemporal variability. Finally, the thesis aimed at relating physical oceanographic conditions to the migratory behavior of Atlantic postsmolts at the HL.

The above objective were achieved in this thesis based on analyses of in situ oceanographic observations and three-dimensional model results. The in-situ observations used in this study consisted of current and hydrographic measurements at high temporal resolution collected from moored instruments, and of high-spatial-resolution data collected using underwater gliders. Based on the analysis of these in situ observations, a simplistic conceptual model was developed to study the relative role of buoyancy and surface wind forcing on the dynamics of the NSC. To assess the spatial variability associated with these forcing mechanisms, the conceptual model was applied to the HL using ocean observations, and to other transects over the Scotian Shelf using numerical model results. These three-dimensional model results were obtained from a multi-nested ocean circulation modeling

system. The research work was also inter-disciplinary, as it provided linkages between the newly acquired knowledge on the variability of oceanographic conditions over the Scotian Shelf, and the acoustic detections of the Atlantic salmon postsmolts during their migration across the HL. By coupling these oceanographic datasets, we improved our understanding of the seascape experienced by migrating Atlantic salmon postsmolts, and therefore gain insights into the factors driving marine survival, a key factor in migratory species management.

## 7.1 Summary of Main Results

The observational datasets were examined to develop a comprehensive description of the hydrography and circulation, and the associated seasonal and inter-annual variability at the HL. Using a water mass tracing analysis (see Chapters 2 and 3), this thesis confirmed previous findings that the low-salinity water originating from the St. Lawrence Estuary propagates through the Gulf of St. Lawrence (GSL) and penetrates onto the inner Scotian Shelf. This low-salinity water is advected equatorward along the coast of Nova Scotia and reaches the Gulf of Maine (GoM). This important result highlighted the connectivity between the Scotian Shelf and adjacent seas, especially the GSL (see Chapter 4). The water mass analysis also demonstrated that the large warm anomaly observed over the Scotian Shelf in 2012 (*Hebert et al.*, 2013) was due to both the advection of already anomalously warm water from offshore, combined with a smaller volume of cold water coming from either the GSL or the Inshore Branch of the Labrador Current.

The analysis of the currents measured at the HL confirmed that the alongshore circulation is dominated by the NSC: a buoyancy-driven coastal current flowing southwestward along the Nova Scotian coastline. The NSC was found to be highly coherent in the along-shelf direction (i.e., on the order of hundreds of kilometers), while the cross-shelf coherency rapidly decreases (i.e., on the order of tens of kilometers; see Chapter 4). This short decorrelation scale of the NSC in the cross-shore direction highlights the importance

of capturing the core of the NSC to properly describe the alongshore coastal current (see Chapter 2). Furthermore, the high alongshore coherency provided additional evidence of the connectivity between the conditions at the HL and the oceanographic conditions at Cabot Strait and in the Gulf of St. Lawrence, going as far as the St. Lawrence River (see Chapter 4). This has major implications when considering the dispersion of physical (e.g., freshwater), biological (e.g., fish larvae), and anthropogenic (e.g., pollutants) parameters over the Scotian Shelf.

My doctoral research also investigated the major driving mechanisms associated with the NSC (Chapters 4 and 5). A HEOF analysis was applied to the alongshore component of the velocity records collected along the HL using bottom-mounted, upward-looking ADCPs. The HEOF analysis separates the observed signal into modes of variability that may be linked to possible dynamical mechanisms The first two dynamical modes extracted from the field data explained a high percentage of the current's total variance (92%). The first mode (72%) seemed to be associated with the geostrophic flow at the HL. The important role of the first dynamical mode in explaining the NSC suggests that the geostrophic flow alone constitutes a good approximation to the total alongshore flow. This is confirmed by the good agreement obtained between the geostrophic flow derived from the glider and the total alongshore flow measured by the ADCPs (see Chapter 3). The second dynamical mode (19%) presented some features that partially links it to the circulation driven by surface winds.

Based on these findings, a conceptual model (i.e., the Hydrographic Wind Index; HWI) was developed to separate and quantify the buoyancy-driven flow and the wind-driven flow within the NSC (Chapter 4). Estimations of the buoyancy-driven flow relied on knowledge of the shape of the density front (width and depth) separating the low-density coastal water from the ambient shelf water, and on the average density of these two water masses. The wind-driven flow was estimated from the surface wind speed using a set of parameters. The ratio of those two quantities was used to define the HWI and to

determine the relative role of each mechanism in driving the NSC. This newly-suggested index was based on previous work suggested by WG05, but is more appropriate for the analysis of coastal buoyancy-driven current systems of the order of $\mathcal{O}$(100 km), such as the NSC, than the traditional approach proposed by WG05. Estimates of the HWI are based on the knowledge of the cross-shelf density structure and includes the effects of alongshore surface winds on the stratification of the water column. This new method differs from WG05's method, since WG05 relied on knowledge of the river freshwater discharge generating the buoyancy-driven coastal current exclusively. However, since the HWI method relies on local conditions to estimate the buoyancy-driven flow, it is important to quantify the impact of alongshore winds on the vertical density structure. Wind-driven isopycnal tilting should be accounted for to properly assess the contribution of the buoyancy-driven flow to the total alongshore current.

Applying the HWI conceptual model to the glider data collected along the HL suggested that the frontal shape played a greater role than the density gradient in modulating the seasonal cycle of the buoyancy-driven term. However, applying the wind-driven isopycnal tilting correction affected that result: As surface winds at the HL are dominantly upwelling-favorable and therefore tend to flatten the density front, the buoyancy-driven flow tends to be underestimated. Once this correction is applied, the seasonal maximum of the buoyancy-driven flow occurred in the fall as opposed to the winter, increasing the role of the density gradient in modulating the seasonal cycle of the geostrophic flow. The HWI show that the NSC is buoyancy-driven all year at the HL (-1<HWI<1). Results also showed that surface winds play an important role not only in driving an alongshore barotropic flow, but also in modulating the shape of the density front separating coastal waters from ambient shelf water (see Chapter 4). This is an important result when considering the effects long-term changes in wind patterns or buoyant water discharge could have on the Shelf dynamics.

While the observational datasets collected along the HL provided an unprecedented spatiotemporal coverage, the spatial coverage was not sufficient to study the spatial

variability of the wind-driven and buoyancy-driven flows over the Scotian Shelf. Part of this thesis work therefore estimated the HWI using numerical simulations from an ocean circulation modeling system at four different locations along the NSC (see Chapter 5; *Shan et al.*, 2016). It revealed that the spatial variability observed in the buoyancy-driven component of the NSC was mainly driven by a change in ambient shelf water density, with the water becoming denser as the NSC propagates downshelf. Despite this alongshore change in ambient shelf density, the buoyancy-driven flow was fairly coherent over the Scotian Shelf, from the Cape Canso Line to the Cape Sable Line. The buoyancy- and wind-driven flows at Cabot Strait were significantly different than over the rest of the Scotian Shelf: the buoyancy-driven term followed the density gradient's seasonal cycle, as the frontal slope was relatively constant compared to the other transects. The wind-driven flow was also significantly different at Cabot strait, due to a different coastal orientation.

Interesting results came to light when studying the spatial variability in the dynamics of the NSC (Chapter 5): Firstly, the conditions between Cape Canso and Cape Sable were remarkably similar, confirming the high alongshore coherency observed in Chapter 4. Secondly, the analysis revealed that the NSC regularly detached from the coast, becoming a surface-advected current, as opposed to a bottom-trapped current. This highlighted the limits of the conceptual model used to represent the wind-driven isopycnal tilting, which did not allow the current to detach from the coast.

The newly-acquired knowledge of the variability in oceanographic conditions at the HL (see Chapter 3) was combined with acoustic detections of Atlantic salmon postsmolts during their northeastward sea migration. By considering both of these datasets, linkages between oceanographic conditions and Atlantic salmon postsmolts migratory behavior were identified (Chapter 6). It revealed that the difference in the timing of arrival of the postsmolts on inter-annual timescales was linked to the warming of surface waters occurring in spring. No apparent features in the salinity or current velocity fields that could explain this temporal variability were observed. The study of the spatial variability in

acoustic detections demonstrated that more postsmolts were detected in colder and fresher water. Once again, the local currents (strength or direction) were not correlated to the presence of postsmolts along the HL. While this study demonstrated that the postsmolts preferred the colder and fresher coastal water mass, it did not necessarily prove that it is because of the hydrographic signature. Other variables not available for this study (e.g., dissolved oxygen, nutrient concentration, etc.) distinguishing coastal water from ambient shelf water could also be playing an important role.

## 7.2 Future Work

Although significant achievements were made in this thesis research on examining the dynamics of the NSC and its effect on the migration of Atlantic salmon postsmolts over the Scotian Shelf, many important scientific questions, however, remain to be studied.

In the water mass analysis presented in Chapter 3, it was demonstrated that the water coming from the Inshore Labrador Current and the CIL coming from the GSL could not be differentiated in the T-S space, therefore requiring a third tracer. Potential candidates are nutrients concentrations (i.e., nitrate, phosphate, and silicate) that could be assumed to be conservative tracers under certain conditions. Linear combinations of nutrient concentrations could also constitute reliable conservative tracers (i.e., $Si^{\star}$ and $N^{\star}$; see *Gruber and Sarmiento*, 1997; *Sarmiento et al.*, 2004). Despite this limitation, the water mass tracing analysis presented in Chapter 3 provided valuable insights into the change in dynamics driving inter-annual variability over the Scotian Shelf, and more specifically generating the 2012 warm anomaly. The anomaly was the result of the advection of already anomalously warm water from the Shelf slope, associated with a smaller volume of cold water reaching the HL than in other years. Exact reasons as to why this was the case remain unknown. Future efforts should be made on understanding the "pulsing effect" of the penetration of cold water from the Labrador Sea onto the Grand Banks and the Scotian Shelf. Furthermore, this thesis highlighted the need for a better understanding of

the exchanges between the continental shelf and slope in order to characterize inter-annual variability and extreme marine events such as the 2012 anomaly.

The analysis provided in Chapter 4 characterized the NSC and highlighted the remarkably high alongshore coherency of oceanographic conditions within the NSC. The HEOF analysis demonstrated that, while buoyancy and surface winds are dominating the Shelf dynamics in this region, these two forcing mechanisms alone cannot explain the total variability observed. Important questions to be addressed include: what other mechanisms could be involved in generating the NSC's variability? To what extent those mechanisms impact the NSC, and over which timescales? Processes such as the alongshore pressure gradient, downshelf-traveling coastally-trapped waves, and hydrodynamic instabilities could potentially have an impact and should be investigated in the future.

The HWI is a generalized approach that could be applied to other buoyancy-driven coastal currents. A future study will be conducted to apply the HWI to the Norwegian Coastal Current and other density-driven coastal currents. The HWI could also be used for research purposes; depending on the freshwater discharge coming from land, the Norwegian Coastal Current can demonstrate large inter-annual variability in strength and path, affecting retentions area of fish larvae for commercially important species (e.g., cod and herring; *Vikebø et al.*, 2005; *Sætre*, 2007; *Vikebø et al.*, 2007). The HWI could be used to characterize the Norwegian Coastal Current in years of high versus low recruitment, linking the inter-annual variability of the coastal circulation to fish abundance. Another important application of the HWI could be done by investigating buoyancy-driven coastal currents where either alongshore winds or buoyant water discharge have undergone an abrupt change. This was seen on the Norwegian Shelf when large dams were constructed over a relatively short period, therefore regulating the input of freshwater onto the continental shelf. Dams tend to smooth out the precipitation's seasonal cycle, with the retention of the water in reservoirs, and a more progressive release of the freshwater.

The application of the HWI to several locations along the NSC over the Scotian Shelf

highlighted some of the limitations of the conceptual model used to characterize the wind-driven isopycnal titling of the density front (Chapter 5). The analysis revealed that the buoyancy-driven coastal current can sometimes detach from the coast and become a surface-advected current. Investigating the frequency, duration, characteristics and drivers of these seldom observed events in the NSC would be a significant step toward further understanding the distribution of nutrients and freshwater over the Scotian Shelf. The analysis presented in this thesis suggested that little cross-frontal mixing occur between coastal water and ambient shelf water. The role played by the bottom-trapped density front in regulating cross-shelf mixing and the distribution of nutrients and freshwater over a continental shelf is an interesting topic that arises from this thesis. Furthermore, numerical models could be used to investigate the relative role of buoyancy and surface winds in driving the coastal current by conducting idealized numerical simulations (e.g., no river runoff, no surface winds, etc.). Such an analysis would not require the important assumptions made to develop the HWI (see Chapter 4) and would include dynamical terms ignored in the HWI approach (e.g., non-linear terms, alongshore pressure gradient term, etc.).

Chapter 6 provided an example of an inter-disciplinary studies made possible by combining oceanographic datasets. While this work demonstrated the tendency of Atlantic salmon postsmolts in selecting the colder and fresher coastal water mass during their northeastward migration, this result could be due to the selection of some other water mass-specific signature by the postsmolts (e.g., food availability, nutrient concentration or dissolved oxygen). Unfortunately, we did not have the capability of testing these hypotheses, lacking measurements of other potentially important variables such as food availability. Future work could include the use of the backscatter as measured by ADCPs to estimate food concentration available to the migrating postsmolts, and determine whether or not this is a factor influencing their migratory behavior.

Finally, other scientific questions that were not directly related to this thesis' topic but

are worth investigating in the future were identified. Amongst those, is the potential for cross-disciplinary studies to improve our understandings of the dynamics involved in the chlorophyll maximum observed over the Scotian Shelf. Underwater gliders provide the opportunity to concurrently collect information on both the chlorophyll concentration and the oceanographic conditions. Combining these informations would provide unprecedented insights into the mechanisms driving both the spatial and temporal variability associated with the patches of high chlorophyll concentration, and is possible over a wide range of spatiotemporal scales (e.g., synoptic to inter-annual in time, and from tens to hundreds of kilometers in space). Another example is the capacity of underwater gliders to measure accurately the internal wave field: transects completed along the HL showed the presence of large amplitude internal waves ($\mathcal{O}$(10 m)) over the Scotian Shelf. While challenges arise from the fact that gliders are moving platforms, this constitutes a topic worth investigating as these internal waves could play an important role in vertical mixing over the Shelf, bringing nutrients to the euphotic zone (*Sandstrom and Elliott*, 1984).

# APPENDIX A

# GLIDER-BASED CURRENT ESTIMATIONS

Every time the glider surfaces, an estimate of the vertically-integrated current experienced by the glider since the last surfacing can be computed. This appendix goes over the sequence of events occurring between two glider surfacings, and the method used to estimate the depth-averaged currents (Figure A.1).

The glider first records its location ($x_1$, $y_1$) through GPS at a time $T_1$. The glider then starts the diving sequence, sampling the water column for a given amount of time, and surfaces again at a time $T_2$. The coordinates ($x_2$, $y_2$) of the glider when surfacing at time $T_2$ are extrapolated from the last known position using a dead reckoning algorithm relying on a flight model of the underwater glider (thick line in Figure A.1). The glider thus "thinks" it surfaces at ($x_2$, $y_2$). In reality, the glider surfaces at a location ($x'_2$, $y'_2$) due to the currents it experienced during the dive, which are not included in the dead-reckoning algorithm. The difference between ($x_2$, $y_2$) and ($x'_2$, $y'_2$) therefore corresponds to the depth- and time-averaged currents the glider experienced throughout its last dive (red arrow in Figure A.1).

However, the coordinates ($x'_2$, $y'_2$) are not exactly known, as the first GPS fix does not occur immediately at the time of the glider surfacing (i.e., $T_2$), but at a later time $T_3$. The depth- and time-averaged current is therefore calculated by comparing ($x_2$, $y_2$) and ($x_3$,

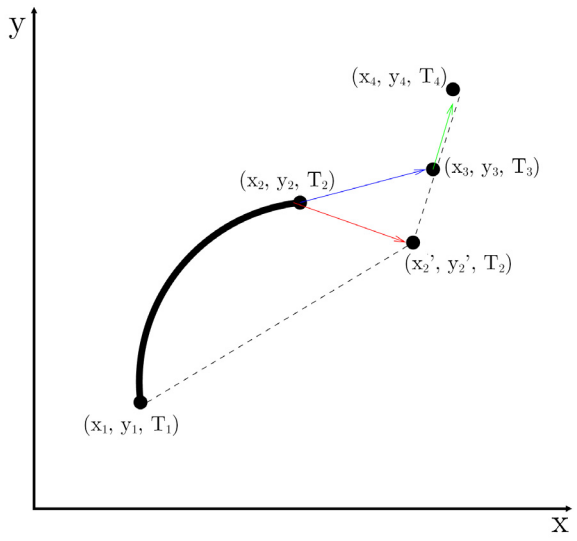


Figure A.1: Schematic showing the sequence of events occurring during a glider dive. $T_1$, $T_2$, $T_3$ and $T_4$ refer to the diving time, surfacing time, first GPS fix, and second GPS fix, respectively. The glider coordinates are indicated by ($x_i$, $y_i$). The thick line represents the path of glider as extrapolated by dead reckoning. The red arrow shows the depth-averaged current experienced by the glider between the last two surfacings, the blue arrow is the depth-averaged current calculated by the glider and the green arrow represents the surface drift.

$y_3$), which includes the surface drift experienced by the glider between the times $T_2$ and $T_3$ (blue arrow in Figure A.1).

To correct for this surface drift, a second GPS fix is obtained by the glider at a later time $T_4$. The surface drift experienced by the glider between $T_3$ and $T_4$ (green arrow in Figure A.1) is extrapolated back in time to estimate the location of the glider at time $T_2$, assuming that the surface drift remained constant between $T_2$ and $T_4$. Finally, depth- and time-averaged current estimations from the gliders' missions are associated with the coordinates of the mid-point in between the two surfacings ($\frac{x_2'-x_1}{2}$, $\frac{y_2'-y_1}{2}$).

Glider-based observations located within a 2 km radius from an ADCP station (T1, T2 or T3; Figure 2.1) are then compared to the corresponding ADCP record, when it exists. 36 current estimations are used to calculate a linear fit between current measurements from both the glider and the ADCPs, which is applied to the glider-based current observations for validation (Figure A.2).

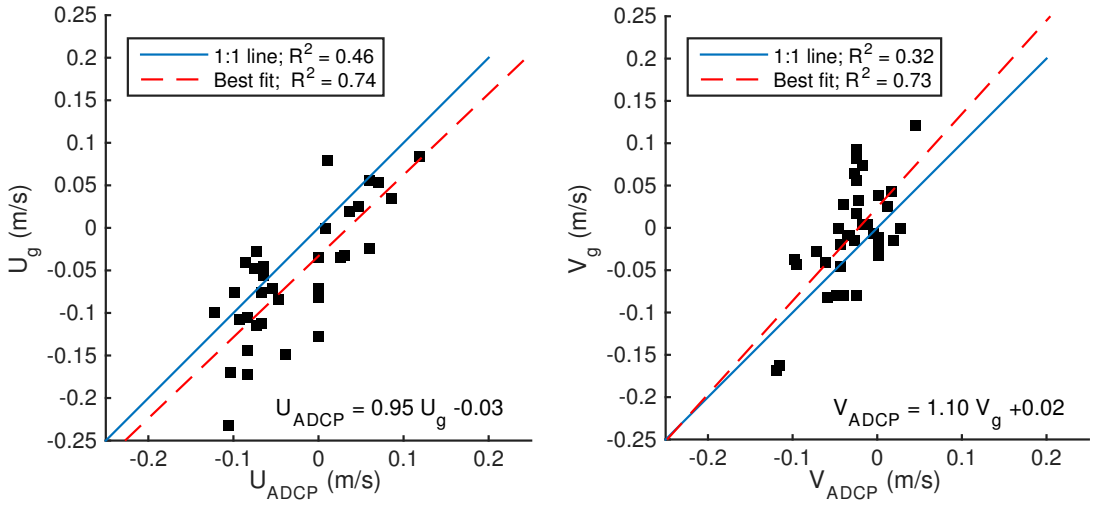


Figure A.2: Depth-averaged current experienced by the glider ($U_g, V_g$) during a dive ($\sim$6 hrs), using the corresponding ADCP measurements ($U_{ADCP}, V_{ADCP}$). Current estimations located within a 2 km radius from an ADCP station were selected (N = 36) and two distinct linear fits were used to validate the zonal ($U_g$) and meridional ($V$) glider-based currents. The 1:1 ratio (blue line) is indicated to illustrate a perfect fit, and the best linear fit is shown with a dashed red line. Coefficients of determination before and after validation are both indicated, showing the significant improvement in $R^2$ when applying the linear corrections.

# APPENDIX B

# DERIVATION OF MARGULES EQUATIONS

Consider a two-layer geostrophic flow, where $h_f$ is the $z$-coordinate of the interface between the two layers and $\zeta$ is the height of the free surface. The upper layer is formed of coastal water and has a density $\rho_c$. The lower layer is composed of ambient shelf water of density $\rho_a$. The velocity in each layer can be deduced from the equations for the geostrophic balance:

$$-fv_{geo} = -\frac{1}{\rho}\frac{\partial P}{\partial x} \tag{B.1a}$$

$$fu_{geo} = -\frac{1}{\rho}\frac{\partial P}{\partial y} \tag{B.1b}$$

Under the hydrostatic approximation ($\partial P/\partial z = -\rho g$), the pressure in the upper layer is:

$$P_c(z) = g\rho_c(\zeta - z) + P_{atm} \tag{B.2}$$

where $P_{atm}$ is the atmospheric pressure at $z = 0$ and is assumed to be homogeneous in space ($\partial P_{atm}/\partial x = \partial P_{atm}/\partial y = 0$). Substituting the partial derivative of Equation B.2 into Equation B.1, the velocity in the upper layer can be written:

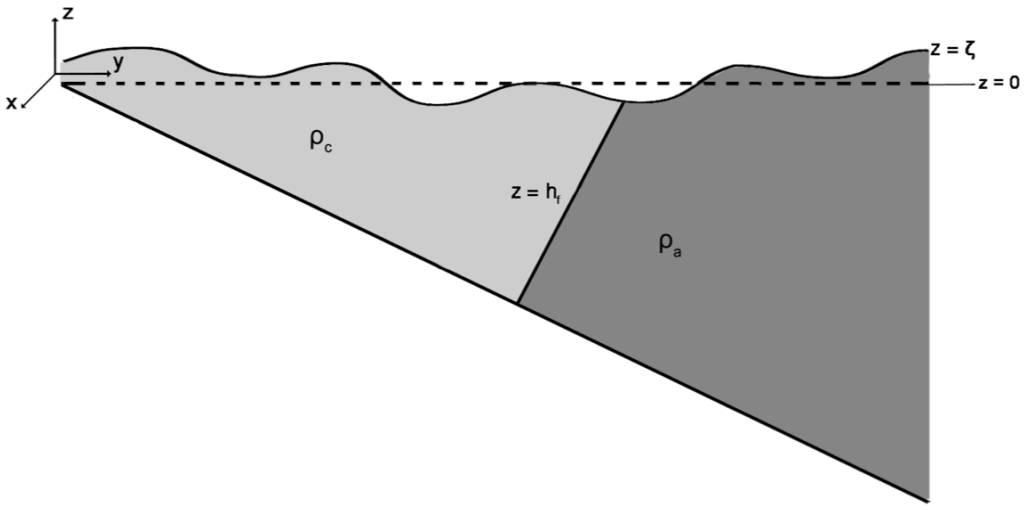


Figure B.1: Definition schematic for a two-layer flow, with the level ocean surface ($z = 0$), a free surface at $z = \zeta(x, y)$, and an interface between the two layers at $z = h_f(x, y)$. Subscripts c and a denote values of quantities in the upper and lower values, respectively.

$$v_{geo,c} = \frac{g}{f}\frac{\partial \zeta}{\partial x} \tag{B.3a}$$

$$u_{geo,c} = -\frac{g}{f}\frac{\partial \zeta}{\partial y} \tag{B.3b}$$

The pressure in the lower layer is:

$$P_a(z) = g\rho_a(h_f - z) + g\rho_c(\zeta - h_f) + P_{atm} \tag{B.4}$$

The lower layer velocity can derived by substituting the partial derivative of Equation B.4 into Equation B.1:

$$v_{geo,a} = \frac{g}{f}\left[\frac{\rho_a - \rho_c}{\rho_a}\frac{\partial h_f}{\partial x} + \frac{\rho_c}{\rho_a}\frac{\partial \zeta}{\partial x}\right] \tag{B.5a}$$

$$u_{geo,a} = -\frac{g}{f}\left[\frac{\rho_a - \rho_c}{\rho_a}\frac{\partial h_f}{\partial y} + \frac{\rho_c}{\rho_a}\frac{\partial \zeta}{\partial y}\right] \tag{B.5b}$$

which, under the Boussinesq approximation, can be simplified to:

$$v_{geo,a} = \frac{g}{f}\left[\frac{\rho_a - \rho_c}{\rho_a}\frac{\partial h_f}{\partial x} + \frac{\partial \zeta}{\partial x}\right] \tag{B.6a}$$

$$u_{geo,a} = -\frac{g}{f}\left[\frac{\rho_a - \rho_c}{\rho_a}\frac{\partial h_f}{\partial y} + \frac{\partial \zeta}{\partial y}\right] \tag{B.6b}$$

Considering the velocity difference between the two layers, we obtain:

$$v_{geo,c} - v_{geo,a} = \frac{g}{f}\frac{\rho_a - \rho_c}{\rho_a}\frac{\partial h_f}{\partial x} \tag{B.7a}$$

$$u_{geo,c} - u_{geo,a} = -\frac{g}{f}\frac{\rho_a - \rho_c}{\rho_a}\frac{\partial h_f}{\partial y} \tag{B.7b}$$

These are Margules equations for a two-layer flow. In the case of a quiescent lower layer (i.e. one-and-a-half layer flow), the velocity in the upper layer can be written as:

$$v_{geo,c} = \frac{g}{f}\frac{\rho_a - \rho_c}{\rho_a}\frac{\partial h_f}{\partial x} \tag{B.8a}$$

$$u_{geo,c} = -\frac{g}{f}\frac{\rho_a - \rho_c}{\rho_a}\frac{\partial h_f}{\partial y} \tag{B.8b}$$

# APPENDIX C

# ERROR PROPAGATION IN THE HYDROGRAPHIC WIND INDEX CALCULATIONS

The measurement error associated with the estimated buoyancy-driven flow ($U_{geo}$), wind-driven flow ($U_{wind}$), and their respective transports are calculated based on the assumption that the variables are independent. It uses the following general equation for a function $F = F(X, Y, ...)$:

$$\sigma_F = \sqrt{\left(\frac{\partial F}{\partial X} \cdot \sigma_X\right)^2 + \left(\frac{\partial F}{\partial Y} \cdot \sigma_Y\right)^2 + ...} \tag{C.1}$$

The error associated with $U_{geo}$ (see Equation 4.12) can thus be expressed as:

$$\sigma_{U_{geo}} = |U_{geo}| \times \sqrt{\left[\left(\frac{\rho_c}{\rho_a - \rho_c}\right)^2 \left[\left(\frac{\sigma_{\rho_a}}{\rho_a}\right)^2 + \left(\frac{\sigma_{\rho_c}}{\rho_c}\right)^2\right] + \left(\frac{\sigma_H}{H}\right)^2 + \left(\frac{\sigma_L}{L}\right)^2\right]} \tag{C.2}$$

The error associated with $U_{wind}$ (see Equation 4.17) is expressed as:

$$\sigma_{U_{wind}} = |U_{wind}| \times \sqrt{\left[\frac{1}{2^2}\left[\left(\frac{\sigma_{\rho_{air}}}{\rho_{air}}\right)^2 + \left(\frac{\sigma_\rho}{\rho}\right)^2 + \left(\frac{\sigma_{C_{10}}}{C_{10}}\right)^2 + \left(\frac{\sigma_{C_D}}{C_D}\right)^2\right] + \left(\frac{\sigma_{U_{10}}}{U_{10}}\right)^2\right]} \tag{C.3}$$

The error associated with the transport (see Equation 4.13) can therefore be expressed as:

$$\sigma_Q = |Q| \times \sqrt{\left[\left(\frac{\sigma_H}{H}\right)^2 + \left(\frac{\sigma_L}{L}\right)^2 + \left(\frac{\sigma_U}{U}\right)^2\right]} \tag{C.4}$$

The error associated with the HWI (see Equation 4.25) is expressed as:

$$\sigma_{HWI} = |HWI| \times \sqrt{\left(\frac{\sigma_{U_{wind}}}{U_{wind}}\right)^2 + \left(\frac{\sigma_{U_{geo}}}{U_{geo}}\right)^2} \tag{C.5}$$

# BIBLIOGRAPHY


Anderson, C., and P. Smith, Oceanographic observations on the scotian shelf during CASP, *Atmosphere-ocean*, *27*, 130–156, 1989.

Azumaya, T., T. Nagasawa, O. S. Temnykh, and G. V. Khen, Regional and seasonal differences in temperature and salinity limitations of Pacific salmon (Oncorhynchus spp.), *North Pacific Anadromous Fish Commission*, *4*, 179–187, 2007.

Barnett, T. P., Interaction of the monsoon and pacific trade wind system at interannual time scales part i: The equatorial zone, *Monthly Weather Review*, *111*, 756–773, 1983.

Belkin, I. M., P. C. Cornillon, and K. Sherman, Fronts in large marine ecosystems, *Progress in Oceanography*, *81*, 223–236, 2009.

Booker, D. J., N. C. Wells, and I. P. Smith, Modelling the trajectories of migrating Atlantic salmon (Salmo salar), *Canadian Journal of Fisheries and Aquatic Sciences*, *65*, 352–361, 2008.

Bourgault, D., and V. G. Koutitonsky, Realtime monitoring of the freshwater discharge at the head of the St. Lawrence Estuary, *Atmosphere-Ocean*, *37*, 203–220, 1999.

Brink, K. H., Continental shelf baroclinic instability. Part I: Relaxation from upwelling or downwelling, *Journal of Physical Oceanography*, *46*, 551–568, 2015.

Burke, B. J., J. J. Anderson, and A. M. Baptista, Evidence for multiple navigational sensory capabilities of Chinook salmon, *Aquatic Biology*, *20*, 77–90, 2014.

Byron, C. J., and B. J. Burke, Salmon ocean migration models suggest a variety of population-specific strategies, *Reviews in Fish Biology and Fisheries*, *24*, 737–756, 2014.

Chapman, D. C., and S. J. Lentz, Trapping of a coastal density front by the bottom boundary layer, *Journal of Physical Oceanography*, *24*, 1464–1479, 1994.

Chaput, G., C. Legault, D. Reddin, F. Caron, and P. Amiro, Provision of catch advice taking account of non-stationarity in productivity of Atlantic salmon (Salmo salar L.) in the Northwest Atlantic, *ICES Journal of Marine Science*, *62*, 131–143, 2005.

Chen, K., G. Gawarkiewicz, Y.-O. Kwon, and W. G. Zhang, The role of atmospheric forcing versus ocean advection during the extreme warming of the Northeast U.S. continental shelf in 2012, *Journal of Geophysical Research*, pp. n/a–n/a, 2015.

Cooke, S. J., S. Iverson, M. Stokesbury, S. Hinch, A. Fisk, D. VanderZwaag, R. Apostle, and F. Whoriskey, Ocean Tracking Network Canada: A network approach to addressing critical issues in fisheries and resource management with implications for ocean governance, *Fisheries*, *36*, 583–592, 2011.

Core Writing Team, R., Pachauri, and A. Reisinger, *Climate Change 2007: Synthesis Report. Contribution of Working Groups I, II and III to the Fourth Assessment Report of the Intergovernmental Panel on Climate Change*, IPCC, Geneva, Switzerland, 2007.

Csanady, G. T., Barotropic currents over the continental shelf, *Journal of Physical Oceanography*, *4*, 357–371, 1974.

Csanady, G. T., *Circulation in the Coastal Ocean*, Springer, 1982.

Cushman-Roisin, B., and J.-M. Beckers, *Introduction to Geophysical Fluid Dynamics Partim I: Physical Aspects*, Academic press, 2009.

Dee, D. P., S. M. Uppala, A. J. Simmons, P. Berrisford, P. Poli, S. Kobayashi, U. Andrae, M. A. Balmaseda, G. Balsamo, P. Bauer, P. Bechtold, A. C. M. Beljaars, L. van de Berg, J. Bidlot, N. Bormann, C. Delsol, R. Dragani, M. Fuentes, A. J. Geer, L. Haimberger, S. B. Healy, H. Hersbach, E. V. Hólm, L. Isaksen, P. Kållberg, M. Köhler, M. Matricardi, A. P. McNally, B. M. Monge-Sanz, J.-J. Morcrette, B.-K. Park, C. Peubey, P. de Rosnay, C. Tavolato, J.-N. Thépaut, and F. Vitart, The era-interim reanalysis: configuration and performance of the data assimilation system, *Quarterly Journal of the Royal Meteorological Society*, *137*, 553–597, 2011.

Dever, M., D. Hebert, B. J. W. Greenan, J. Sheng, and P. C. Smith, Hydrography and coastal circulation along the Halifax Line and the connections with the Gulf of St. Lawrence, *Atmosphere-Ocean*, *54*, 199–217, 2016.

Døving, K. B., and O. B. Stabell, *Trails in Open Waters: Sensory Cues in Salmon Migration*, pp. 39–52, Springer New York, New York, NY, 2003.

Drinkwater, K., B. Petrie, and W. Sutcliffe, Seasonal geostrophic volume transports along the Scotian Shelf, *Estuarine and Coastal Marine Science*, *9*, 17–27, 1979.

El-Sabh, M. I., Oceanographic features, currents, and transport in Cabot Strait, *Journal of the Fisheries Research Board of Canada*, *34*, 516–528, 1977.

Emery, W. J., and R. Thomson, *Data Analysis Methods in Physical Oceanography*, New York, Elsevier, 2001, 2001.

Fay, C., M. Bartron, S. Craig, A. Hecht, J. Pruden, R. Saunders, T. Sheehan, and J. Trial, Status Review for Anadromous Atlantic Salmon (Salmo salar) in the United States, *Report to the National Marine Fisheries Service and U.S. Fish and Wildlife Service*, p. 294, 2006.

Fong, D. A., and W. R. Geyer, Response of a river plume during an upwelling favorable wind event, *Journal of geophysical research*, *106*, 1067–1084, 2001.

Franks, P. J., Sink or swim: Accumulation of biomass at fronts, *Marine ecology progress series*, *82*, 1–12, 1992.

Friedland, K. D., L. P. Hansen, D. A. Dunkley, and J. C. MacLean, Linkage between ocean climate, post-smolt growth, and survival of Atlantic Salmon (Salmo salar L.) in the North Sea area, *ICES Journal of Marine Science: Journal du Conseil*, *57*, 419–429, 2000.

Friedland, K. D., G. Chaput, and J. C. MacLean, The emerging role of climate in post-smolt growth of Atlantic salmon, *ICES Journal of Marine Science*, *62*, 1338–1349, 2005.

Friedland, K. D., J. P. Manning, J. S. Link, G. J. R., A. T. Gilbert, and A. F. O'Connell, Variation in wind and piscivorous predator fields affecting the survival of Atlantic salmon, Salmo salar, in the Gulf of Maine, *Fisheries Management and Ecology*, *19*, 22–35, 2012.

Furey, N. B., S. P. Vincent, S. G. Hinch, and D. W. Welch, Variability in migration routes influences early marine survival of juvenile Salmon Smolts, *PLoS ONE*, *10*, 2015.

Galbraith, P. S., J. Chassé, P. Larouche, D. Gilbert, D. Brickman, B. Pettigrew, L. Devine, and C. Lafleur, Physical oceanographic conditions in the Gulf of St. Lawrence in 2012, *DFO Can. Sci. Advis. Sec. Res. Doc.*, *2013/026*, v + 89p., 2013.

Galbraith, P. S., J. Chassé, D. Gilbert, P. Larouche, C. Caverhill, D. Lefaivre, D. Brickman, B. Pettigrew, L. Devine, and C. Lafleur, Physical oceanographic conditions in the Gulf of St. Lawrence in 2013, *DFO Can. Sci. Advis. Sec. Res. Doc.*, *2014/062*, vi + 84p, 2014.

Gatien, M. G., A study in the slope water region south of Halifax, *Journal of the Fisheries Research Board of Canada*, *33*, 2213–2217, 1976.

Geshelin, Y., J. Sheng, and R. J. Greatbatch, Monthly mean climatologies of temperature and salinity in the western North Atlantic, *Canadian Data Report of Hydrography and Ocean Sciences*, *153*, vi + 62p, 1999.

Gilbert, D., and B. Pettigrew, Interannual variability (1948-1994) of the CIL core temperature in the Gulf of St. Lawrence, *Canadian Journal of Fisheries and Aquatic Sciences*, *54*, 57–67, 1997.

Gill, A. E., *Atmosphere-Ocean Dynamics*, vol. 30, Academic press, 1982.

Gruber, N., and J. L. Sarmiento, Global patterns of marine nitrogen fixation and denitrification, *Global Biogeochemical Cycles*, *11*, 235–266, 1997.

Han, G., and J. W. Loder, Three-dimensional seasonal-mean circulation and hydrography on the eastern Scotian Shelf, *Journal of Geophysical Research*, *108*, 1–21, 2003.

Han, G., C. Hannah, J. Loder, and P. Smith, Seasonal variation of the three-dimensional mean circulation over the Scotian Shelf, *Journal of Geophysical Research*, *102*, 1011–1025, 1997.

Handeland, S. O., A. K. Imsland, and S. O. Stefansson, The effect of temperature and fish size on growth, feed intake, food conversion efficiency and stomach evacuation rate of Atlantic salmon post-smolts, *Aquaculture*, *283*, 36–42, 2008.

Hannachi, A., I. T. Jolliffe, and D. B. Stephenson, Empirical orthogonal functions and related techniques in atmospheric science: A review, *International Journal of Climatology*, *27*, 1119–1152, 2007.

Hayes, S., and J. Kocik, Comparative estuarine and marine migration ecology of Atlantic salmon and steelhead: blue highways and open plains, *Reviews in Fish Biology and Fisheries*, *24*, 757–780, 2014.

Hebert, D., R. Pettipas, D. Brickman, and M. Dever, Meteorological, sea ice and physical oceanographic conditions on the Scotian Shelf and in the Gulf of Maine during 2012, *DFO Can. Sci. Advis. Sec. Res. Doc.*, *2013/058*, v +46p, 2013.

Holbrook, C. M., M. T. Kinnison, and J. Zydlewski, Survival of migrating Atlantic salmon smolts through the Penobscot River, Maine: a prerestoration assessment, *Transactions of the American Fisheries Society*, *140*, 1255–1268, 2011.

Horel, J. D., Complex principal component analysis: Theory and examples, *Journal of Climate and Applied Meteorology*, *23*, 1660–1673, 1984.

Houghton, R. W., and J. Marra, Physical/biological structure and exchange across the thermohaline shelf/slope front in the New York Bight, *J. Geophys. Res*, *88*, 4467–4481, 1983.

Hussey, N. E., S. T. Kessel, K. Aarestrup, S. J. Cooke, P. D. Cowley, A. T. Fisk, R. G. Harcourt, K. N. Holland, S. J. Iverson, and J. F. Kocik, Aquatic animal telemetry: a panoramic window into the underwater world, *Science*, *348*, 1255642–1 – 1255642–10, 2015.

ICES, Report of the working group on north Atlantic salmon (wgnas), 17-26 March, Moncton, Canada. ices cm 2015/acom:09. 332 pp, 2015.

Johnson, W. R., T. C. Royer, and J. L. Luick, On the seasonal variability of the Alaska Coastal Current, *Journal of Geophysical Research*, *93*, 12423–12437, 1988.

Judd, D. B., A maxwell triangle yielding uniform chromaticity scales, *Journal of the Optical Society of America*, *25*, 24–35, 1935.

Kessel, S., S. Cooke, M. Heupel, N. Hussey, C. Simpfendorfer, S. Vagle, and A. Fisk, A review of detection range testing in aquatic passive acoustic telemetry studies, *Reviews in Fish Biology and Fisheries*, *24*, 199–218, 2014.

Khatiwala, S. P., R. G. Fairbanks, and R. W. Houghton, Freshwater sources to the coastal ocean off northeastern North America: Evidence from $H_2{}^{18}O/H_2{}^{16}O$, *Journal of Geophysical Research*, *104*, 18241–18255, 1999.

King M., A. J., Fenton D., and S. A., Offshore Ecologically and Biologically Significant Areas in the Scotian Shelf Bioregion, *DFO Can. Sci. Advis. Sec. Res. Doc.*, *2016/007*, viii+ 92p, 2016.

Kocik, J. F., J. P. Hawkes, T. F. Sheehan, P. A. Music, and K. F. Beland, Assessing estuarine and coastal migration and survival of wild Atlantic salmon smolts from the Narraguagus River, Maine using ultrasonic telemetry, in *Challenges for diadromous fishes in a dynamic global envi-ronment*, edited by A. Haro, K. L. Smith, R. A. Rulifson, C. M. Moffittand, R. J.Klauda, M. J. Dadswell, R. A. C. J. E. Cooper, K. L. Beal, and T. S.Avery, vol. 69, pp. 293–310, Maryland, Bethesda, 2009.

Large, W., and S. Pond, Open ocean momentum flux measurements in moderate to strong winds, *Journal of Physical Oceanography*, *11*, 324–336, 1981.

Le Fevre, J., Aspects of the biology of frontal systems, *Advances in marine biology*, *23*, 163–299, 1986.

Lentz, S. J., and K. R. Helfrich, Buoyant gravity currents along a sloping bottom in a rotating fluid, *Journal of Fluid Mechanics*, *464*, 251–278, 2002.

Lentz, S. J., and J. Largier, The influence of wind forcing on the Chesapeake Bay buoyant coastal current, *Journal of Physical Oceanography*, *36*, 1305–1316, 2006.

Loder, J., G. Han, C. Hannah, D. Greenberg, and P. Smith, Hydrography and baroclinic circulation in the Scotian Shelf region: winter versus summer, *Can. J. Fish. Aquat. Sci.*, *54 (Suppl. 1)*, 40–56, 1997.

Loder, J., C. Hannah, B. Petrie, and E. Gonzalez, Hydrographic and transport variability on the Halifax section, *Journal of Geophysical Research*, *108 (C11)*, 1–18, 2003.

MacKenzie, K. M., C. N. Trueman, M. R. Palmer, A. Moore, A. T. Ibbotson, W. R. Beaumont, and I. C. Davidson, Stable isotopes reveal age-dependent trophic level and spatial segregation during adult marine feeding in populations of salmon, *ICES Journal of Marine Science*, pp. 1054–3139, 2012.

Mann, C., A summary of variability observed with monitoring sections off the east and west coasts of Canada, *Progress in Oceanography*, *5*, 17–30, 1969.

Mann, C., and G. Needler, Effect of aliasing on studies of long-term oceanic variability off Canada's coasts, *Journal of the Fisheries Board of Canada*, *24*, 1827–1831, 1967.

Margules, M., Über temperaturschichtung in stationär bewegter und ruhender luft, *Hann-Band. Meteor. Z*, *23*, 243–254, 1906.

Mazzini, P. L. F., J. A. Barth, R. K. Shearman, and A. Erofeev, Buoyancy-driven coastal currents off Oregon during fall and winter, *Journal of Physical Oceanography*, *44*, 2854–2876, 2014.

McDougall, T., and P. Barker, Getting started with TEOS-10 and the Gibbs Seawater (GSW) oceanographic toolbox, *SCOR/IAPSO WG127*, p. 28, 2011.

McLellan, H. J., Temperature-salinity relations and mixing on the Scotian Shelf, *Journal of the Fisheries Board of Canada*, *11*, 419–430, 1954.

Mellor, G., Users guide for a three-dimensional, primitive equation, numerical ocean model, *Tech. rep.*, Atmospheric and Oceanic Sciences Program, Princeton University, 2004.

Mellor, G., and T. Yamada, Development of a turbulence closure model for geophysical fluid problems, *Reviews of Geophysics and Space Physics*, *20*, 851–875, 1982.

Merckelbach, L. M., R. D. Briggs, D. A. Smeed, and G. Griffiths, Current measurements from autonomous underwater gliders, *2008 IEEE/OES 9th Working Conference on Current Measurement Technology*, pp. 61–67, 2008.

Merrifield, M. A., and C. D. Winant, Shelf circulation in the Gulf of California: A description of the variability, *Journal of Geophysical Research*, *94*, 18133–18160, 1989.

Mesinger, F., G. DiMego, and E. e. a. Kalnay, North American regional reanalysis, *Bulletin of the American Meteorological Society*, *87*, 343–360, 2006.

Mills, K. E., A. J. Pershing, T. F. Sheehan, and D. Mountain, Climate and ecosystem linkages explain widespread declines in North American Atlantic salmon populations, *Global Change Biology*, *19*, 3046–3061, 2013.

Minke-Martin, V., J. Brian Dempson, T. F. Sheehan, and M. Power, Otolith-derived estimates of marine temperature use by West Greenland Atlantic salmon (Salmo salar), *ICES Journal of Marine Science: Journal du Conseil*, *72*, 2139–2148, 2015.

Moat, B., D. Smeed, C. Marcinko, S. Popinet, and S. Turnock, Flow distortion around underwater gliders and impacts on sensor measurements: a pilot study using large-eddy simulations, 2016.

Mork, K. A., J. Gilbey, L. P. Hansen, A. J. Jensen, J. A. Jacobsen, M. Holm, J. C. Holst, N. Ó Maoiléidigh, F. Vikebø, P. McGinnity, W. Melle, K. Thomas, E. Verspoor, and V. Wennevik, Modelling the migration of post-smolt Atlantic salmon (Salmo salar) in the Northeast Atlantic, *ICES Journal of Marine Science: Journal du Conseil*, *69*, 1616–1624, 2012.

Mork, M., Circulation Phenomena and Frontal Dynamics of the Norwegian Coastal Current, *Philosophical Transactions of the Royal Society of London A: Mathematical, Physical and Engineering Sciences*, *302*, 635–647, 1981.

Munchow, A., and R. W. Garvine, Buoyancy and wind forcing of a coastal current, *Journal of Marine Research*, *51*, 293–322, 1993.

Ohashi, K., and J. Sheng, Influence of St. Lawrence River discharge on the circulation and hydrography in Canadian Atlantic waters, *Continental Shelf Research*, *58*, 32–49, 2013.

Paloheimo, J. E., and P. F. Elson, Reduction of Atlantic salmon (Salmo salar) catches in Canada attributed to the Greenland fishery, *Journal of the Fisheries Research Board of Canada*, *31*, 1467–1480, 1974.

Pershing, A. J., M. A. Alexander, C. M. Hernandez, L. A. Kerr, A. Le Bris, K. E. Mills, J. A. Nye, N. R. Record, H. A. Scannell, and J. D. Scott, Slow adaptation in the face of rapid warming leads to collapse of the Gulf of Maine cod fishery, *Science*, *350*, 809–812, 2015.

Petrie, B., The Halifax section: A brief history, *Atlantic Zone Monitoring Program Bulletin*, pp. 26–29, 2004.

Petrie, B., Does the North Atlantic Oscillation affect hydrographic properties on the Canadian Atlantic continental shelf?, *Atmosphere-Ocean*, *45*, 141–151, 2007.

Petrie, B., and K. Drinkwater, Temperature and salinity variability on the Scotian Shelf and in the Gulf of Maine 1945–1990, *Journal of Geophysical Research: Oceans*, *98*, 20079–20089, 1993.

Pickart, R. S., T. K. McKee, D. J. Torres, and S. A. Harrington, Mean structure and interannual variability of the slopewater system south of Newfoundland, *Journal of Physical Oceanography*, *29*, 2541–2558, 1999.

Powell, M. D., V. P. J, and T. A. Reinhold, Reduced drag coefficient for high wind speeds in tropical cyclones, *Nature*, *422*, 279–283, 2003.

Reddin, D., and W. Shearer, Sea-surface temperature and distribution of Atlantic salmon in the Northwest Atlantic Ocean., in *American Fisheries Society Symposium*, vol. 1, pp. 262–275, 1987.

Renkawitz, M. D., T. F. Sheehan, H. Dixon, and R. Nygaard, Changing trophic structure and energy dynamics in the Northwest Atlantic: implications for Atlantic salmon feeding at West Greenland, *Marine Ecology Progress Series*, *538*, 197–211, 2015.

Robertis, A. D., C. A. Morgan, R. A. Schabetsberger, R. W. Zabel, R. D. Brodeur, R. L. Emmett, C. M. Knight, G. K. Krutzikowsky, and E. Casillas, Columbia River plume fronts. II. Distribution, abundance, and feeding ecology of juvenile salmon, *Marine Ecology Progress Series*, *299*, 33–44, 2005.

Rogers, E. C., Modelling the movement of marine particles in discrete time and space with application to Scotian Shelf connectivity, Master's thesis, Dalhousie University, 2015.

Sætre, R., *The Norwegian Coastal Current*, Tapir Academic Press, 2007.

Sanders, T. M., and R. W. Garvine, Fresh water delivery to the continental shelf and subsequent mixing: An observational study, *Journal of Geophysical Research*, *106*, 27087–27101, 2001.

Sandstrom, H., On the wind-induced sea level changes on the Scotian shelf, *Journal of Geophysical Research*, *85*, 461–468, 1980.

Sandstrom, H., and J. A. Elliott, Internal tide and solitons on the Scotian Shelf: A nutrient pump at work, *Journal of Geophysical Research*, *89*, 6415–6426, 1984.

Sarmiento, J. L., N. Gruber, M. A. Brzezinski, and J. P. Dunne, High-latitude controls of thermocline nutrients and low latitude biological productivity, *Nature*, *427*, 56–60, 2004.

Schwing, F. B., Subtidal response of the Scotian Shelf bottom pressure field to meteorological forcing, *Atmosphere-Ocean*, *27*, 157–180, 1989.

Schwing, F. B., Subtidal response of Scotian Shelf circulation to local and remote forcing. I: Observations, *Journal of physical oceanography*, *22*, 523–541, 1992a.

Schwing, F. B., Subtidal response of Scotian Shelf circulation to local and remote forcing. II: barotropic model, *Journal of physical oceanography*, *22*, 542–563, 1992b.

Shan, S., Eulerian and Lagrangian Studies of Circulation on the Scotian Shelf and Adjacent Deep Waters of the North Atlantic with Biological Implications, Ph.D. thesis, Dalhousie University, 2016.

Shan, S., J. Sheng, and B. J. W. Greenan, Modelling study of three-dimensional circulation and particle movement over the Sable Gully of Nova Scotia, *Ocean Dynamics*, *64*, 117–142, 2014a.

Shan, S., J. Sheng, and B. J. W. Greenan, Physical processes affecting circulation and hydrography in the Sable Gully of Nova Scotia, *Deep Sea Research Part II: Topical Studies in Oceanography*, *104*, 35–50, 2014b.

Shan, S., J. Sheng, K. Ohashi, and M. Dever, Assessing the performance of a multi-nested ocean circulation model using satellite remote sensing and in situ observations, *Satellite Oceanography and Meteorology*, *1*, 2016.

Sheng, J., Dynamics of a buoyancy-driven coastal jet: The Gaspé Current, *Journal of Physical Oceanography*, *31*, 3146–3162, 2001.

Smagorinsky, J., General circulation experiments with the primitive equations, *Monthly Weather Review*, *91*, 99–164, 1963.

Smith, P., and F. Schwing, Mean circulation and variability on the Eastern Canadian continental shelf, *Continental Shelf Research*, *11*, 977–1012, 1991.

Smith, P., B. Petrie, and C. Mann, Circulation, variability, and dynamics of the Scotian Shelf and slope, *Journal of the Fisheries Board of Canada*, *35*, 1067–1083, 1978.

Stich, D. S., M. M. Bailey, and J. D. Zydlewski, Survival of Atlantic salmon Salmo salar smolts through a hydropower complex, *Journal of Fish Biology*, *85*, 1074–1096, 2014.

Stich, D. S., G. B. Zydlewski, J. F. Kocik, and J. D. Zydlewski, Linking behavior, physiology, and survival of Atlantic salmon smolts during estuary migration, *Marine and Coastal Fisheries*, *7*, 68–86, 2015.

Sutcliffe, W. H. J., R. H. Loucks, and K. F. Drinkwater, Coastal circulation and physical oceanography of the Scotian Shelf and the Gulf of Maine, *Journal of the Fisheries Research Board of Canada*, *33*, 98–115, 1976.

Therriault, J., B. Petrie, P. Pepin, J. Gagnon, D. Gregory, J. Helbig, D. Lefaivre, M. Mitchell, B. Pelchat, J. Runge, and D. Sameoto, Proposal for a Northwest Atlantic zonal monitoring program, *Canadian technical report of hydrography and ocean sciences*, *194*, 1998.

Thomas, J. B., *An Introduction to Statistical Communication Theory*, John Wiley & Sons, 1969.

Thompson, K. R., and J. Sheng, Subtidal circulation on the Scotian Shelf: Assessing the hindcast skill of a linear, barotropic model, *Journal of Geophysical Research*, *102*, 24987–25003, 1997.

Thomson, K. A., W. J. Ingraham, M. C. Healey, P. H. Leblond, C. Groot, and C. G. Healey, The influence of ocean currents on latitude of landfall and migration speed of sockeye salmon returning to the Fraser River, *Fisheries Oceanography*, *1*, 163–179, 1992.

Todd, C. D., S. L. Hughes, C. Marshall, J. C. MacLean, M. E. Lonergan, and E. Biuw, Detrimental effects of recent ocean surface warming on growth condition of Atlantic salmon, *Global Change Biology*, *14*, 958–970, 2008.

Todd, R. E., D. L. Rudnick, and R. E. Davis, Monitoring the greater San Pedro Bay region using autonomous underwater gliders during fall of 2006, *Journal of Geophysical Research: Oceans (1978–2012)*, *114*, 2156–2202, 2009.

Umoh, J. U., and K. R. Thompson, Surface heat flux, horizontal advection, and the seasonal evolution of water temperature on the scotian shelf, *Journal of Geophysical Research*, *99*, 20403–20416, 1994.

Urrego-Blanco, J., Subtidal circulation, hydrography, sea ice and associated variability over the Eastern Canadian shelf using a coupled ocean-ice model, Ph.D. thesis, Dalhousie University, 2014.

Urrego-Blanco, J., and J. Sheng, Interannual Variability of the circulation over the Eastern Canadian Shelf, *Atmosphere-Ocean*, *50*, 277–300, 2012.

Urrego-Blanco, J., and J. Sheng, Study on subtidal circulation and variability in the Gulf of St. Lawrence, Scotian Shelf, and Gulf of Maine using a nested-grid shelf circulation model, *Ocean Dynamics*, *64*, 385–412, 2014.

Vikebø, F., S. Sundby, B. Ådlandsvik, and Ø. Fiksen, The combined effect of transport and temperature on distribution and growth of larvae and pelagic juveniles of Arcto-Norwegian cod, *ICES Journal of Marine Science: Journal du Conseil*, *62*, 1375–1386, 2005.

Vikebø, F., S. Sundby, B. Ådlandsvik, and O. Otterå, Impacts of a reduced thermohaline circulation on transport and growth of larvae and pelagic juveniles of Arcto-Norwegian cod (Gadus morhua), *Fisheries Oceanography*, *16*, 216–228, 2007.

Von Storch, H., and F. W. Zwiers, *Statistical Analysis in Climate Research*, Cambridge University Press, 2001.

Whitney, M. M., and R. W. Garvine, Wind influence on a coastal buoyant outflow, *Journal of Geophysical Research: Oceans*, *110*, 1–15, 2005.

Williams, C. D., R. Bachmayer, and B. deYoung, Progress in predicting the performance of ocean gliders from at-sea measurements, in *OCEANS 2008*, pp. 1–8, 2008.

Yankovsky, A. E., and D. C. Chapman, A simple theory for the fate of buoyant coastal discharges, *Journal of Physical oceanography*, *27*, 1386–1401, 1997.

Yankovsky, A. E., B. M. Hickey, and A. K. Münchow, Impact of variable inflow on the dynamics of a coastal buoyant plume, *Journal of Geophysical Research*, *106*, 19809–19824, 2001.

Zydlewski, G. B., A. Haro, and S. D. McCormick, Evidence for cumulative temperature as an initiating and terminating factor in downstream migratory behavior of Atlantic salmon (Salmo salar) smolts, *Canadian Journal of Fisheries and Aquatic Sciences*, *62*, 68–78, 2005.